Durham E-Theses

Development and experimental analysis of a micromachined Resonant Gyrocope

Young, Michael

How to cite:

Young, Michael (1999) *Development and experimental analysis of a micromachined Resonant Gyrocope*, Durham theses, Durham University. Available at Durham E-Theses Online: http://etheses.dur.ac.uk/4313/

Use policy

The full-text may be used and/or reproduced, and given to third parties in any format or medium, without prior permission or charge, for personal research or study, educational, or not-for-profit purposes provided that:

- a full bibliographic reference is made to the original source
- a link is made to the metadata record in Durham E-Theses
- the full-text is not changed in any way

The full-text must not be sold in any format or medium without the formal permission of the copyright holders.

Please consult the full Durham E-Theses policy for further details.

Academic Support Office, Durham University, University Office, Old Elvet, Durham DH1 3HP
e-mail: e-theses.admin@dur.ac.uk Tel: +44 0191 334 6107
http://etheses.dur.ac.uk

Development and Experimental Analysis of a Micromachined Resonant Gyroscope

Michael Young BSc.
School of Engineering
University of Durham

The copyright of this thesis rests with the author. No quotation from it should be published without the written consent of the author an information derived from it should be acknowledged.

A thesis submitted to the University of Durham
for the Degree of Doctor of Philosophy
Summer 1999

2 4 AUG 1999

ABSTRACT

This thesis is concerned with the development and experimental analysis of a resonant gyroscope. Initially, this involved the development of a fabrication process suitable for the construction of metallic microstructures, employing a combination of nickel electroforming and sacrificial layer techniques to realise free-standing and self-supporting mechanical elements. This was undertaken and achieved.

Simple beam elements of typically 2.7mm x 1mm x 40μm dimensions have been constructed and subject to analysis using laser doppler interferometry. This analysis tool was used to implement a full modal analysis in order to experimentally derive dynamic parameters. The characteristic resonance frequencies of these cantilevers have been measured, with 3.14kHz, 23.79kHz, 37.94kHz and 71.22kHz being the typical frequencies of the first four resonant modes. Q-factors of 912, 532, 1490 and 752 have been measured for these modes respectively at 0.01mbar ambient pressure. Additionally the mode shapes of each resonance was derived experimentally and found to be in excellent agreement with finite element predictions.

A 4mm nickel ring gyroscope structure has been constructed and analysed using both optical analysis tools and electrical techniques. Using laser doppler interferometry the first four out-of-plane modes of the ring structure were found to be typically 9.893 kHz, 11.349 kHz, 11.418 kHz and 13.904 kHz with respective Q-factors of 1151, 1659, 1573 and 1407 at 0.01 mbar ambient pressure. Although electrical measurements were found to be obscured through cross coupling between drive and detection circuitry, the in-plane operational modes of the gyroscope were sucessfully determined. The Cos2θ and Sin2θ operational modes were measured at 36.141 kHz and 36.346 kHz, highlighting a frequency split of 205kHz. Again all experimentally derived modal parameters were in good agreement with finite element predictions. Furthermore, using the analysis model, the angular resolution of the gyroscope has been predicted to be approximately 4.75°/s.

For my mother and father.

The copyright of this thesis rests with the author. No quotation from it should be published without their prior written consent and information derived from it should be acknowledged.

ACKNOWLEDGEMENTS

Firstly, I would like to acknowledge the contribution of my supervisor Dr. David Wood, for all his support and encouragement throughout the last four years. I would also like to thank the Durham University Society for sponsoring my Ph.D. studies.

I would also like to thank Mr. John Gibson for his tireless assistance, in and out of the cleanroom, which was much appreciated. In addition I would like to thank the members of the engineering workshop for all the help and advice that they offered.

Also I would like to thank all the members of my research group, and all those other people in the department and the rest of the University that have made the past four years so pleasurable.

Finally, and most importantly, I would like to thank my family, especially my parents for all their love, support and encouragement.

DECLARATION

I declare that no material in this thesis has previously been submitted for a degree at this or any other university.

The initial design of the ring gyroscope structure presented in chapter seven is the work of Professor J.S. Burdess of the University of Newcastle Upon Tyne.

Table of Contents

Chapter One
Introduction

1.1 MicroElectroMechanical Systems (MEMS)

Microelectromechanical systems or MEMS is an emerging technology that has gradually developed over the last four decades. The technology, which has evolved from within the microelectronics industry, offers the capability to construct great numbers of miniature sensors and actuators with sub-millimetre dimensions and sub-micron accuracy. The ability to engineer components on this scale can only be appreciated with an understanding of the dimensions involved; device feature sizes are typically 10-1000μm, in comparison with the width of a single human hair, 150-200μm.

The potential of this technology is vast and virtually unlimited. With fabrication processes evolving constantly it is now possible to construct devices of increasing complexity with increasing accuracy. With a large number of applications identified for such devices, development of new and improved products continues at a rapid pace.

The initial development of a silicon-based microsensor was initiated in the early 1950's with the discovery of a piezoresistive effect in silicon. Combined with the excellent mechanical properties of single crystal silicon (a material stronger than steel and lighter than aluminium), this offered the prospect of developing simple mechanical sensors with integrated strain gauges. It was recognised that such devices had a great potential. This potential was first realised in the 1970's with the development of the first low-cost, practical and reliable pressure transducer. As part of a US government objective to increase the fuel economy of passenger vehicles and reduce pollution, the first manifold absolute pressure transducers (MAPs) were introduced. These were used as an integral part of engine management systems that allowed tighter control of efficiency by monitoring fuel stoichiometry (ratio of fuel to air). With widespread application of these systems the desired aims were achieved; fuel economy increased from an average of 10 mpg in 1974 to 27.5 mpg in 1994 with significant pollution reduction [1]. These first devices were produced by Honeywell for General Motors in 1976.

The MEMS industry is driven by the virtue that significant cost reduction can be obtained through miniaturisation and batch fabrication. This involves constructing a large number of identical devices on a single wafer and processing a large number of wafers in a single batch. For example, Lucas NovaSensor produces 6000 pressure sensors (with a die area of $1mm^2$) on a single 4-inch wafer. In a batch of 25 wafers this yields 150,000 sensors in a single process run. This high volume capability, which leads to low unit cost, cannot be matched by any other technology. Miniaturisation also overcomes some of the restrictions imposed by the size and weight of traditional devices, allowing widespread application in low-cost consumer areas.

The rapid development of this technology has been further aided by the close support of the microelectronics industry. The MEMS industry has evolved using established fabrication techniques that have already been highly developed. Additional support has included the availability of high purity raw materials, commercially available manufacturing equipment and design tools, and access to a large source of educated personnel. In addition, the close alliance of the two industries allows the integration of silicon microsensor and signal conditioning electronics onto a single silicon chip, allowing the production of complete microsystems.

The significance assigned to this technology is highlighted by the massive government investment that has been made in MEMS in various countries. In particular US MEMS units have received massive funds from government agencies, such as NASA who funded most of the early projects. MEMS activities are also heavily supported in Germany and Japan. The impact of such heavy investment can now be seen in the commercial market; in 1995 the total revenue for the world sensor market (broken-down in table 1.1) was estimated at 6 billion US dollars, 25% of which was attributed to MEMS technology [1]. This is remarkable considering the relative infancy of the industry.

Application	% Market
Pressure	40 %
Temperature	25 %
Acceleration	16 %
Flow	9 %
Force	5 %

Table 1.1. *Breakdown of world sensor market.*

1.2 MEMS Applications

In the past it has been only the pressure sensor, and more recently the accelerometer, that have achieved commercial success. However with the emergence of new technology and increased application, the total MEMS market is expected to grow rapidly over the next decade, with a predicted market increase of 460% between 1995 and 2005 [1]. This growth will involve both increased application of current devices (the pressure sensor and the accelerometer, which currently constitutes 97% of the total MEMS market) and the introduction of new products.

MEMS is a very diverse, multi-discipline research field that encompasses most areas of science and technology. However, the main areas of interest that are expected to lead to future commercialisation can be categorised below:

Pressure Sensors

Since its initial introduction, pressure sensor technology has been continually developed and refined using new materials, technologies and operating principles. This has led to the development and commercialisation of a large variety of devices that can operate over a broad spectrum of conditions. Pressure sensors still dominate the commercial MEMS market, holding a 67% share [1]. Future applications are anticipated to further increase application, especially in the automotive industry with the expected introduction of fuel vapour sensing and electronic braking. Current manufacturers include numerous Silicon Valley (California, US) companies such as Lucus NovaSensor and Motorola, and UK based Druck.

Inertial sensors

On the back of the overwhelming success of the silicon pressure sensor, the accelerometer was the next device to develop into a mature commercial product. The main application of these devices has again been in the automotive industry for the development of air bag safety systems. The role of the accelerometer is to detect the rapid accelerations associated with high-speed impacts and to initiate the deployment of restraint and protection systems. Similar devices have also been exploited to detect other parameters such as force and fluid flow. Although the introduction of the micromachined accelerometer is only relatively recent, its impact has been enormous and is reflected in a 28% share of the total MEMS market. These structures have been extensively developed using a number of different fabrication techniques and are manufactured by a variety of companies. Again, the highest density of manufacturers is located in Silicon Valley and includes Analogue Devices and Motorola [2].

With micromachined accelerometers now also a highly developed and proven technology, interest has now turned towards the development of a second type of inertial sensor, the gyroscope. Gyroscopes are devices that detect rotational motion and micromachined versions have a potentially vast area of application. Gyroscope technology has not, as yet, developed to a commercial level owing to the increased complexity of the sensing element. However, system performance is improving constantly and it is expected that such transducers will be the next to be fully exploited.

Applications include active suspension control for sports and passenger vehicles, camcorder control, inertial pointers and virtual reality sensors [3].

Optical MEMS

The precision of micromachining technology lends itself to the pursuit of micro-optics. Systems include fibre optic aligners, torsional mirrors for optical switching, adaptive mirrors for optical processing and micro-mirror arrays for projection displays. Most of these structures have not been developed to a commercial level, but the activity still accounts for 0.7% of the current MEMS market.

Fluidics

One of the first examples of a micromachined fluid handling system was the ink-jet nozzle developed by IBM in the early 1970's. Since then interest in this field has been modest until quite recently with the development of a series of structures designed to undertake a variety of fluidic functions. Interest has driven the development of discrete components such as micro-pumps, micro-valves, mixers and filters, and also complete fluid handling systems consisting of all these elements [4]. Current systems account for only 0.7% of the total MEMS market, but with the likelihood of future high-volume applications, such as fuel injection and hydraulic suspension control in automotive systems, this is expected to rapidly increase.

Biotechnology

There are needs in the discipline of biotechnology for the manipulation of biological species, such as cells, chromosomes, DNA and protein molecules. Example applications include the separation and identification of bacteria from blood samples; current analysis techniques take days to complete whereby a MEMS analysis tool has the potential to complete such tests in a matter of few minutes [5]. The development of such systems is hoped to lead to the elusive 'laboratory-on-a-chip' that could replace traditional chemical analysis techniques leading to significant improvements of cost and performance. At the time of writing no such devices are commercially manufactured.

1.3 Thesis Outline

The long-term aim of this research has been the development of a fabrication process suitable for the manufacture of micromachined sensors and actuators. Although the whole range of micromachining activities is very diverse, the bias of this research has been towards gyroscope technology, due largely to the previous experience of the MEMS research group at Durham. A great number of applications have been identified for micromachined gyroscopes. These include smart munitions for the military, free space pointers and smart robots in the commercial sector, and active suspension and anti-skid systems in the automotive industry. Although these applications have been identified for some time, the technology to construct the devices has not been available. It is only with recent technological advances and the intensive development of the accelerometer and pressure sensor that interest has now turned to such devices.

This thesis presents the development and evaluation of a nickel ring gyroscope. Prior to the construction of these devices it was necessary to develop and optimise a fabrication process suitable for the purpose. With this in mind it was necessary to conduct a review of current micromachining process technology which is presented in chapter two. This includes examples of traditional wet etching techniques, conventional bulk machining, surface micromachining technology and a review of modern high aspect ratio techniques.

Chapters three and four present a summary of the complete fabrication process that has been developed at Durham for the construction of metallic microstructures. A large proportion of research time was dedicated to its development and this is reflected in the amount of detail presented. Test samples are fabricated and analysed.

Chapter five documents the optical analysis of simple test structures. This provides an assessment of the fabrication process and allows the dynamic properties of the test samples to be evaluated by comparison with finite element predictions. The study employs laser Doppler vibrometery, the theory of which is discussed prior to the experimental results.

As from the onset it was always intended that the fabrication process would be demonstrated by manufacturing a resonant gyroscope, a review of current gyroscope technology was conducted and is presented in chapter six. This includes a description of traditional devices such as the well-known rotating wheel gyroscope, the modern inertial instrument and vibratory devices.

Chapter seven discusses the theory and finite element analysis of shell-type gyroscopes with special reference to ring devices. The design of a particular micromechanical ring gyroscope is discussed together with actuation and sensing mechanisms. Finite element analysis is required to evaluate the performance of the device prior to manufacture and allows experimental results to be compared to theory.

Chapter eight presents all the experimental results collected from the analysis of the nickel ring devices. This data includes optical determination of resonant frequencies and modeshapes and also electrical measurements of in-plane motion. Comparison with finite element predictions provides the basis of final evaluation.

Finally, chapter nine presents the conclusions of the research and provides suggestions for future work.

Chapter Two

MEMS Fabrication Technology

This chapter highlights the different types of micromachining techniques that are used to construct micromechanical devices. The vast majority of published literature concerns devices constructed through either bulk micromachining of silicon, or polysilicon surface micromachining. These techniques have been developed exhaustively over the past few decades and have been demonstrated in the fabrication (and in some cases commercial manufacture) of a vast range of microdevices. These processes are described in the following subsections.

With new processes developing continuously it is now becoming possible to fashion mechanical elements with increasing levels of dimensional control. These newer processes in general allow the production of very tall microstructures without loss of lateral resolution. High aspect ratio techniques can either enhance existing techniques or are designed to replace them completely; these processes are also described.

2.1 Traditional Micromachining Techniques

Bulk etching of silicon and polysilicon surface micromachining can be regarded as the traditional micromachining techniques although both only have a very short history - the first bulk and surface micromachined devices did not appear until the end of the 1960's [6]. Bulk micromachining involves the selective removal of the substrate to construct mechanical elements directly from single crystal silicon. In contrast, surface micromachining employs the manipulation of surface deposited thin films to construct mechanical elements, using the silicon substrate only as a mechanical support and leaving it completely intact. Although the results obtained from each technique differ, both can be used effectively to construct mechanical devices with an order of magnitude greater accuracy than the best precision engineering techniques.

2.1.1 Bulk Micromachining

Bulk etching is most commonly achieved through either crystallographic etching or plasma etching. Both techniques are described in the following subsections.

2.1.1.1 Crystallographic Etching of Silicon

Anisotropic etching of single crystal silicon [6,7] can be achieved using alkaline solutions such as EDP (a mixture of ethylene diamine, pyrocatechol and water) or KOH. The silicon etch rate in these solutions is highly direction dependent; {111} planes within the single crystal lattice are etched at a significantly slower rate than {100}, {110} or higher order planes. This property allows highly defined structures to be etched into the silicon, the geometry of which depends greatly upon mask design, etch time and substrate orientation. The easiest features to machine are v-grooves and square shaped nozzles in {100} orientated silicon or vertical etching of prismatic features in

{110} silicon (figure 2.1). In all cases the position of the {111} planes within the crystal lattice determines the geometry of the final etch feature.

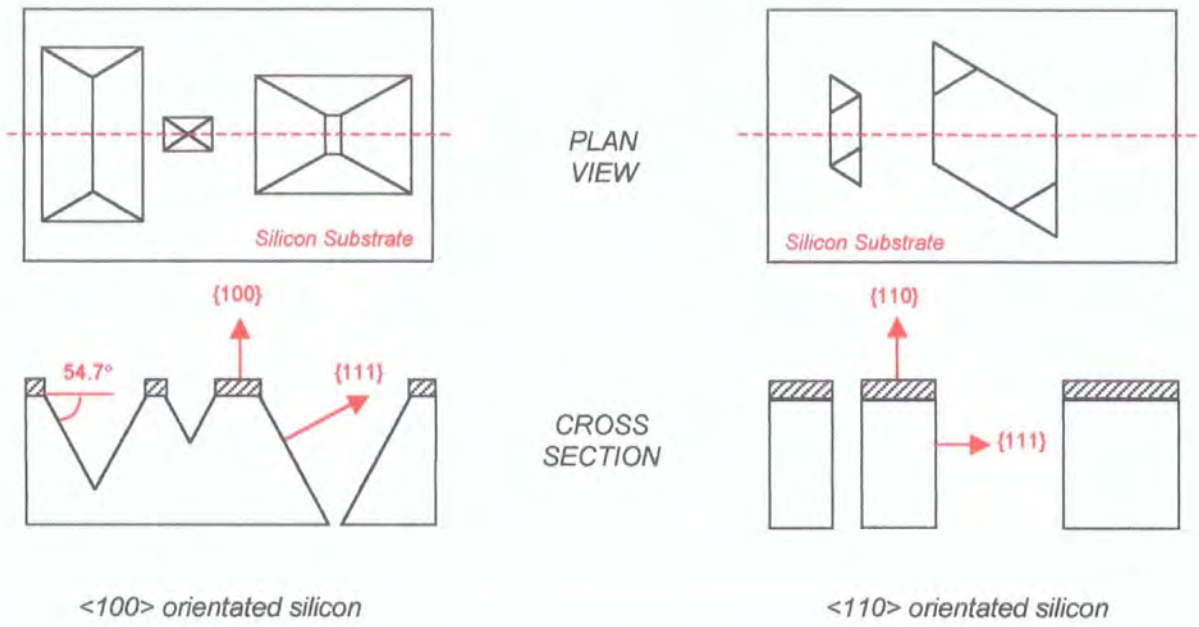

Figure 2.1. *Crystallographic etching of Silicon.*

The etch rate of {100} and {110} planes can be greatly influenced by the introduction of boron doping. At high levels (>4×10^{19} atoms/cm^3) the etch rate of these planes in both EDP and KOH is significantly reduced [8]. This property allows boron doped regions to act as etch stops, allowing the production of thin membranes in the silicon (typically 1-10μm thick) that can be machined to produce more flexible structures. Examples of the boron etch stop in practice are shown in figure 2.2.

The limitation of crystallographic etching is that the size and geometry of the etched structures is greatly restricted and determined by the location of the {111} planes. In general only very simple geometric designs can be machined. Another important factor is that although in principle the process should yield highly defined etch features, undercutting of external corners (these reveal higher order planes) leads to erratic etch

results. The effects of this problem can be reduced by the use of corner compensation techniques but this increases the complexity of mask designs. Crystallographic etching is nonetheless a very effective process for producing mechanical sensors including accelerometers [9], pressure sensors [10,11], gyroscopes [12], flow sensors and vapour sensors [13]. If, however, more intricate designs are required, other fabrication techniques must be used.

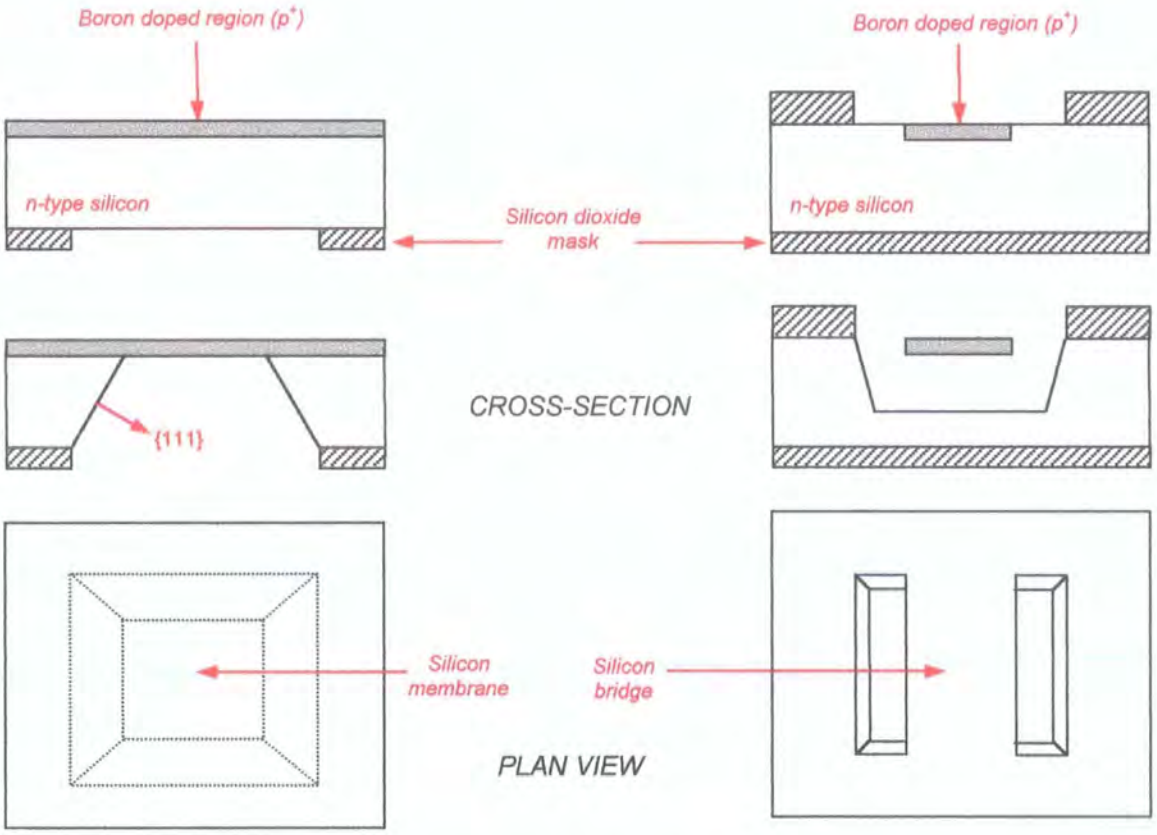

Figure 2.2. *Boron etch stop technique.*

2.1.1.2 Dry Etching of Silicon

Plasma etching of silicon involves the selective removal of the silicon substrate using gaseous species formed within a glow discharge. The mechanism of material removal depends upon the exact nature of the plasma process and is described in some detail in [14,15]. In general plasma etching of silicon is achieved through reactive ion etching

(RIE) using fluorine based chemistry (CF_4/O_2 or SF_6/O_2). The process can be considered as a combination of both physical ion bombardment and chemical reaction. The profiles of etched features depends upon the exact process conditions; a predominantly physical etch results in highly directional vertical etching at slow rates while a purely chemical etch is characterised by isotropic etching at high rates (figure 2.3). The specific process conditions must be tuned for particular requirements. RIE can be used for etching great depths but highly directional etching of silicon can only be maintained over limited depths of approximately 100μm [15]. For this reason, RIE of silicon is generally performed on previously thinned areas as described in the following subsection. The great advantage of RIE is that the geometry of etch features is free of crystallographic constraints and defined only by a suitable mask.

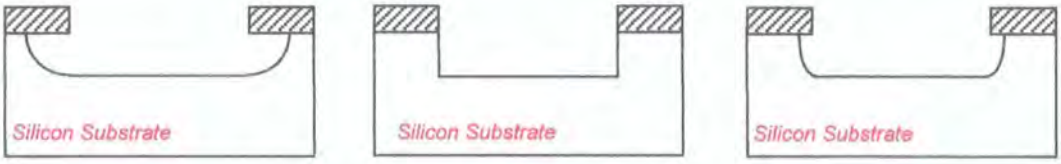

Figure 2.3. *RIE profiles: (a) isotropic, (b) anisotropic, (c) intermediate.*

2.1.1.3 Dissolved Wafer Technology

The dissolved wafer process uses a combination of wet and dry etching techniques [16,17]. It is a more complicated procedure employing crystallographic etching, reactive ion etching, boron doping and glass bonding, and is shown in figure 2.4. The first stage of the process defines the spacing between the final silicon structure and the glass substrate when the two are bonded. This is achieved by anisotropic etching, typically using KOH. The whole silicon surface is then boron doped to a depth of 5-10μm to define the final thickness of the device. After doping, the mechanical features of the microsensor are then defined through directional plasma etching. The wafer is then electrostatically bonded to a glass substrate, which forms a permanent

mechanical support. The final stage is the removal of the excess silicon substrate in KOH or EDP. All undoped silicon is removed leaving the final mechanical structure.

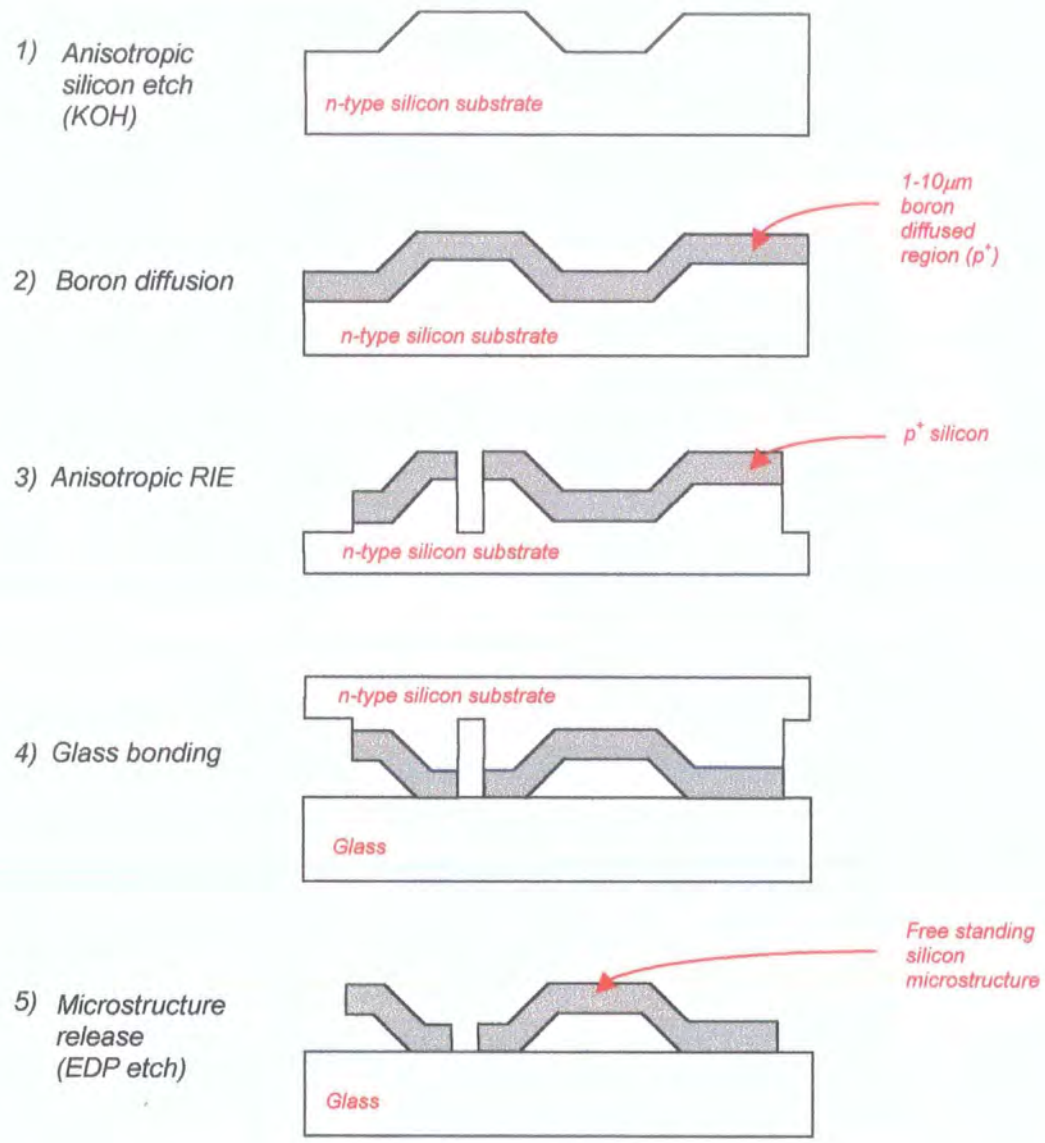

Figure 2.4. *Dissolved wafer fabrication technique.*

This type of processing is very versatile, allowing the fabrication of more intricate designs by using a combination of all the traditional etching techniques. It is an

involved procedure but can be exploited to produce highly complex devices. It has been shown in the production of silicon gyroscopes [17] and lateral oscillators [16].

2.1.2 Polysilicon Surface Micromachining

Surface micromachining involves the manipulation of thin films deposited on the silicon substrate to construct micromechanical devices. The basic concept is very simple and is shown in figure 2.5. A sacrificial layer, typically 1-3μm of silicon dioxide (thermal or plasma deposited) is initially patterned on the surface of the silicon substrate. On top of this layer is deposited a layer of polysilicon up to a thickness of 1-5μm. Patterning of this layer defines the main polysilicon mechanical elements. The final stage involves the selective removal of the sacrificial layer to create freestanding regions of the structure.

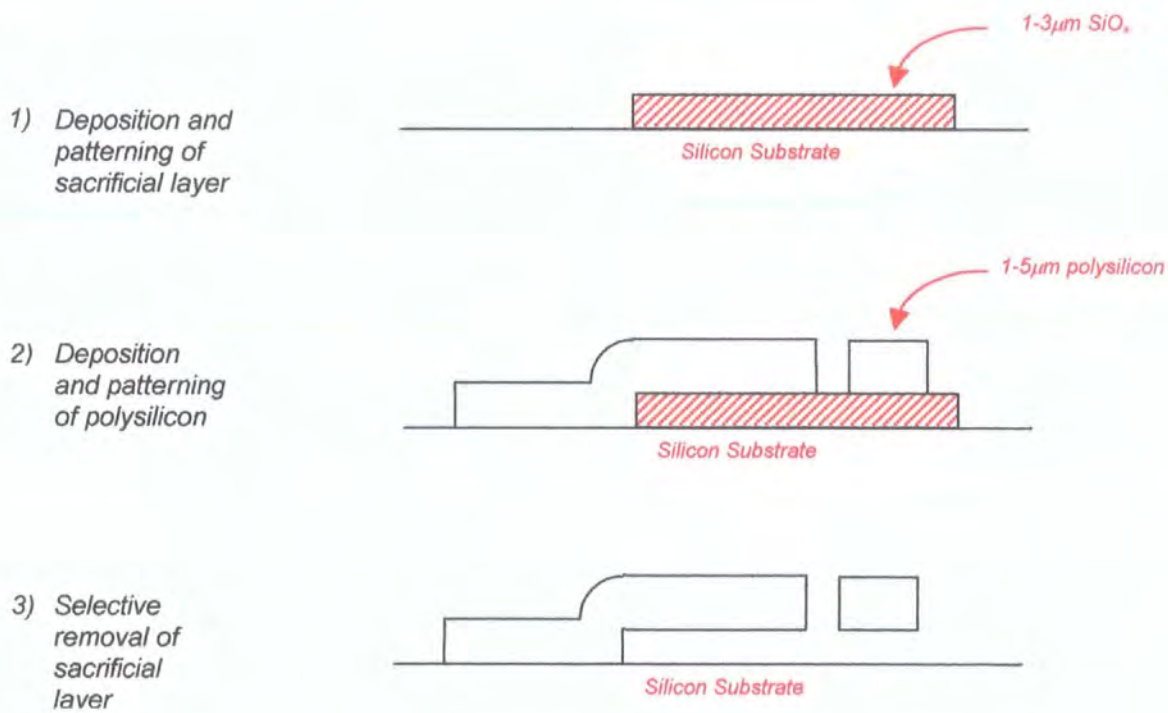

Figure 2.5. *Surface micromachining.*

The dimensions involved in this type of technique are generally an order of magnitude smaller than those of crystallographic etching, as no restrictions are imposed on surface geometry and feature sizes are only limited by lithography.

A great problem associated with this type of processing is stiction [18]. This is a problem that occurs during final drying of released structures after the sacrificial layer has been removed. Capillary forces can cause the freestanding polysilicon regions to come into physical contact with the substrate. Once in contact the structure cannot be freed and the device is rendered useless. Although stiction is a serious problem it can be overcome using a variety of techniques. These include dimple formation (to reduce area of contact) and increased surface roughness [18], dry release processes [19], and freeze drying [20]. Although great care must be taken during the fabrication of surface micromachined devices to avoid stiction, the benefits are that the process is completely CMOS compatible and the silicon substrate is not consumed during fabrication. This allows the construction of microsensors next to, or directly on top of, CMOS circuitry to produce a complete microsystem on a single piece of silicon.

Surface micromachining has been used in the fabrication of a vast number of devices. Again, the most widely demonstrated structures are the pressure sensor [21] and the accelerometer [22], although surface micromachined gyroscopes [17] have also been developed.

2.2 High Aspect Ratio Micromachining Techniques

Many micromachined devices are designed to allow motion in the plane of the wafer surface. The most common way of controlling this motion is by the combination of electrostatic actuation and capacitive detection. The magnitude of the electrostatic drive forces and the sensitivity of capacitive detection can be maximised by optimising electrode spacings and maximising total electrode areas. Optimum electrode spacings lie in the 1-5μm region and can be easily achieved using standard lithography.

Electrode areas can be increased by utilising comb arrangements and by increasing the structural height of the device. Comb drive arrangements are easier to implement as it is very difficult to increase the height of structures indefinitely without compromising lateral resolution. For this reason the thickness of most micromechanical devices is restricted to less than 100μm. However, with new techniques it is now possible to overcome these limitations, allowing the production of very tall and very thin (high aspect ratio) mechanical elements with heights in the 100-1000μm range. In addition to improving the drive and detection mechanisms, high aspect ratio structures offer further benefits especially for laterally oscillating devices. Mechanical rigidity of structures can be increased in the out-of-plane direction whilst in-plane flexibility is maintained. This is greatly beneficial as unwanted out-of-plane vibration can be suppressed allowing enhancement of in-plane motion. Restricting motion to only that desired can greatly improve performance. Finally, the sensitivity of inertial sensors (accelerometers and gyroscopes) is directly proportional to the mass of the sensing element. Increased thickness yields increased mass and therefore increased sensitivity, allowing detection of smaller inertial movements. The total effect of increasing the thickness of sensors to produce high aspect ratio microstructures is to greatly improve sensitivity and overall performance. The next few sections describe some specialist processes that have recently been used to demonstrate the fabrication of such structures.

2.2.1 Deep Reactive Ion Etching

Deep reactive ion etching (DRIE) of silicon has been developed to offer significant improvements in anisotropy, etch rate, and selectivity over conventional dry etch processes. Although conventional SF_6/O_2 plasma based RIE can be used to achieve high aspect ratio etching, the process conditions must be finely balanced and etch depths are limited to less than 100μm. Additionally maximum etch rates are limited to approximately $1.0\mu m.min^{-1}$.

DRIE technology widens the process window for anisotropic etching and allows deep etching up to 500μm at high etch rates. These systems use conventional fluorine based plasma chemistry and achieve highly anisotropic etching through a complex procedure of sidewall passivation. The process involves the suppression of chemical reactions on the sidewalls of trenches through deposition of an inhibiting organic layer [23,24,25]. This layer is deposited non-selectively over all etch features but is removed at the bottom of trenches through directional ion bombardment, allowing vertical etching to proceed. Removal of the inhibiting layer only at the bottom of trenches requires highly directional ion bombardment, that is generally achieved with a high-density low pressure plasma.

The way that sidewall passivation is achieved can differ as is demonstrated by two DRIE systems currently commercially produced. Alcatel produce a system that employs a cryogenically cooled stage to reduce substrate temperatures below -100°C. The reduced temperature causes normally volatile etch products to freeze and deposit over the substrate, forming a organic passivating layer [23,24]. Murakami et al. [24] have published data from a similar cryogenic plasma system. These results have shown etch features of high anisotropy[1] (0.98) at etch rates of 1.6μm/min at -120°C. High mask selectivity is also observed (~900:1). Anisotropy can be increased (>0.99) at the expense of etch rate (0.7μm/min). This trade-off between anisotropy, etch rate and selectivity requires the process to be adapted for specific mask designs. Cryogenic RIE has been shown to offer great advantages in high aspect ratio etching of silicon but has several disadvantages. The requirement for liquid nitrogen cryo-cooling increases the capital cost of the RIE equipment. Condensation of contaminants, particles and other normally volatile species is also a problem. Thermal stress induced in photoresist layers can cause it to crack at reduced temperatures.

A DRIE system produced by Surface Technology Systems (STS) avoids these problems by introducing the passivating layer at room temperature through a cyclic deposition and etch process [25]. The STS advanced silicon etch (ASE^{TM}) modifies the etch

[1] Defined as 1-(the ratio of lateral etch rate to vertical etch rate).

similar results. Figure 2.6 shows some typical results obtained with the STS advanced silicon etch. Figure 2.7 shows some typical DRIE test structures produced by STS and Plasmatherm.

The non-aggressive and predominantly chemical nature of DRIE allows high selectivity between substrate and mask material. Although there is a trade-off between directionality, etch rate and selectivity, typical results of the ASE show high anisotropy (0.99), aspect ratios in excess of 40:1 with high etch rates (typically 3 - 5μm/min) and selectivities of 75:1 to resist and 150:1 to thermal oxide. An additional feature of the ASE is the smooth etched surfaces that can minimise residual stress. Sidewall roughness has been measured at 0.15μm compared to 0.10μm for trench bottoms.

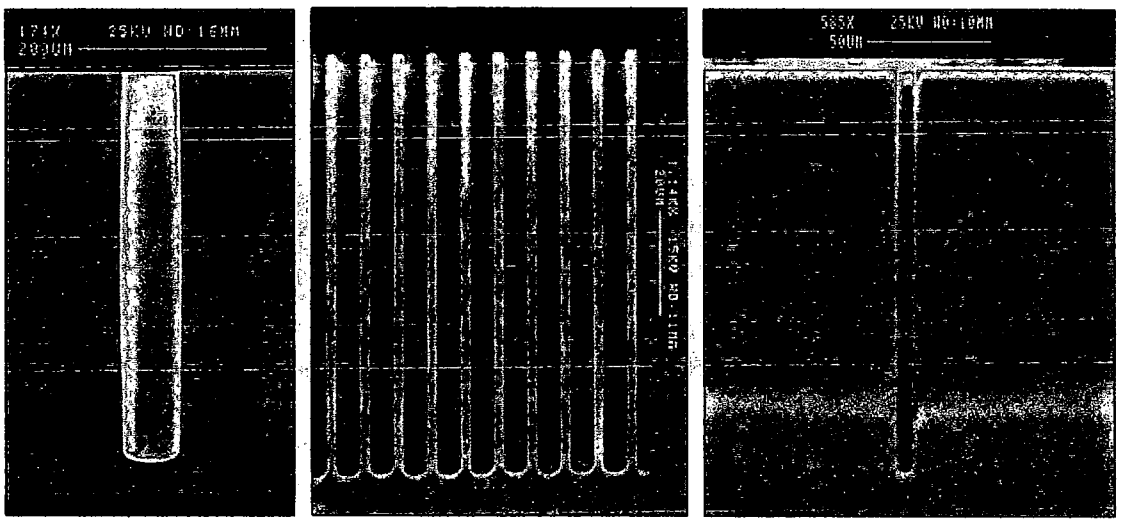

Figure 2.6. *STS Deep RIE etch profiles.*

Together with wafer bonding, DRIE can be used to produce fully released microstructures of any geometrical shape up to 500μm in thickness. This overcomes the restrictions imposed on surface geometry by orientation dependent wet etching. Lucas Novasensor has developed such a process to produce a variety of silicon sensors and actuators. Examples include wobble motors, electrostatic resonators and thermal

[1] Defined as 1-(the ratio of lateral etch rate to vertical etch rate).

actuators [26]. Alternatively SOI (silicon on insulator) wafers can be used to reduce complexity. This process is shown in figure 2.8.

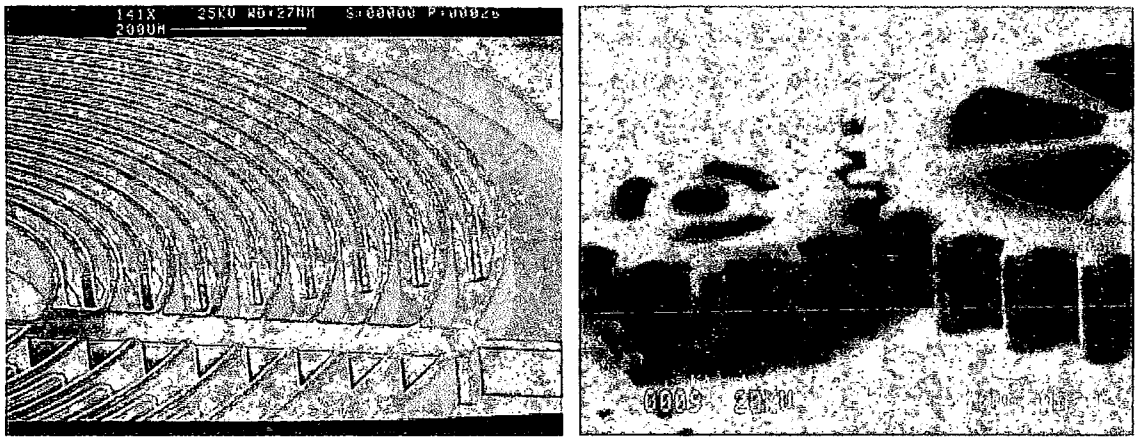

(a) Electrostatic comb drive structure. (b) Gear wheels.
(Courtesy of Surface Technology Systems)

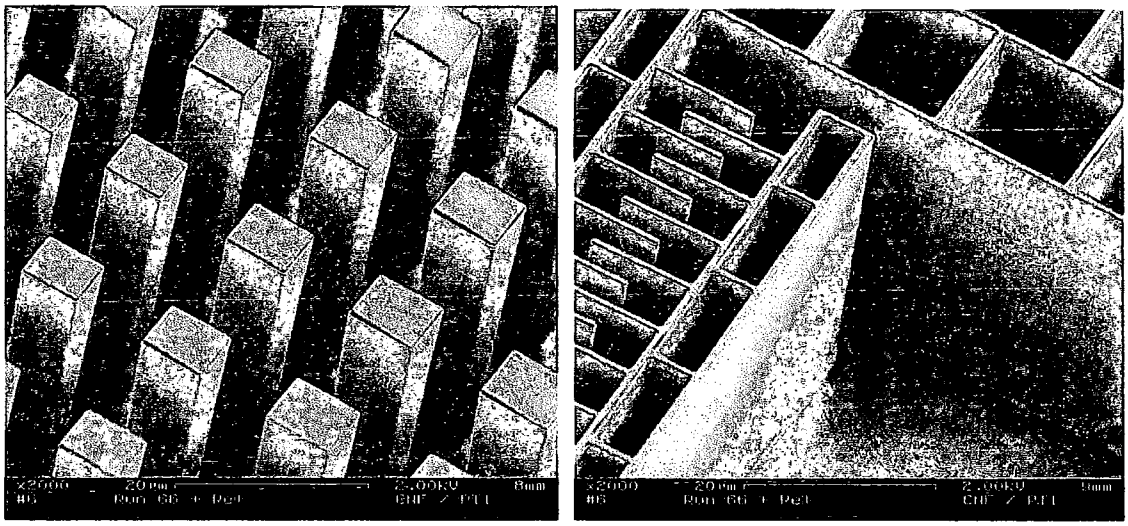

(c) High aspect ratio silicon structures.

Figure 2.7. *Deep RIE silicon structures.*

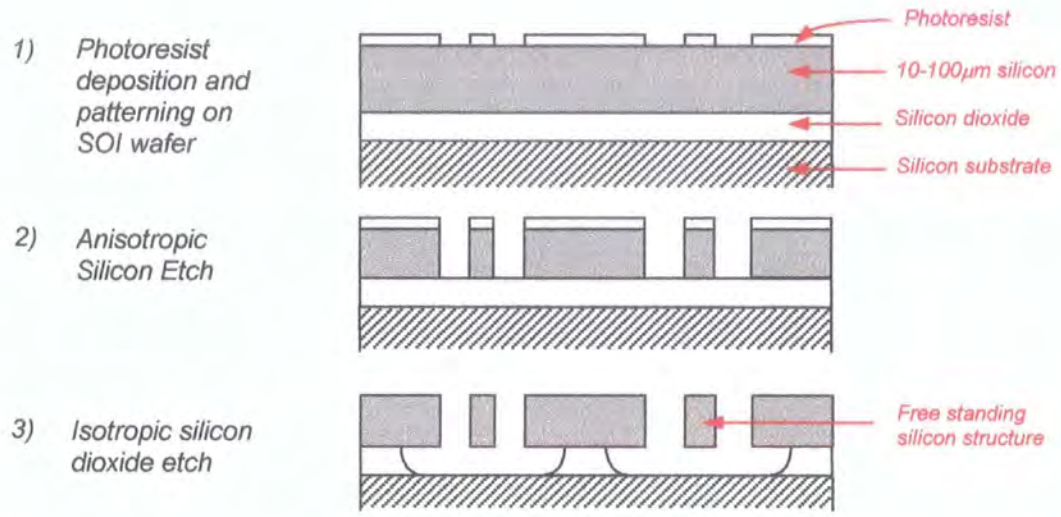

Figure 2.8. *SOI process concept.*

2.2.2 The LIGA Technique

The LIGA[2] process [27] is a second advanced technique for producing high aspect ratio microstructures (figure 2.9). This technique allows the production of metallic structures with great accuracy, large structural heights and almost vertical sidewalls. It involves a combination of synchrotron radiation lithography, electroplating and injection moulding to construct devices with sub-micron lateral resolution and thicknesses approaching 1mm. The quality of the metallic components depends greatly on the quality of the PMMA mould. To produce a metallic microstructure with a structural height approaching 1mm with near vertical sidewalls requires a PMMA mould of similar characteristics. This can only be achieved using a highly collimated x-ray source such as synchrotron radiation of 0.2-0.3nm wavelength. Prior to exposure, the PMMA is cast on the substrate and hardened using a heating process to minimise residual stress. Exposure and then development yields the required mould. Aspect ratios up to 100 have been demonstrated with minimal vertical pattern deviation. Typical deviation is

approximately 0.1μm over 500μm of structural height, equating to a sidewall angle of 90° ± 0.01°.

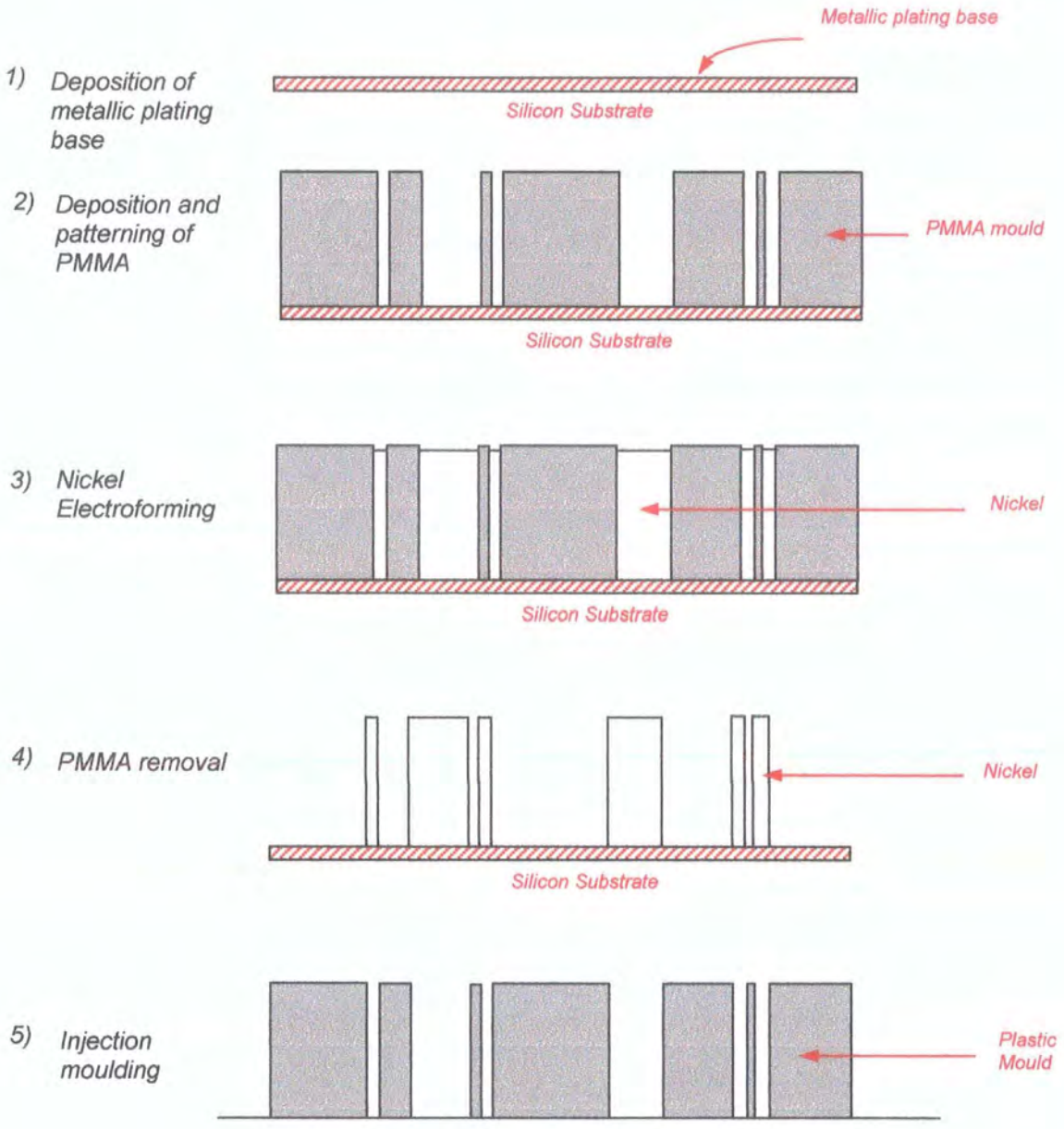

Figure 2.9. *The LIGA technique.*

[2] LIGA is an acronym of the German ***LI***thographie (lithography), ***G***alvanoformung (electroforming) and ***A***bformung (moulding)

In the basic process a polymethyl methacrylate (PMMA) layer is patterned through synchrotron radiation lithography. The use of a synchrotron source allows the definition of an electroplating mould with unrivalled accuracy. Sub-micron tolerances can be achieved in all lateral dimensions and only minimal vertical pattern deviation is observed. The patterned PMMA layer is used as a mould for a subsequent electroplating process that produces an exact metal replica. Removal of the sacrificial PMMA mould yields the metallic structure. However, the production of microstructures in this way will rarely be commercially viable due to the high costs associated with the synchrotron radiation source. To overcome this problem the metal replica is used to produce secondary plastic moulds via injection moulding. These secondary moulds, produced free of a synchrotron source, are then used for mass production of metallic components.

Nickel is generally the chosen material for electroplating due to ease of deposition, corrosion resistance and its relatively good mechanical properties, although the process allows for the use of a large range of metals and alloys. Figure 2.10 shows some example LIGA structures produced at the University of Wisconsin MEMS Unit. These show electrostatic motors, gear wheels and a resonator structure.

The potential of the LIGA technique has been demonstration through the fabrication of highly precise micromechanical sensors and actuators with sub-micron tolerances. Examples include microturbines, micromotors, micropumps, gear transmission systems [28] and accelerometers [28,29]. Improvements to LIGA processing have allowed further increases in the maximum obtainable structural height. In the original LIGA process structural heights were limited to 500-700μm due to limitations imposed by stress induced in the PMMA layers. Using powerful x-ray tools, pre-treated PMMA sheets in excess of 1cm can be exposed to produce precision-engineered parts [30]. However, the main disadvantage of LIGA remains that it requires specialist x-ray mask production and a high intensity synchrotron radiation source. The lack of these facilities and associated running costs are the main reasons LIGA remains inaccessible to all but a few MEMS facilities.

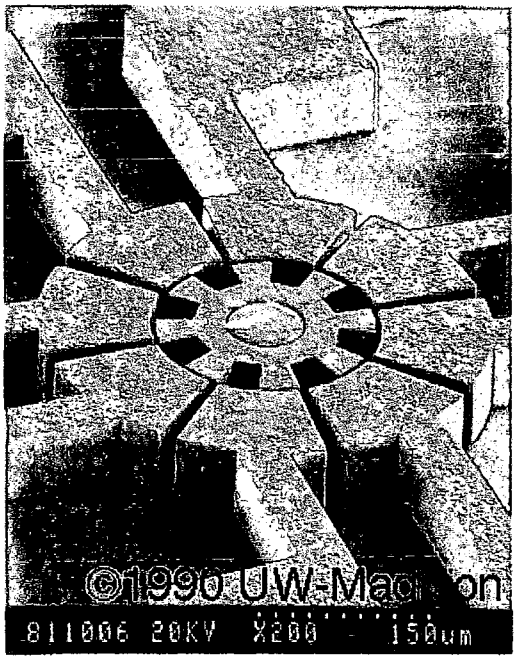

(a) Electrostatic motor I.

(b) Electrostatic motor II.

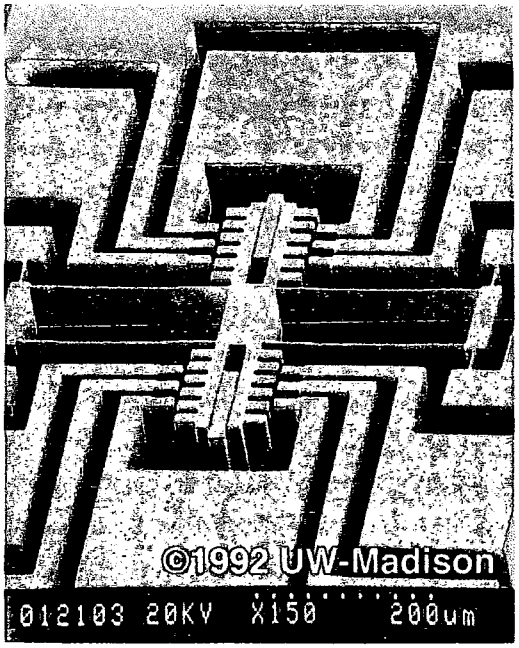

(c) Electrostatic resonator.

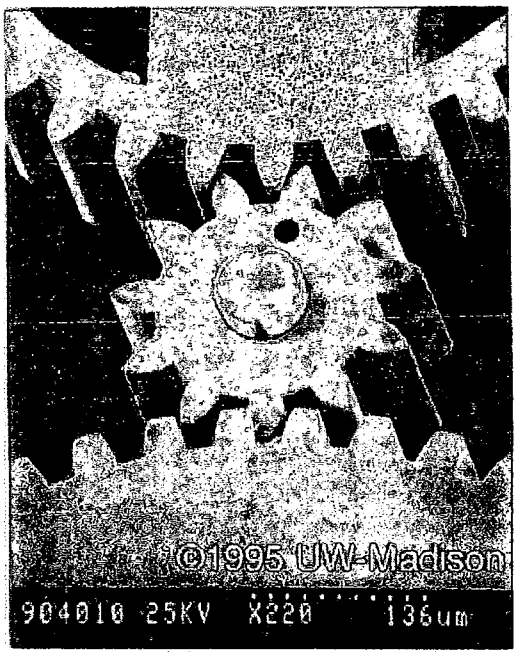

(d) Gear transmission system.

Figure 2.10. *Nickel electroplated LIGA test structures.*
(Courtesy of the University of Wisconsin)

2.2.3 UV HARMST

In an attempt to exploit the nature of LIGA without the involved expense, LIGA-like processes have developed using more conventional clean room technologies. These employ UV exposure of very viscous photoresists of high transparency to produced plating moulds up to 100μm in thickness. Like LIGA these photoresist moulds are used as an electroforming template to realise metallic components. As the final quality of the metallic components is determined by the quality of the plating moulds, good edge profiles and pattern fidelity is essential. Aspect ratios up to 10 with sidewalls in excess of 87° and excellent pattern fidelity have been demonstrated [31,32]. Similar results have been displayed with photosensitive polyimides up to 150μm in thickness [33]. Although UV high aspect ratio lithography cannot achieve the high levels of anisotropy or produce the structural height of LIGA, it can offer significant improvements to surface micromachining. Many sources have produced devices using this type of technology. Examples include planar and 3D microcoils, gearwheels, electrostatic micromotors, accelerometers [34-37] and also gyroscopes [16].

More recently, a negative photoresist has been developed by IBM [38]. EPON SU-8 is a negative photoresist that can applied up to 450μm in thickness in a single spin coating at 60 rpm with a GYRSET Karl Suss spin coater with rotating covers. Layers up to 250μm are obtainable in a single step with a conventional spin coater. Aspect ratios near 15 have been produced for lines and 10 for trenches offering significant improvements on the first generation of thick photoresists.

Chapter Three

Electrodeposition of Nickel

This chapter describes the theory of electrodeposition and its practical application towards the production of miniature mechanical components. The first sections describe the fundamentals of electrodeposition and highlight the inherent problems associated with the processes. The latter sections describe and discuss experimental results.

3.1 Fundamentals of Electrodeposition

3.1.1 Electrode Reactions

When a metal electrode is immersed into an ionic solution a potential difference is created across the interface between solid and liquid. This ***electrode potential*** exists as a result of electronic interaction between charged species across the phase boundary. Metal ions on the surface of the electrode that possess sufficient energy can break free from the lattice structure and pass into the solution, forming hydrated metal ions. Likewise hydrated ions in the solution can possess enough energy to interact with electrons at the electrode surface and undergo the reverse process and become attached

to the electrode. Under steady state conditions these two processes occur at the same rate and a dynamic equilibrium is established:

$$M^{n+}_{(aq)} + ne^- \Leftrightarrow M_{(s)} \qquad (3.1)$$

In the forward process hydrated metal ions are reduced resulting in metal deposition. This reaction consumes electrons at the electrode surface, which acquires a local positive charge. In the reverse process atoms in the lattice are dissolved into the solution, leaving a surplus of electrons on the electrode surface which develops a negative local charge. The net charge that develops on the electrode is determined by which process occurs most readily. This is influenced by a number of factors such as the nature of the metal, concentration of ions in the solution, temperature and pressure. Whether dissolution or deposition is the preferred process, a net separation of charge results and a potential difference is established across the electrode / solution interface.

For a better understanding let us consider the situation under which immersion of a metal electrode into a solution of its ions results in its initial dissolution. As the metal electrode dissolves to form hydrated ions, the electrode surface acquires a net negative charge and the adjacent solution a net positive charge. Due to electrostatic attraction these charges line up opposite each other analogous to an electrical capacitor. The excess surface charge on the electrode is balanced (equal and opposite) by the excess charge in the solution. Further interaction is prevented due to the presence of the primary hydration sheath of the aqueous ions (figure 3.1). Hydrated ions cannot approach closer to the electrode than this plane which is called ***the outer Helmholtz plane***. Due to the mobility and thermal energy of the hydrated ions, the excess charge in the solution is not held compactly in the outer Helmholtz plane, but is smeared out over a diffuse region of about 1μm. In addition, when the metal is immersed, water molecules and other chemical species can become adsorbed over a large portion of the electrode surface. Water molecules are mobile and relatively small and so they can approach closer to the electrode surface than large hydrated ions. This second plane of adsorbed material is known as ***the inner Helmholtz plane***. This system of charges is known as the ***electrical double layer*** and is shown schematically in figure 3.1. The close

proximity of water molecules to the electrode encourages the dissolution of metal ions from the electrode. As dissolution progresses, the electric field induced across the double layer increases due to the increasing separation of charge. This field eventually discourages further dissolution and begins to encourage the reverse deposition process. After a short period of 10^{-4} to 10^{-3} s, an equilibrium is established whereby the rate of dissolution equals the rate of deposition.

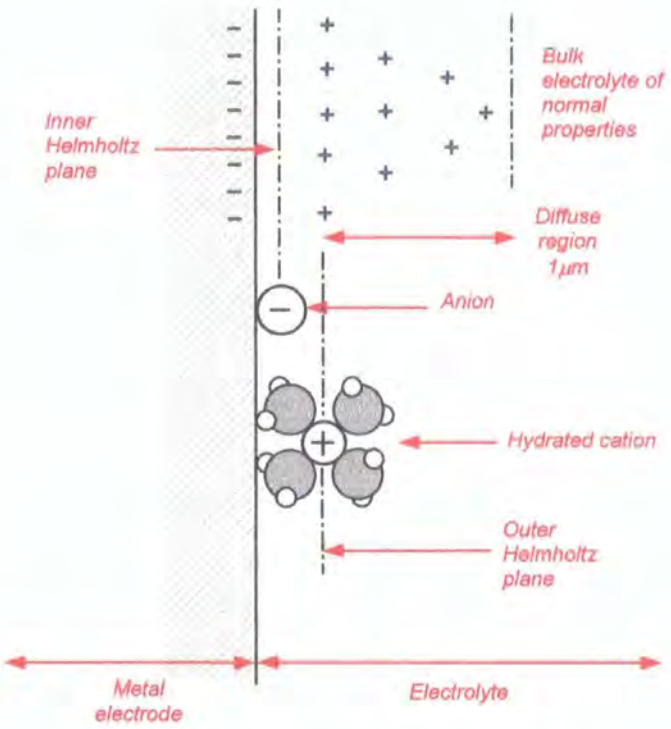

Figure 3.1. *Electrical double layer.*

Because motion of charged entities is involved, a current can be associated with both the forward and reverse reactions of equation 3.1. Under dynamic equilibrium the ***oxidation current density*** and the ***reduction current density*** are equal and opposite, the magnitude of which defines the ***exchange current density***. In order for a net effect to be realised the equilibrium must be disturbed so that a net current flows through the electrode. This causes a corresponding change in the electrode potential and the electrode becomes polarised. The amount by which the electrode potential is altered is expressed as the ***activation overpotential***, η. Current and overpotential are related by the Tafel equation:

$$\eta = a + b \log I \qquad (3.2)$$

where *a* and *b* are constants. To create a net flow of current through an electrode an external circuit must be used (figure 3.2). The applied voltage across the cell causes deposition to occur at the cathode and dissolution at the anode.

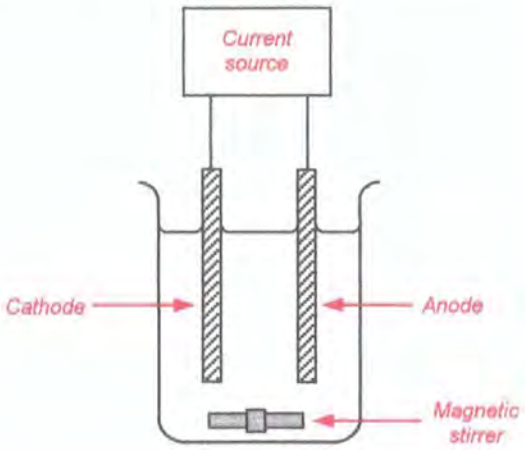

Figure 3.2. *Electrolytic cell design.*

3.1.2 Mass Transport

As the electrode reactions progress the concentration of ions near the electrical double layer is altered. These ions must be replenished for the reaction to progress. This must be done through movement of material from the bulk solution i.e. via mass transport. Mass transport arises from differences in electrical or chemical potential between two different locations or from the direct movement of a volume of the solution. The three main modes of mass transport are:

(1) ***Migration*** - the movement of a charged body under the influence of an electric field (electrical potential gradient).

(2) ***Diffusion*** - the movement of a species under the influence of a concentration gradient.

(3) ***Convection*** - the movement of a species due to stirring. Natural convection occurs due to density or temperature gradients.

Under low current and efficient stirring conditions the rate of electrode reaction is determined by interfacial dynamics (equation 3.2). As the rate of ion consumption is increased due to increased polarisation of the electrode, ions must be supplied more and more quickly to the double layer. Eventually the situation arises whereby ions can no longer be supplied fast enough. Once this point is reached the rate of reaction is no longer determined by electrode kinetics but by the rate of mass transport. Further polarisation does not increase the net current flow and ***the limiting current density*** (i_{lim}) is reached.

Effective stirring of the solution can help replenish the ion concentration near the electrical double layer, but the presence of a thin stagnant boundary layer next to the electrode prevents the supply of ions reaching the electrode interface. The boundary layer exists due the viscosity of the electrolyte and friction between the electrode. The efficiency of the stirring, the temperature and pressure can all influence its thickness (which can have a value of up to 500μm) but cannot remove it entirely. As most of the electrode potential is dropped across the electrical double layer, it is only through the mechanism of diffusion that mass transport can proceed. Consequently, the rate of reaction at the electrode interface is determined by Fick's first law of diffusion (equation 3.3). This states that the flux of a species is directly proportional to its concentration gradient:

$$J_D = -D\frac{dC}{dX} \qquad (3.3)$$

where J_D is the diffusional flux (units mol. $sec.^{-1}cm.^{-2}$), D is a diffusion constant and $\frac{dC}{dX}$ is the concentration gradient. The flux of diffusing material (and hence rate of reaction) reaches a maximum when the concentration gradient across the boundary layer is a maximum. This occurs when the ion concentration at the double layer is effectively zero, increasing to the bulk value (C_o) across the thickness of the boundary layer (δ):

$$J_D(max) = -\frac{D \cdot C_o}{\delta} \qquad (3.4)$$

This motion of ions constitutes a current; the ***diffusion current*** (i_D) is related to the diffusional flux by equation 3.5:

$$\frac{i_D}{nF} = J_D \qquad (3.5)$$

where n is the valency of the diffusing species and F is the Faraday constant (which is the charge carried by one mole of electrons or single ionised ions and has a value of 9.65×10^4 coulombs.mol.$^{-1}$). The limiting current density (i_{lim}) can therefore be found from equations 3.4 and 3.5:

$$i_{lim} = i_D(max) = nFJ_D(max) = -\frac{nFDC_o}{\delta} \qquad (3.6)$$

3.1.3 Electrode Efficiency

Faraday's Law relates the quantity of electric current that passes through an electrode to the amount of chemical transformation at that electrode. It states:

(1) The electrochemical reactions take place only at the surface of an electrode.
(2) The quantity of matter (M) that reacts at the electrode is directly proportional to the electric charge (Q) flowing through the cell, i.e.

$$M = \zeta \cdot Q = \zeta \cdot It \qquad (3.7)$$

where ζ is called the electrochemical equivalent and for Ni^{2+} is equal to 0.304×10^{-4}g.C^{-1}, and I is the current flowing for a time t. Equation 3.7 allows the calculation of the theoretical amount of matter that can be deposited for a given amount of electricity. It is however valid for only one specified ion. The reduction of other ions at the electrode e.g. the reduction of hydrogen ions to produce gaseous hydrogen can occur. These processes also consume electrons. The cathodic current efficiency can therefore be defined as the ratio of actually deposited material to the maximum

theoretically possible deposited amount. The cathodic current efficiency greatly depends upon the number of different ions present in the solution and their concentration.

3.1.4 Anodic Dissolution and Cathodic Deposition

A metal surface that appears macroscopically smooth is not necessarily smooth on a microscopic scale. In general the surface will not be perfect but contain discontinuities i.e. steps, vacancies and dislocations. These defect sites constitute sites of increased chemical activity as atoms located here have a reduced number of nearest neighbours. For instance an atom located in the interior of a close packed crystal lattice will occupy a site with twelve nearest neighbours whilst an atom located in a surface plane will have only eight. An atom at a surface defect site will possess even fewer, and the energy required to remove it is therefore much less. For this reason dissolution and deposition tend to occur preferably at these sites of atomic disorder. As electrodeposits grow at these active sites, growth edges sweep over the surface until they interact with each other to form grain boundaries. The resulting deposits are therefore usually polycrystalline. The size and orientation of the crystal grains is highly influenced by the content of the electroplating solution. Random deposition (resulting in amorphous deposits) can be encouraged by modifying the external current or by the inclusion of certain organic additives into the electroplating bath. These additives adsorb on growth edges to reduce the number of active sites leading to grains of smaller size and in general a more atomically smooth deposit. For micromechanical applications the physical structure of the metallic deposit is largely unimportant. Polycrystalline materials have been used in these applications and the only requirement is for a small grain size that is negligible compared to the minimum feature sizes of the structure. Other parameters such as electrical and mechanical properties vary only slightly with crystal structure (the Young's modulus of a crystalline material will have a direction dependent value that can vary up to 10% from the bulk average).

3.2 Electroforming

Electroforming is the process of selective electrodeposition through a predefined mould. The mould is an insulating film that defines the areas into which the electrodeposit can grow, isolating the remaining surface to prevent deposition. It is an inherently non-uniform process that can cause metal distribution to vary greatly across substrate surfaces, especially when moulds of varying lateral dimensions are present. The origins of this non-uniformity are discussed in the following sub-sections.

3.2.1 Pattern Scale Non-Uniformity

Unlike evaporation, sputtering or surface controlled processes such as chemical vapour deposition, electrodeposition is influenced by many parameters. Charge transfer kinetics, mass transport and current distribution all play an important role in determining local deposit characteristics. To understand this it is necessary to realise that electrodeposition onto a conducting substrate partially covered by an insulating layer (in this case photoresist) differs to that of a macroscopic substrate. The former must be considered as an array of recessed microelectrodes with individual properties. Moreover, in order for deposition to occur uniformly, the local properties at each microelectrode must be identical. In particular the current density through each microelectrode must be equal. This, however, is greatly influenced by the particular distribution of resist over the electrode surface. In general, regions with a high percentage of resist coverage attract higher current densities and allow deposited layers to grow faster.

In addition to the resist coverage, the aspect ratio of individual features can artificially influence the deposition rate. As demonstrated in figure 3.3, it is more difficult for convective flow to reach the bottom of narrow trenches than wide features. This results in the boundary layer assuming a thickness dependent upon the local geometry, which in-turn directly controls the limiting current density (c.f. equation 3.6) and hence deposition rate.

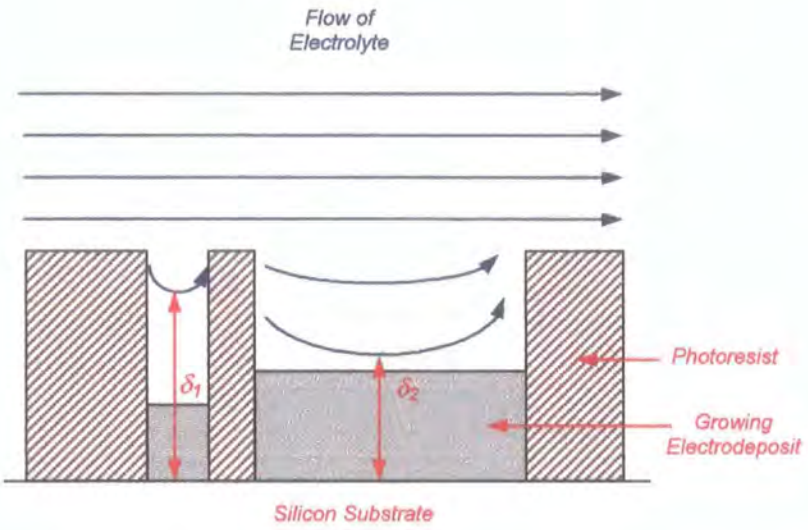

Figure 3.3. *Variation in diffusion layer thickness with feature geometry.*

Whatever the rate determining mechanism of the deposition process, it can be seen that the deposition rate itself can vary from one feature to the next, displaying the inherent problem of electroforming processes.

3.2.2 Feature Scale Non-Uniformity

The previous section highlighted some causes of thickness variation between separate structures. Thickness variations can also exist across individual features. Under conditions whereby mass transport has a major influence on deposition rate, non-linear diffusion effects can be a source of non-uniformity. For instance deposition at the edges of features can be enhanced due to an additional contribution from radial diffusion of ions. This is shown in figure 3.4. These effects become more significant when the deposit nears the top of the mould. If the limiting current density is not reached, edge overgrowth can be reduced if not eliminated.

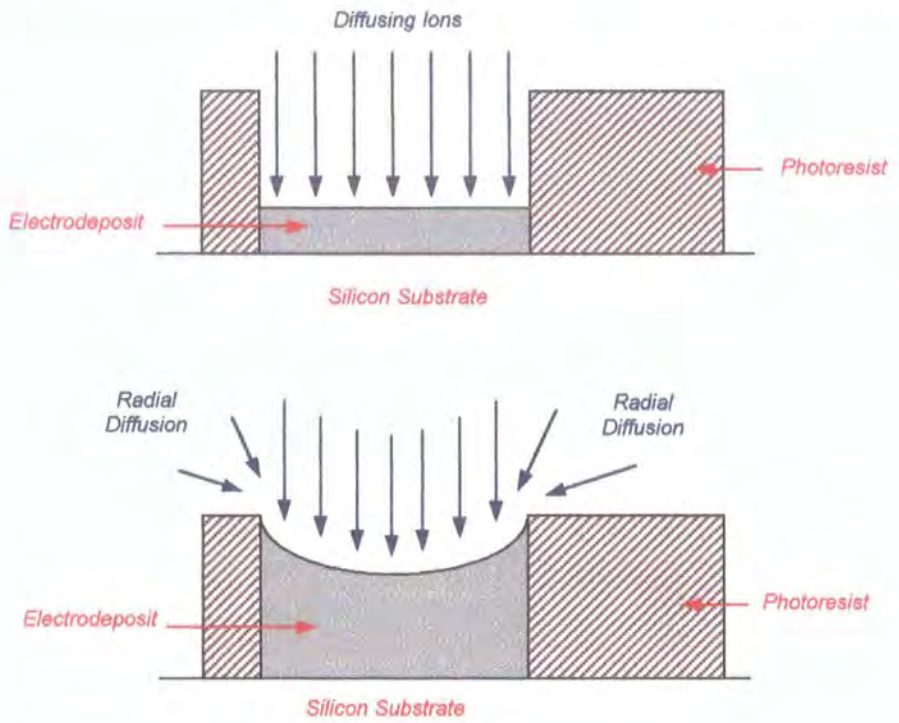

Figure 3.4 *Non linear diffusion effects across features.*

Another cause of feature scale non-uniformity arises due to the surface roughness of the growing deposit. This effectively modulates the diffusion layer thickness across the feature allowing enhanced deposition over protrusions, amplifying the effect. It can however be suppressed by the use of organic levelling agents (section 3.1.4).

3.3 Experimental Considerations

This section describes the experimental results gathered concerning the selective deposition of nickel through a predefined electroforming mould produced on a metallised silicon wafer. The electroforming procedure was performed using a nickel sulfamate based bath buffered with boric acid [27] on a pre-prepared substrate. The full composition of the electroplating solution is detailed in table 3.1. Bath temperatures between 50 and 55°C were used to produce low stress deposits that faithfully conformed to the lateral dimensions of the photoresist mould. It was observed that temperatures below 45°C resulted in poor adhesion between the electro-deposit and the plating base.

Bath Chemistry	Quantity
Nickel Sulfamate $[Ni(H_2NSO_3)_2.4H_2O]$	400g/l
Boric Acid	40g/l
Nickel Chloride	1.5g/l
Sodium Dodecyl Sulphate	4g/l
Plating Conditions	
Temperature	50 - 55 °C
pH	~3.4
Current Density	0.1-0.2 mA/cm^2

Table 3.1. *Summary of bath chemistry and plating conditions.*

As can be seen from table 3.1, various additives are included to the basic electroplating solution to enhance deposition properties. The next few sub-sections describe the effects of these additives.

3.3.1 Boric Acid

Chemical species are constantly evolved and consumed during the electroplating process and can cause the pH of the bulk solution to fluctuate. Such changes in pH can drastically alter the properties of the electro-deposit so it is essential that it be maintained at a constant value. This can be achieved by additions of boric acid, which is commonly used as a buffering agent to resist small changes in pH.

Boric acid partially dissociates to produce the following equilibrium:

$$H_3BO_3\,(aq) + H_2O \Leftrightarrow H_3O^+(aq) + H_2BO_3^-(aq)$$

A small addition of acid shifts the equilibrium to the left, removing the additional H_3O^+ ions and maintaining the pH at a constant value. Small additions of a base are neutralised by the oxonium ions, again maintaining the pH.

3.3.2 Nickel Chloride

Small quantities of nickel chloride can increase the dissolution efficiency of the anode. The chloride ion is a very aggressive ion and will displace water molecules and hydroxyl ions from the anode surface, preventing the formation of any oxide or hydroxide layer over the anode that would render it passive. In addition, it is known that specifically adsorbed negative ions (such as Cl^-) promote the dissolution of metal atoms from the anode surface and inhibit deposition. A nickel salt is used to avoid the contamination that would be introduced if a different salt were used.

3.3.3 Sodium Dodecyl Sulphate ($C_{12}H_{25}OSO_3.Na$)

Sodium dodecyl sulphate acts as a wetting agent that reduces the surface tension of the electroplating solution. This reduces bubble formation and allows complete filling of high aspect ratio trenches to allow efficient deposit growth.

3.4 Preliminary Measurements

The plating rate and texture of the electro-deposit is greatly influenced by the current density [39] and so characterisation of these properties was required. Using the plating bath listed in table 3.1, electro-deposits were readily obtained using current densities in the region 10-120mA/cm^2. Corresponding deposition rates of 5-40 μm/hour were observed as presented in figure 3.5. The texture of the electro-deposit and hence surface roughness is greatly influenced by plating conditions. Preliminary measurements showing the influence of current density is illustrated in figure 3.6.

As expected the thickness of the electro-deposits were found to vary non-uniformly across individual features and from feature to feature. The extent of these deviations was found to depend upon the geometry of features and in general large area structures suffered most heavily. Figure 3.7 shows the thickness profile of a 2.7mm x 500μm cantilever beam along its length as determined with a surface profilometer (Tencor Instruments Alpha Step 200).

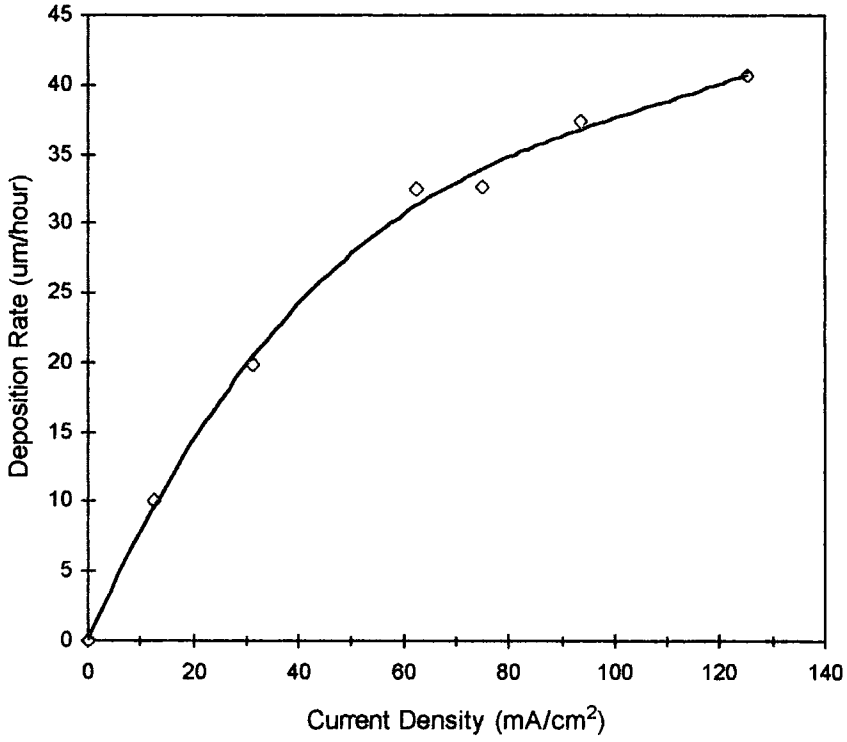

Figures 3.5. *Nickel deposition rate as a function of current density.*

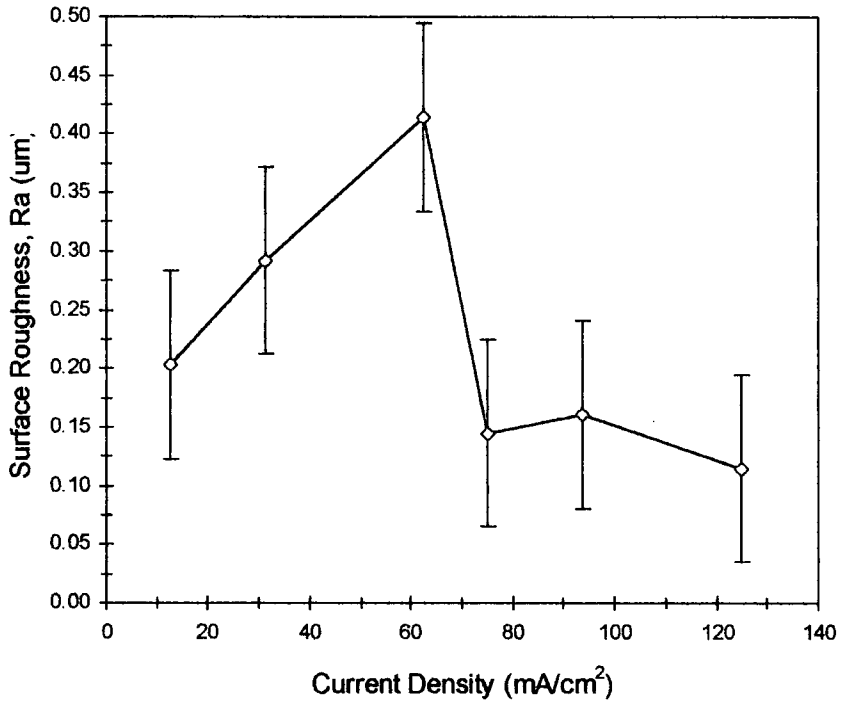

Figure 3.6. *Surface roughness as a function of current density.*

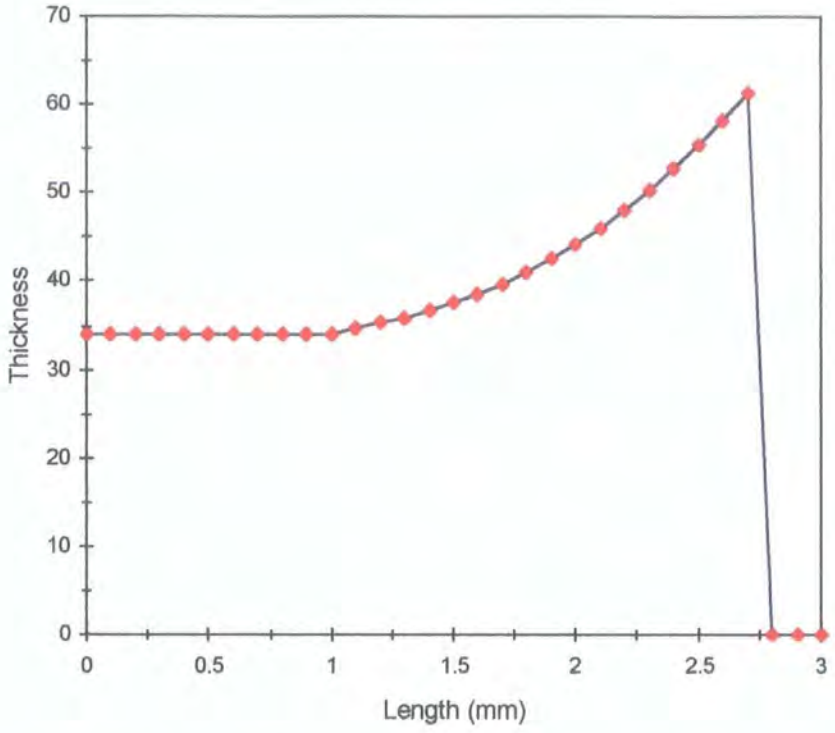

Figure 3.7. *Typical thickness profile of a 2.7mm x 500μm cantilever.*

The thickness of the deposit towards the end of the cantilever can be seen to vary by up to 25% of the bulk thickness. A smaller variation of around 6% was also determined across the 500μm width of the same cantilever. The non-uniformity originates from the radial diffusion of ions to the over-plated regions during the electrodeposition (section 3.2.2).

3.5 Summary of Electrodeposition Processes

This chapter has described the theory of electrodeposition. The process has been shown to be inherently non-uniform, resulting in deposition rates and textures that are highly dependent upon current densities and local conditions. Despite this it has been shown that the process has potential for the production of micromechanical components.

Chapter Four
Fabrication

This chapter describes in detail the fabrication processes that have been developed for the construction of free-standing nickel microstructures. The technology exploits the electroforming process investigated in chapter four together with sacrificial layer techniques to produce free moving and self supported nickel structures. The nature of the process is shown in figure 4.1. Although this shows only 6 fabrication steps, the complete sequence is an involved process consisting of 62 individual steps (table 4.1) with a run time of approximately 6 days.

In particular, the process has three significant stages; production of the electroforming mould, deposition of the structural material (nickel), and the sacrificial layer process that allows the production of movable devices. In this chapter, all fabrication steps are discussed, with particular reference to the production of high aspect ratio electroplating moulds.

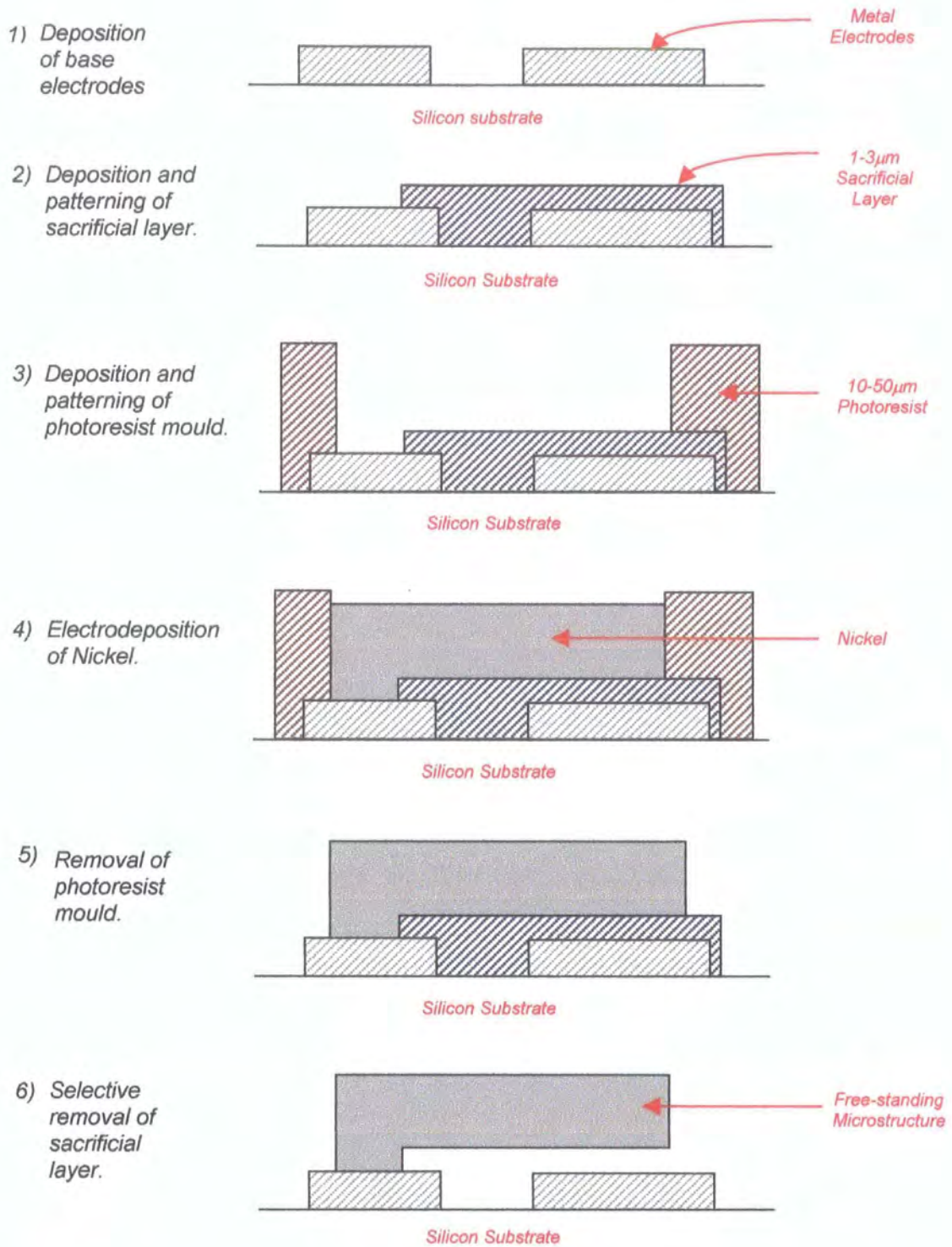

Figure 4.1. *Production of nickel microstructures.*

Fabrication Sequence	
1) H_2SO_4/H_2O_2 (1:1) clean	32) DI rinse
2) DI rinse	33) Resist removal (acetone)
3) 10% HF dip	34) IPA rinse
4) DI rinse	35) DI rinse
5) Dry (N_2)	36) Dry (N_2)
6) Thermal oxidation (1100°C, 4hrs)	37) 120°C bake (30 mins)
7) Cr/Au evaporation	38) Resist deposition (AZ 4562)
8) 120°C bake (30 mins)	39) 100°C bake (variable)
9) Resist deposition (S1813)	40) Exposure of **MASK 3** (edge bead removal)
10) 100°C bake (20 mins)	41) Development (AZ 351B1:4)
11) Exposure of **MASK 1** (base electrodes)	42) DI rinse
12) Development (AZ 351B 1:4)	43) Dry (N_2)
13) DI rinse	44) Excess bead removal (acetone)
14) Dry (N_2)	45) Exposure of **MASK 4** (device definition)
15) 120°C bake (20 mins)	46) Development (1:5)
16) Gold etch (KI/I_2)	47) DI rinse
17) DI rinse	48) Dry (N_2)
18) Dry (N_2)	49) Passivate wafer
19) Resist removal (acetone)	50) Ni electroplate
20) IPA rinse	51) DI rinse
21) DI rinse	52) Resist removal (acetone)
22) Chromium etch ($NaOH/K(CN)_6Fe_2$	53) IPA rinse
23) DI rinse	54) DI rinse
24) 120°C bake (30 mins)	55) Dry (N_2)
25) Sputter 1-4μm Ti Sacrificial layer	56) 10% HF (sacrificial layer removal)
26) Resist deposition (S1813)	57) DI rinse
27) 100°C bake (20 mins)	58) IPA rinse (20°C)
28) Exposure of **MASK 2** (sacrificial layer)	59) IPA rinse (80°C)
29) Development (AZ 351B 1:4)	60) 1,2-Chlorobenzene soak (80°C)
30) 120°C bake (20mins)	61) Cool in air (20°C)
31) 10% HF (Ti etch)	62) Low pressure microstructure release

Table 4.1. *Full fabrication sequence.*

4.1 Thermal Oxidation

One reason why silicon has been used extensively in microelectronics is the ability to grow thermal oxides directly onto single crystal substrates. Thermally grown silicon dioxide exhibits excellent dielectric properties that has enabled the production of high quality MOS transistor devices. It also provides electrical isolation between electronic structures and is chemically and physically resistant to many of the chemical etchants used to construct micromechanical devices.

Thermal oxidation of silicon typically takes place in a quartz furnace at elevated temperatures between 900 and 1200°C. High quality oxides (for applications such as MOS transistor gate oxides) are produced in a 'dry' atmosphere of oxygen. Dry oxides possess very few crystallographic imperfections and excellent dielectric properties but growth rates are very slow. Introduction of water vapour into the furnace tube drastically increases growth rates but the resulting wet oxides are not as crystographically perfect. They do however, still exhibit excellent properties. Figure 4.2 shows the experimentally derived growth curves for oxide formation using both wet and dry regimes, showing that the growth rates decrease as a logarithmic function of time.

Other methods of oxide formation include chemical vapour deposition (CVD) and spin-on-glass (SOG). Oxides deposited in this way generally exhibit a polycrystalline or amorphous nature and possess inferior electrical properties due to formation of pinholes and incorporation of impurities.

4.2 Metallisation

Metallisation layers are required for the production of contact pads, interconnects, electrode sites and sacrificial layers. In general such layers are deposited by evaporation or sputtering.

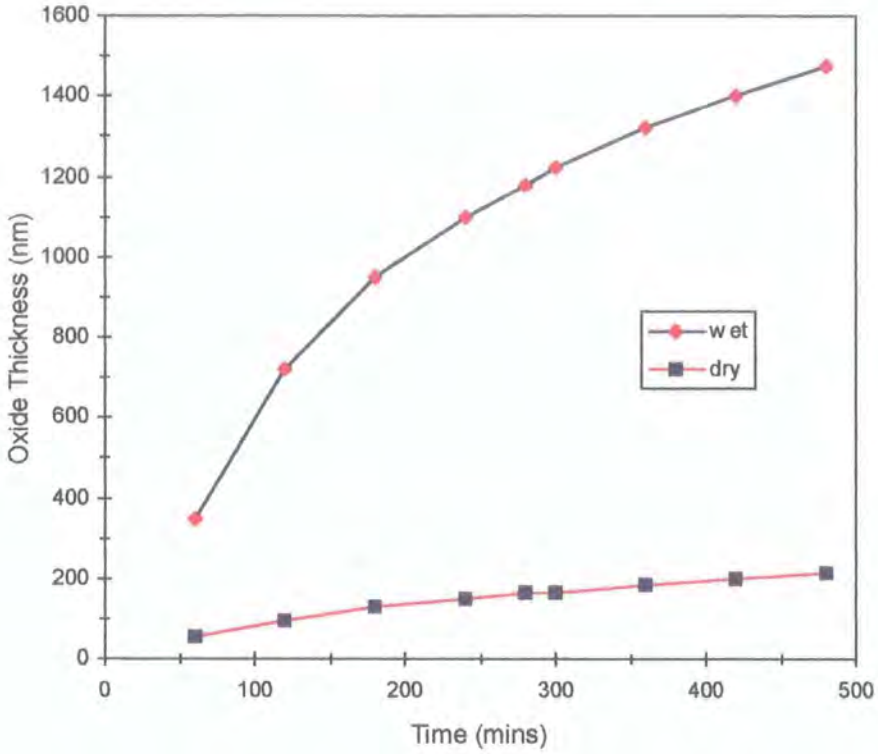

Figure 4.2. *Wet and dry oxidation growth curves.*

4.2.1 Evaporation

Evaporation methods used to deposit thin metal films involve the heating of a source material under high vacuum conditions. The method of heating can vary, with the most common being resistive or electron beam. Base pressures of ~10^{-7} Torr are typical which ensures a large mean free path (~100m) for the vaporised atoms. Under these conditions evaporated atoms will strike and condense on the substrate and chamber walls without colliding with any other gas molecules to produce a dense film. The thickness of films deposited by evaporation is limited to a few microns as thicker layers are subject to large internal stresses that cause the films to crack or peel.

Thin films of chromium, gold and titanium were deposited using a Varian dual source e-beam evaporator that allows the deposition of multilayers without breaking vacuum. In this way both chromium and gold, and titanium and gold layers were deposited. In both cases the chromium and titanium layers are used to increase adhesion between the

gold and the substrate. Aluminium metallisation was performed using a 12" thermal evaporator.

4.2.2 Sputtering

Sputter deposition involves the kinetic bombardment of a source target by energetic ions (typically argon) produced within a glow discharge. Base pressures of 10^{-7} Torr are again typical but operating pressures are much higher at around 10^{-3} Torr. High operating pressures cause sputtered atoms to suffer multiple collisions prior to condensation and therefore exhibit good step coverage. Incorporation of a process gas into the deposit yields a less dense layer but modification of process parameters allows production of uniform and low stress deposits.

In general sputtering allows much greater control of film properties and allows deposition of thicker films as a result of lower intrinsic stresses. This is due primarily to the mechanism of film formation. For instance, atoms that are evaporated from a heated source (typically > 1000°C) have a high degree of thermal energy. As these atoms strike and condense on the substrate to form the thin film, the layer cools resulting in a significant amount of thermal contraction, inducing a tensile stress within the film. Although the temperature of the substate may also be elevated through thermal radiation from the source, the differential thermal properties of the substrate and thin film will again induce stress in the film. By contrast sputtering is effectively a room temperature process; the target and substrate are usually cooled to room temperature ensuring minimal thermal contraction takes place. In these films the source of internal stress is caused mainly by crystallographic defects e.g. neighbouring crystals impinging on one another to form grain boundaries, and the incorporation of small quantities of process gas molecules and atoms.

A Chemex RF Sputter Unit was used for deposition of all titanium sacrificial layers. This system allowed the deposition of low stress titanium layers up to 4μm in thickness at rates of approximately 1μm/hour.

4.3 Photolithography

Photolithography is used extensively in microelectronics and microengineering to pattern thin films of material and define device features. Two different types of photoresist have been used during this research project. For the general patterning of thin films, Shipley S1813 photoresist has been used. This is a thin positive tone resist which produces a layer of approximately 1.3μm under standard dispense and baking procedures. For the production of high aspect ratio electroplating moulds Hoechst AZ 4562 photoresist was used. This is a very viscous and highly transparent photoresist capable of being applied in layers in excess of 20μm. The following subsections described the application and processing of these resists.

4.3.1 Thin Photoresist Processing

An overview of the photolithographic process is shown in figure 4.3. The first step involves the deposition of a photosensitive compound (photoresist) over the surface of the film to be patterned. This is achieved through a spin coating process in which the resist liquid is dispensed onto the wafer surface and then spun at high speed to form a uniform defect free layer. Baking then removes the excess solvent, producing a solid photosensitive layer. Exposure to UV modifies the molecular composition of the resist to make it either more soluble (positive resist) or less soluble (negative resist) than the unexposed regions. Development yields a patterned layer that is then baked to remove any last traces of solvent and to improve the chemical and physical resilience of the patterned photoresist. At this stage introduction of an etchant allows the selective pattering of the underlying layer. Final removal of the photoresist layer in a suitable solvent yields the patterned film.

In order to produce high resolution image transfer of fine features (<10μm) between photomask and resist it is necessary to carefully characterise all five process steps i.e. resist dispensing, prebake, exposure, development and postbake. However as the minimum linewith required to be defined with S1813 was 25 μm the manufacturers guidelines [40] were found to be adequate.

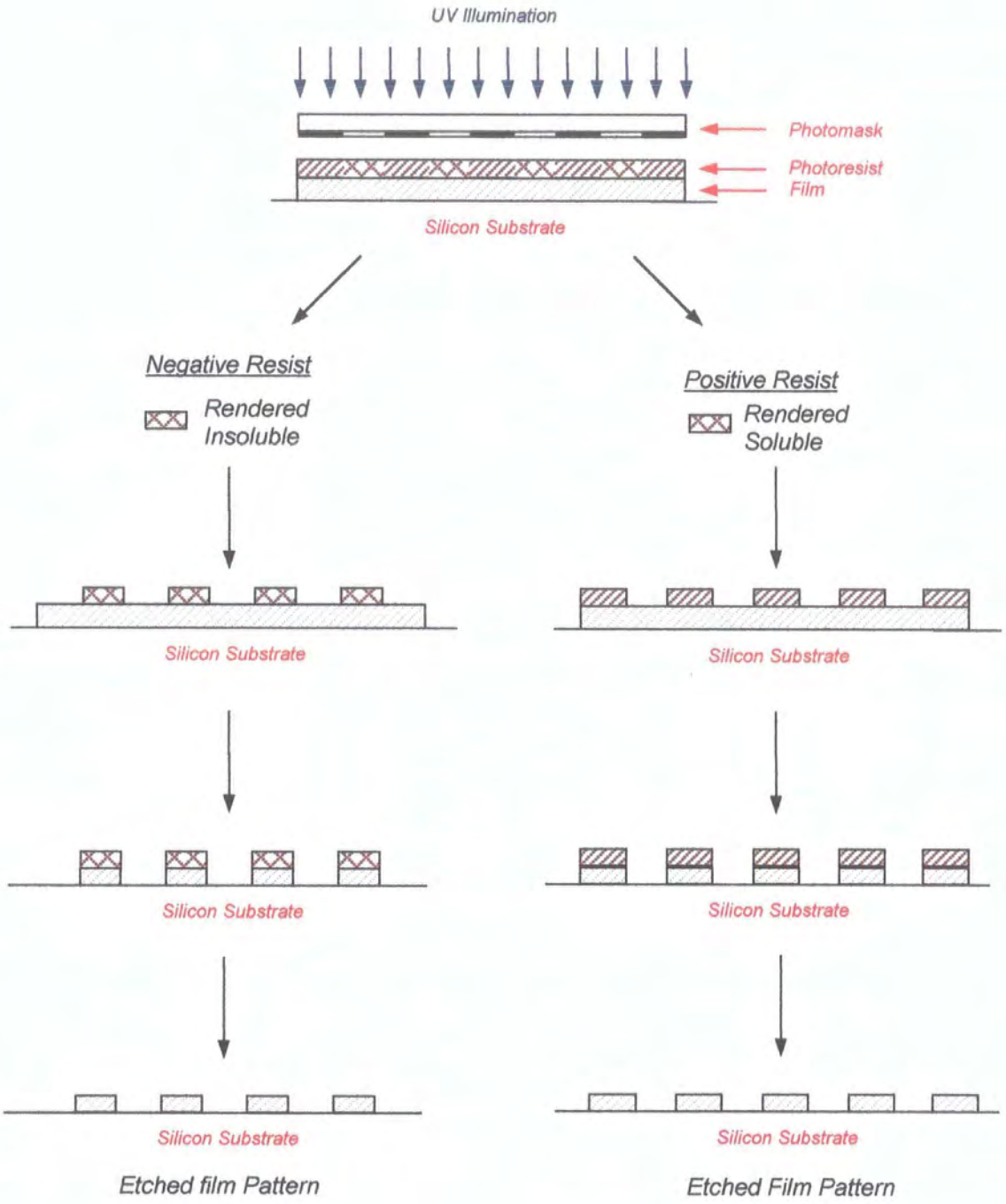

Figure 4.3. *UV photolithography.*

4.3.2 Thick Photoresist Processing

Hoechst AZ 4562 is a viscous photoresist that has been used to produce sacrificial moulds many tens of microns thick into which electroplated nickel structures can be formed. The process is a variant on the LIGA technique (chapter two), replacing synchrotron x-ray lithography with standard UV processing. Although UV structuring techniques cannot hope to match the precision of LIGA due to the much longer wavelength of the exposing radiation, with good understanding and careful characterisation the process can be optimised to offer promising results. This has been achieved through careful optimisation of each process step. These steps are described in the following subsections and the results of the characterisation are presented.

4.3.2.1 Resist Dispensing

Hoechst AZ 4562 was chosen to construct sacrificial plating moulds due to the ability to apply it in layers in excess of 10μm. It was found that layers in the region of 6 to 28μm thick could be produced in a single spin cycle by modifying the spin speed. This data is shown in figure 4.4. The graph also shows the minimal effect of the subsequent prebake temperature on the final layer thickness.

Adopting a process of multiple spin coating can produce thicker layers. This involves the application of multiple layers after intermediate bake cycles. In this way layers in excess of 100μm can be deposited. The relationship between resist thickness and number of resist layers spun at 1000rpm is shown in figure 4.5. An interesting feature of this graph is that the thickness of the initial layer is approximately 14μm whilst all subsequent layers are 21μm thick. This is likely to be caused by change of interface; friction between the resist/resist interface may be greater than that of resist/silicon.

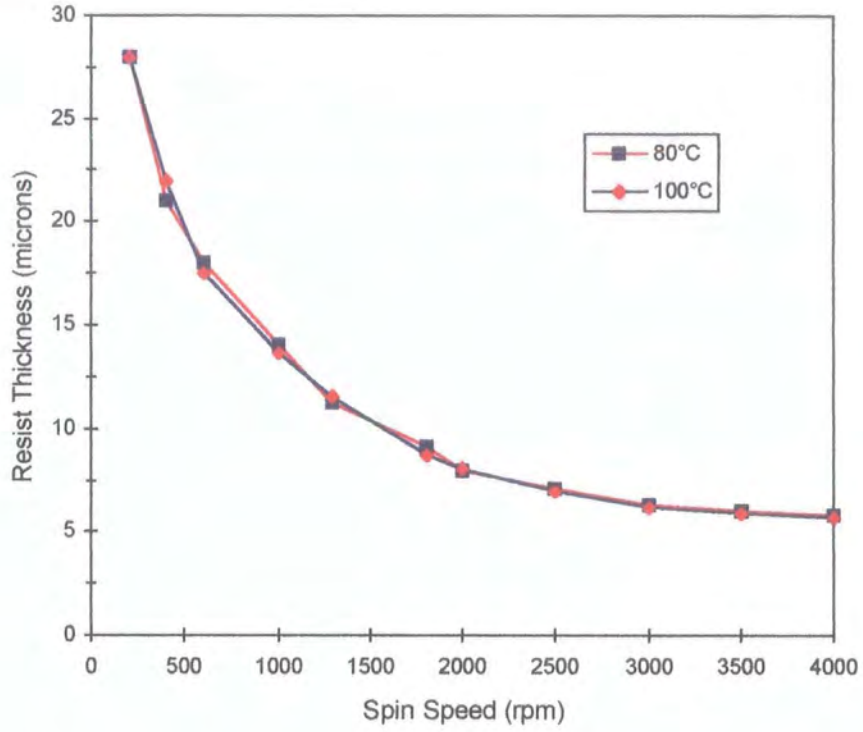

Figure 4.4. *Influence of spin speed on final resist thickness.*

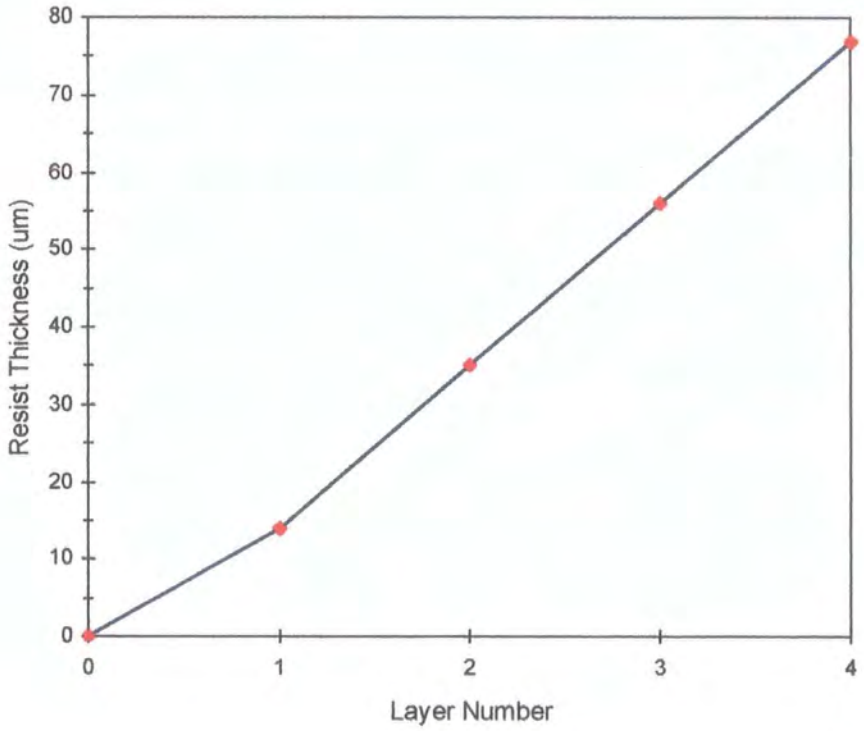

Figure 4.5. *Resist thickness as a function of layer number.*

4.3.2.2 Prebake

Prebaking is required to drive off most of the solvent content of the resist to produce a solid deposit containing a base resin and a photoactive compound. Although the temperature of the baking process was found to have negligible effect on the final resist thickness, it does however have a significant influence on the subsequent exposure and development stages [14]. For this reason the prebake conditions must be carefully optimised.

Characterisation is aimed at maximising the differential dissolution rates of the exposed and unexposed resist to maintain high aspect ratios and steep sidewalls. This is achieved by optimising the prebake time and temperature for a specific thickness of resist. As the resist thickness influences these parameters, optimal prebake conditions must be determined for all thicknesses of resist. The problem is compounded by the fact that both underbaking and overbaking of the resist can present problems in later processing stages. Underbaking leaves the resist with a high solvent content causing rapid development of both exposed and unexposed regions, leading to loss of pattern fidelity and poor edge definition[1]. Overbaking can cause degradation of the photoactive compound, leading to reduced UV sensitivity, increased exposure and development times, and loss of pattern fidelity.

These problems are magnified as the thickness of the resist increases. Ideally the solvent would be removed uniformly throughout the thickness of the resist. This, however, is not generally possible. For example hot plate baking heating removes solvent more effectively from the bottom of the resist than the top, encouraging solvent removal through the resist. This can potentially lead to overbaking at the bottom of the resist (leading to degradation of the photoactive compound) whilst the top of the resist remains underbaked (leading to overdevelopment of unexposed regions). This highlights the potential problems and need for good characterisation.

[1] Edge definition is a term indicating the steepness of the resist profile.

Initial trials were directed at obtaining the optimal prebake temperature for single layers of resist approximately 22μm thick. To standardise the results, all other parameters were held constant; standard exposure times of 30s and a 1:5 developer dilution (1 part Hoechst AZ 351B developer to 5 parts deionised water, as recommended by the manufacturer for high contrast processes [41]) were employed. Under these conditions, prebake temperatures ranging between 80 and 110°C were first investigated. By visual inspection it was found that the optimum prebake temperature for a layer of this thickness was approximately 100°C. Layers baked below 90°C suffered from poor edge definition and those baked above 110°C were difficult to fully develop. In addition it was found that samples baked for less than 15-20 minutes were visually poorer than those baked for longer. The influence of the prebake time for samples baked for in excess of 20-30mins was minimal. It was determined from these preliminary experiments that the optimal prebake conditions for a 22μm resist layer was a temperature of 100°C and a time of 30mins. Further it was found that the optimum prebake temperature for all samples (regardless of thickness) was 100°C. The prebake time, however, was required to be adjusted according to the thickness of the resist. For all layers it was found necessary to adopt a careful heating and cooling cycle in order to prevent cracking of the resist.

Prior to exposure of mask features it was necessary to remove the edge bead which forms during the spinning of the resist. In some cases the thickness of the edge bead can be many times the thickness of the inner resist layer and causes poor wafer/mask contact on exposure, resulting in poor image transfer. Removal of the edge bead was achieved with a preliminary exposure/development stage to leave a central area of resist with uniform thickness that could be further processed. Any stubborn areas of the edge bead that could not be cleared in this way were removed manually with an acetone soaked cotton bud.

4.3.2.3 Exposure

Exposure and development are closely interrelated and must be optimised to produce minimum pattern distortion. A Karl Suss contact aligner was used for exposure of all samples. Contact between mask and wafer was achieved mechanically and exposure times adjusted according to the thickness of the resist and the prebake conditions.

The purpose of the initial experiments was to determine the approximate relationship between exposure dose and penetration depth i.e. the dose required to clear a given thickness of resist. To do this test samples of resist (77μm thick) were exposed to varying doses and then developed in a standard solution (1:5). The relationship is shown in figure 4.6. The graph gives the approximate exposure times necessary to clear a particular thickness of resist, and shows the influence of prebake conditions on exposure requirements. It can be clearly seen that samples baked at higher temperatures in general require longer exposure times to clear a given thickness of resist than samples baked at lower temperatures.

To further investigate the influence of exposure dose on pattern attributes the exposure times of a standard resist sample was varied and the linewidth distortion[2] measured. For this experiment resist layers of 22μm (100°C, 30min prebake) were used as the standard test piece. Exposure times were varied in the range of 10 to 70s and the samples developed in a standard solution (1:5). The dimensional difference between the top of resist features and the photomask was then determined using a linewidth measurement system (Bio-Rad Nanoquest Ltd). This data is shown in figure 4.7. The optimum exposure dose of the standard test piece can be found from the graph to be approximately 30s. This exposure dose results in a minimum pattern distortion of approximately 2μm. This relates well with the approximate exposure dose identified in figure 4.6. Underexposure results in increased pattern distortion and doses less than 15s were difficult to develop. Overexposure also results in increased pattern distortion through back scattering and increased diffraction effects. It is notable with both heavily

[2] Linewidth distortion is defined as the dimensional difference between mask and patterned feature.

under and over exposed samples that the edge quality of the resist features is also reduced and sidewall profiles are not as vertical.

The scale of the linewidth distortion sets the minimum patternable feature that can be structured in a particular thickness of resist. For example feature sizes less than 2μm could not be produced in the 22μm test piece investigated. As expected the pattern distortion is a function of thickness and this relationship is shown in figure 4.8.

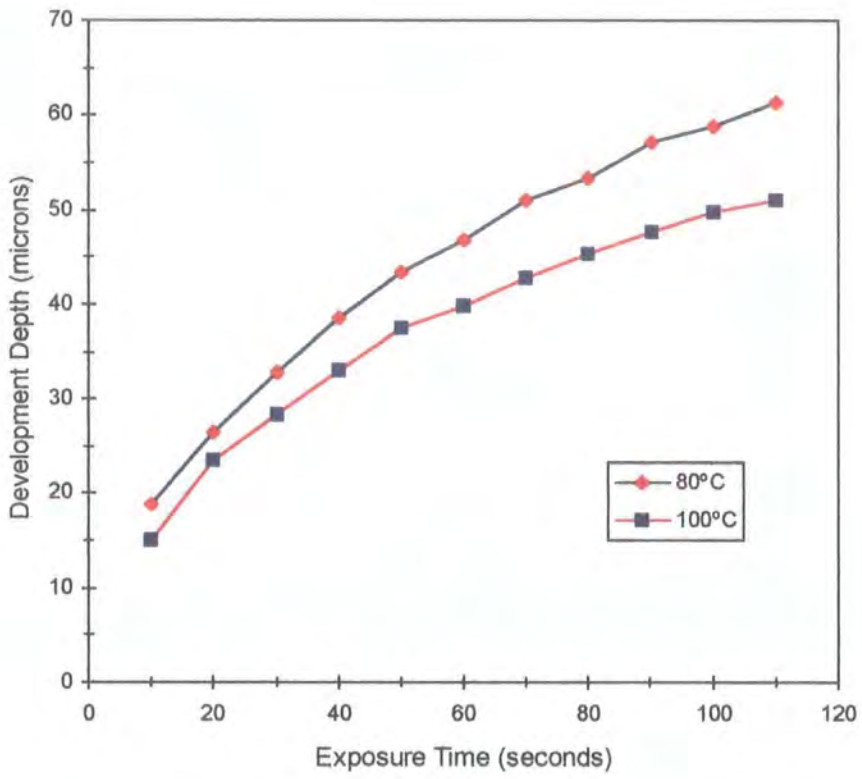

Figure 4.6. *Development Depth as a function of exposure time.*

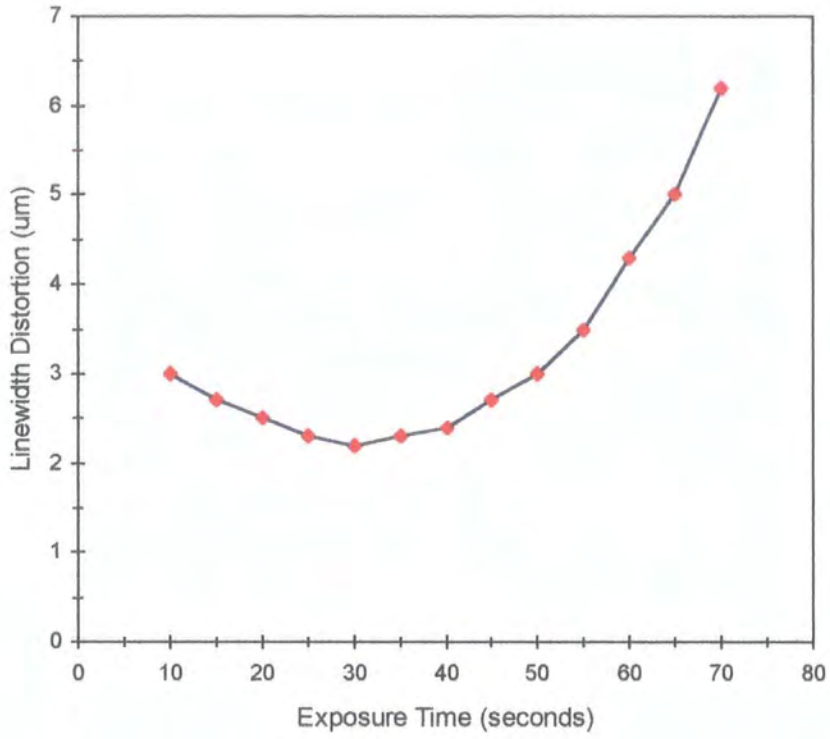

Figure 4.7. *Typical linewidth distortion as a function of exposure time.*

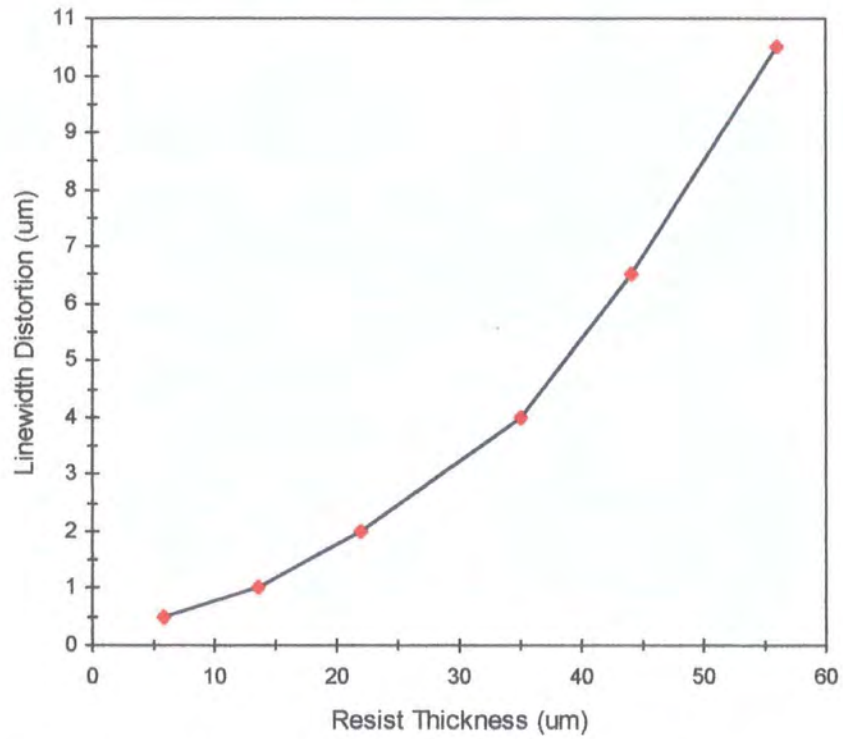

Figure 4.8. *Relationship between thickness and typical linewidth distortion.*

4.3.2.4 Development

As with the prebake and exposure conditions, the strength of the developer solution can highly influence the linewidths of patterned features. In general a high-resolution process employs an extended prebake, standard exposure and a dilute developer solution [14]. In all initial experiments the manufactures guidelines [41] were adopted for high resolution patterning i.e. a 1:5 solution of Hoechst AZ 351B developer. After optimisation of prebake and exposure, the influence of developer concentration was investigated. Figures 4.9 and 4.10 show the variation of linewidth distortion and dissolution rates with developer dilution observed for the standard 22μm thick resist. Figure 4.9 shows that the developer concentration has a direct influence on pattern distortion.

4.3.2.5 Postbake

The purpose of the postbake stage is to drive off the resist's remaining solvent content to improve adhesion, and to improve the physical and chemical resistance of the resist. To achieve this, postbake temperatures usually exceed those of the prebake to ensure removal of all residual solvent. Postbaking can also cause reflowing of the resist allowing removal of any small defect or modifying the resist profile.

Initial attempts at post baking were found to cause degradation of high aspect ratio resist features leading to pattern distortion. A wide range of times and temperatures were adopted but all had the same effect even when careful heating and cooling cycles were adopted. Even a short low temperature postbaking procedure was to cause degradation of pattern features. This problem has been found by other users [32]. For this reason no postbake cycle was employed. This was found to cause no problems in subsequent processing.

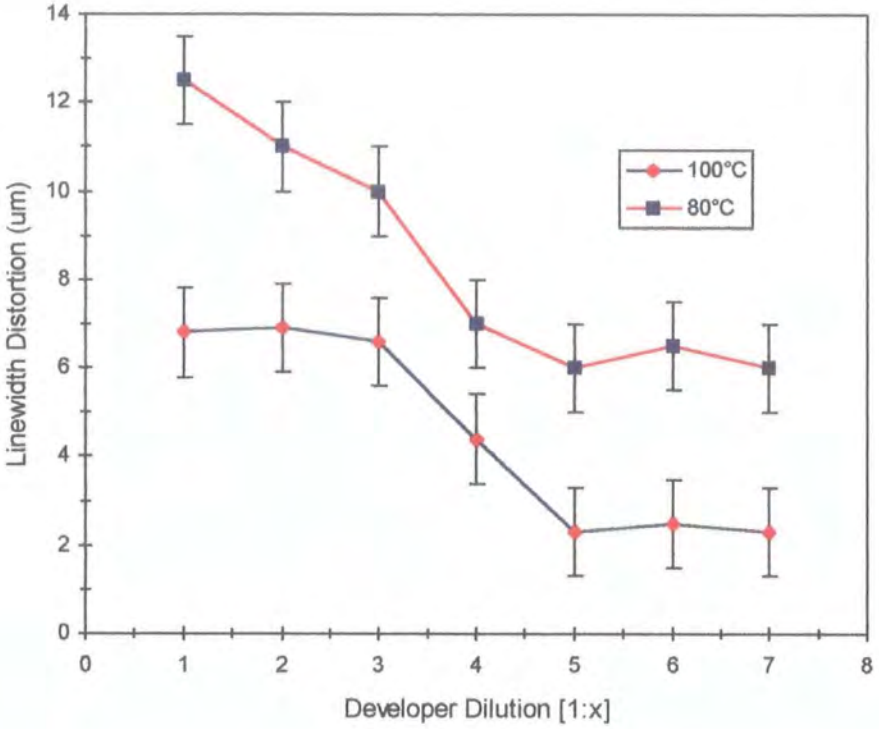

Figure 4.9. *Influence of developer dilution on linewidth deviation.*

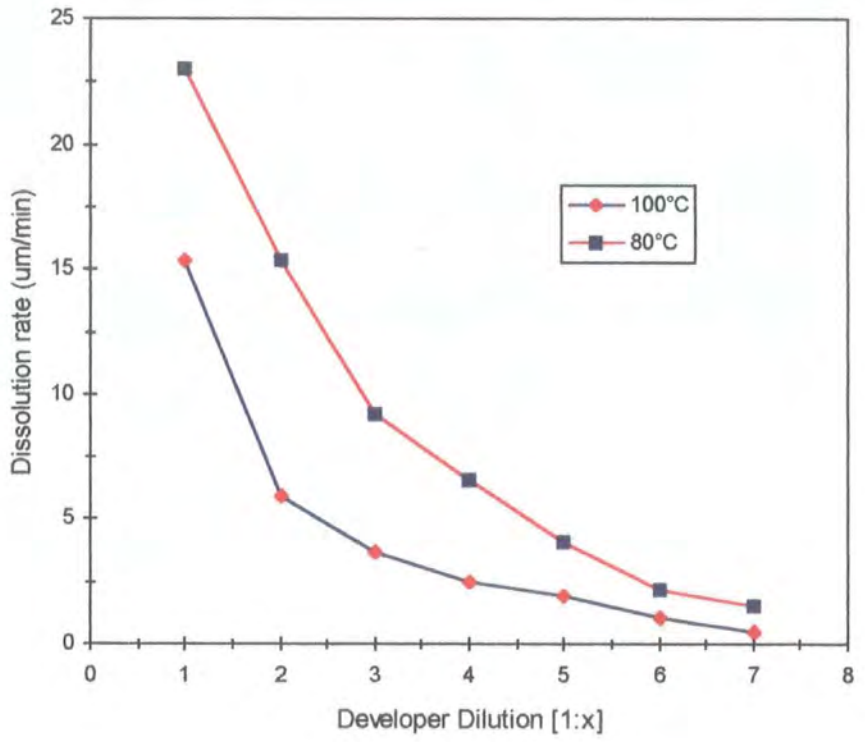

Figure 4.10. *Influence of developer dilution on resist dissolution rate.*

4.3.2.6 Summary of Resist Processing

The table below identifies the optimum processing conditions found for different thicknesses of resist.

Thickness (μm)	Deposition Conditions	Prebake Conditions	Linewidth Distortion (μm)
14 μm	1 layer @ 1000 rpm	20 mins @ 100°C	1.0 μm
22 μm	1 layer @ 400 rpm	30 mins @ 100°C	2.0 μm
35 μm	2 layers @ 1000 rpm	60 mins @ 100°C	4.0 μm
56 μm	3 layers @ 1000 rpm	70 mins @ 100°C	10.5 μm
77 μm	4 layers @ 1000 rpm	80 mins @ 100°C	20.0 μm

Table 4.2. *Summary of resist processing conditions.*

Using these conditions it was possible to successfully pattern photoresist layers and obtain high aspect ratio features suitable to produce electroplating moulds. Some typical resist profiles are shown in figure 4.11. The single column in (a) is approximately 50μm tall, 7μm wide with sidewalls approaching 87° between the top and bottom surfaces. Figure 4.12 shows a close-up of an arbitrary mould structure showing the edge profile and sidewall texture. It must be noted however that the sidewall texture is a result of the edge definition of the photomask and not a characteristic of the mould construction process itself.

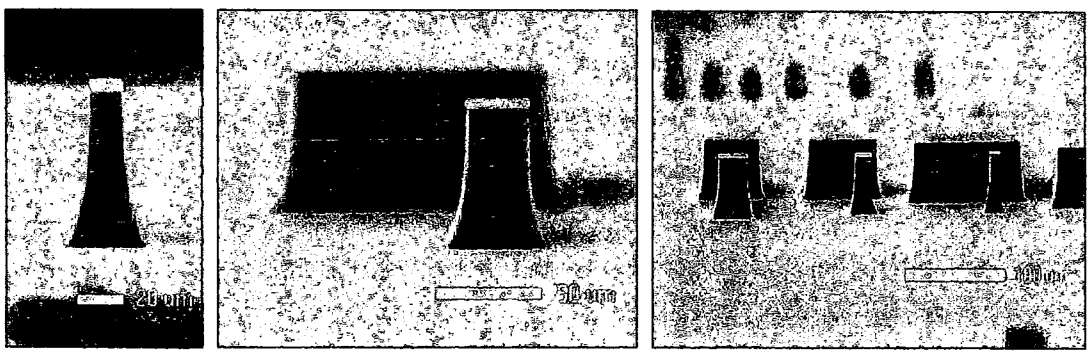

(a) *(b)* *(c)*

Figure 4.11. *SEM images of typical resist profiles.*

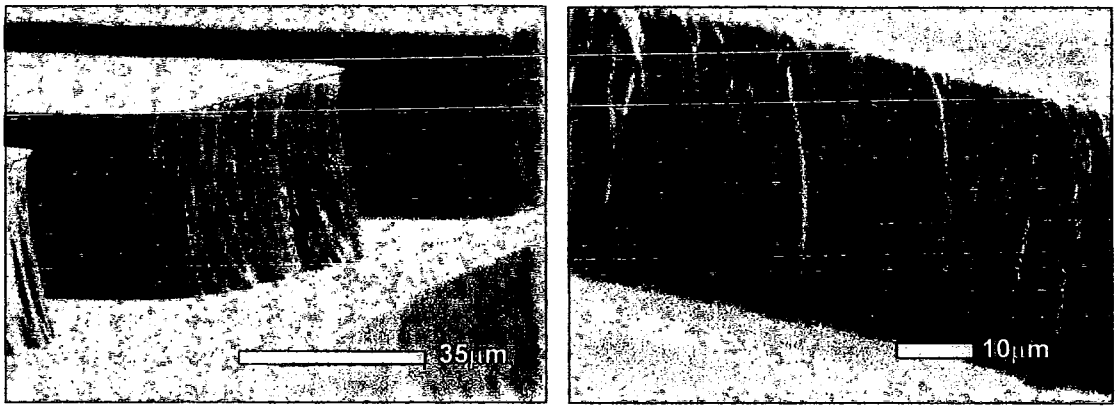

Figure 4.12. *SEM images of a typical resist mould.*

4.4 Electroforming

The production of nickel microstructures is achieved by selective deposition through predefined photoresist moulds. The moulds are formed over metallic seed layers that are required to make electrical contact over the entire substrate.

Using the mould formation techniques described in the section 4.3, together with the electroplating process outlined in chapter three, nickel microstructures have been successfully fabricated. Figure 4.13 presents the results of this combined process. Figure 4.13 (a) shows an array of nickel columns approximately 40μm tall. Figure 4.13 (b) shows some cog-type structures, 50μm thick and 900μm in diameter. This highlights the point that the electrodeposit faithfully conforms to the lateral dimensions of the photoresist mould.

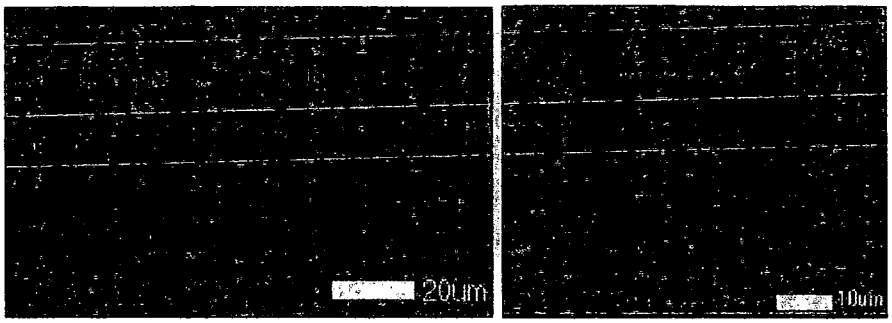

(a). Nickel columns.

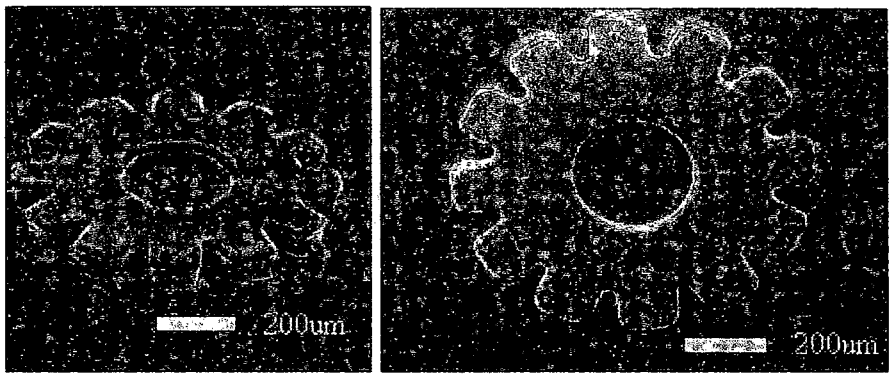

(b). Nickel cog test structures.

Figure 4.13. Electroplated nickel test structures.

4.5 Free-Standing Microstructures

After successfully combining the thick photoresist and electroplating technologies, it was necessary to incorporate a sacrificial layer technique to develop the free-standing microstructures illustrated in figure 4.1. The sacrificial layer technique involves the deposition of a spacer layer prior to the construction of the mechanical elements, which is selectively removed as a final process step to yield a self-supporting structure.

This process is discussed in the following sub-sections together with the special drying techniques necessary to avoid the well-known problem of stiction [18].

4.5.1 Sacrificial Layers

4.5.1 Sacrificial Layers

Materials used as sacrificial layers must have two characteristics. Firstly, it must be possible to deposit the material easily in layers of 1-3μm. This provides a sufficient clearance between the structure and the substrate and allows for its removal in a wet etchant. Secondly, and most importantly, the sacrificial layer must be removed selectively i.e. all other materials employed in the construction of the microstructure must be chemically inert to the etchant used to remove the sacrificial layer. Three such materials were available for this purpose; sputtered titanium, thermally evaporated aluminium and photoresist. All three materials were used successfully as sacrificial layers but preference was given to titanium due to ease of processing and high selectivity. The etchants used for each material are highlighted in table 4.3.

Sacrificial Layer Material	Etchant
Titanium	10% HF
Aluminium	$NaOH / K(CN)_6Fe_2$
Photoresist	Acetone

Table 4.3. *Sacrificial layers and corresponding etchants.*

In order to calculate the total etch time required to completely remove the titanium layers and free a particular device, it was necessary to determine the lateral etch rate of titanium in 10% HF solution (figure 4.14). Although only four data points were taken, the graph indicates an approximate lateral etch rate of 2μm / min, which was found to be independent of the titanium thickness (1-4μm). To ensure complete removal of the sacrificial layer the approximate etch time determined from figure 4.14 was doubled. This caused no problems due to the high selectivity of HF to titanium.

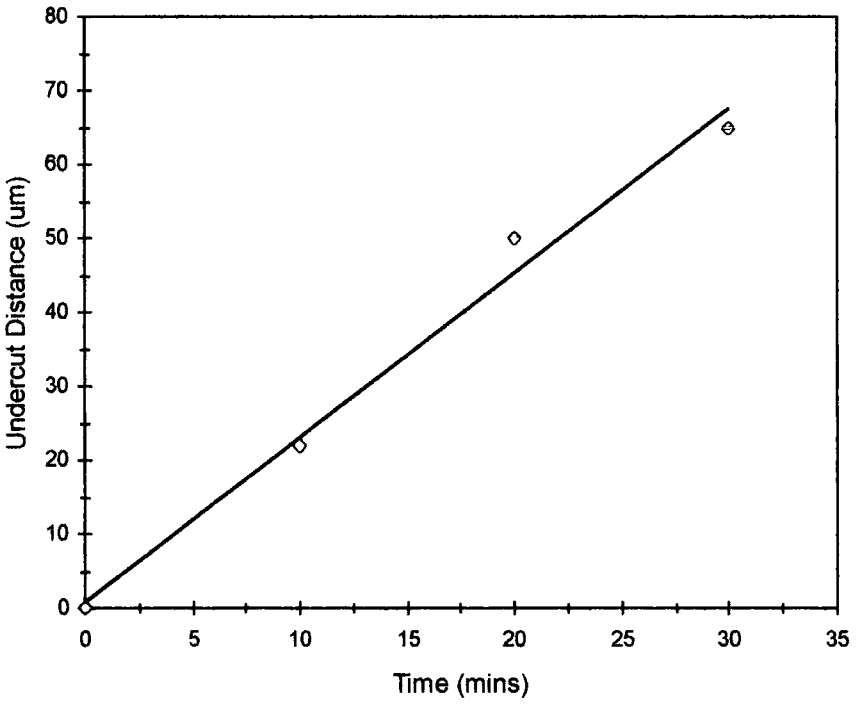

Figure 4.14. *Determination of lateral titanium etch rate for a 3μm layer in 10% HF solution.*

4.5.2 Dry Release Techniques

Inspection of preliminary devices after removal of the sacrificial layer and drying found that the structures had collapsed. It was thought that this was due to the phenomena of stiction. This, as mentioned previously, is a common problem routinely encountered in surface micromachining caused by drying samples from the liquid phase. It can, however, be overcome by adopting careful freeze drying release processes [20]. There are numerous variants of this type of process, the one chosen based on the use of 1,2 dichlorobenzene. This is a solid organic compound at room temperature that has a melting point of 52°C.

The drying process starts after the removal of the sacrificial layer and a DI rinse. The samples are placed in an 80°C solution of the chlorobenzene (which is a liquid at this temperature) and allowed to soak of 1hr. This ensures complete displacement of the DI in the undercut region. After this time the samples are removed from the chlorobenzene

and allowed to cool to room temperature, causing solidification of the chlorobenzene. At this point the microstructures are supported by the solid chlorobenzene which prevents their collapse. Finally the samples are placed in a vacuum chamber, whereby the chlorobenze sublimes and yields the free-standing microstructures. This procedure was found to be necessary with all samples below 10μm in thickness. However, with samples greater than 25μm it was found that this freeze drying process was not required due to the increased vertical stiffness of the devices. The geometry of the devices also has an influence on whether stiction will be a concern as large unsupported structures will be more prone than shorter, more rigid devices.

4.6 Photomask Production

All photomask designs were generated using AutoCad LT technical drawing package and plotted directly onto A3 paper or acetate using an Agfa high-resolution colour plotter. These plots were then photographically reduced onto high-resolution Agfa millimask plates to produce emulsion masks with minimum linewidths of approximately 25μm and spacings of 18μm. Full mask production conditions are listed in table 4.4.

Paper	Acetate
1) 12 min Exposure @ f16	*1) 8min exposure @ f16*
2) Develop (1:2) 4 min	*2) Develop (1:2) 4min*
3) Fixer (2min)	*3) Fixer (2min)*

Table 4.4. *Summary of photomask fabrication.*

Photomasks used for the exposure of thick resist layers resulted in poor resist profiles. This was caused by poor definition at the very edges of mask features. To overcome this problem, metal photomasks were constructed from the primary emulsion masks to yield significant improvements. This was achieved by transferring the mask pattern onto a titanium covered glass plate via standard lithography. By careful optimisation of this procedure, it was possible to reduce the minimum linewidths to approximately 12μm

titanium etch. The actual minimum linewidths measured on the resist features were found to be in the 8-10μm region due to the inherent linewidth distortion that occurs during pattern transfer from mask to resist (section 4.3.2.3).

4.7 Conclusions

This chapter has detailed all the process steps that have been developed to allow the fabrication of surface micromachined nickel microstructures with thickness an order of magnitude greater than traditional polysilicon surface machined devices. This fabrication sequence has been further demonstrated in the production of simple beam structures (chapter five) and more elaborate ring resonators (chapters seven and eight) and can be adapted to develop sensors and actuators of almost any design. Finally as an example, figure 4.15 demonstrates a self-supporting nickel structure.

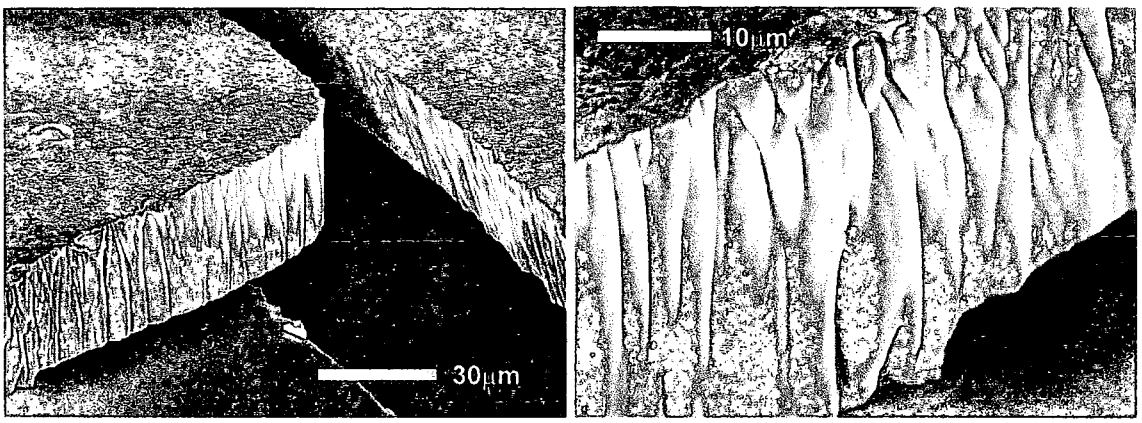

Figure 4.15. *Close-up of a free-standing nickel microstructure.*

Chapter Five
Preliminary Optical Measurements

This chapter presents the results of the optical analysis of an array of nickel cantilever beams. These devices were developed using the fabrication techniques described in chapters three and four and were considered the ideal test structure due to their simple nature and well known mechanical properties. Such structures are used extensively in microengineering, forming the active sensing element in a vast range of sensors and actuators.

The dynamic properties of the cantilever array have been determined optically using laser Doppler vibrometry. All optical measurements were performed at the University of Newcastle-upon-Tyne, using equipment dedicated for the analysis of resonant microstructures. In the following sections, the theory of this analysis tool is first described, then its practical application and finally the experimental results. For comparison, FEM modeling results are also presented.

5.1 Optical Detection of Resonant Structures

Laser Doppler vibrometery is a powerful tool that can be used to detect the small movements of micromechanical devices, offering high resolution and positional accuracy. Although many motion detection schemes have been developed (including capacitive, piezoelectric and electromagnetic), these rely on conversion of motion into electrical signals via electrodes located on or around the moving device. Such interaction between the moving structure and the electrodes can influence the actual behaviour of the device. Optical detection schemes, by comparison, are remote and have negligible influence on the behaviour of the structure under investigation. More importantly, 'classical' detection schemes do not possess the high spatial resolution of optical techniques. Electrode areas are generally maximised to magnify the weak effects that are used to produce the output signals and give only a very generalised indication of motion. In contrast, optical techniques offer high spatial resolution, limited only by the spot size of the probing laser beam - typically a few microns. The optical measurements can be used to build up a vibrational map of the moving surface by scanning sequentially from point to point. In this way a very detailed image of the moving surface can be obtained, including determination of resonant frequencies, damping factors and resonant mode shapes. This process allows comparison of experimental data with finite element predictions.

The system used is a commercial unit made by Polytec consisting of a vibrometer OFV 501 and OFV 3000 control unit.

5.1.1 Working Principles

Optical detection schemes are based on interferometry, a technique that can be used to measure displacements much smaller than the wavelength of light. This is done by monitoring the sinusoidal relationship between the intensity of the interferometer output

and the path difference traveled by two light waves. The vibrometer system is based on a Mach-Zehnder interferometer, pictured schematically in figure 5.1.

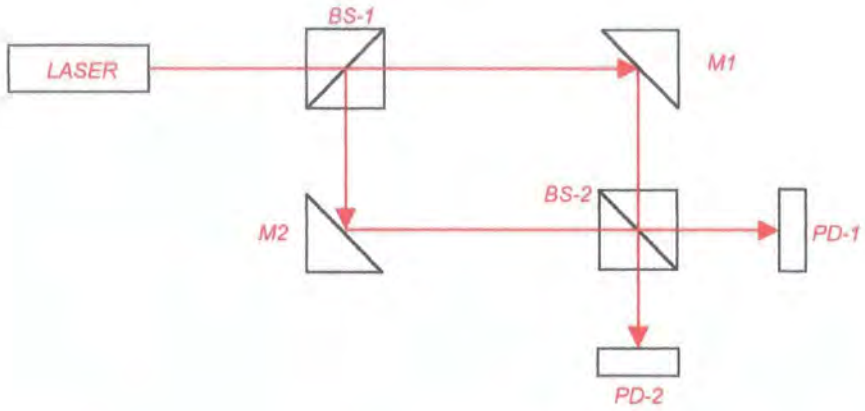

Figure 5.1. *Mach-Zehnder Interferometer.*

In this configuration a polarised laser source is split into two light waves of equal intensity at beam splitter 1 (BS-1). The beams then follow separate paths and are allowed to recombined at BS-2. Superposition of the two waves at BS-2 produces an interference pattern that is converted into electrical signals at the photodetectors, PD-1 and PD-2. The photodetectors are unable to resolve optical frequencies and produce an output voltage proportional to intensity. The intensity of the beam at each photodetector can be shown to be a sinusoidal function of the phase difference between the two waves (see appendix A) and is given by:

$$I_1 = \frac{1}{2}A^2\left[1+\cos(\Delta\vartheta)\right] \tag{5.1}$$

$$I_2 = \frac{1}{2}A^2\left[1-\cos(\Delta\vartheta)\right] \tag{5.2}$$

where A is the output amplitude of the laser and is equal to the square root of the output intensity, and $\Delta\theta$ is the phase difference between the two light waves. Using differential detection schemes the output from the interferometer (V_{out}) is given by:

$$V_{out} \propto I_1 - I_2 = A^2 Cos(\Delta\theta) \qquad (5.3)$$

In order to measure the motion of an external surface the arrangement of figure 5.1 must be modified to allow interaction between one of the light waves and the surface of interest. This modified version is shown in figure 5.2; a probing laser beam is allowed to interact with the moving surface causing its phase to be modulated due to the variations in optical path length. This is achieved by replacing the mirror (M1) with a combination of beam splitter (BS-3) and a quarter wave plate (QWP). These elements allow the polarised output from the laser to travel directly towards the target whilst the reflected beam is redirected towards BS-2 where it is allowed to recombine with the reference beam.

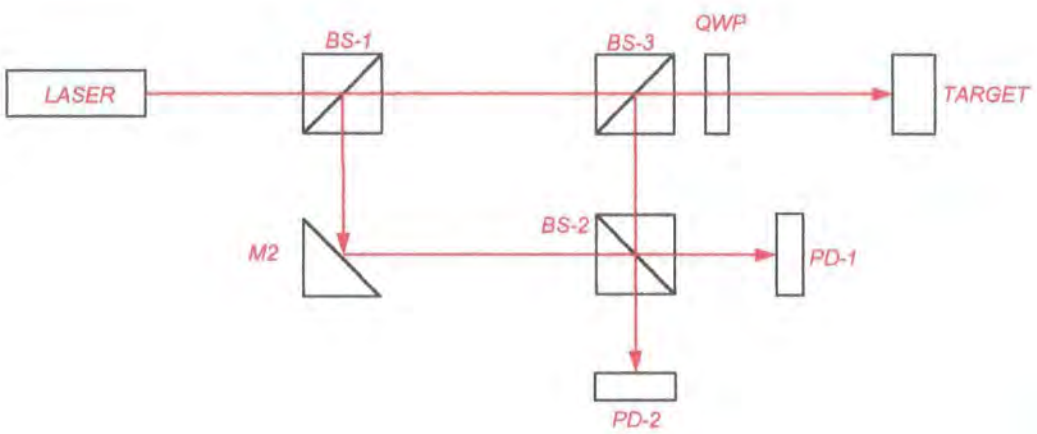

Figure 5.2. *Modified Mach-Zehnder Interferometer.*

If the interferometer is configured symmetrically so that the 'internal' phase difference is zero, then the phase difference between the two waves at BS-2 is caused solely by the external path length. Motion of the target surface modulates this path length and produces a time dependent phase difference, given by:

$$\Delta\theta = \frac{4\pi}{\lambda} \cdot x(t) + \phi_o \qquad (5.4)$$

where λ is the wavelength of the laser output, $x(t)$ is the displacement of the target and ϕ_o is an offset phase difference determined by the external path length to the target.

The output of the interferometer is now:

$$V_{out} \propto A^2 \left[1 + Cos\left(\frac{4\pi}{\lambda} \cdot x(t) + \phi_o \right) \right] \qquad (5.5)$$

the frequency of which is given by:

$$\frac{d}{dt}\left[\frac{4\pi}{\lambda} \cdot x(t) + \phi_o \right] = \frac{4\pi}{\lambda} \cdot \frac{d \cdot x(t)}{dt} \qquad (5.6)$$

$$= \frac{4\pi}{\lambda} \cdot v(t) \qquad (5.7)$$

where $v(t)$ is the velocity of the target. However this configuration still presents a problem; the output from surfaces moving in opposite directions are indistinguishable as a result of $cos(x)$ being equal to $cos(-x)$.

To overcome this problem it is necessary to introduce a small frequency shift to the reference beam. This is done using a RF driven Bragg cell as in the arrangement of figure 5.3. Now, in the presence of a stationary target, the interferometer produces an output beat signal at the shift frequency, f_B. Motion of the target surface modulates the

beat frequency by an amount proportional to the velocity. The output of the interferometer is now given by:

$$V_{out} \propto A^2 Cos\left[2\pi \cdot f_B \cdot t + \frac{4\pi}{\lambda} \cdot x(t) + \phi_o\right] \tag{5.8}$$

where f_B is the Bragg shift frequency introduced to the reference beam. Frequency demodulation of the output signals can now determine the velocity and direction of the moving surface. The output frequency is:

$$\frac{d}{dt}\left[2\pi \cdot f_B \cdot t + \frac{4\pi}{\lambda} \cdot x(t) + \phi\right] = 2\pi\left[f_B + \frac{2}{\lambda} \cdot \frac{dx(t)}{dt}\right] \tag{5.9}$$

$$= 2\pi\left[f_B + \frac{2}{\lambda} \cdot v(t)\right] = 2\pi\left[f_B + f_D\right] \tag{5.10}$$

where f_D is the Doppler shift frequency [42].

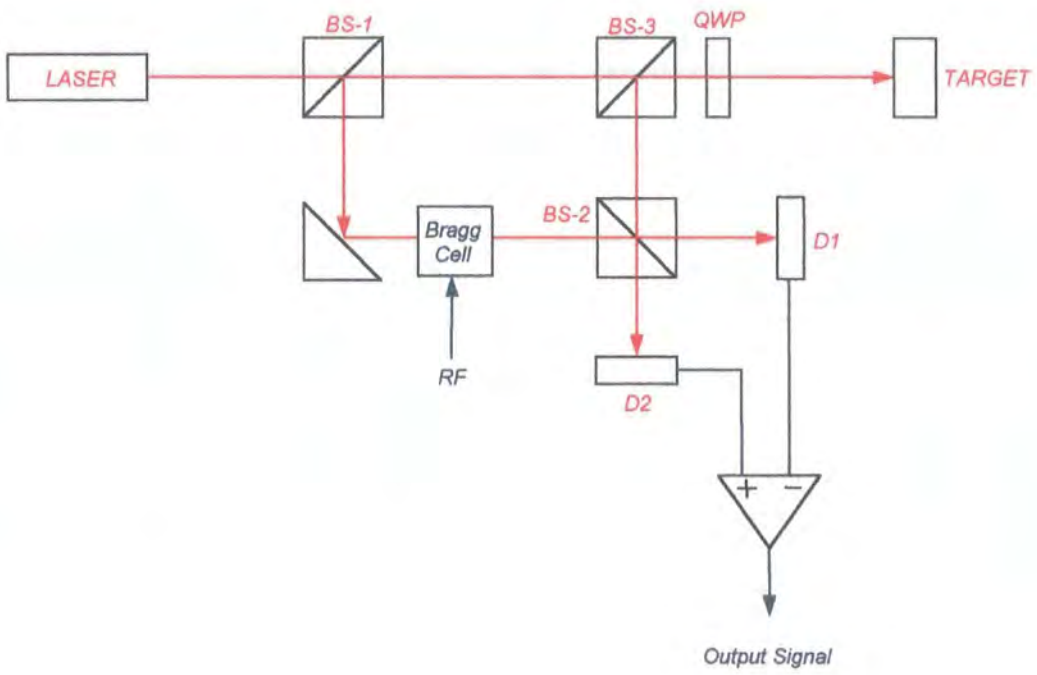

Figure 5.3. *Laser vibrometer configuration.*

5.1.2 Experimental Set-Up

Figure 5.4 shows the experimental set-up used for optical testing. All samples were excited into flexural vibration externally by means of a piezoelectric actuator. The samples were mounted onto a PZT disc with soft wax to provide sufficient adhesion for excitation and also allow removal and replacement of samples without damage. The mounting arrangement is shown in figure 5.5 and incorporates provision for evacuation of the sample cavity to allow low-pressure measurement.

The piezoelectric disks were driven from the swept sine source of an HP3562A dynamic signal analyser providing drive signals of up to $5V_{pk}$ in amplitude. The structural response of the measurement point was determined (using the laser vibrometer unit to measure the absolute velocity of the sample) and used to calculate the frequency response function. This data was stored for later use by STAR modal analysis software for determination of resonant frequencies, damping factors and resonant mode shapes. A full description of the experimental arrangement is given in [43].

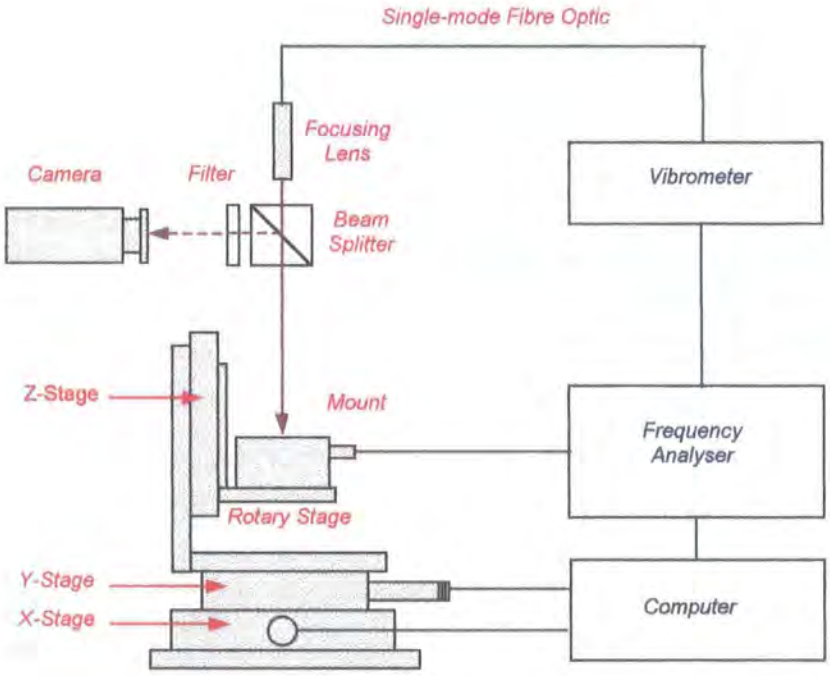

Figure 5.4. *Experimental measurement system.*

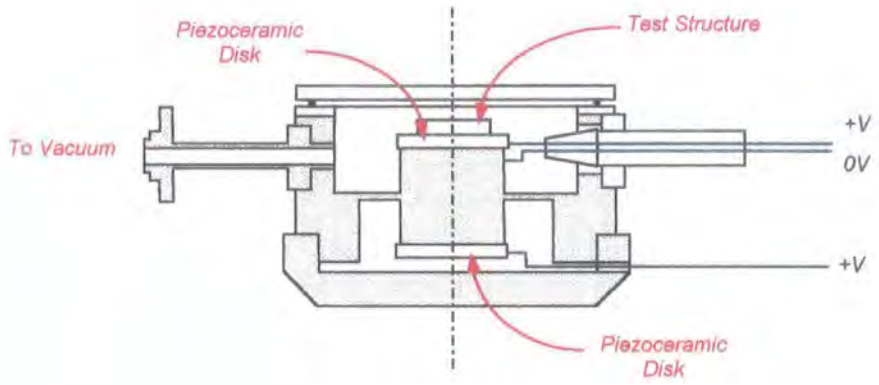

Figure 5.5. *Sample Mount.*

5.2 Finite Element Analysis

This section describes the finite element analysis (FEA) of the test devices. This was done in order for comparison and validation of the experimental results. Although beam theory is well understood and dynamic properties can be easily derived from simple calculations, FEA was considered a better approach due to the complex nature of the thickness profile of each beam. This was a result of the inherent non-uniformity of the electroforming process as described in chapter three. A typical thickness profile of a 2.7mm long cantilever is shown in figure 5.6.

Simulation was performed using PAFEC-FE (version 8.5) suit of programs mounted on a Sun Ultra Workstation. The FE mesh constructed for this purpose is shown in figure 5.7. From this model the first four resonant modes of vibration of the 2.7mm cantilever were determined and are shown in table 5.1. The corresponding modeshapes are shown in figures 5.8 to 5.11, which represent the first three flexural modes (figures 5.8, 5.9 and 5.11) and a torsional mode (figure 5.10).

	Mode 1	Mode 2	Mode 3	Mode 4
Mode Type	1st flexural	2nd flexural	1st torsional	3rd flexural
Frequency	3.07 kHz	23.53 kHz	35.20 kHz	71.70 kHz

Table 5.1. *Summary of simulation results.*

In all simulations the bulk material properties of nickel were assumed, as the exact material properties of the electroplated nickel were not known.

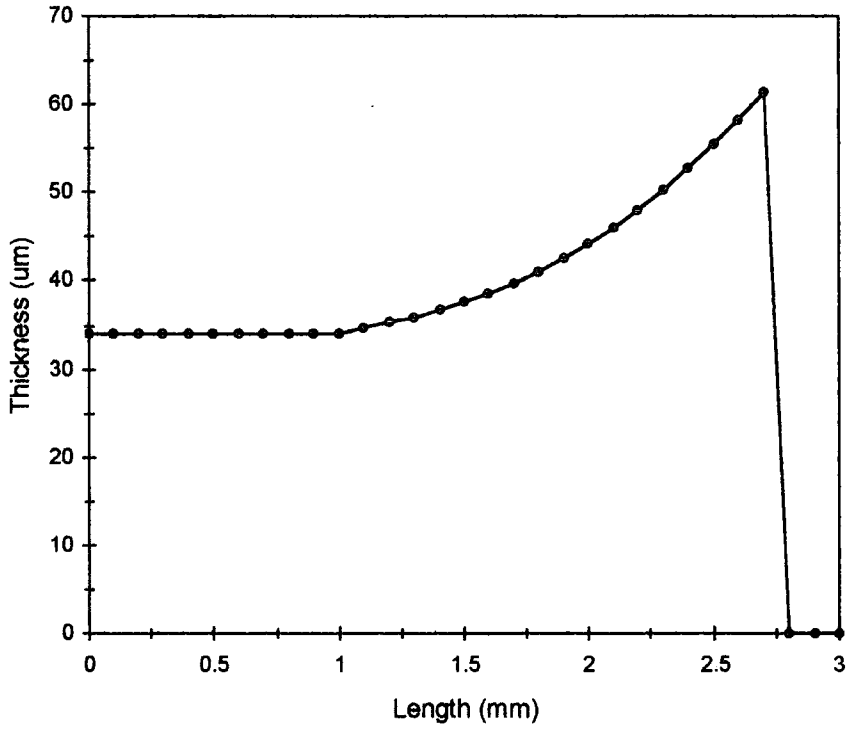

Figure 5.6. *Thickness profile of the 2.7mm long cantilever beam.*

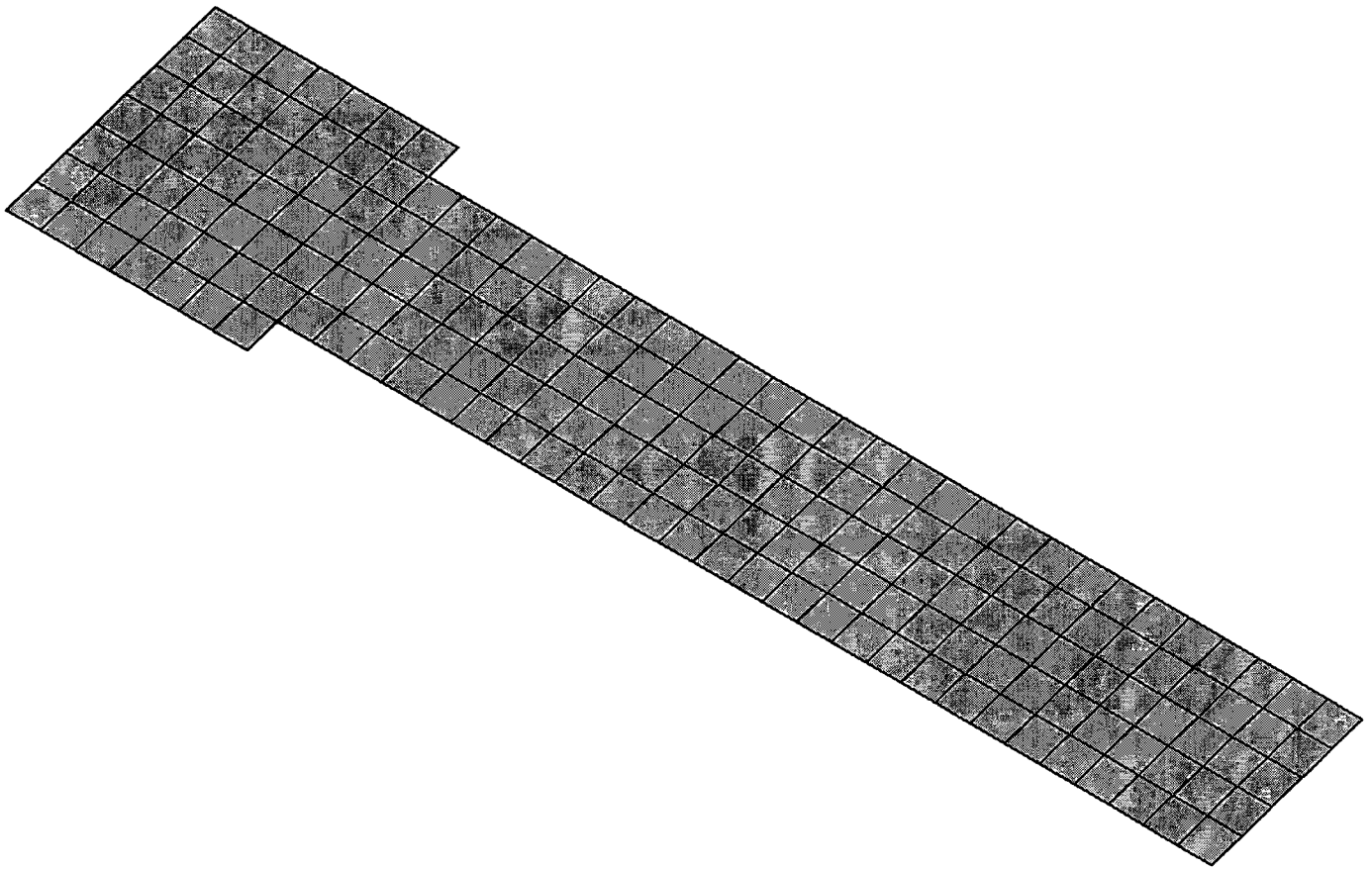

MODES-FREQ
MODE 0
0.000 E 0
(HZ)

ROTATION
X = 330
Y = 330
Z = 330

TITLE UNDEFORMED CANTILEVER

Figure 5.7. *Undeformed Simulation Model.*

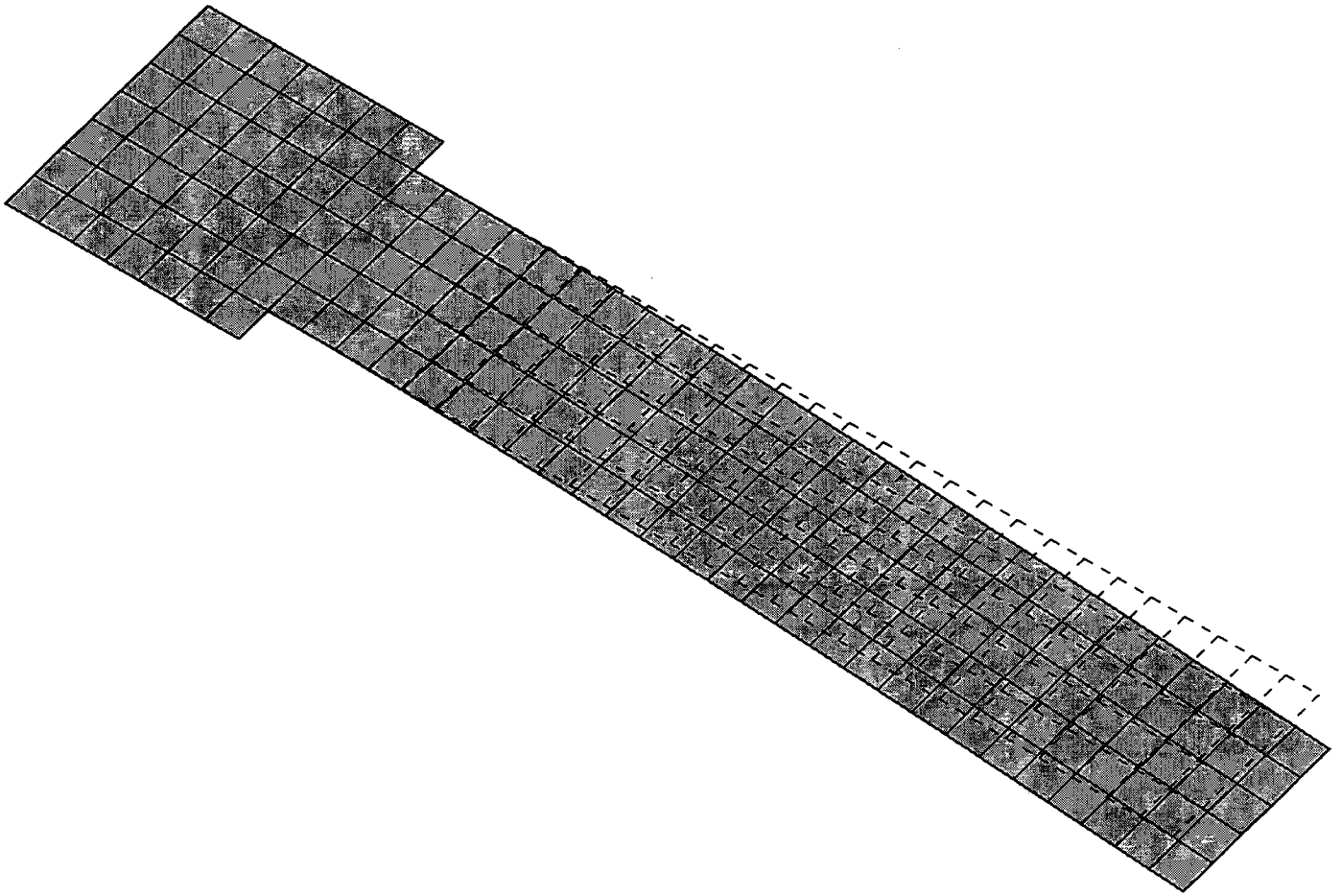

MODES-FREQ
MODE 1
3.072 E 3
(HZ)

ROTATION
X = 330
Y = 330
Z = 330

TITLE FUNDAMENTAL FLEXURAL MODESHAPE

***Figure 5.8.** Mode One.*

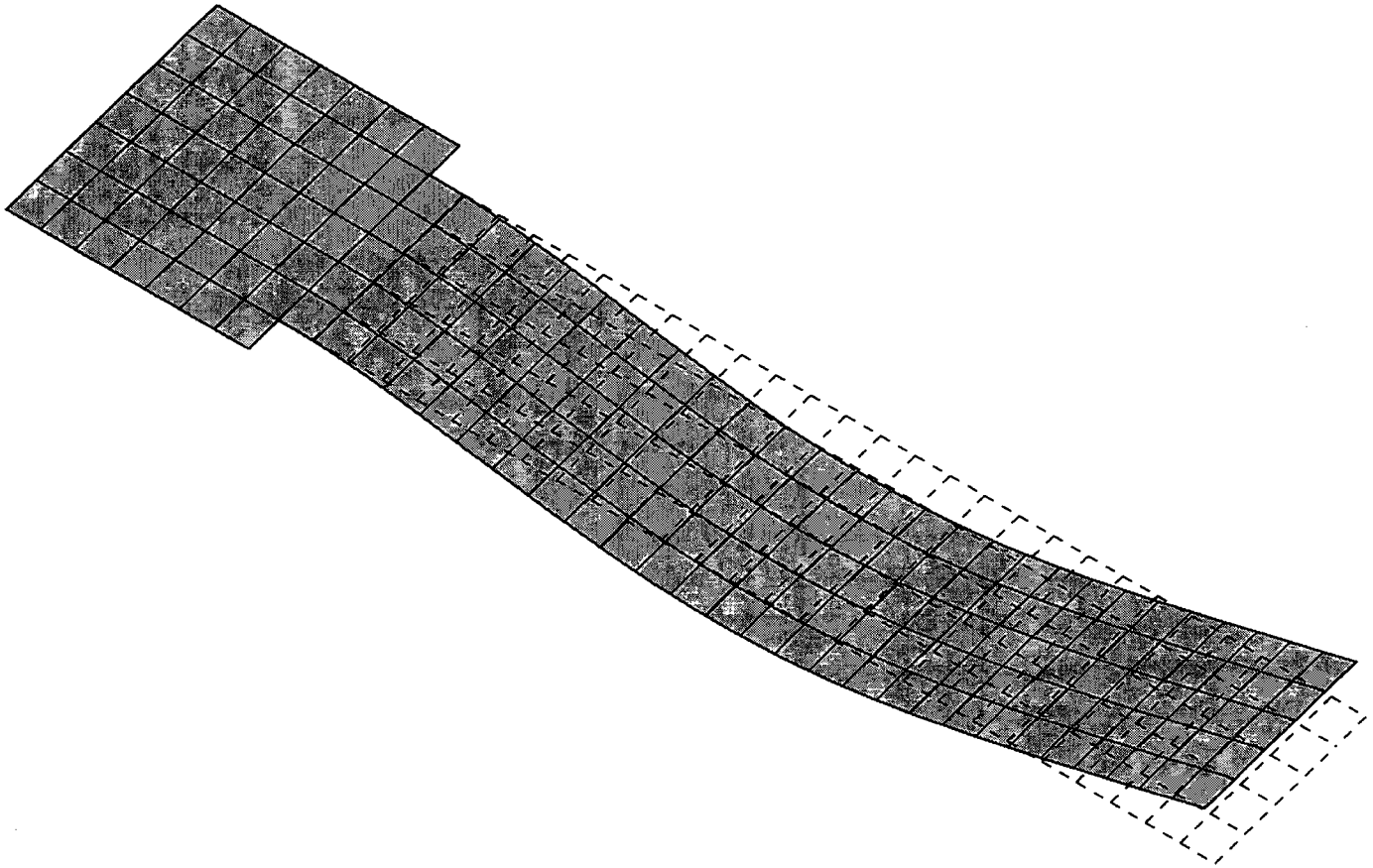

MODES-FREQ
MODE 2
2.353 E 4
(HZ)

ROTATION
X = 330
Y = 330
Z = 330

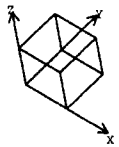

TITLE 2ND FLEXURAL MODESHAPE

Figure 5.9. *Mode Two.*

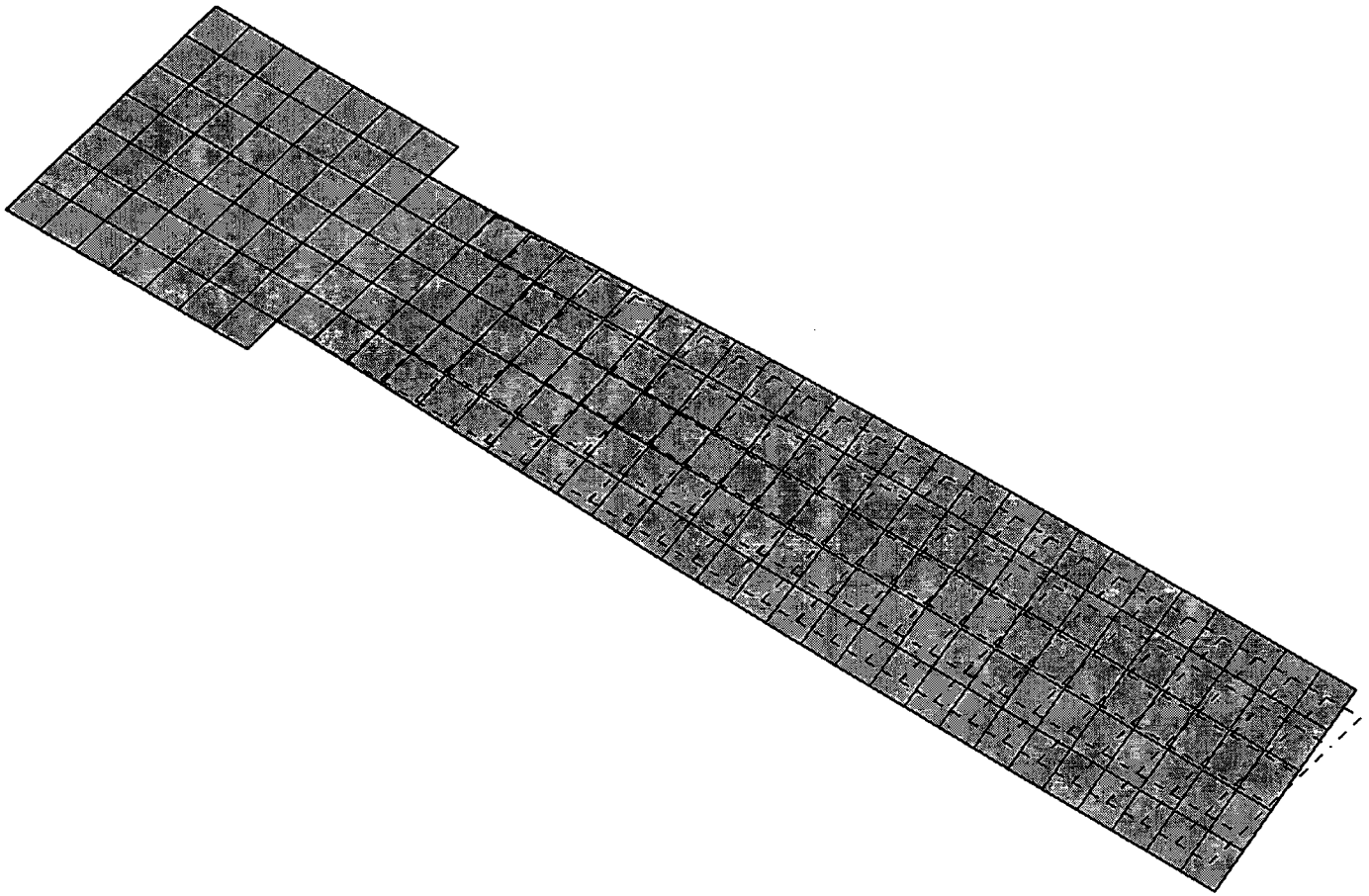

MODES-FREQ
MODE 3
0.352 E 5
(HZ)

ROTATION
X = 330
Y = 330
Z = 330

TITLE 1ST TORSIONAL MODESHAPE

Figure 5.9. *Mode Three.*

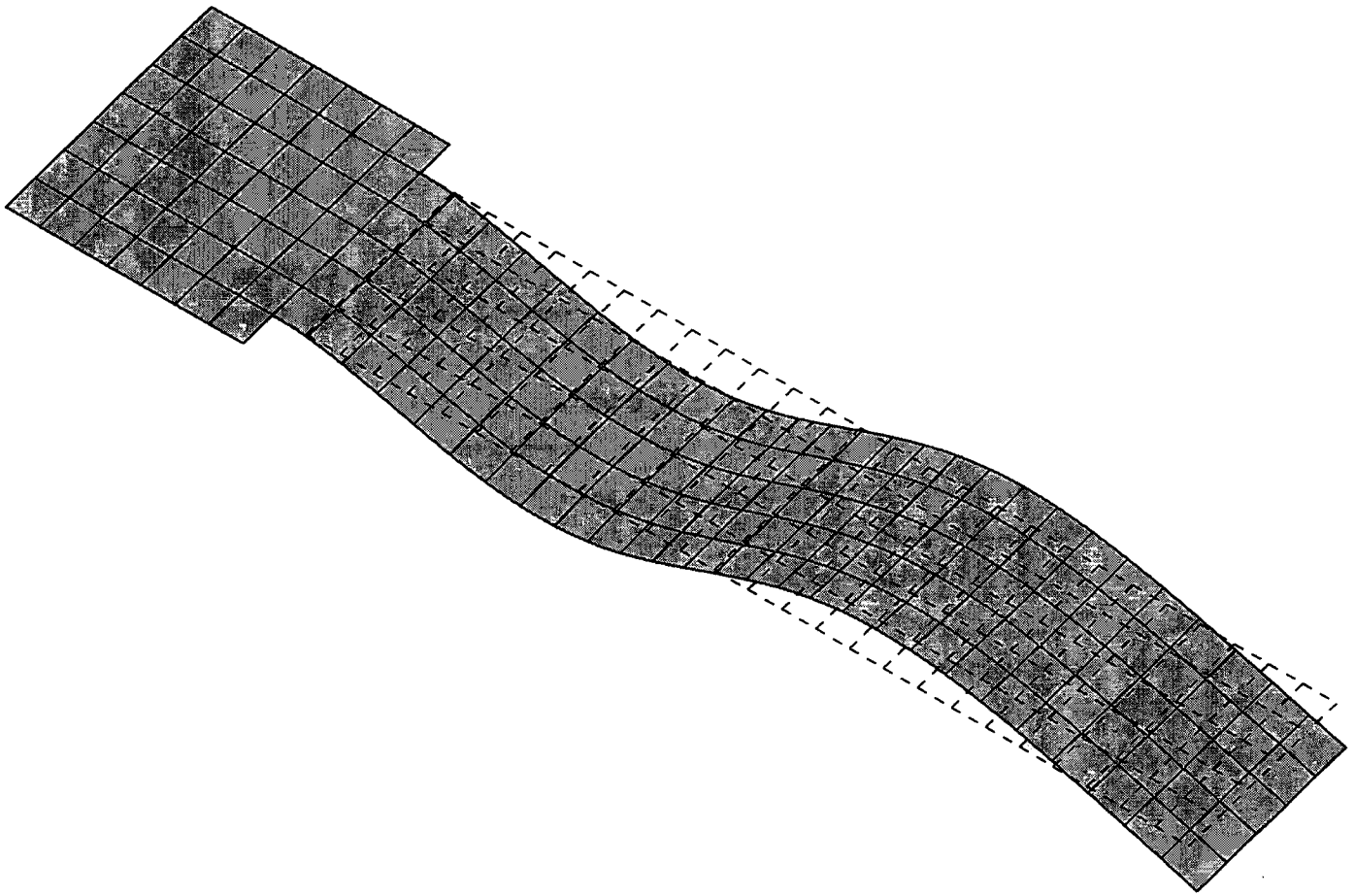

MODES-FREQ
MODE 5
0.717 E 5
(HZ)

ROTATION
X = 330
Y = 330
Z = 330

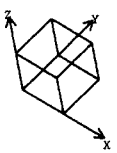

TITLE 3RD FLEXURAL MODESHAPE

Figure 5.11. *Mode Four.*

5.3 Experimental Results

Using the laser Doppler vibrometer described in section 5.1, the dynamic properties of the array of cantilever beams were determined experimentally. Using piezoelectric excitation of the array, initial measurements of resonant frequency and damping were obtained. Further measurements were taken to determine resonant mode shapes. Finally an attempt to determine the mechanical properties of the beam material was made.

5.3.1 Frequency Response

Preliminary measurements taken at the unrestrained end of a 2.7mm long beam were made to confirm the release of the structures. Surface micromachined devices often suffer from stiction in which released devices collapse during the final rinse and drying stages of the fabrication process (chapter four). After measurement of the background response of the piezoceramic disks, point measurements were taken on the cantilevers at reduced pressures (typically 0.01mbar). Initially a wide frequency sweep was performed to identify the main resonance peaks. These were located at 3.14 kHz, 23.79 kHz, 37.94 kHz and 71.22 kHz. More detailed measurements were then obtained around these frequencies so that accurate determination of resonant frequency and Q-factor could be obtained. A typical frequency response measurement taken about the 3.14 kHz resonance is shown in figure 5.12. The frequency response shows a characteristic resonance curve with a peak amplitude of approximately 970 nm at a drive voltage of 1V and a pressure of 0.005 mbar. The corresponding phase response is given in figure 5.13 showing the expected 180° sweep through resonance. This data is combined in the Nyquist plot of figure 5.14, which shows the characteristic circular relationship associated with resonance. Due to good mode separation there is little influence of coupling from other modes as indicated by the position of the modal circle at the origin of the graph. The rotation of the modal circle results from the damping within the system (the modal circle of an ideal undamped system is aligned with the imaginary axis) [44].

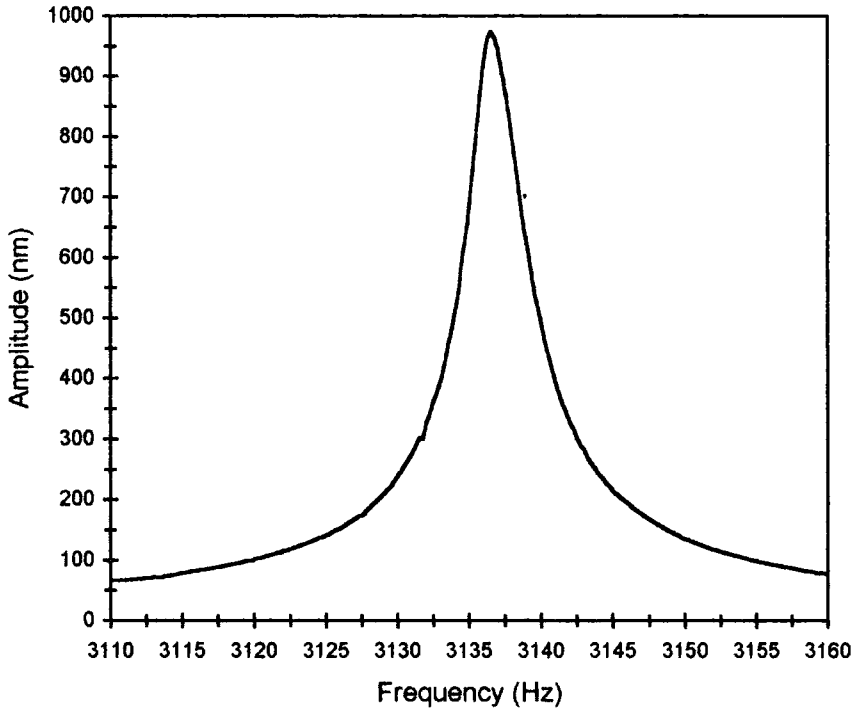

Figure 5.12. *Amplitude response of 2.7mm cantilever.*

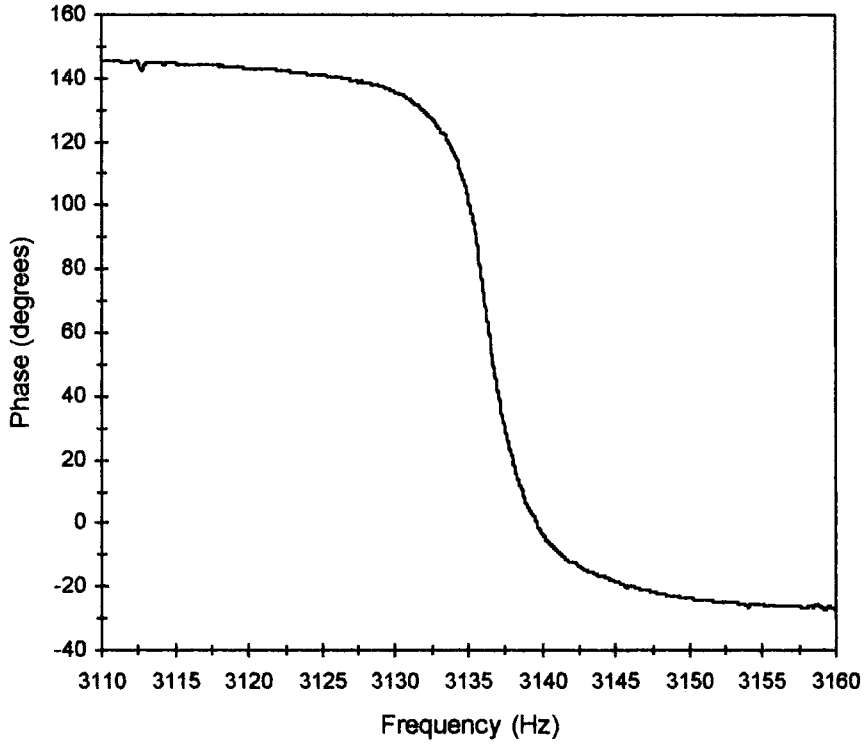

Figure 5.13. *Phase response of the cantilever.*

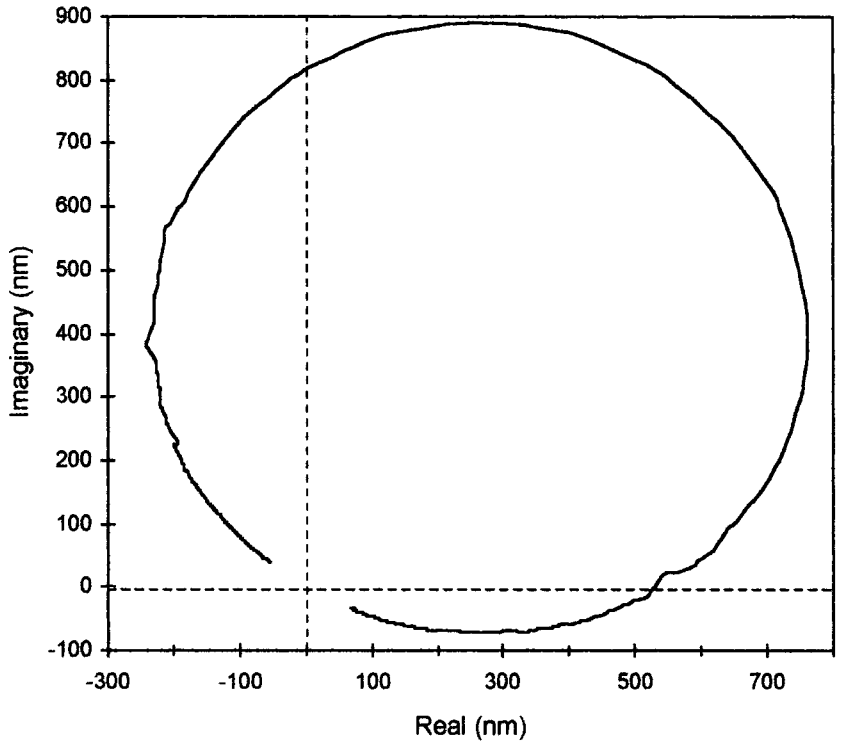

Figure 5.14. *Nyquist diagram.*

5.3.2 Quality factor

The quality factor or Q-factor of a particular vibration is a very important characteristic in relation to resonant microsensors. It is a measure of the energy losses from within the system and has a great influence on sensor performance. Resonant sensors of high Q can demonstrate high sensitivity, resolution and accuracy, and so it is essential that this parameter be maximised. The Q-factor is related to the amount of damping that is present within the vibratory system; the greater the damping the greater the energy dissipation from within the system and the greater the resistance to the vibration. Consequently, vibrations of high Q can be driven and sustained by the application of smaller drive forces reducing power consumption. The Q-factor can be measured directly from the amplitude frequency spectrum of the vibration (figure 5.15) by dividing the resonance frequency by the frequency bandwidth at the 3dB point.

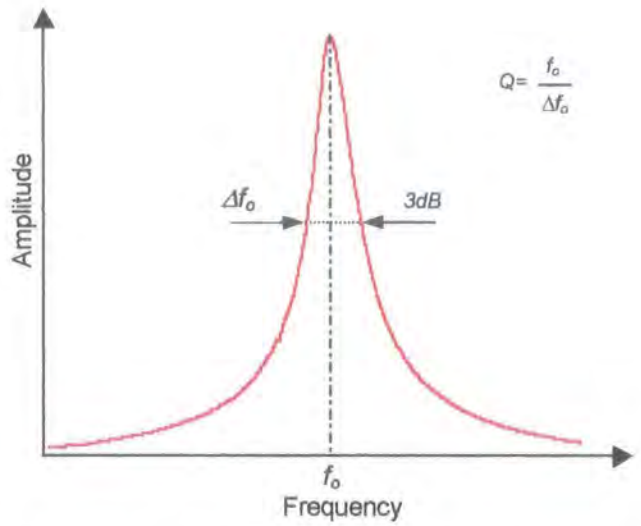

Figure 5.15. *Determination of Q-factor from amplitude frequency response curve.*

In order to maximise the Q it is necessary to reduce the amount of damping present within the system. Damping originates from a combination of sources, but the most significant contribution results from operation within a viscous fluid e.g. air. Motion of the vibrating element causes a disturbance of the surrounding medium resulting in frictional losses and acoustic radiation. Lowering the ambient pressure can significantly reduce the effect of viscous damping. This can be seen from figure 5.16. The graph shows the experimentally derived relationship between Q-factor and pressure for one of the nickel cantilevers. It can be seen that a small reduction from atmospheric pressure has a relatively small effect, but in the region between 1.0 - 0.1 mbar the Q-factor increases two orders of magnitude. Further reduction in pressure has a less profound effect as the Q-factor begins to level off. The Q peaks at a value of approximately 912 at 0.01mbar.

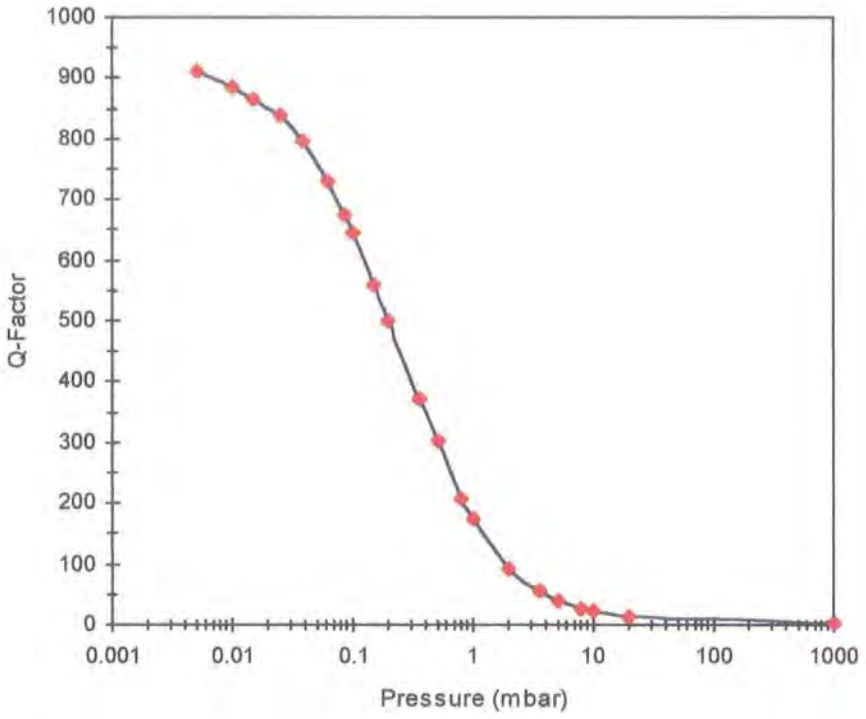

Figure 5.16. *Quality Factor of fundamental vibration as a function of pressure..*

With the effects of viscous damping effectively eliminated by low-pressure operation, other sources of damping become significant and limit the maximum Q that can be obtained. These sources of damping are more intrinsic and cannot be easily removed. They are caused by the design of resonator or originate from within the resonator material itself. For example, unbalanced resonators can suffer energy losses whereby the energy of the vibrating element is dissipated through the mechanical supports. Under these conditions material based damping also becomes very significant. This is the most fundamental form of damping and is caused by internal friction between grain boundaries

and other crystallographic defects. The amount of material damping is inherent to a particular material and can only be minimised by shrewd choice. This is why low defect single crystal materials such as silicon and quartz are widely used in resonant systems.

Table 5.2 lists Q-factors measured for each mode of the 2.7mm cantilever.

	Mode 1	Mode 2	Mode 3	Mode 4
Q-factor	912	532	1490	752

Table 5.2. *Measured values of Q-factors for first four modes.*

5.3.3 Resonant Modeshapes

By scanning the surface of interest at discrete points it was possible to accurately determine the resonant modeshapes of the cantilevers. This was achieved for the first three flexural modes of vibration as shown in figures 5.17 to 5.19 together with the predicted modeshapes obtained from the FEA model. Higher modes (above 100 kHz) could not be detected due to the finite range of the measurement system. Not shown is an intermediate torsional mode measured at 37.94kHz.

The experimental data shown in figures 5.17 and 5.18 show excellent correlation with the predicted modeshapes and accurately identify the first two flexural modes of the beam. The correlation between the data points and the predicted modeshape of the third flexural modeshape (figure 5.19) is also good but shows slight deviation towards the end of the beam. This could be due to calculation errors or more likely fundamental errors in the model. Although the variation of the thickness profile of the beam was taken into account, lateral deviations in thickness were not. In addition the exact material properties of the beam material are unknown which will account for a particular degree of uncertainty in the model.

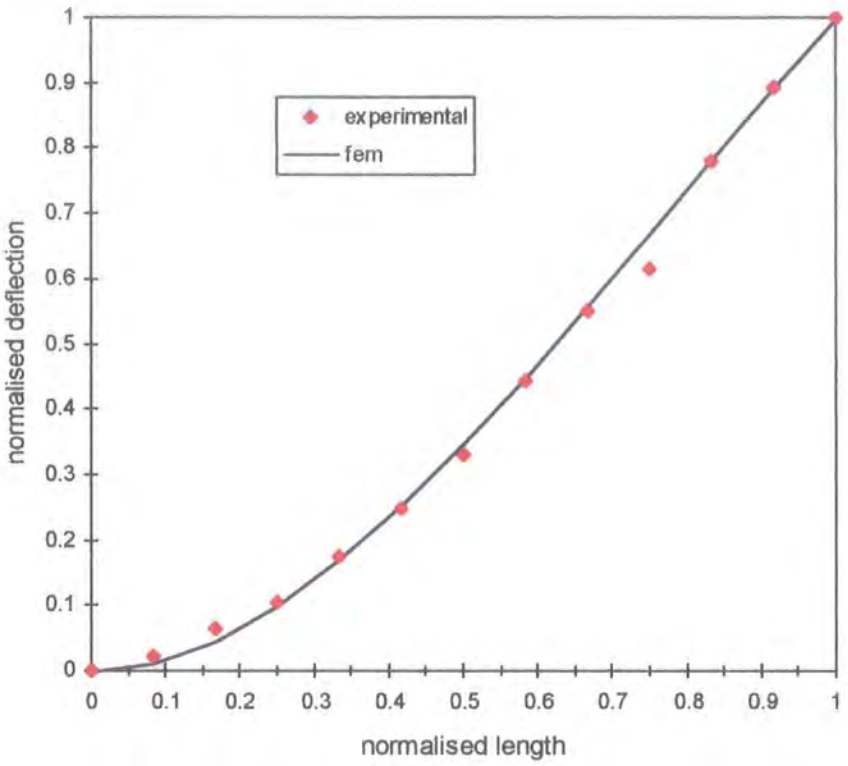

Figure 5.17. *Fundamental flexural modeshape of the 2.7mm cantilever beam.*

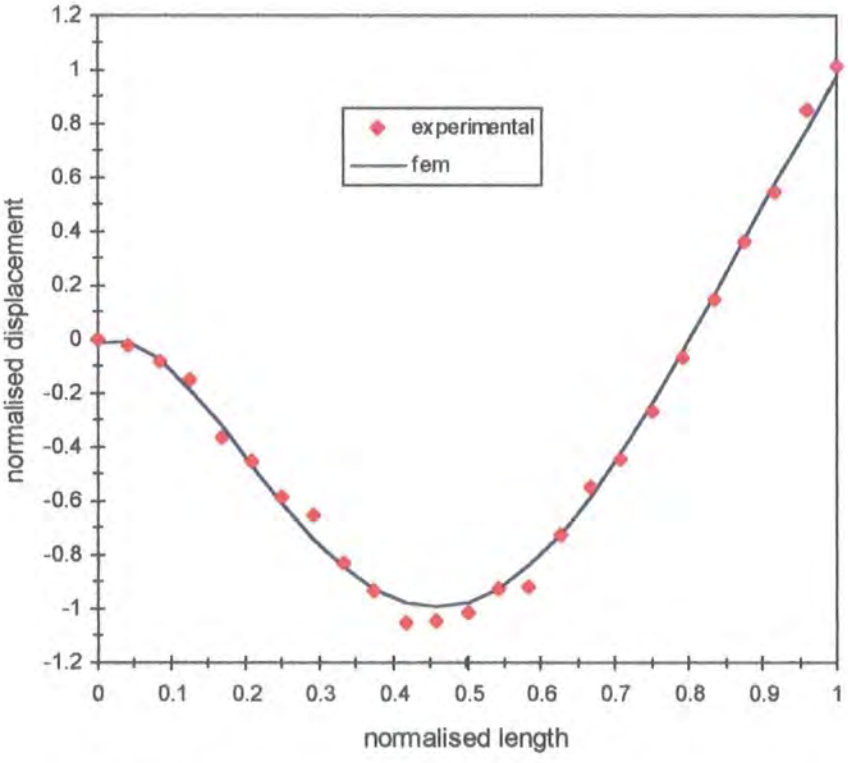

Figure 5.18. *Second flexural modeshape of the 2.7mm cantilever beam.*

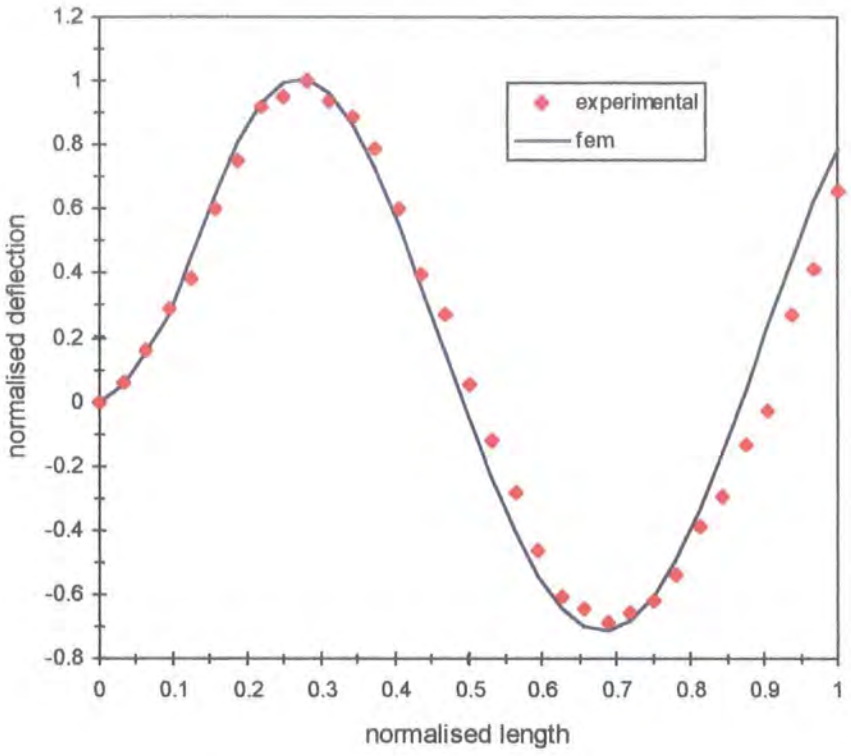

Figure 5.19. *Third flexural modeshape of the 2.7mm cantilever beam.*

Using STAR modal analysis software it was possible to animate the motion of the vibrating surface in a Windows based environment. Figures 5.20 to 5.23 show the still frame animation of the first three flexural modes of the cantilever.

MODE 1
FREQUENCY = 3.14 kHz
Q-FACTOR = 912

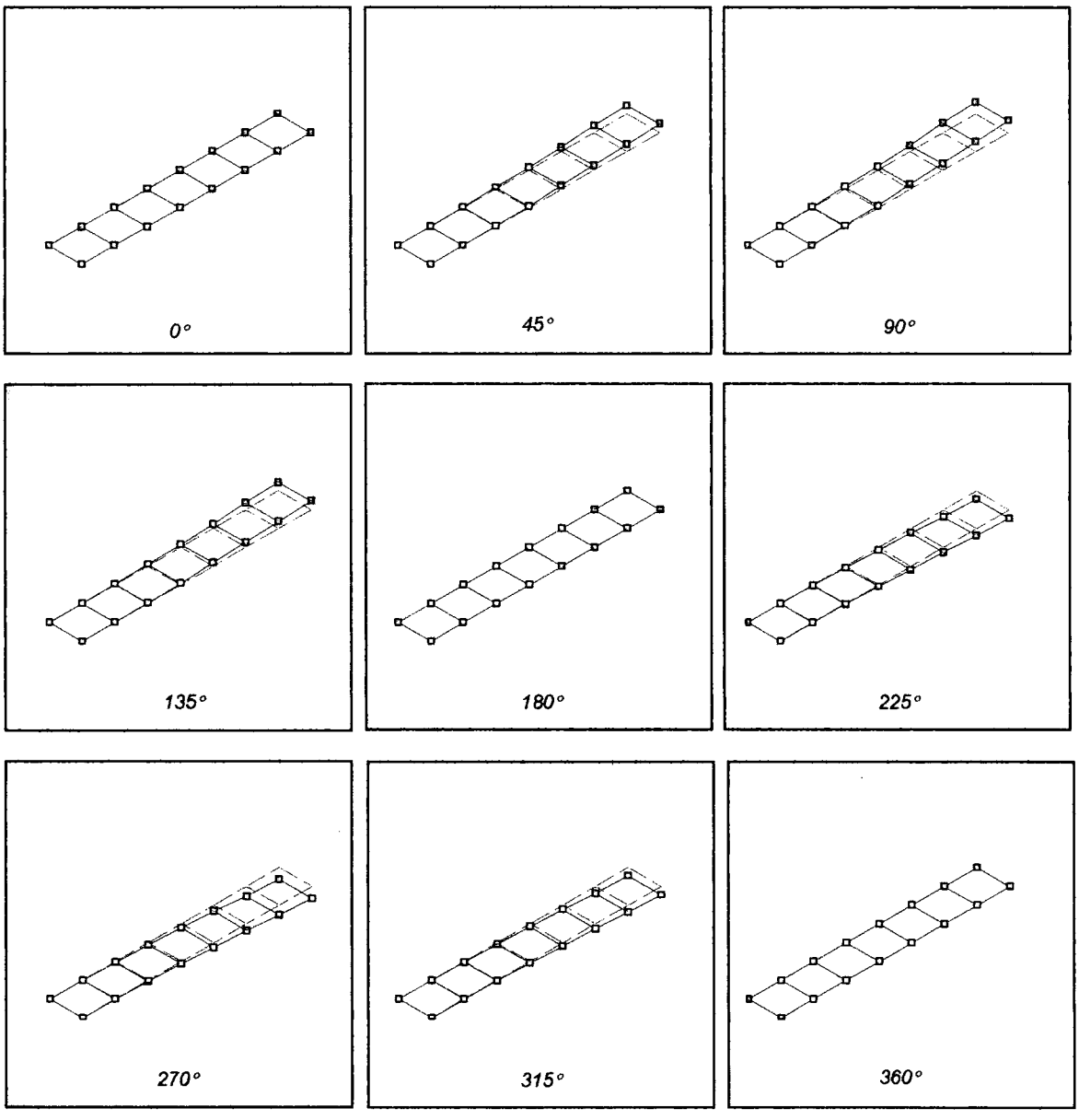

Figure 5.20. *Still frame animation of first flexural mode of vibration.*

MODE 2
FREQUENCY = 23.79 kHz
Q – FACTOR = 532

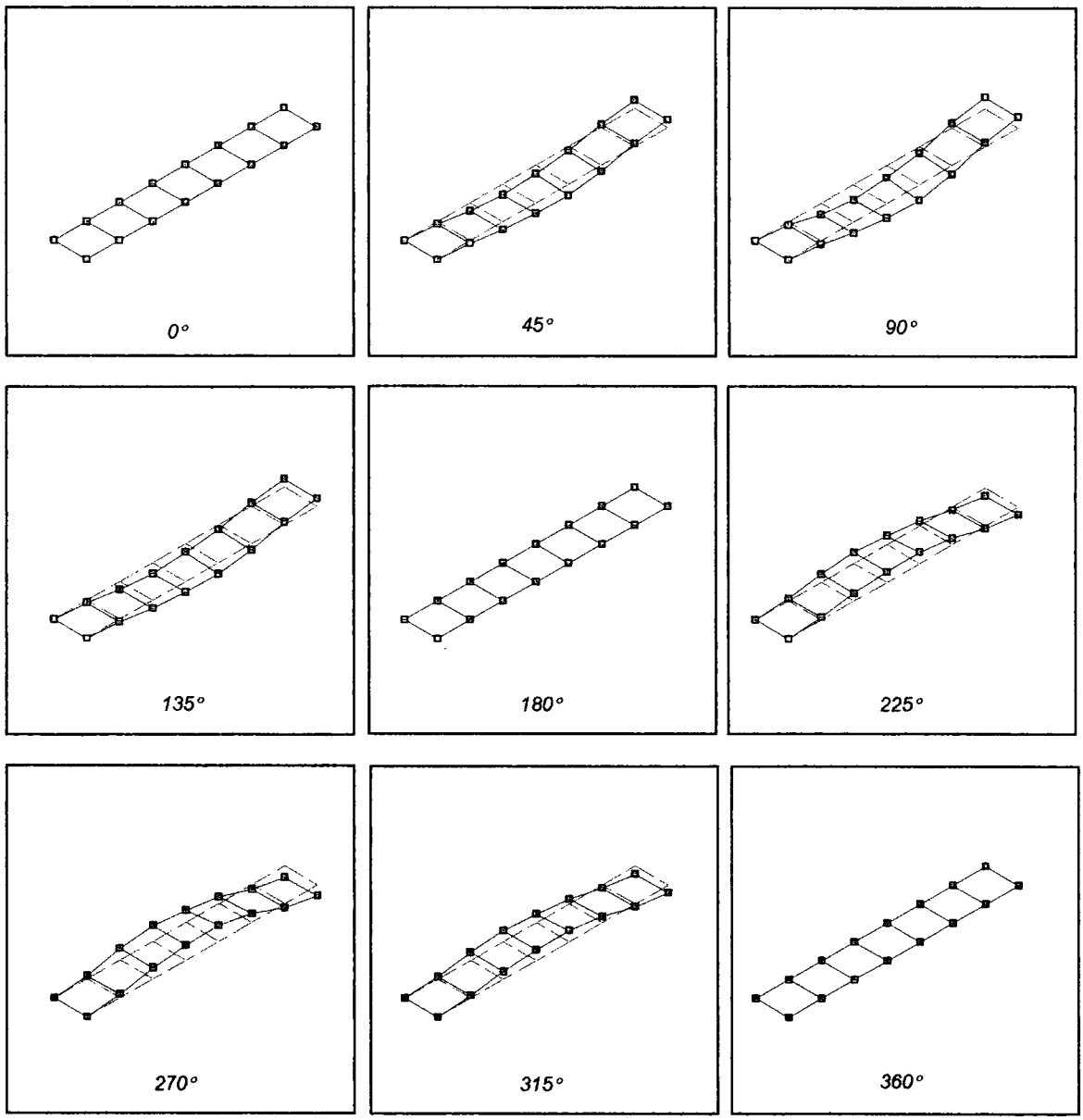

Figure 5.21. *Still frame animation of second flexural mode of vibration.*

MODE 3
FREQUENCY = 37.94 kHz
Q – FACTOR =1490

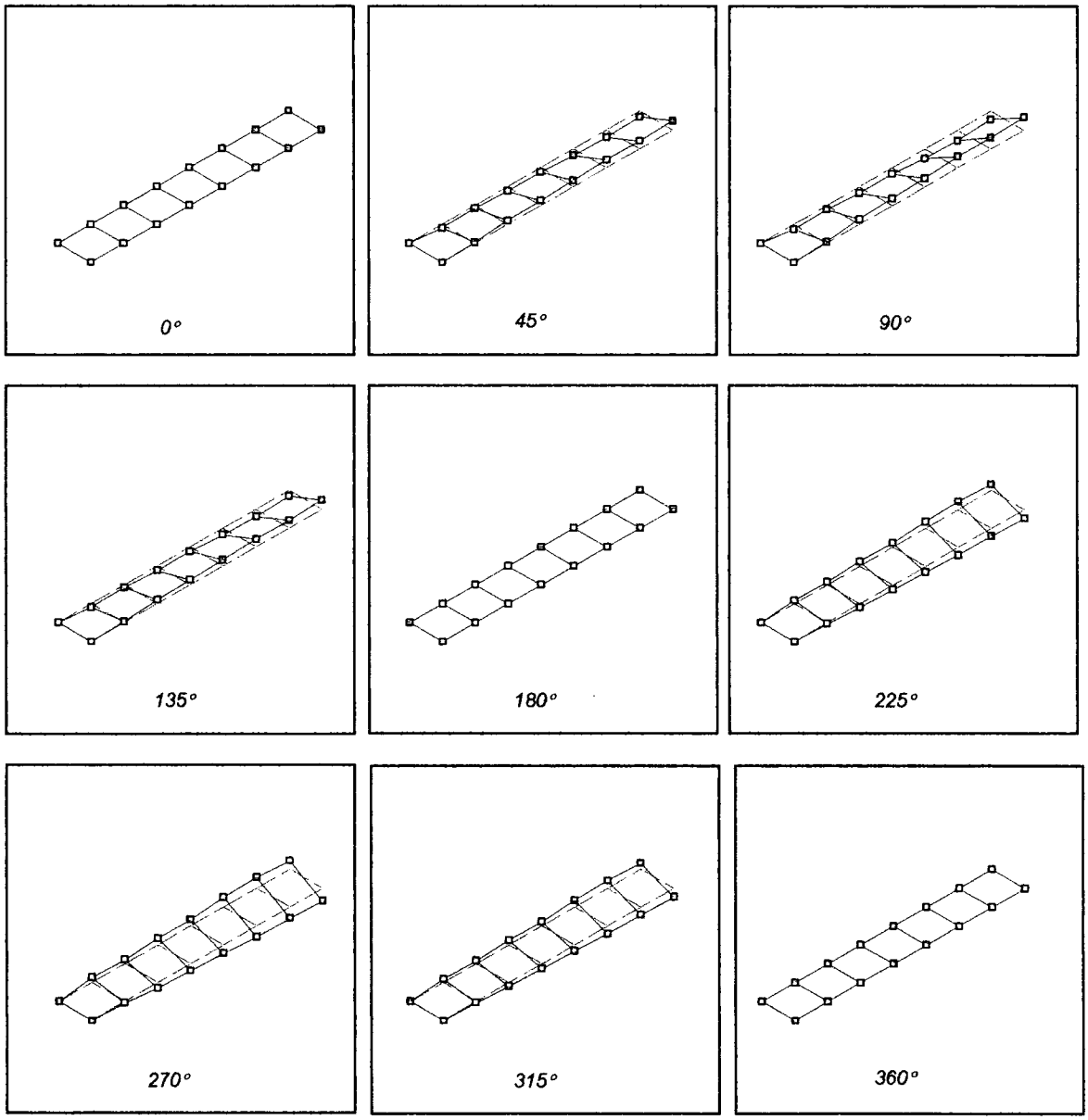

Figure 5.22. *Still frame animation of first torsional mode of vibration.*

MODE 4
FREQUENCY = 71.22 kHz
Q - FACTOR = 752

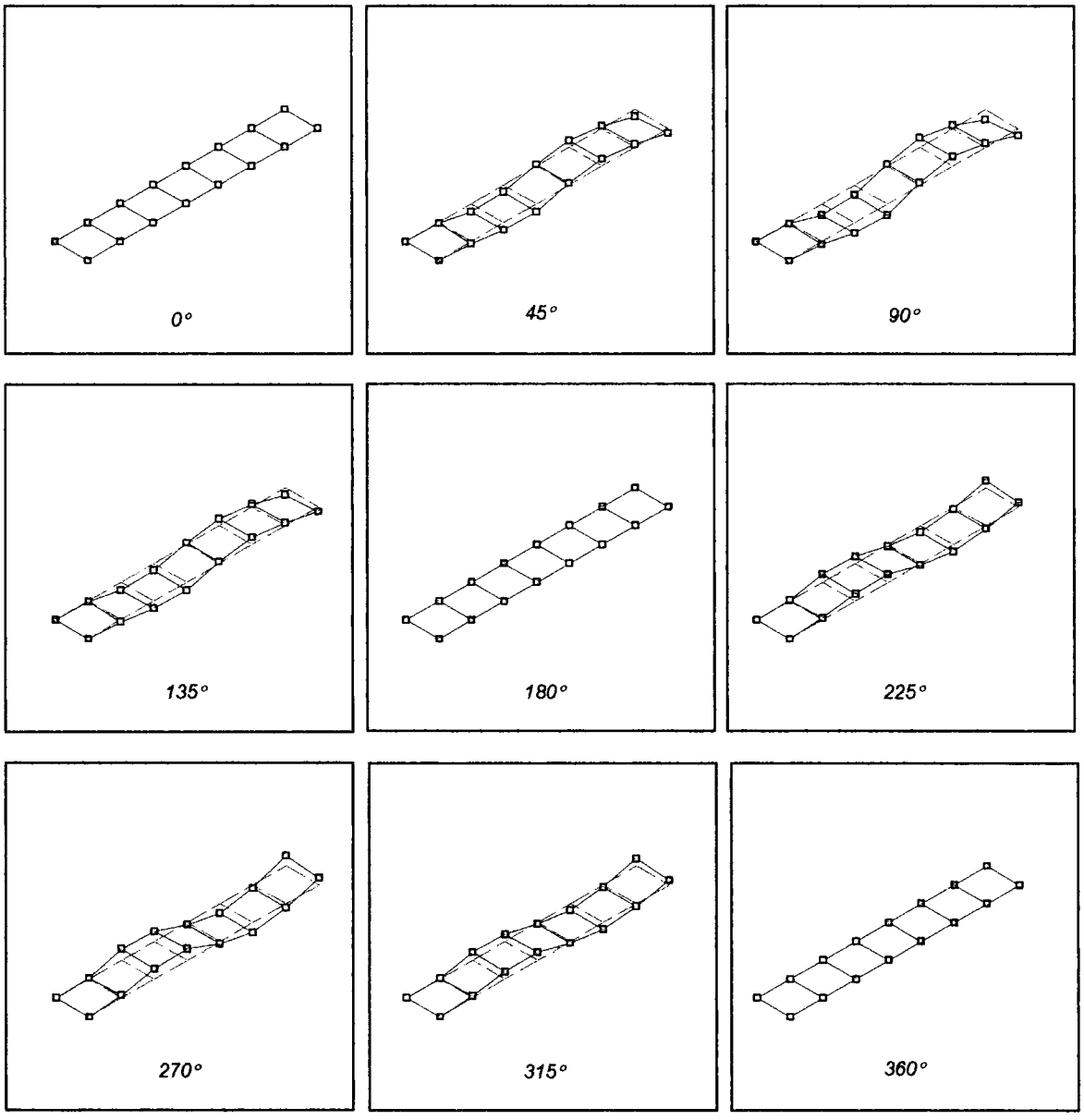

Figure 5.23. *Still frame animation of third flexural mode of vibration*

Table 5.3 summarises the data obtained relating to the dynamic analysis of a 2.7mm cantilever beam comparing the measured and predicted values of resonant frequencies.

	Mode 1	Mode 2	Mode 3	Mode 4
Mode Type	1st flexural	2nd flexural	1st torsional	3rd flexural
Experimental	3.14 kHz	23.79 kHz	37.94 kHz	71.22 kHz
FEM	3.07 kHz	23.53 kHz	35.20 kHz	71.70 kHz
Error	2.28 %	1.10 %	7.78 %	0.67%

Table 5.3. *Comparison of measured and predicted resonant frequencies.*

In general the model and experimental results show excellent correlation with only marginal errors between measured and predicted resonant frequencies and modeshapes.

5.4 Further Measurements

The vibrometer measurements have been used to determine the dynamic behavior of a single nickel cantilever and allow comparison with beam theory. Extending these measurements over an array of cantilevers of different length allows the determination of the Young's modulus of the beam material itself. The method was proposed by Peterson [6] and involves measuring the fundamental frequency of each beam. The equation relating the length of a uniform beam to its fundamental frequency is:

$$f_o = 0.162 \frac{d}{l^2} \sqrt{\frac{E}{\rho}} \qquad (5.12)$$

where f_o is the fundamental frequency, d and l are the thickness and length of beam, and E and ρ are the Young's Modulus and density of the beam material. Rearranging gives:

(5.13)

$$f_o = \left(0.162d\sqrt{\frac{E}{\rho}}\right)\left(\frac{1}{l^2}\right)$$

highlighting the linear relationship between frequency and inverse square of length. Knowing values for the constants d and ρ allows the determination of E from the gradient of a suitable graph. Although the thickness profile was found to be non-uniform (figure 5.6), a value for Young's modulus can still be determined, only the constant of equation 5.13 would differ [45].

The test sample consisted of an array of cantilevers with lengths varying between 1.8 and 2.7mm. A graph of resonant frequency against length is shown in figure 5.24. The relationship between frequency and inverse square of length is shown in figure 5.25. This second graph shows the expected linear relationship, but does not pass through the origin. This can be accounted for by the variations in the thickness profile of the test beams (although the origin of the graph represents a beam of infinite length and practical deviations from the theoretical curve are not entirely unexpected). Even beams of the same lateral dimensions were found to have slightly different profiles, and hence different mechanical properties. For example, the resonant frequency of two 2.0mm cantilevers were found to be 6.52 kHz and 7.12 kHz, a difference of 600 Hz. Regardless of these points, the ratio of (E/ρ) was still calculated. Using an average thickness value of 38.9μm (calculated from figure 5.6), and a value of 33.25×10^{-3} for the gradient of figure 5.25, the value of (E/ρ) can be calculated to be 27.84×10^{6} Nm^{-1} (equation 5.13). This compares to a theoretical value of 22.58×10^{6} using the bulk crystalline material properties of nickel ($E=2.01\times10^{11}$ Nm^{-1} and $\rho=8900kg.m^{3}$); a percentage error of 23%.

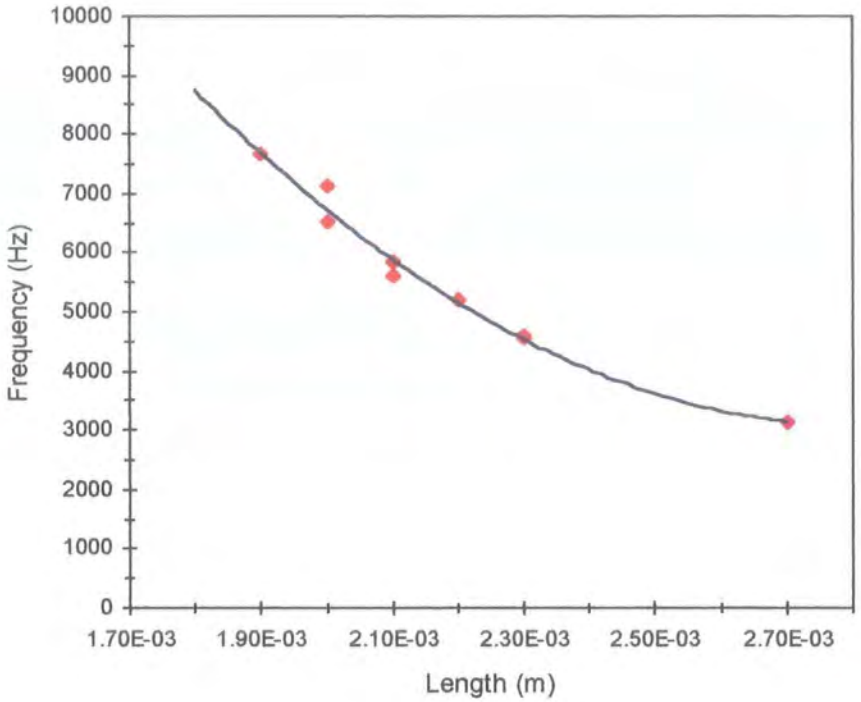

Figure 5.24. *Variation of resonant frequency with beam length.*

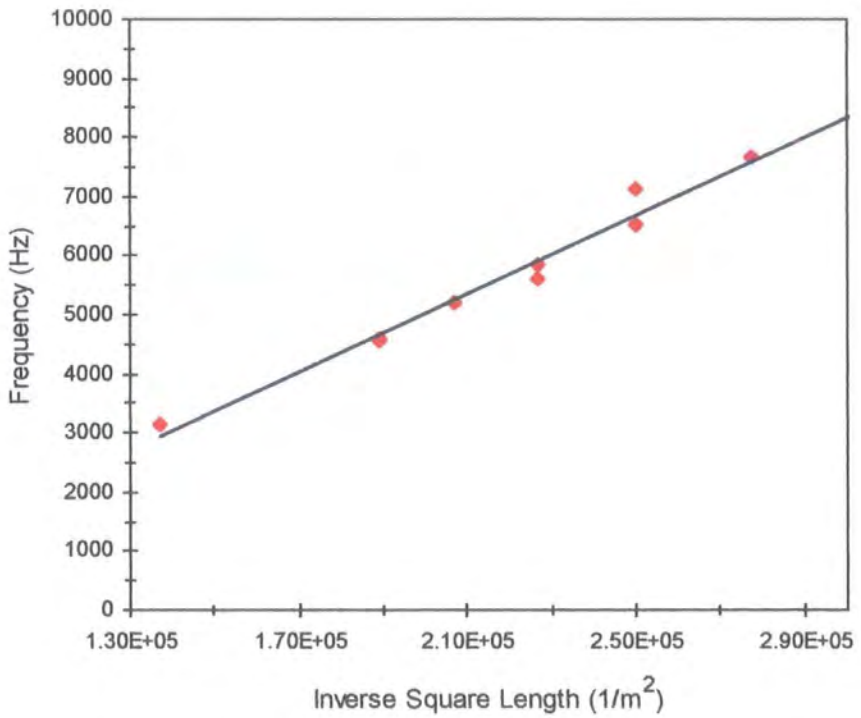

Figure 5.25. *Resonant frequency and inverse square of length.*

5.5 Discussion of Preliminary Beam Results

Primarily, the dynamic analysis of the cantilevers documented in this chapter has shown that the fabrication process discussed in chapters three and four is capable of being used for the construction of self-supporting and movable mechanical components. In addition, the analysis has allowed the detailed comparison of experimental data with finite element calculations to show close correlation.

5.5.1 Modal Analysis

Relatively little information is available on the dynamics of microsensors even though such data is very important with respect to device operation. This is especially true for resonant microsensors, where resonant frequencies, mode shapes and Q-factors can have a significant effect on performance. Recently, it has been shown that with the use of special analytical techniques it is possible to determine these parameters with a high degree of accuracy. However, as these techniques require the use of highly specialised equipment, they have been employed only by a number of research establishments.

To date such equipment has been used primarily in the analysis of relatively simple structures such as beams and cantilevers. This is because the properties of such structures are well known (and easily pedicted from beam theory) and therefore allow a means of system evaluation. The system used in this research was developed by Burdess et al and is based on a commercially available laser interferometer. The full system is described in [43] together with preliminary measurements made on silicon cantilever and beam structures. Modes of vibration, natural frequencies and modal damping factors have been determined for these devices, all of which have been shown to compare favourably with theory. The influence of boron doping on the dynamic properties of silicon is also discussed.

A similar system has been employed by Lärmer et al. [46]. Again, this system has been in the analysis of simple microbeams. In this case the system has been used to optically validate 'on-chip' electrical measurements to investigate the problem of 'cross-talk' or

'cross-coupling' which is prevalent in electrical drive and detection schemes. Published data has shown excellent correlation between optically and electrically derived measurements of resonant frequency and Q-factor for displacements as small as 35nm. Comparison of initial frequency response curves has highlighted the problem of cross-talk and this information has been used to minimise the phenonemon by modification of electrode arrangements. Although the system is capable of mode shape analysis, no data is presented.

The dynamic properties of simple cantilevers have also been subject to investigation by Jenkins et al [47]. This has been done using an optical beam deflection technique in which a laser beam is reflected off the surface of a cantilever onto a position sensitive detector. Deflection of the cantilever modulates the beam position with respect to the detector, which is converted into a suitable output signal. By employing appropriate signal processing techniques the system has been extended to allow the determination of resonant frequencies and mode shapes. Published literature shows good correlation between experimental and predicted mode shapes for the first four flexural modes of a 23.5mm x 2mm x 0.5mm pyrex cantilever. Although this work was done using relatively large 'macroscopic' beams, it would be expected that an extension towards micromachined beams would be possible as this is largely determinded by the spot size and poitional accuracy of the laser beam.

5.5.2 Q-Factor

The level of damping that is present in a vibratory system is an another important parameter that has been investigated in this chapter. Resonances with Q-factors in excess of 1000 have been measured for the nickel beams under low-pressure conditions. Although this figure represents the highest achievable Q for the beams investigated, it would be expected that higher values could be obtained with balanced resonators. Investigation of the influence of viscous damping has also been achieved. A curve showing the influence of ambient pressure on the Q of vibration has been determined which illustrates the benefits of low-pressure operation of these devices. Similar curves have been produced for both silicon [48] and polysilicon [49] micro-cantilevers by other

research institutions, which highlight the intrinsic high-Q nature of these materials. For both silicon and polysilicon micro-cantilevers Q-factors in excess of 20,000 have been determined, emphasising the importance of these materials for use as low-loss resonator materials. Although for many applications high Q's are favourable, in others (such as gyroscopes where it becomes difficult to match resonant modes of high Q (see chapter six)) it is not so crucial and a lower Q of 1000 may be more acceptable.

5.5.3 Young's Modulus

In order to determine the Youngs modulus of electroformed nickel, the resonance method first described by Peterson [6] was employed. However, due to the non-uniform nature of the beams dimensions this was found to be difficult to achieve. The measured thickness profiles of individual beams and similar devices of identical lateral dimensions have been found to vary, illustrating the inherent problem of thickness control in electroforming processes. In some processes (e.g. LIGA) this is overcome by lapping the electrodeposited structures to ensure uniform dimensions.

The resonance method has however, been used to determine the Young's modulus of a number of materials commonly used in microengineering, for example silicon nitride [50]. This has been possible because, unlike electrodeposition processes, CVD deposited layers of these materials can be tightly controlled which subsequently allows the construction of beams of pecise dimensions.

5.6 Summary

The literature described above has shown that optical detection schemes are powerful analytical tools that allow the determination of many dynamic properties of micromachined structures. These systems offer higher accuracy and higher spatial resolution than on-chip detection schemes. Although these detection systems are not sensible for practical devices, their use in the laboratory for the dynamic analysis of micromachines is unequalled.

Chapter Six
Review of Gyroscope Technology

Having successfully fabricated, simulated and experimentally analysed an array of simple test structures, it was decided to repeat the exercise with devices of greater significance. As the group at Durham and Newcastle has previous experience with gyroscope technology, this was considered the best route to follow. With this in mind a comprehensive review of current gyroscope technology was conducted and is presented in this chapter. This begins with a short description of both the traditional rotary gyroscope and the modern optical device, and leads on to the vibratory gyroscope, a class of device that is of greatest relevance to this thesis. The main body of the chapter is dedicated to the theory and operation of vibratory gyroscopes and describes the most common designs and implementations of this technology.

6.1 Introduction

Traditionally the term 'gyroscope' was used with reference to a number of instruments that possessed a rapidly spinning rotor as the main mechanical element. Today the term is used more broadly to describe a large range of devices that can independently sense

rotation without the need for any external reference. Gyroscope technology is very wide-ranging, utilising principles as diverse as the invariance of the speed light and the modulation of acoustic waves. Although the implementation of this technology can be equally diverse, the principles involved are in most cases identical, and arise from the generation of Coriolis forces. It is only optical gyroscopes that exploit other principles. The origins of the Coriolis force are discussed in detail in appendix B.

Gyroscopes are inertial sensors; devices that can detect their own motion and infer the motion of the objects to which they are attached. They, when used in conjunction with accelerometers, can provide the main basis of a full inertial reference system that can detect position, motion and orientation in three-dimensional space, independent of the external world. The number of applications of this type of sensor are innumerable but due to the high construction costs of traditional devices, it has only been the defence and aerospace industries that have generally been able to afford the technology. The requirements of these applications have also demanded the highest performance devices; sensors with drift rates in the 0.1 to 0.01 °/hr for inertial navigation or in the 10-100 °/hr range for missile stabilisation [52]. However, with new and improved fabrication techniques in place, it is now possible to develop miniature low cost devices that can find applications in many less demanding areas. For these applications high performance is not essential; drift rates are of less importance, as it is rapid changes in angular motion that are of interest. To this end, good sensitivity in the 10-100°/s range is sufficient [3].

The automotive industry has already taken advantage of this new technology by developing air bag safety systems that use low cost accelerometers. With this type of device now a mature and proven technology, interest has turned towards the production of similarly low cost gyroscopes, and again, it is the automotive industry that is poised to benefit from this technology and develop active suspension and anti-skid systems.

6.2 Rotary Gyroscopes

The conventional rotary gyroscope is a device that has been developed extensively since its first practical application at the beginning of the century. A typical rotary gyroscope consists of a rapidly spinning rotor supported within a frame that allows the spin axis to adopt any orientation in space. Rotation of the device along any axis perpendicular to the spin axis generates a torque along the third mutually perpendicular axis that acts to restore the rotor to its original orientation. The restoring torque (the magnitude of which is proportional to the rotation rate) manifests from the production of Coriolis forces that act on the rotor during rotation.

Rotary gyroscopes have evolved into complex devices containing hundreds of precision-engineered components. With this complexity comes high sensitivity but also high cost and fragility. Heavy rotors are spun at high angular velocities on delicate bearings, making them inherently prone to mechanical damage through shock and vibration. It is these concerns that have restricted their application to the defence and aerospace industries, in critical applications such as inertial navigation and motion control systems for aircraft, spacecraft and satellites. In an attempt to widen the market for these high specification devices a number of compact systems have been developed. These include the Minitact gyro [53] produced by Allied-Signal and the FG314 [54] produced by British Aerospace. Table 6.1 lists the performance figures of these two sensors, which show exceptional bias stabilities in the low and sub °/hr range and low scale factor errors.

	MINITACT	FG314
Range (continuous)	± 300 °/s	±100 °/s
Range (peak)	± 1000 °/s	± 200 °/s
Bias Offset	0.3 °/hr	2 °/hr
Scale factor Error	500 ppm	500 ppm
Size	25mmØx 38mm	22.5mmØx 30mm
Weight	75grams	47grams

Table 6.1. *Performance characteristics of the Minitact and FG314 gyroscopes.*

These two parameters are the main specifications that describe gyroscope performance. The bias offset or drift rate, is the output of the gyroscope (expressed as an angular rate) in the absence of an input rate. Rates below this threshold cannot be resolved and cause an increasing drift of the estimated body position with time. Scale factor errors are proportional to the applied input rate and cause uncertainties that are a function of past history. The intended application for these devices is inertial guidance and control, which is directly reflected in the price. The FG314 is approximately £4,000 per unit.

It has been demonstrated, by using micromachining techniques, that miniature rotary gyroscopes can be constructed. One such device is currently being developed [55], in which an electromagnetically levitated and driven aluminium rotor is spun at high angular velocities (>1000 rpm). The device, measuring only 500μm in diameter, has a predicted sensitivity of 2°/s and offers the potential of high performance at low cost and a fraction of the size.

6.3 Optical Gyroscopes

The development of optical gyroscopes was driven to address some of the reliability problems associated with rotary gyros. With intensive development since the 1960's, high-grade systems are now standard and dominate the inertial navigation market. However, concerns over size and cost were not overcome and the result was an equally costly and bulky alternative.

Unlike mechanical devices, optical gyroscopes [51] exploit the invariance of the speed light (the Sagnac effect) to detect rotation. Operation is based on the rotation induced phase changes that occur between two counter-propagating light waves travelling within a closed optical loop. Consider figure 6.1, which shows two light waves travelling in opposite directions within a circular path. The two beams travel the same optical path length and recombine at the detector. When the system is at rest the relative phase of

the two beams remains constant. However, when the system is rotated the effective path length of each beam differs and, due to the invariance of the speed of light, induces a phase change at the detector that is directly related to the angle of rotation.

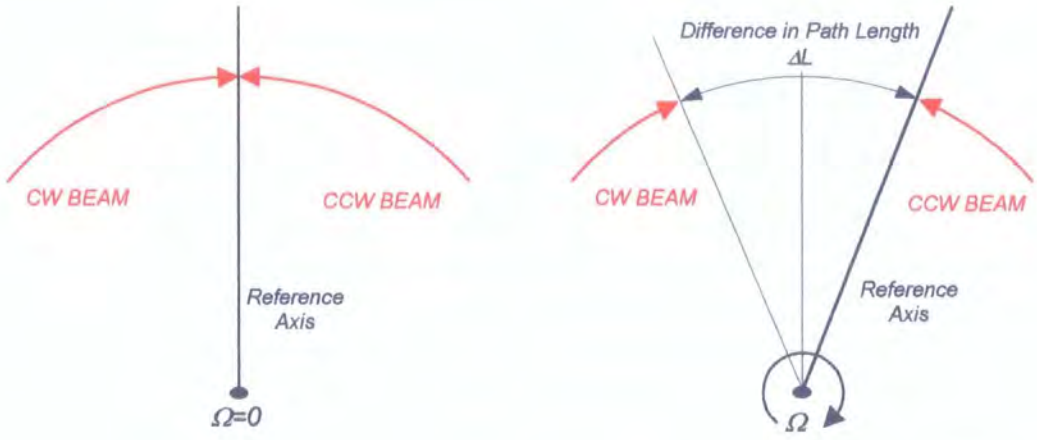

Figure 6.1. *Operating principle of an optical gyroscope.*

Different implementations of this technology have resulted in the development of three different versions: the ring laser gyroscope (RLG), the resonant ring gyroscope (RRG) and the fibre optic gyroscope (FOG) [51]. The RLG is the active form in which the optical loop is created by a series of reflectors that are an integral part of the laser cavity. In this system the optical path length is adjusted to induce resonance, producing a standing wave pattern that is used as the inertial reference. As the gyro body is rotated relative to the standing wave, the maximum and minima sweep across the face of the photodetector and can be counted to determine the angle of rotation. The FOG and RRG were developed to reduce the construction costs associated with the RLG by using standard optical components. In these devices the optical loop is created externally from the laser cavity with the use of fibre optics. The FOG uses direct interferometry to monitor phase changes whilst the RRG (like the RLG) adjusts the optical path length to produce a standing wave inertial reference.

The RLG is the only form of optical gyroscope to develop into a navigational grade instrument and now dominates the market for navigation and inertial guidance. Although the FOG and RRG can potentially obtain the same performance as the RLG, the need for precise optical alignment of components and losses within the fibre optic cable limits performance.

6.4 Vibratory Gyroscopes

Vibratory gyroscopes are a second group of mechanical device that employ a vibrating element to sense rotation. As with rotary gyroscopes, the principle involves detecting the effects of the Coriolis force that are generated upon a mass undergoing both translational and rotational motion. However, as the sensing element is much less complex than that of the rotary gyroscope, vibratory gyroscopes can be made highly compact, highly rugged and at much lower cost.

In the past many vibratory gyroscope designs have been developed but none could attain the high performance of rotary or optical gyros. It is only quite recently with the aid of new micromachining techniques and the availability of high quality resonator materials, that high-grade vibratory gyroscopes have been developed.

The following sections describe the operating principles of vibratory gyroscopes. A simple model of this system is first described and the remaining subsections deal with particular examples.

6.4.1 Model of a Vibratory Gyroscope

The vibratory gyroscope concept is based on the rotation induced energy transfer between two normally uncoupled modes of a vibrating structure. A simple mass-spring model of this system is given in figure 6.2. The gyroscope is designed to have two modes of free vibration, in this case a primary vibration in the x-direction and a secondary vibration in the y-direction. Operation of the gyroscope requires the excitation of the primary motion by the application of an external force that maintains the vibration at a constant amplitude.

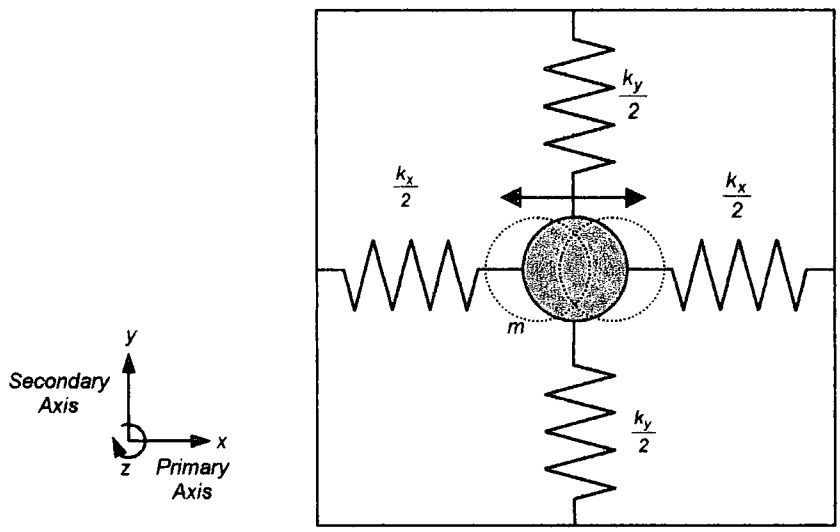

Figure 6.2. *General model of a vibratory gyroscope.*

When the system is at rest, the primary and secondary modes remain uncoupled and it is only the primary vibration that is observed. However, when the system is rotated, Coriolis forces are generated that cause the two modes to become mechanically coupled, which induces a vibration in the secondary direction. The magnitude of this secondary vibration is proportional to the rotation rate. The magnitude of the Coriolis force is given by:

$$F_c = 2mV_p\Omega \qquad (6.1)$$

where m is the mass, V_p is the velocity vector of the primary motion and Ω is the applied rate of rotation (appendix B). To ensure maximum sensitivity the gyroscope is operated at resonance. This means that the primary and secondary frequencies of the mass must be matched by careful design and dimensional control to ensure the spring constants k_x and k_y are identical. Operation at resonance ensures large vibrational amplitudes and maximum coupling between modes during rotation.

When the system is operated in an open loop configuration the amplitude of the secondary vibration is measured directly to determine the rotation rate. However, if this motion is significant, additional Coriolis components will be induced back in the primary direction causing the output to become non-linear. A second problem is that the response of the gyroscope can be very poor due to long signal decay times, resulting from the use of low loss resonator materials. The decay of large secondary vibrations may take several minutes in which time the gyro will remain insensitive to smaller signals. To overcome these problems, vibratory gyroscopes are often operated in a closed loop configuration whereby the secondary vibration is suppressed by the application of a harmonic nulling force. The magnitude of this force is then used as the measure of rotation rate. Suppression of the secondary vibration results in the suppression of secondary Coriolis forces and produces a linear output. Suppression of large secondary amplitudes also increases the response time (and bandwidth) of the device.

6.4.2 Examples of Vibratory Gyroscopes

In principle any vibrating body can be used to measure rotation and so many designs have been proposed. Good design is aimed at producing devices that can exhibit high levels of accuracy, sensitivity and resolution. In general most designs fall into one of three sub-groups: vibrating beams, tuning forks or vibrating shells. The following sections describe these designs with examples of practical devices.

6.4.2.1 Vibrating Beams

As is often the case, technology is frequently found to mirror the mechanisms that have evolved in nature over millions of years. It is therefore, not surprising that the simplest form of vibratory gyroscope, the vibrating beam, is thought to be the basis of the flight control system of the insect order Dipteria, which includes the common housefly [56]. These insects have two vibrating club shaped protrusions on either side of the thorax known as Halteres, which have been shown vital for controlled flight.

The operation of a simple beam gyroscope can be directly related to the model of figure 6.2. The practical situation is shown in figure 6.3. When a beam is excited into its fundamental flexural mode of vibration, rotation about its longitudinal axis generates Coriolis forces that drive the beam into a secondary resonance. The direction of this secondary vibration is perpendicular to both the direction of the primary vibration and the axis of rotation, and its magnitude is directly proportional to the rate of rotation. The requirement that the primary and secondary modes of vibration should be identical to maximise sensitivity means that the geometry of the beam must be accurately controlled. Generally this requires the beam to have a perfectly square cross section that is uniform along its entire length.

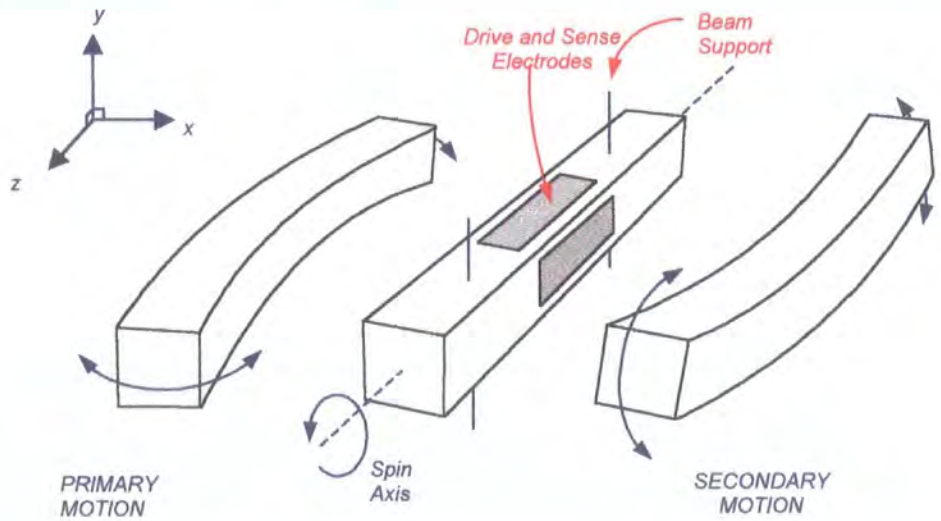

Figure 6.3. *Operation of a vibrating beam gyroscope.*

Vibrating beam designs have been successfully manufactured but problems of mounting and susceptibility to environmental vibration limits performance. The next two subsections described two such designs.

6.4.2.1.1 Triangular Cross Section

A vibrating beam gyro is currently commercially produced by the Murata Electronics Corporation [57]. The GyroStar™ is a machined metallic beam of triangular cross section with surface mounted piezoelectric transducers (figure 6.4). Although the device has a triangular cross-section, its geometry is such that (like the square cross-sectioned beam) it has two orthogonal flexural modes of vibration. The operation of this device is therefore very similar to a square cross-sectioned beam.

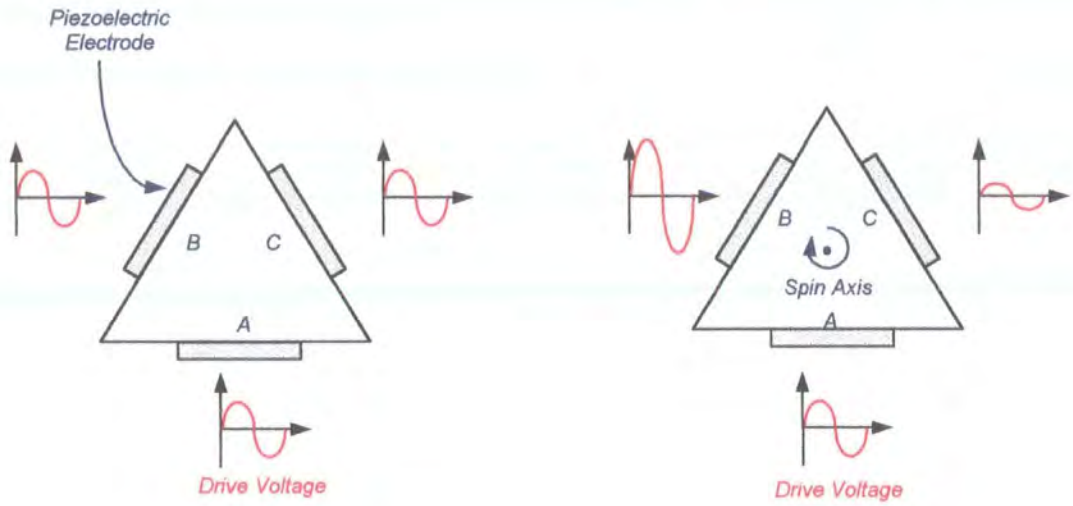

Figure 6.4. *Operation of Murata's GyroStar.*

The surface mounted piezoelectric transducers are used to both drive and sense the vibrations of the beam. Electrode A is used to drive the beam into resonance at a constant amplitude and when the gyro is at rest both signals from the piezoelectric sense electrodes (B and C) are equal. When the beam is rotated, the magnitudes of these two signals differ due to the Coriolis acceleration and the output determined from the

difference between each. Table 6.2 lists the performance specifications published for this device.

Murata GyroStar™	
Input range	± 90°/s
Bias Offset	0.09 °/min
Output Sensitivity	22.2 mV/°/s
Bandwidth	7Hz
Linearity	0.5%
Size	24 x 24 x 58 mm
Weight	41g

Table 6.2. *Murata GyroStar Specifications.*

It can be seen that the GyroStar™ does not attain the high performance of the two rotary gyroscopes discussed in section 6.2. A bias offset level of 0.09 degrees per minute (5.4 degrees per hour) is quoted, suitable for short-term stabilisation applications. In fact the Gyrostar™ has quickly found applications as the inertial sensing element in new inertial mice and pointing devices that are now being manufactured.

6.4.2.1.2 Circular Cross Section

To overcome the problems of mounting piezoelectric transducers on a vibrating metallic surface, the Tokin Corporation has produced a vibrating piezoelectric beam with surface mounted metallic electrodes [58,59]. This device consists of a piezoelectric-ceramic beam of circular cross-section with metallic electrodes deposited onto its surface. These electrodes have a dual purpose; they are used after manufacture to polarise the piezoelectric rod and then used for ac excitation and detection of angular rate. A circular cross-section is chosen to simplify machining of the piezoelectric material and to allow easy support. Again tight control of geometry is required to ensure two matched orthogonal flexural modes of vibration. The same operating principles apply as those of the square and triangular cross-sectioned beams. Table 6.3 shows the available data from this device, showing only a limited operating range of ±50 °/s.

Tokin Corporation	
Input Range	± 50 °/s
Output Sensitivity	~0.5 mV/°/s
Size	2mm∅ x 14mm

Table 6.3. *Specifications circular cross-sectioned beam.*

6.4.2.2 Tuning Fork Gyroscopes

A simple tuning fork gyroscope consists of two masses (tines) vibrating in antiphase with each connected to the same mechanical base. The advantage of this device is that the beams are balanced structures and are inherently less sensitive to spurious vibrations than single beam designs. The use of two vibrating elements effectively doubles the available output signal and the use of differential detection can reduce noise levels leading to significant performance improvements. The response of the gyro to rotation depends upon the cross-section of the tines. Tines of square cross-section respond in the same way as the single beam designs, i.e. rotation induces an orthogonal secondary vibration. As the primary motion of the tines are in antiphase the secondary response is similarly in antiphase (figure 6.5). If however, the cross-section of the tines is rectangular, then rotation induces a torsional vibration about the stem of the tuning fork due to the increased stiffness of the tines. To maximise sensitivity the primary vibration and the torsional response are matched.

Sources of error in tuning fork gyroscopes originate from the differing temperature dependence of the bending and torsional elastic moduli of beam material. This causes a large frequency separation over temperature. Also mass asymmetry of the tines can generate parasitic torques and the device is sensitive to angular environmental vibrations about the stem.

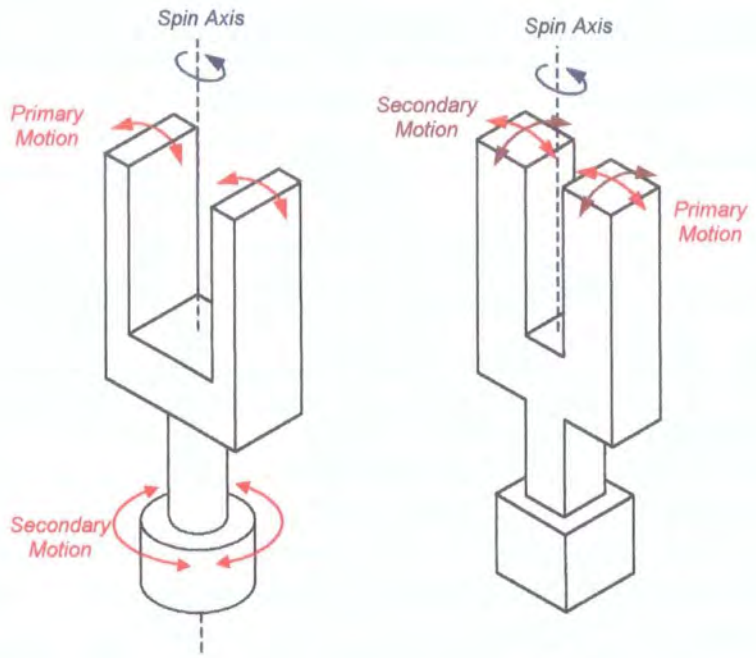

Figure 6.5. *Operation of tuning fork gyroscopes.*

6.4.2.2.1 Double Tuning Fork Designs

The quartz rate sensor (QRS) and the GyroChip™ family of devices are double tuning fork designs commercially produced by Systron Donner [60]. The structure is chemically etched from a single piece of crystalline quartz using micromechanical techniques to form the arrangement shown in figure 6.6.

This double tuning fork arrangement incorporates an additional set of tines for detection of angular rates. Instead of directly measuring the torque generated at the stem due to rotation, the alternating torque is used to drive this second pair of pick-up tines. The vibrational amplitude of these pick-up tines gives the measure of rotation rate. Table 6.4 lists some of the performance specification of these devices.

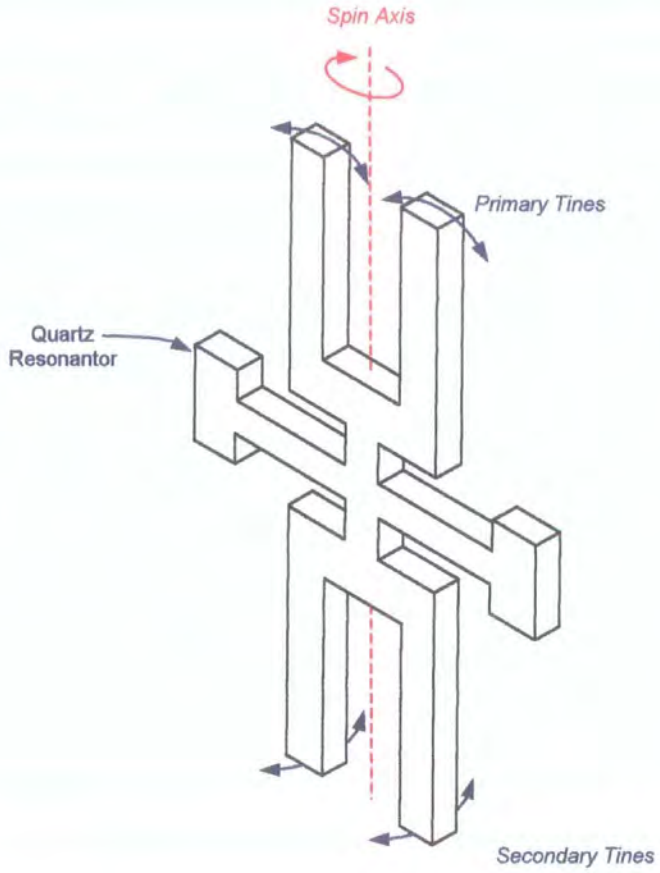

Figure 6.6. *Operation of the Systron Donner GyroChip.*

	GyroChip II	QRS 11
Input Range	*± 100 °/s*	*± 50 – 1000 °/s*
Bias Offset	*0.5 °/s*	*<0.5-10 °/s*
Output Sensitivity	*2.5 - 50 mV/°/s*	*2.5 - 50 mV/°/s*
Size	*25 x 25 x 68mm*	*38mm∅ x 16mm*
Weight	*<50 grams*	*<60 grams*

Table 6.4. *Specifications of GyroChip II and QRS 11 quartz gyroscopes.*

Although the above devices do not exhibit exceptional performance characteristics, the superior size and weight of this type of device led to its application in NASA's Pathfinder mission to Mars in July 1996. The QRS 11 was used in the directional control system of the autonomous Sojourner land rover that explored the Martian surface. Although good performance is essential for such an application, size and weight are also vital criteria.

6.4.2.2.2 Trident Type Tuning Fork

A three tined trident tuning fork design has been demonstrated [61] by the Alps Electric Company of Japan. The structure of the device is shown in figure 6.7. The main body of the device is constructed from a metal alloy and surface mounted piezoelectric detectors are included for drive and sense functions. The primary vibration has the two outer tines vibrating in phase with the central tine vibrating at the same frequency in antiphase. Rotation about the long axis of the structure generates a secondary motion out of plane.

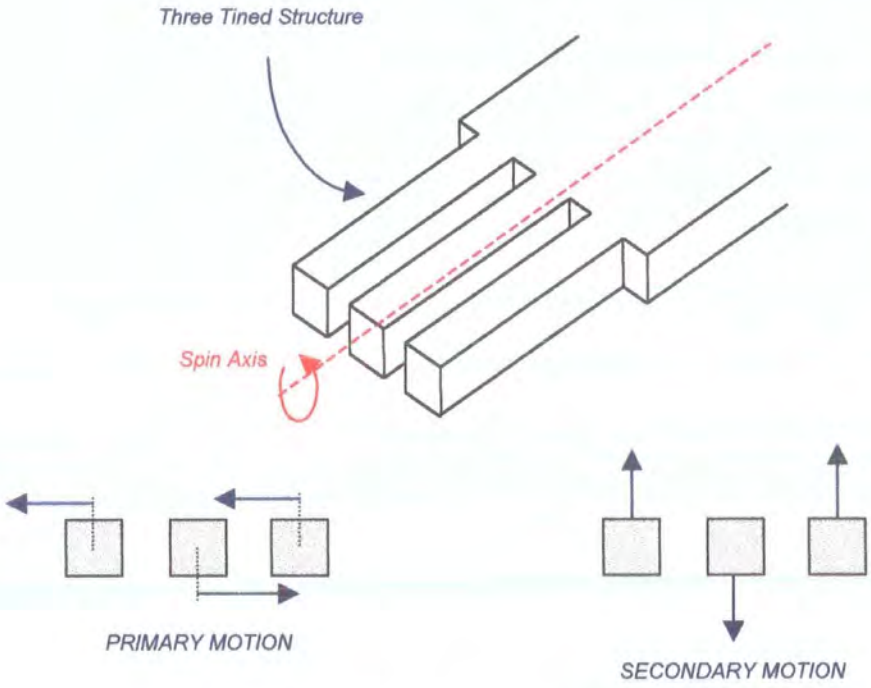

Figure 6.7. *Trident Tuning Fork Arrangement.*

Surface mounted piezoelectric sensors detect the angular rate. Table 6.5 lists the current published performance figures.

Trident Type Tuning Fork	
Output Sensitivity	*0.055mV$_{pp}$/°/s*
Size	*15 x 1.6 x 1 mm*
f_{drive}	*13.226kHz*
Q_{drive}	*1422*

Table 6.5. *Trident Tuning Fork.*

6.4.2.3 Vibrating Shells

Vibrating shell gyroscopes are a third class of vibratory device that employ a thin walled vessel as the active sensing element [51]. These vessels usually take the form of a cylinder or wineglass depending upon the application, although cylinders are more popular due to ease of manufacture. The primary mode consists of a standing wave pattern in which the radial and tangential displacements of the shell vary sinusoidally. This produces an elliptical modeshape with four nodes located symmetrically around the circumference of the ring (figure 6.8). Rotation of the shell causes the vibration pattern (and therefore the location of the nodes) to precess relative to the shell, which can be used to determine the angular motion.

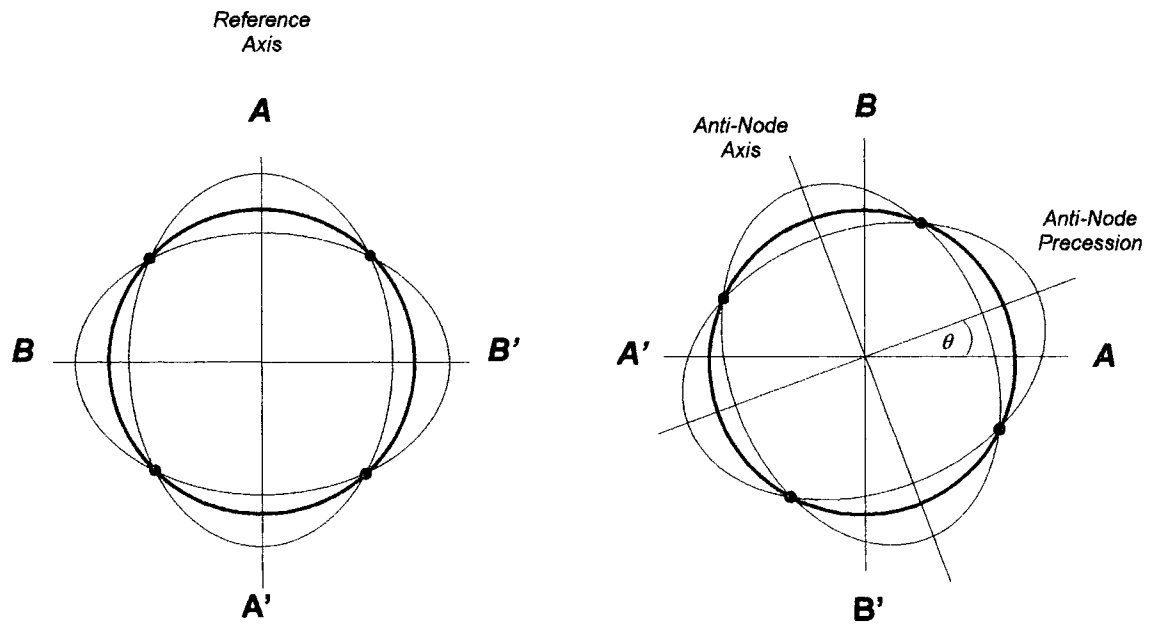

Figure 6.8. *Operation of a shell type vibratory gyro.*

The following subsections describe the most common vibrating shell gyroscope structures. The theory of operation of this type of device is discussed more fully in chapter seven.

6.4.2.3.1 Hemispherical Gyroscope

The Hemispherical Resonator Gyroscope (HRG) produced by the Delco Corporation is a state of the art vibratory gyroscope that achieves navigational grade performance [62]. The shell is in the form of a wineglass and is machined from low loss fused quartz (figure 6.9). To ensure maximum performance, the resonator and other mechanical components are precision engineered to high accuracy and low tolerances and the device is operated in a low-pressure environment. The vibration of the shell is excited by case mounted electrostatic actuators, and the location of the nodes detected capacitively.

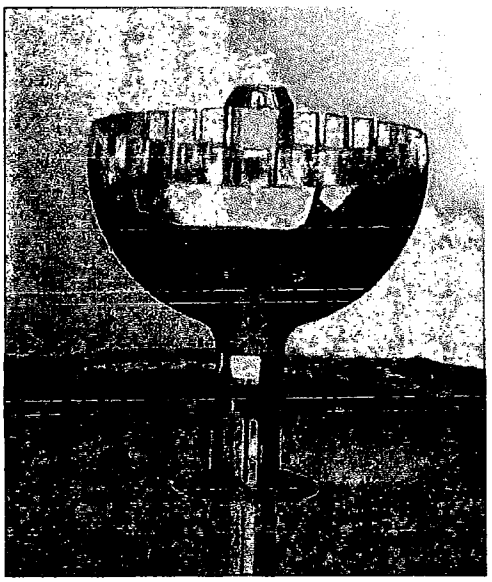

Figure 6.9. *The hemispherical resonator structure.*

Although in general vibratory gyroscopes do not attain the high performance of rotary or optical gyros, the HRG has been manufactured to high specifications to produce the only navigational grade vibratory device. Bias offset levels of <0.005 degree per hour, and scale factor errors of 0.02 ppm are typical, matching the best rotary and optical devices. Due to the superior performance to weight ratio of the HRG, it is used for attitude reference on board the NASA space shuttles.

6.4.2.3.2 Cylinder Gyroscope

6.4.2.3.2 Cylinder Gyroscope

Many devices based on the vibrations of a thin walled cylinder have been developed [52,63,64]. The cylinder is typically supported at one end and driven into resonance at its open end by surface mounted transducers. The situation is shown in figure 6.10. One such device is the Solid State Angular Rate Transducer (START) manufactured by GEC. This is a metallic shell with PZT transducers bonded directly to the cylinder surface. Variations on this theme have also been developed using radially polarised PZT for the shell material and surface deposited metal electrodes [65]. The START gyroscope is designed as a medium grade device developed for stabilisation applications. This has included the development of active suspension mechanisms for automotive systems and stabilisation of military surveillance cameras [63].

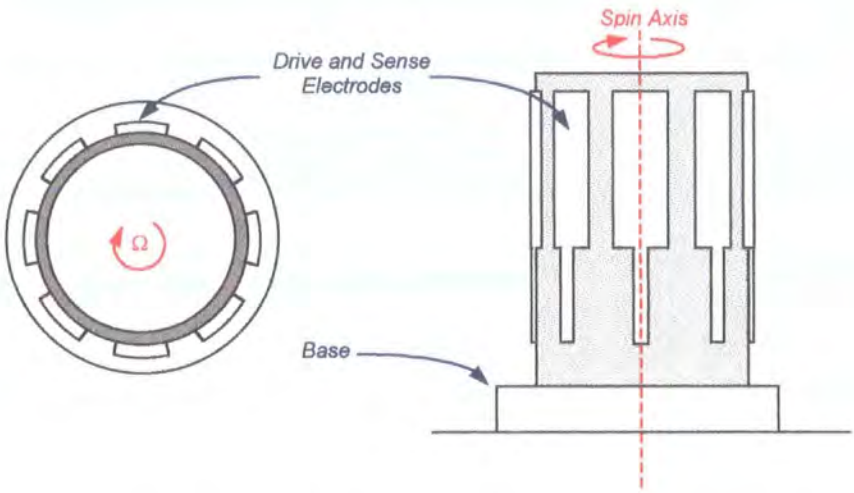

Figure 6.10. *A typical cylinder gyroscope.*

The operation of this type of device is identical to that of the HRG, but does not attain the same high performance. The complexity and high cost of the HRG is exchanged for simplicity and reduced performance. The use of metallic or ceramic shells that exhibit higher damping levels than the fused quartz shell of the HRG leads to reduced performance. Damping levels are further increased by the surface mounted drive and sense transducers.

START™ (GEC)	
Input Range	± 50 to ± 500 °/s
Bias Offset	< ± 2.00 °/s
Scale Factor Error	< ± 4.00 %
Resolution	< 0.03 °/s
Noise	< 0.10 °/s
Bandwidth	40Hz
Weight	250g

Table 6.6. *START performance figures.*

Table 6.6 lists the published performance figures of the START gyroscope. It can be seen that the device exhibits low levels of noise and can achieve good sensitivity. The factor that limits its performance is the bias offset level. At around 2 °/s (20 revolutions per hour) the device is suitable for short-term stabilisation applications.

6.4.2.3.3 Vibrating Rings

A third variation of the vibrating shell is the ring gyroscope. This type of device was first demonstrated in 1975 [66] and is identical in operation to the HRG and START gyroscopes. A ring gyroscope device is currently manufactured by British Aerospace [67] and is shown in figure 6.11. To support the ring without restraining its motion, the central support structure is required. This consists of six suspension arms that radiate from a central support pin. The motion of the ring is driven electromagnetically and sensed electrostatically. The performance of this device is marginally superior to that of the START gyroscope but has the added premium of reduced size and weight (table 6.7).

VSG 2000 (British Aerospace)	
Input Range	± 100 °/s
Bias Offset	0.01 °/s
Resolution	0.01 °/s
Size	44mm∅ x 36mm
Weight	150 grams

Table 6.7. *VSG 2000 performance figures.*

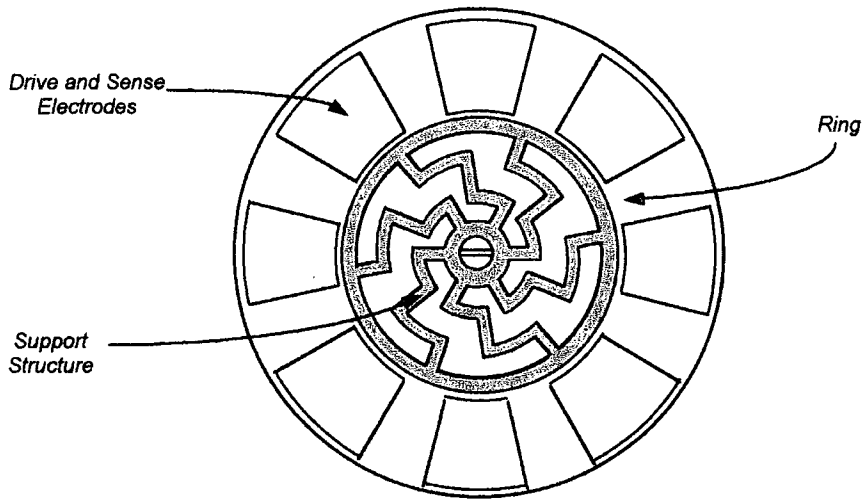

Figure 6.11. *The British Aerospace VSG 2000 ring gyroscope.*

6.4.3 Micromachined Gyroscopes

This section identifies the main types of micromachined gyroscopes that have been developed. Again this technology can be very diverse but generally mirrors the macroscopic devices previously described. The range of processing technology is also very diverse and ranges from bulk etching of quartz and silicon, polysilicon surface micromachining and metal electroforming.

6.4.3.1 Micromachined Beams

As with the macroscopic devices, the simplest gyroscopic element that can be fashioned using micromachining technology is the vibrating beam [68,69]. A typical device crystallographically etched from {110} silicon is shown in figure 6.12. This particular device is actuated using a piezoceramic plate bonded to the underside of the silicon die. The vertical vibration of the structure couples into a lateral oscillation when the structure is rotated, which is sensed by the two electrodes located on either side of the cantilever element.

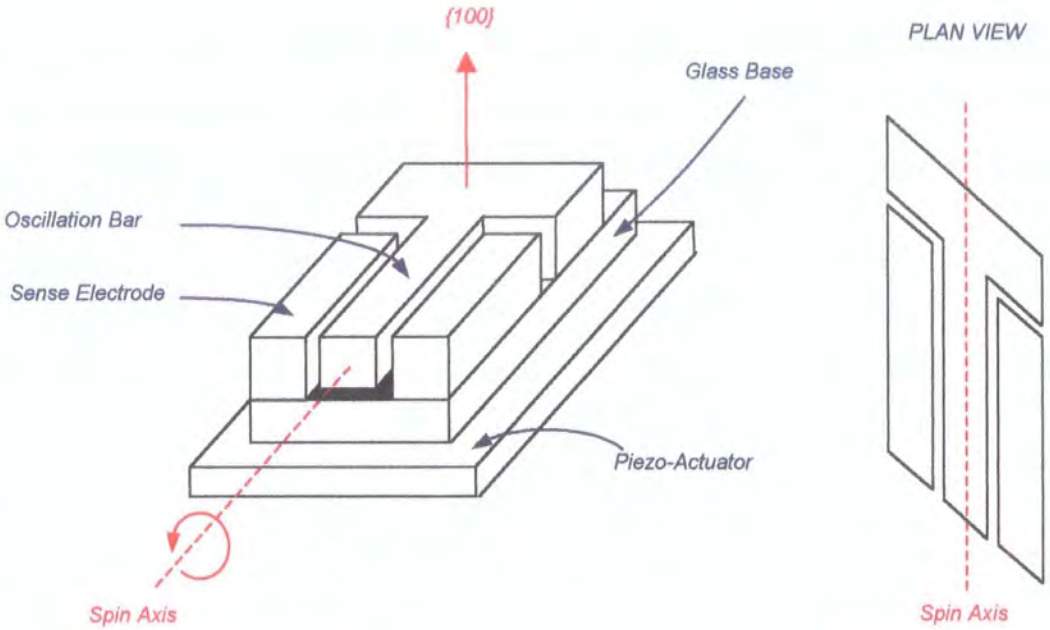

Figure 6.12. *Micromachined vibrating beam gyroscope.*

Despite residual machining errors that cause a split of approximately 110 Hz between the primary and secondary modes of the cantilever, the device has been successfully operated as a gyroscope; rates up to 700 °/s have been detected with an output sensitivity of 0.28mV/°/s. The minimum (noise-limited) detection rate is approximately 5.7°/s The available specifications of this device are compiled in table 6.8.

Micromachined Cantilever	
Input Range	*±700 °/s*
Sensitivity	*0.28 mV/°/s*
Size	*2 x 5 x 20mm*

Table 6.8. *Specifications of micromachined cantilever gyroscope.*

6.4.3.2 Micromachined Tuning Forks

The tuning fork design is probably the most common micromachined gyroscope structure and has been developed by various institutions [17,70,71]. The principle of operation is unchanged from the macroscopic devices although the technology has been implemented in a variety of micromachining techniques.

Two examples of this type of device come from the Charles Stark Draper Laboratory and the Murata Electronics Corporation (manufacturer of the Gyrostar™). Murata's device is constructed using polysilicon surface micromachining, whilst the Draper Labs have primarily constructed a silicon structure but have also demonstrated polysilicon and nickel versions. Table 6.9 highlights the available performance figures of these two devices.

	Draper	Murata
Input Range	±90°/s	±90°/s
Bias Offset	1.4 °/s	2.0 °/s
Output Resolution	1.6 mV/°/s	-
Bandwidth	60Hz	-
Size	1mm x 1mm	400μm x 800μm x 5μm

Table 6.9. *Draper and Murata silicon micromachined tuning fork gyroscopes.*

The structure of these devices is very similar, which is mirrored in the available performance figures. Both gyros show excellent noise limited bias offset levels in the low °/s range.

6.4.3.3 Ring Gyroscopes

Recent interest in the development of micromechanical ring gyroscopes has seen the idea being developed by a number of institutions. British Aerospace is currently developing a silicon micromachined ring gyro as their next generation product to replace the piezoceramic cylinder and metal ring VSG range [72]. Reduction of size and batch fabrication is hoped to reduce cost without performance, allowing increased application. The vibration patterns of the silicon VSG are generated and detected by surface deposited electromagnetic transducers. A similar device has been developed by the General Motors Corporation using nickel electroforming in conjunction with surface machining techniques to construct the main mechanical elements [73,74]. The motion of this device is driven electrostatically and detected capacitively. Table 6.10 shows some preliminary performance figures published on these devices.

	British Aerospace Silicon Ring	General Motors Nickel Ring
Input Range	*± 100 °/s*	*± 10 °/s*
Bias Offset	*<0.1 °/s*	-
Output Resolution	*20mV/°/s*	-
Resolution	*0.2 °/s*	*0.5 °/s*
Bandwidth	*35-45 Hz*	*10 Hz*
Q-factor	-	*2000*

Table 6.10. *Performance figures of two micromachined ring gyroscopes.*

The performance figures for the GM ring gyroscope are limited but show the device to have excellent resolution. Comparison of the performance figures of the British Aerospace device with their previous VSG ring gyroscope shows excellent promise. Although the bias offset level and the scale factor error of the micromachined version does not meet the performance of the VSG 2000, they are in the same performance bracket and the micromachined ring has a potentially vast size and cost advantage.

6.4.3.4 Gimballed Plate Gyroscope

This is a device developed at the Charles Stark Draper Laboratory, and has many features common to the traditional rotary gyroscope [75]. An inertial mass is suspended within a gimballed frame machined from silicon. Flexure pivots provide the inertial mass with two rotational degrees of freedom about the primary and secondary axes. The concept is shown in figure 6.13 although the actual device is a monolithic structure with an active area of approximately 350×500μm.

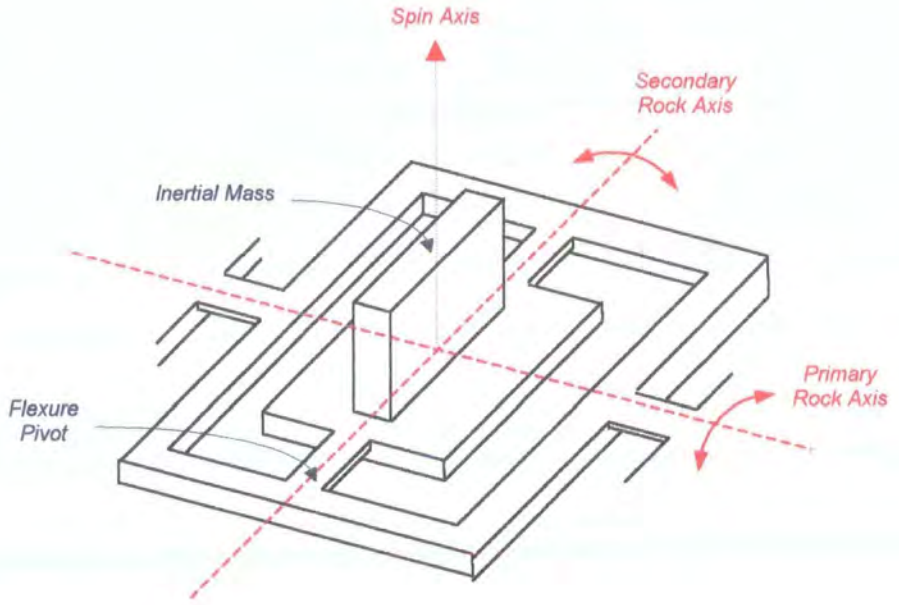

Figure 6.13. *Gimballed frame vibratory gyroscope.*

The operation of this device differs from the previous examples in that the primary motion consists of an angular rather than a linear vibration. This motion is excited electrostatically so that the inertial mass rocks about the primary axis. Rotation about the spin axis drives the mass into an orthogonal angular vibration about the second flexure pivot. This motion is detected electrostatically to determine the angular rate. A noise-limited bias offset of 4 degrees.sec^{-1} has been detected.

6.4.3.5 Membrane Gyroscope

This device has been developed with collaboration between Durham and Newcastle Universities [12]. Operation is identical to that of the gimballed frame gyroscope although the implementation is different; the frame is replaced with a flexible silicon membrane machined using boron etch stop technology. The membrane supports the inertial mass (figure 6.14), which is excited in its primary angular vibration by electrostatic actuation. As with the previous device, rotation about the spin axis generates a secondary angular vibration about the secondary axis.

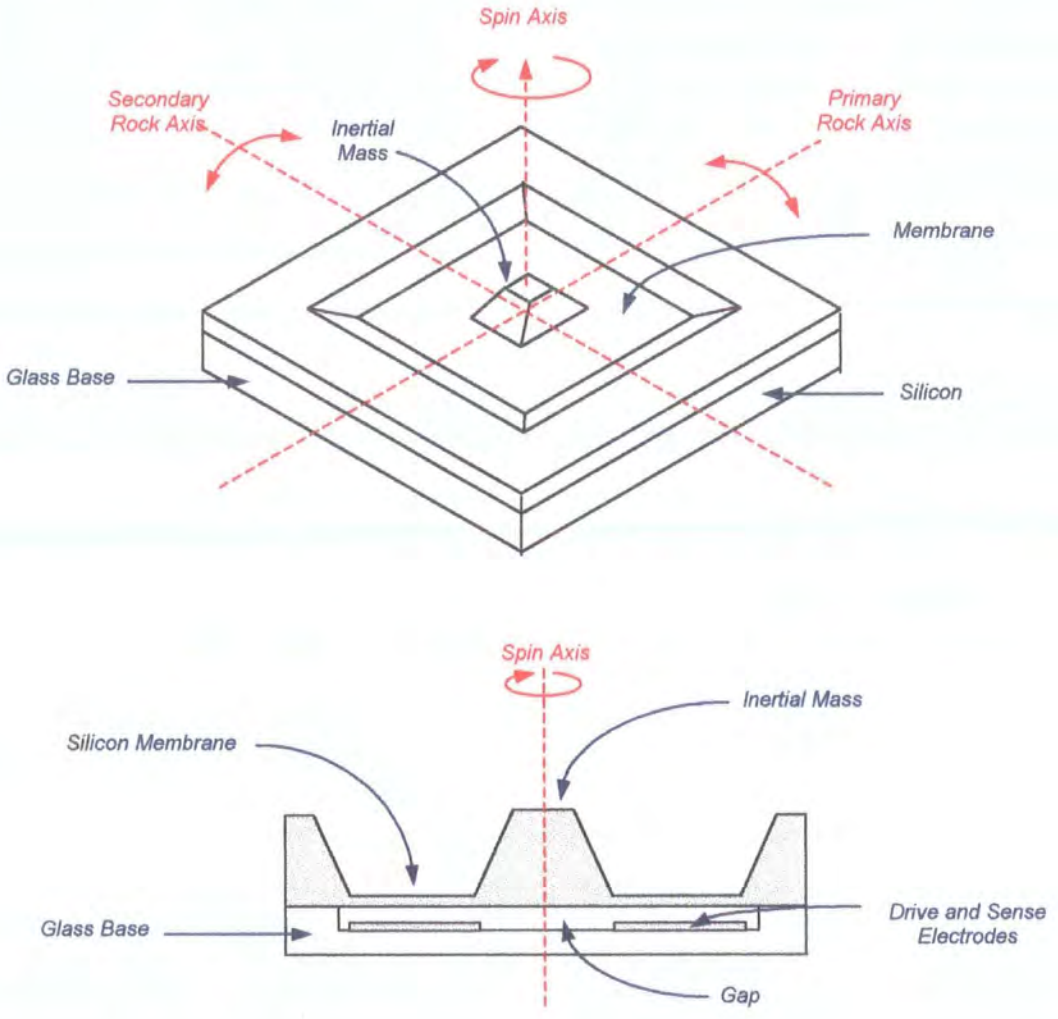

Figure 6.14. *Schematic of the plate gyroscope.*

The device has been shown to operate successfully at angular rates above 300 °/s. High levels of noise within the detection and readout circuitry have prevented detection of lower rates. Performance is further limited by a large frequency split of 600Hz between the primary and secondary resonant frequencies of the structure, caused by residual machining errors.

6.4.3.6 Torsional Resonator

This design again employs angular vibrations of an inertial mass to detect rotation. Working on the same principles as the vibrating gimballed plate and membrane gyroscopes, this device employs a torsional resonator as the active sensing element. A plan and cross-section of a typical structure is shown in figure 6.15.

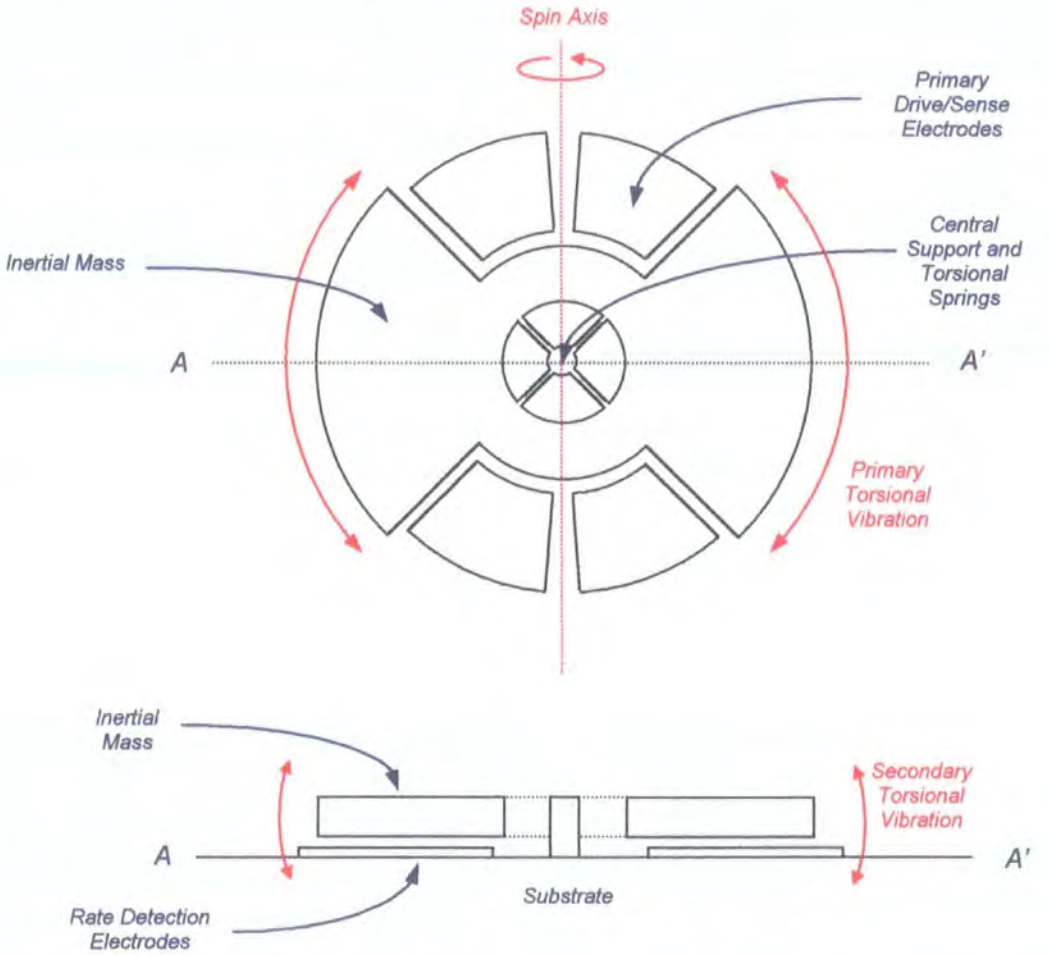

Figure 6.15. *Torsional resonator gyroscope.*

The primary motion consists of an in-plane torsional vibration about a central support. Rotation about the sensitive axis, generates a secondary out-of-plane vibration that is detected by surface deposited electrodes. A similar device has demonstrated showing excellent linearity in a ± 350 °/s range and noise limited resolution of 0.5°/s [76].

6.4.3.7 Acoustic Gyroscope

Acoustic gyroscopes are based on the rotation induced energy transfer between two acoustic vibrations of a closed cavity [77]. The basic concept is identical to that of the vibratory gyroscopes described previously, it is only that acoustic vibrations are employed rather than mechanical vibrations. A schematic of a typical device is shown in figure 6.16. An acoustic wave is generated within a cavity by a loudspeaker. This primary vibration consists of a standing wave with a node point located at the centre of the cavity. When the structure is rotated, Coriolis forces act on the vibrating gas molecules and generate an orthogonal acoustic vibration. This vibration is detected to give an estimate of the angular rate.

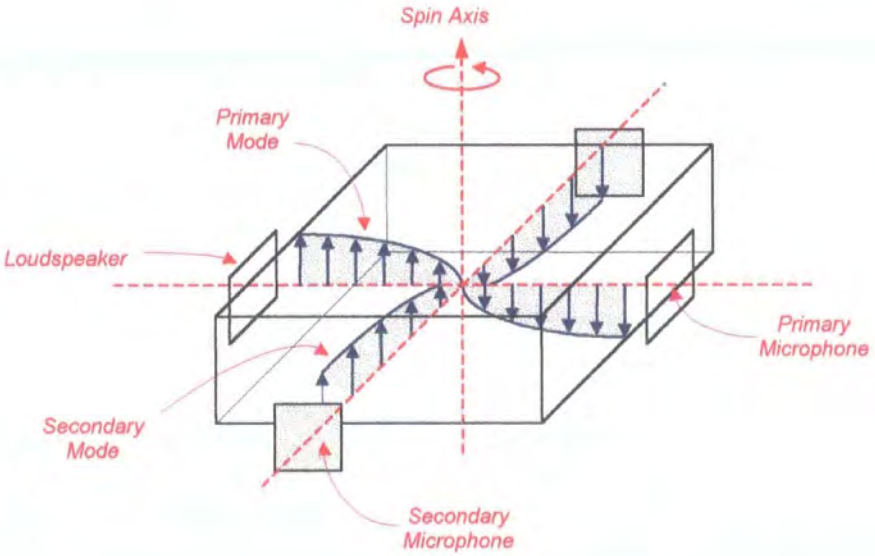

Figure 6.16. *Concept of the Acoustic gyroscope.*

A micromachined acoustic gyroscope has been constructed through a combination of silicon machining and traditional precision engineering. The transducers (loudspeaker and detection microphones) are constructed using crystallographic / boron etch-stop technology and assembled with a glass or metallic cavity. The device has demonstrated an output resolution of 2.5mV/°/s and a noise limited detection rate of 2°/s. A second device has also been constructed, integrating the transducers and cavity on a single silicon die. In this structure (figure 6.17) the cavity is constructed through crystallographic etching and wafer bonding. No experimental data relating to this device has been published.

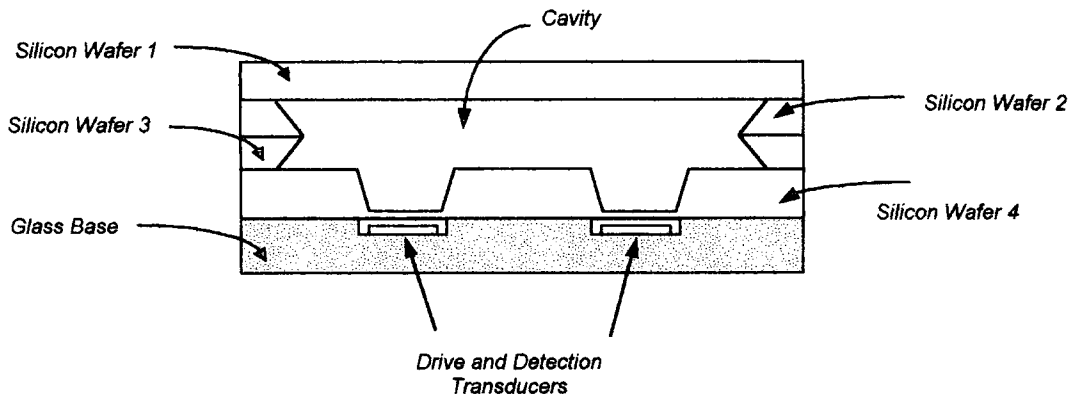

Figure 6.17. *Cross-section through a silicon micromachined acoustic gyroscope,*

6.5 Applications of Micromachined Gyroscopes

The first generation of micromachined gyroscopes are unlikely to attain the performance required for navigation quality instruments, although the favoured use of low loss resonator materials such as silicon and quartz will surely allow for the future development of high grade devices. For this reason it will be the low-grade motion control market that will initially benefit from the commercial production of micromachined gyroscopes. The benefits offered will make them very competitive products, generating new markets as well as competing against traditional medium quality devices in those already established. This section aims to identify the main applications foreseen for these devices.

6.5.1 Automotive

Possibly the largest market for medium grade gyros lies within the automotive industry. It has already taken advantage of the recent development of low cost miniature accelerometers to develop air bag safety systems that are now installed as standard on many vehicles. Availability of similarly low cost rotation sensors will drive the development of advanced safety systems which will take into account both linear and rotational vehicle accelerations. Anti-skid, traction control and active suspension systems require information about vehicle rotations (yaw, pitch and roll) in order to apply stabilising corrections to the vehicle.

6.5.2 Hybrid Navigation Systems

Current inertial reference systems used for navigation are evolving into hybrid systems, deriving information from more than one source. For example, systems used on aircraft incorporate receivers to intercept data from the global positioning system (GPS). GPS is a world-wide radio navigation system that uses a network of 24 satellites to provide positional information anywhere in the world. NASA uses similar hybrid systems in spacecraft and orbiting satellites. Although out of range of GPS they use star trackers to update the onboard inertial reference units by determining orientation with visual reference to known star clusters. The additional data supplied by the hybrid system provides long-term accuracy and a system whose performance is greater than that of its individual components. In this way high quality navigation systems may be produced through integration of medium quality gyroscopes and GPS technology. This type of technology could find use in non-critical areas such as navigation of cars and small marine vessels.

6.5.3 Military

In the past the military have been one of the largest consumers of inertial sensors. They have been used in the development of high quality navigation instruments and also stabilisation systems for ballistic missiles and other long-range artillery shells. Many systems used for motion control are similar (as are the associated costs) to those used for navigation. This is due to the unavailability of lower cost systems. Further applications could include stabilisation of weapon sighting systems that remove spurious vehicle or user motion. A similar system has recently been launched by British Aerospace to position and aim mobile weaponry. The modern artillery sighting system (MASS) [78] uses inputs from a ring laser gyro and a GPS receiver to calculate the precise position and aim of artillery weapons. Future systems may well employ vibratory devices. Although many applications envisioned for micromachined gyros are already in place using traditional components, the availability of rugged 'throw away' sensors will allow reduction of cost and encourage extended application.

6.5.4 Aerospace

It has been proposed that future deep space probes may weigh as little as 180kg. With approximately 65kg of this total required for fuel to reach Mars, only 115kg remains for all remaining systems [79]. These include propulsion, communications, scientific equipment, and electronics. Micromachined sensors would offer significant advantages over more conventional equipment in this application. NASA have planned a number of low cost missions in the next millennium which may see the use of devices similar to those already used in the Pathfinder mission (section 6.4.2.2.1).

6.5.5 Consumer

The computer industry has already taken advantage of low cost gyroscopes that have recently been made available to develop free space pointers and inertial mice to replace existing desktop versions. Although these are not micromachined gyros they can be made compact enough to fit within the volume of a traditional desktop mouse.

Application of micromachined versions will allow further cost reduction. Stabilisation units, similar to those used in military systems, will be included in the next generation of video cameras to remove spurious movements of the camera either by incorporating an inertial frame or more probably through electronic compensation. Applications also exist for model aircraft control and robotics.

6.5.6 Virtual Reality

Another large market lies potentially in the growing area of virtual reality (VR). Motion sensors can monitor head and body movements to improve the accuracy of the VR environment. The small size of micromachined devices will allow for their incorporation into VR suits without restriction of movement. Application will also be extended to pointing devices similar to those already available as computer peripherals.

6.5.7 Other

Industrial applications include intelligent robot and machine control, provision of automatic guided vehicles on automated factory floors and production of low cost inertial platforms. Medical uses could include monitoring of limb and body motion for diagnosis and treatment of various diseases and conditions. Similar systems may be used in sport science to monitor and improve the performance of athletes.

Chapter Seven
Ring Gyroscope: Theory and Design

This chapter describes the theory and design of a particular gyroscope device. With many potential designs, it was with the fabrication process in mind that a shell-type structure (section 6.4.2.3) was selected. The inherent problem of thickness control in electroforming excluded the choice of beam or tuning fork designs, as these require tight dimensional control. In contrast, shell gyros require only uniform dimensions and good symmetry.

7.1 Theory of Operation

This section describes the general operation of shell-type gyroscopes, encompassing the theory that applies equally to cylinder, hemispherical and ring structures [51]. Figure 7.1 shows these devices, emphasising their physical similarity.

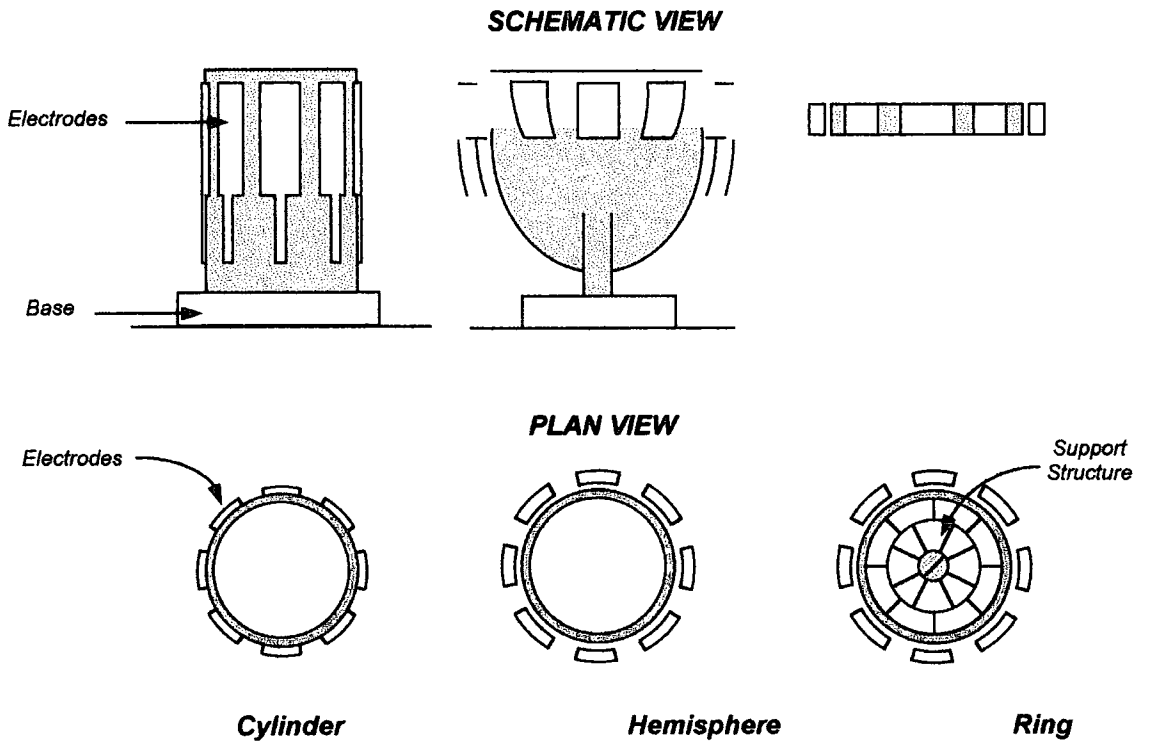

Figure 7.1. *Cylinder, hemisphere and ring structures.*

A uniform ring (cylinder or hemisphere) has a vast number of possible modes of vibration, most of which consist of standing wave patterns. The radial displacements of these modes vary as $\cos 2\theta$, $\cos 3\theta$, $\cos 4\theta$ etc. as shown in figure 7.2. In gyro operation it is only the fundamental flexural mode, the $\cos 2\theta$ mode, that is of interest. This is a standing wave consisting of two full wavelengths around the circumference of the ring and four node points located symmetrically (figure 7.3a). The vibration pattern can adopt any orientation around the ring but will always possess the same frequency as long as the dimensions of the ring are uniform.

Resonance can be excited by the application of sinusoidal drive forces at A and A′, and maintained through feedback from signals at B and B'. In the absence of rotation the vibration pattern remains stationary with anti-nodes aligned to the drive forces and node points located along the 45° lines. However, when the system is rotated, the vibration pattern is observed to precess relative to the ring by an amount proportional to the angle of rotation, independent of the rotation rate. For example, in figure 7.3a, the anti-node

axis will remain aligned to the reference axis in the absence of rotation. When the structure undergoes a 90° clockwise rotation (figure 7.3b), the anti-node axis is observed to precess relative to the reference axis. This phenomenon can be exploited to give a measure of rotation.

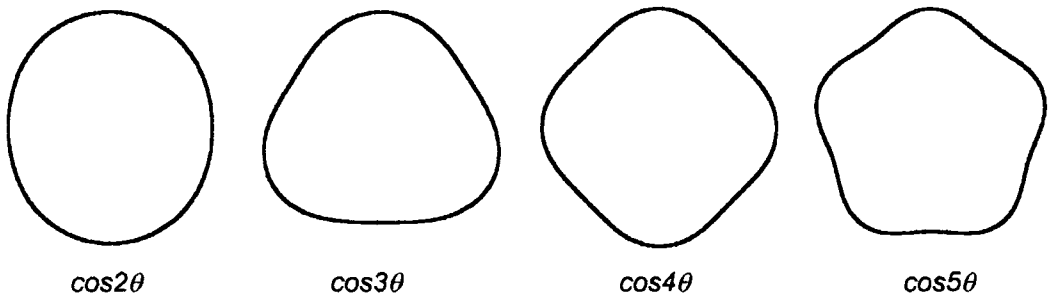

Figure 7.2. *Resonant mode shapes of a uniform ring.*

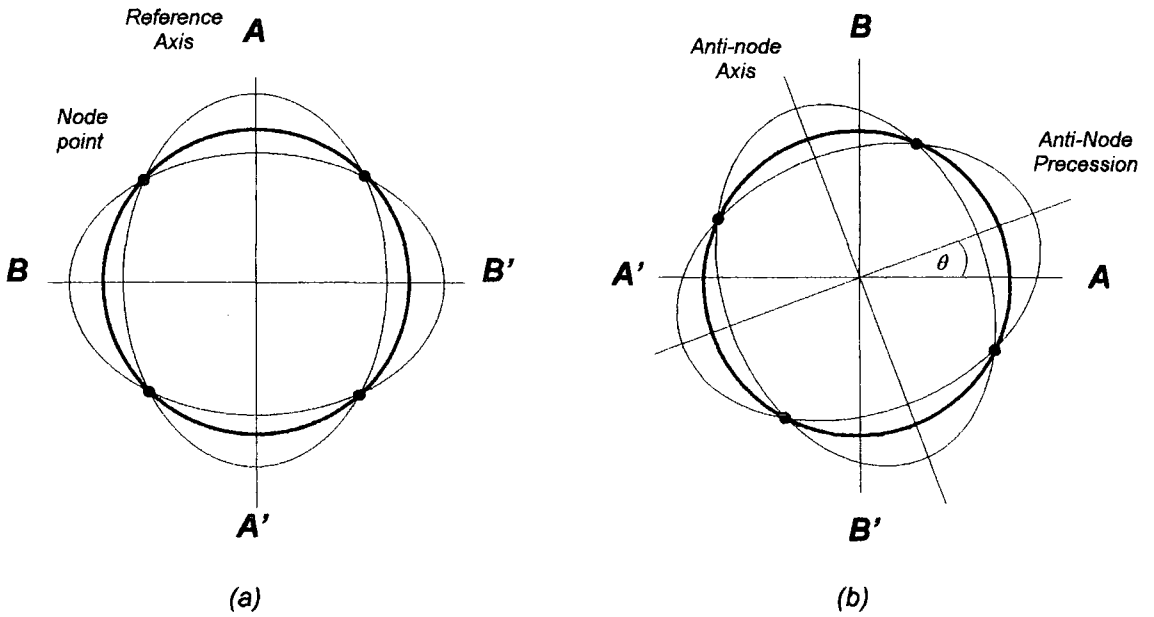

Figure 7.3. *Precession of the standing wave vibration pattern.*

The precession of the vibration pattern can be explained through consideration of the Coriolis forces that act on the ring during rotation. In accordance with the theory presented in chapter six, all parts of the ring with a component of radial velocity are subject to Coriolis acceleration. However, the effect can be explained through consideration of the anti-nodes only:

With reference to figure 7.4, it can be seen that the radial velocity *(V)* of point A gives rise to a Coriolis force *(F_C)* in a direction tangential to the ring. An equal but opposite force is generated at point A′ on the opposite side of the ring. The combined effect of these two forces is to generate a couple about the central axis of the gyroscope in a clockwise direction. A similar couple is generated in a counter-clockwise direction due to the radial motion of points B and B′. Addition of the two couples produces a component of force at 45° to the original vibration and generates a secondary standing wave pattern. This vibration is identical to the cos2θ primary mode but is spatially rotated by 45° (and is hence known as the sin2θ mode). Superposition of the two standing waves causes the resultant vibration pattern to precess around the ring, at a rate determined by the angular motion of the structure.

The orientation of the standing wave pattern can therefore be used to determine the absolute angle of rotation, or, more conveniently, the magnitude of the sin2θ component can be used to give a measure of the rotation rate.

The resonant frequency of shell structures is determined solely by planar dimensions, and is completely uninfluenced by thickness. For a cylinder gyroscope, this means that the resonant frequency is determined solely by the combination of cylinder diameter and wall thickness. The situation is more complicated for ring designs due to the need to incorporate a support structure, but, again, the resonant frequency is still determined by in-plane dimensions only. Mode matching can therefore be achieved by producing a symmetrical design with uniform in-plane dimensions.

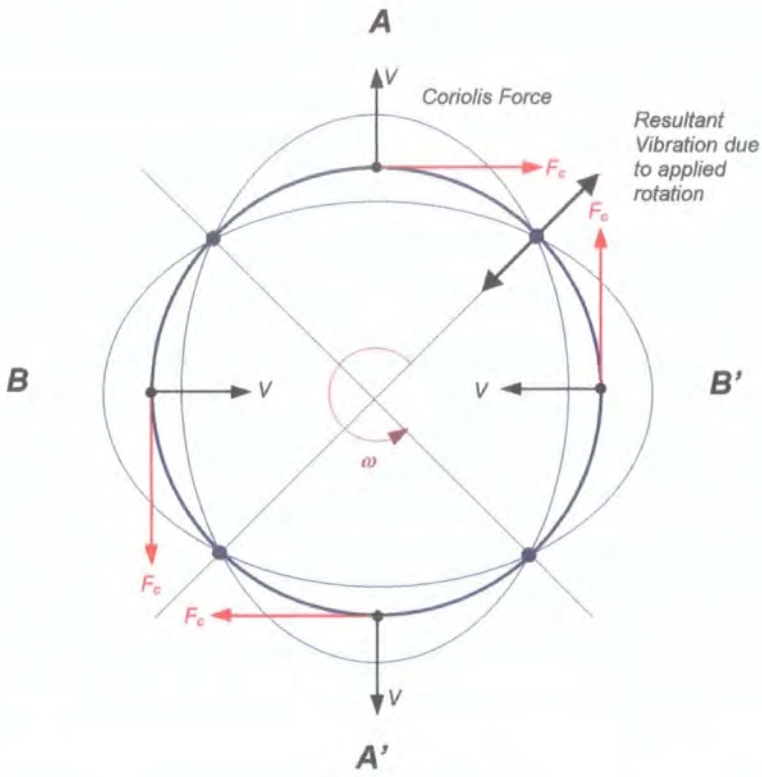

Figure 7.4. *Generation of the secondary vibration.*

7.2 Practical Operation

In a practical arrangement a phase locked loop control system would be employed to excite and maintain the vibration at resonance. A schematic of such a system is shown in figure 7.5. Feedback from the primary sense electrodes into the control loop allows the vibrating structure to be maintained at self-resonance, compensating for any drift in frequency due to temperature or ageing effects. In addition to the two primary drive and sense electrodes, a further four electrodes are positioned symmetrically along the 45° points to detect and null (chapter six) the secondary response of the gyroscope. The use of differential detection schemes would also be employed to boost signal levels and maximise sensitivity.

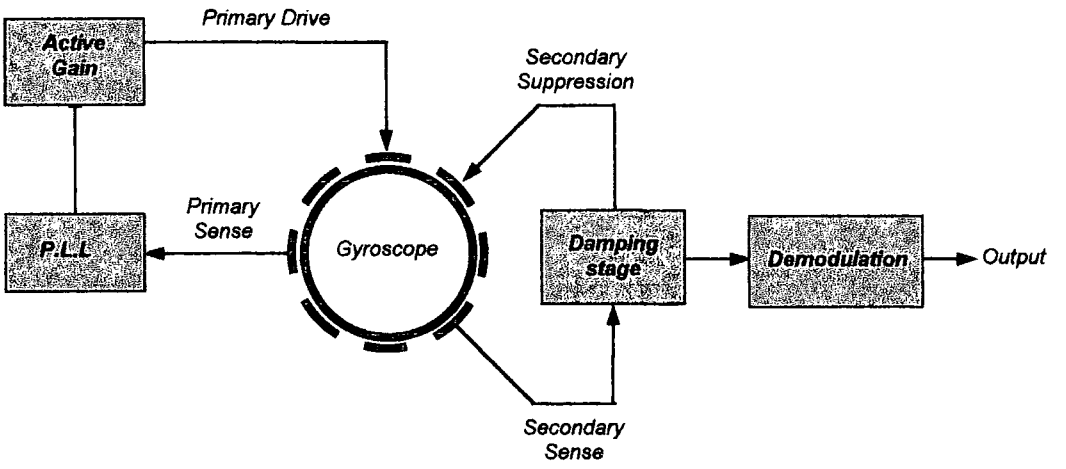

Figure 7.5. *Practical operation of the ring gyroscope.*

7.3 Micromechanical Ring Gyroscope

Interest in the development of micromachined ring gyroscopes is due both to the success of the macroscopic devices and improvements in micromachining technology. Three devices have been produced to-date, two using silicon micromachining [72,81] and a third exploiting electroformed nickel [73].

This section describes the physical design and electrical operation of a similar micromachined nickel ring gyroscope.

7.3.1 Gyroscope Design

The initial gyroscope design was developed at the University of Newcastle-upon-Tyne by Professor J.S. Burdess. Work at Newcastle was centred on the development of a silicon ring gyroscope and this work progressed concurrently with the work presented in this thesis. Although the two devices are based on the same design, the specific geometry of each and the drive and sense mechanisms used for operation differ. A schematic diagram and cross-section of the structure used in this work is presented in

figure 7.6, allowing identification of the main mechanical features. The device consists of three main elements: the ring, the support structure and the drive and sense electrodes. The ring is suspended 2-4μm above the silicon substrate by the support structure, which consists of eight pairs of suspension arms (ligaments) tethered to an outer support that is in direct contact with the silicon substrate. The ring, which constitutes the main dynamic element, is 4mm in diameter and 100μm wide. The whole device is typically 30 - 40μm thick. Eight drive and sense electrodes are located around the inner circumference of the ring and separated by approximately 10μm.

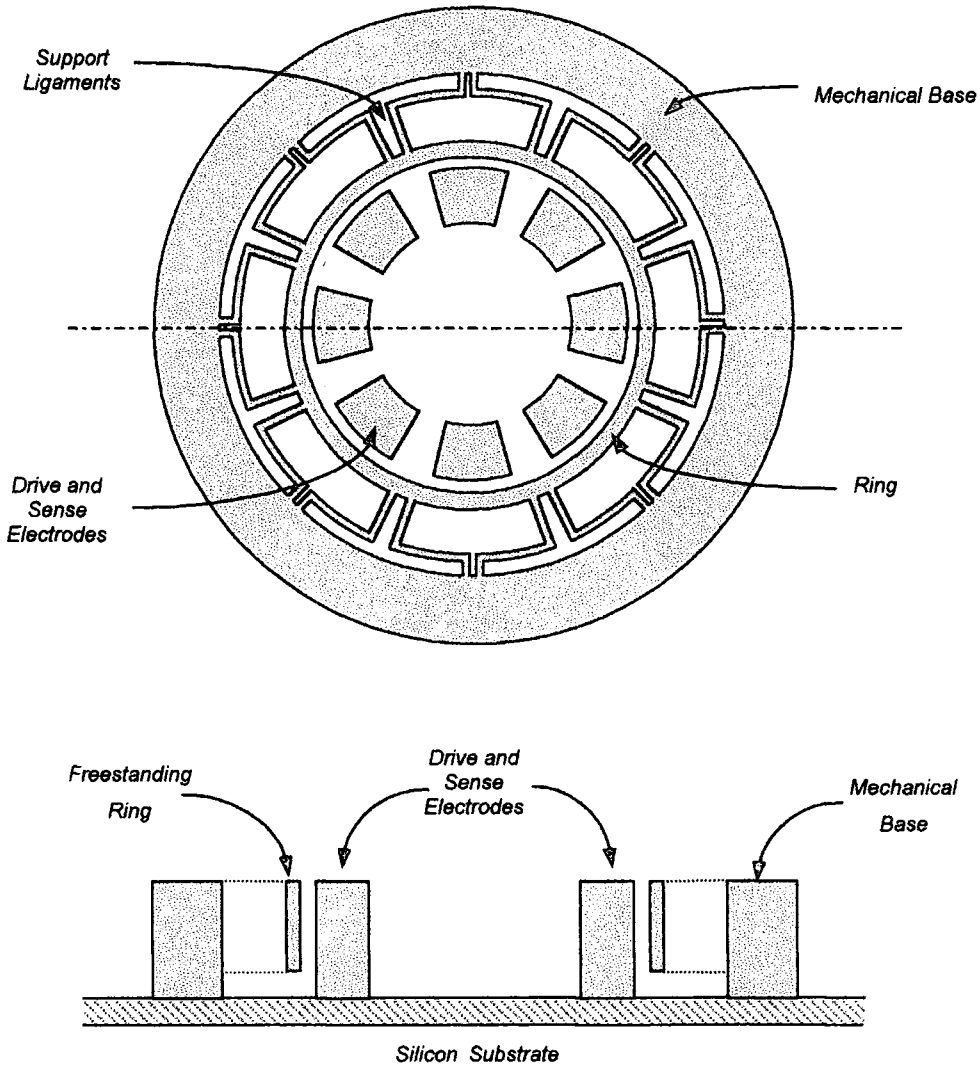

Figure 7.6. *Schematic diagram of the micromechanical nickel ring gyroscope.*

7.3.2 Simulation Model

This section documents the finite element analysis (FEA) of a number of ring type structures in order to predict their dynamic properties. Particular detail has been given to the ring design discussed in the previous section. All simulations were performed using PAFEC-FE (version 8.5) software mounted on a Sun Ultra Workstation.

The initial simulation model is shown in figure 7.7, giving a three dimensional representation of the ring gyroscope. Not shown are the eight drive and sense electrodes, as these play no role in the dynamic operation of the device. For completeness the simulation model data file is supplied in appendix C.

As the preliminary model of figure 7.7 was constructed from three dimensional mesh elements, it proved very expensive in terms of computational time with simulation times running into several hours. To overcome this constraint it was decided to construct a simplified two dimensional model (figure 7.8). Analysis of this revised model greatly reduced simulation times without significant effect on results; comparison showed little difference in predicted modeshapes or resonant frequencies. For this reason all future simulations were run using the simplified 2D mesh.

The next few sections describe the results obtained from the finite element analysis including determination of resonant frequencies and resonant modeshapes.

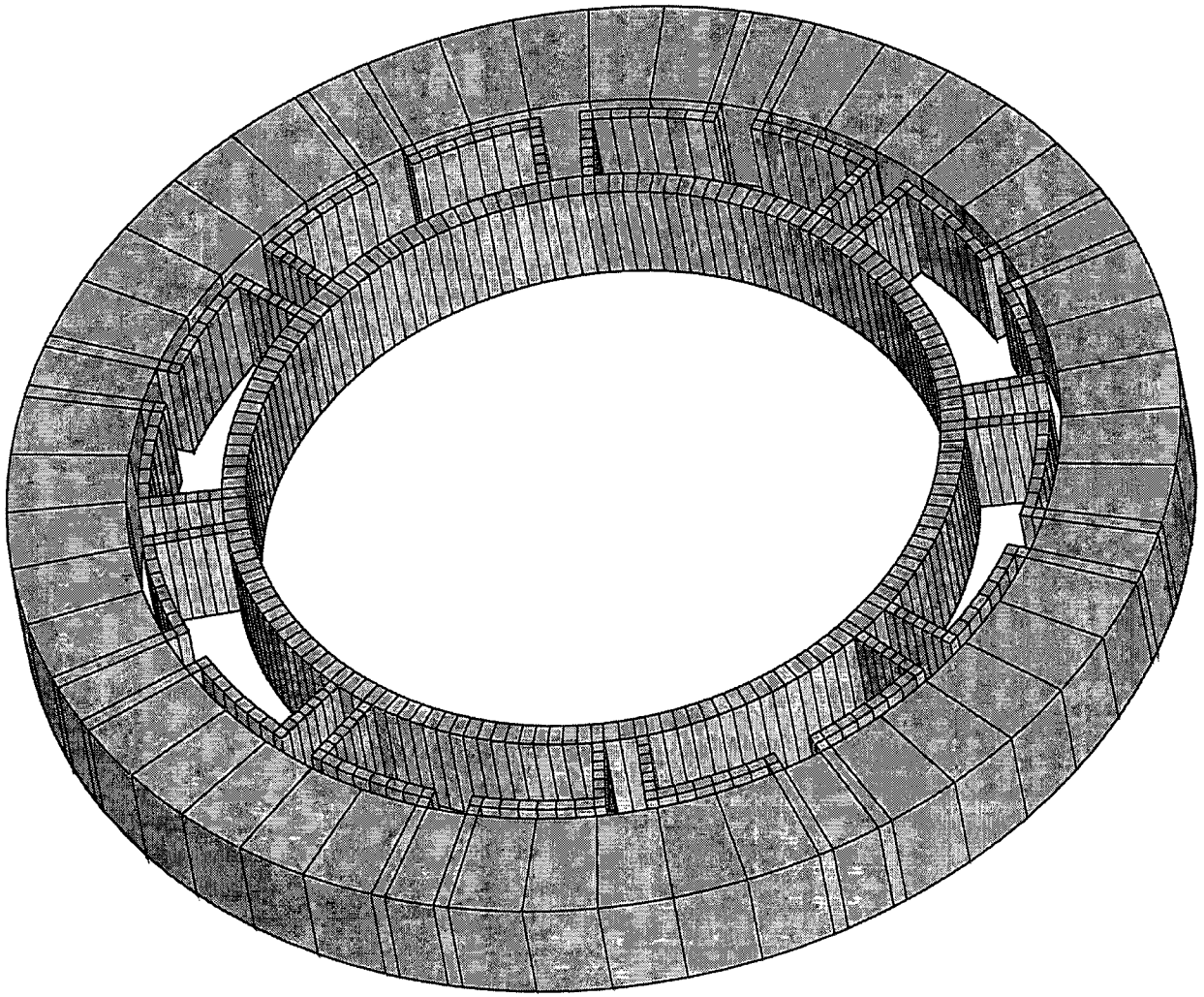

LINEAR

STATICS

ROTATION

X = 330

Y = 330

Z = 330

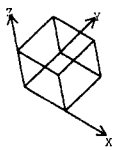

TITLE ***Figure 7.7.*** *3D simulation model.*

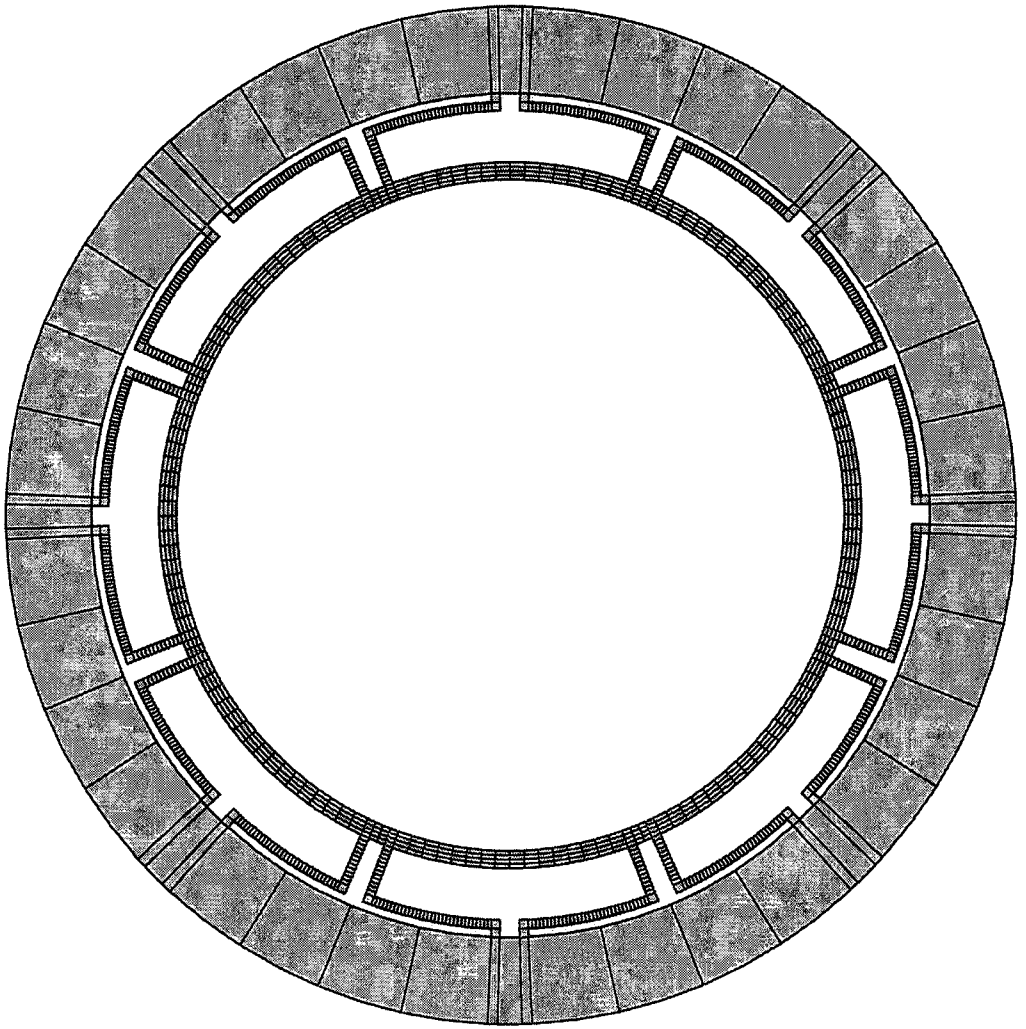

Figure 7.8. *2D simulation model.*

7.3.2.1 Resonant Mode Shapes

The first stage of the finite element analysis involved determining the main resonant modeshapes of the structure. In particular this was aimed at identifying the two operational modes of the gyroscope (i.e. the cos2θ and sin2θ radial displacements of the ring discussed in chapter six) but also at determining out-of-plane resonances.

7.3.2.1.1 Out-of-Plane Modes

The resonant frequencies of the out-of-plane modes were found to be, as expected, strongly influenced by the thickness of the device. This relationship was determined and is shown in figure 7.9. The predicted resonant frequencies of a 27μm test structure were obtained from this graph and are shown in table 7.1.

The corresponding mode shapes relating to these resonances are shown in figures 7.10 to 7.13. The first three modes compromise of rigid body vibrations of the ring and the fourth a more complex flexural vibration. Ideally, all of these modes are suppressed in operation as a gyroscope by increasing the out-of-plane stiffness of the device. Physically this means increasing the thickness of the structure but unfortunately this is not possible due to the constraints imposed by the fabrication process which limits the maximum device thickness to approximately 50μm.

	Mode 1	Mode 2	Mode 3	Mode 4
Resonant Frequency	11.61 kHz	13.28 kHz	13.28 kHz	16.17 kHz

Table 7.1. *Predicted resonant frequencies of 27μm thick test structure.*

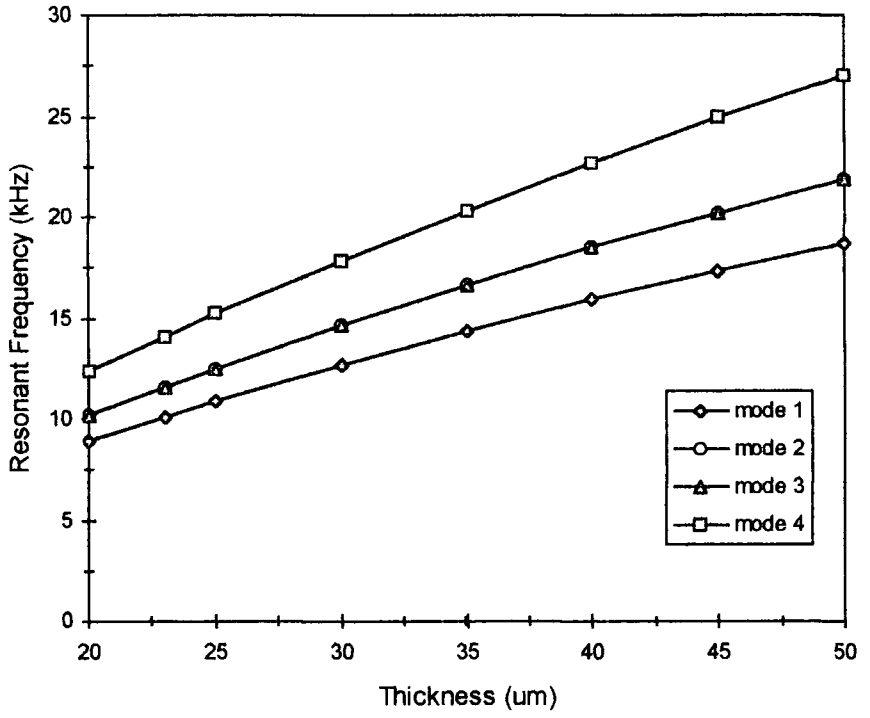

Figure 7.9. *Influence of structural thickness on resonant frequency.*

7.3.2.1.2 In-Plane Modes

The first ten in-plane resonant modeshapes are shown in figures 7.14 to 7.23. The radial displacements of these modes compare well with those of a uniform ring [80] which consist of standing wave patterns of increasing numbers of wavelengths i.e. cos2θ, cos3θ, cos4θ, cos5θ etc. (figure 7.2). The close comparison of the FE model with that of an ideal ring acts as a good indication of the validity of the model.

The cos2θ and sin2θ operational modes of the gyroscope are identified and are shown in figures 7.14 and 7.15. For clarity the resonant frequencies of the first 4 flexural in-plane modeshapes of the gyroscope are listed in table 7.2. As expected these modes were found to be uninfluenced by the thickness of the structure.

	Mode 1	***Mode 2***	***Mode 3***	***Mode 4***
Modeshape	*cos2θ*	*sin2θ*	*cos3θ*	*sin3θ*
Frequency	*36.2 kHz*	*36.2 kHz*	*46.7 kHz*	*46.7 kHz*

Table 7.2. *Summary of resonant frequencies and modeshapes.*

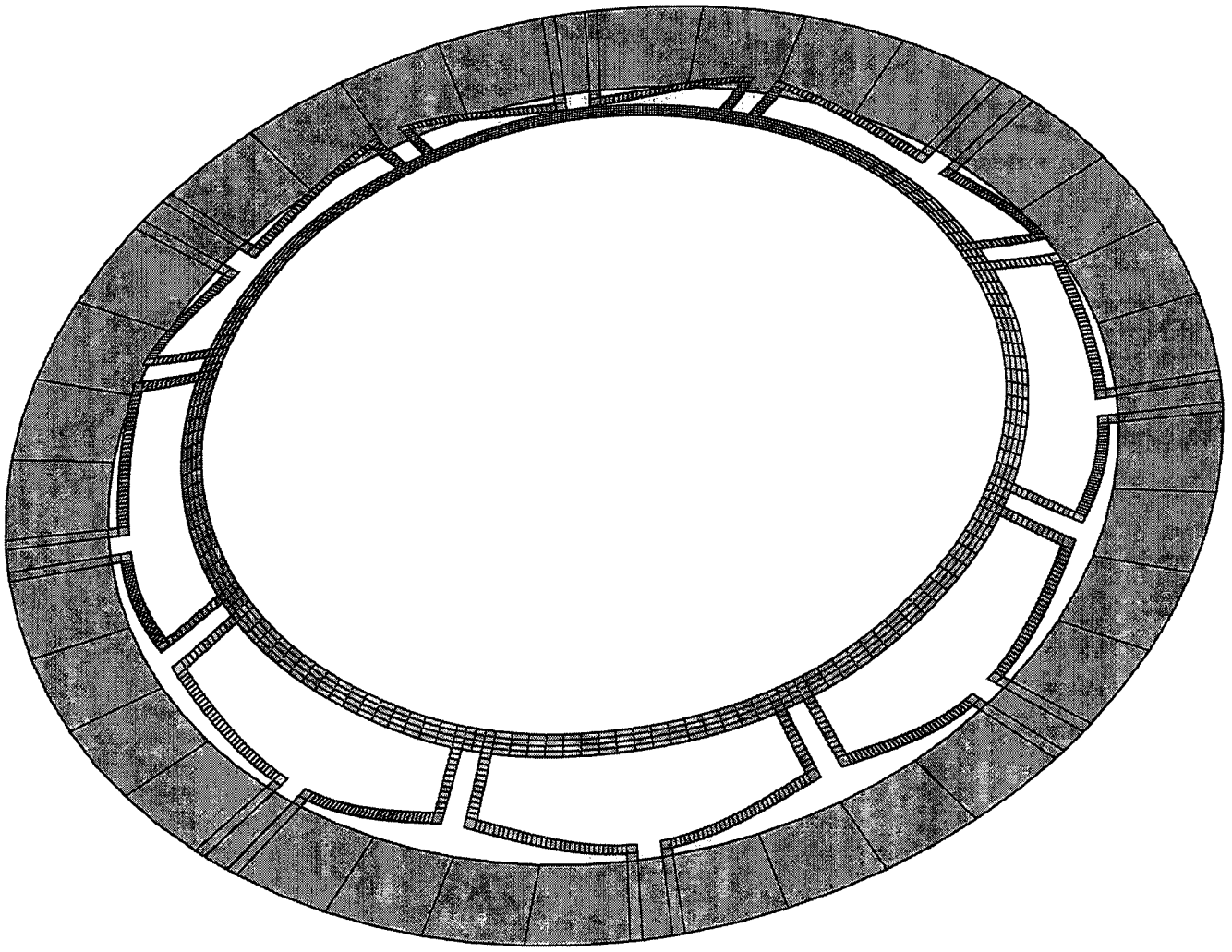

MODES-FREQ
MODE 1
1.161 E 4
(HZ)

ROTATION
X = 330
Y = 330
Z = 330

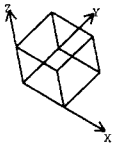

TITLE ***Figure 7.10.*** *First out-of-plane mode shape.*

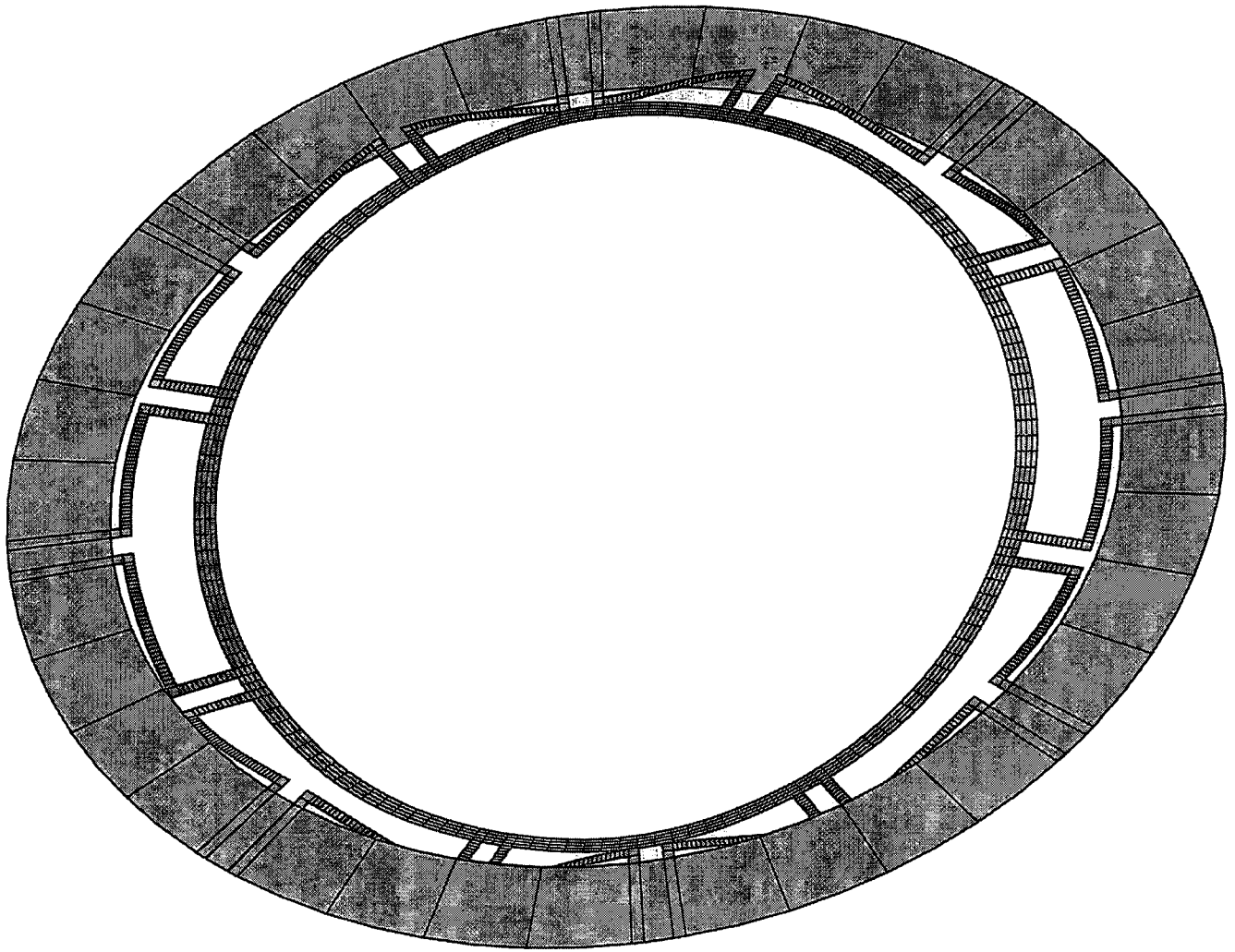

TITLE ***Figure 7.11.*** *Second out-of-plane mode shape.*

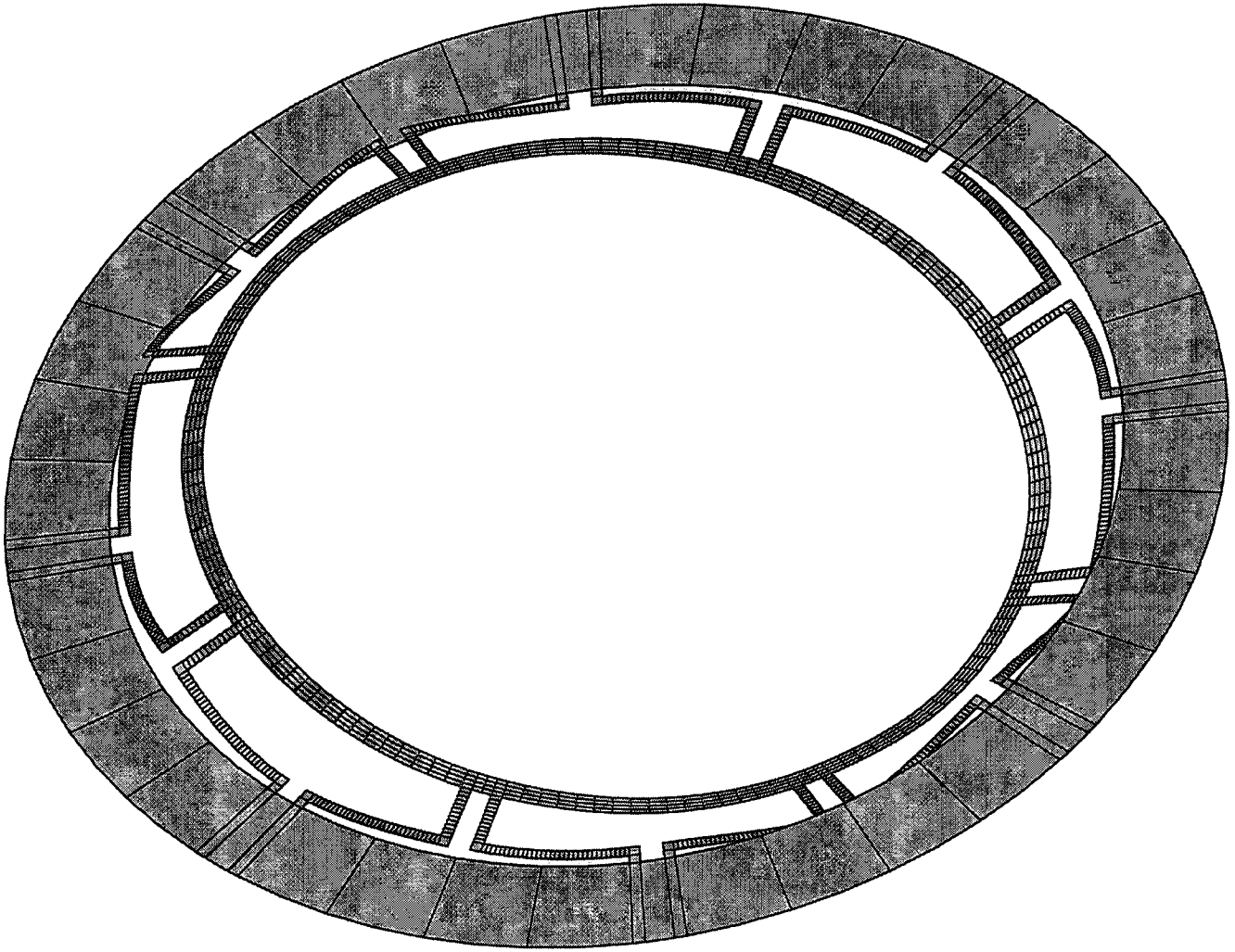

TITLE ***Figure 7.12.*** *Third out-of-plane mode shape.*

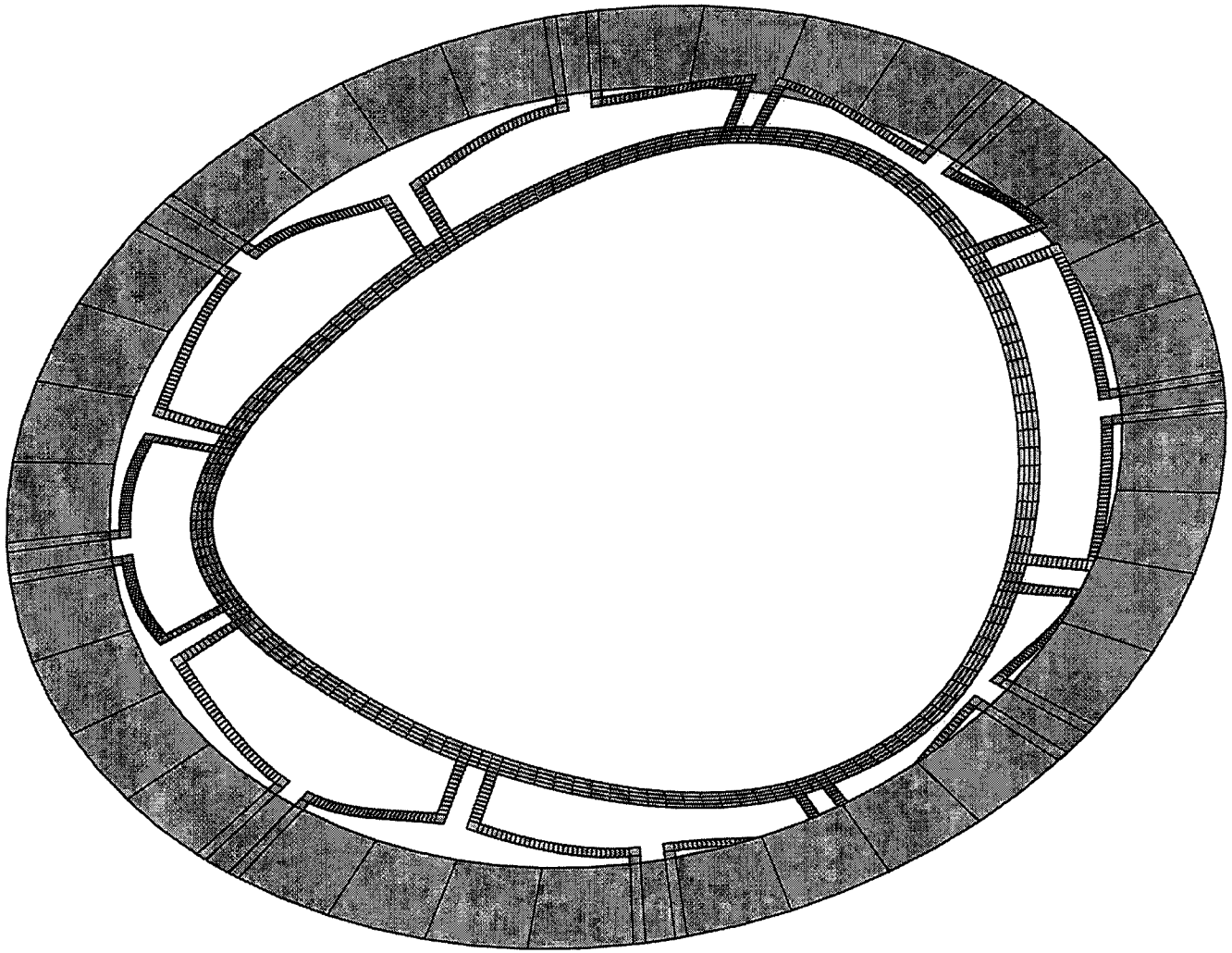

TITLE ***Figure 7.13.*** *Fourth out-of-plane mode shape.*

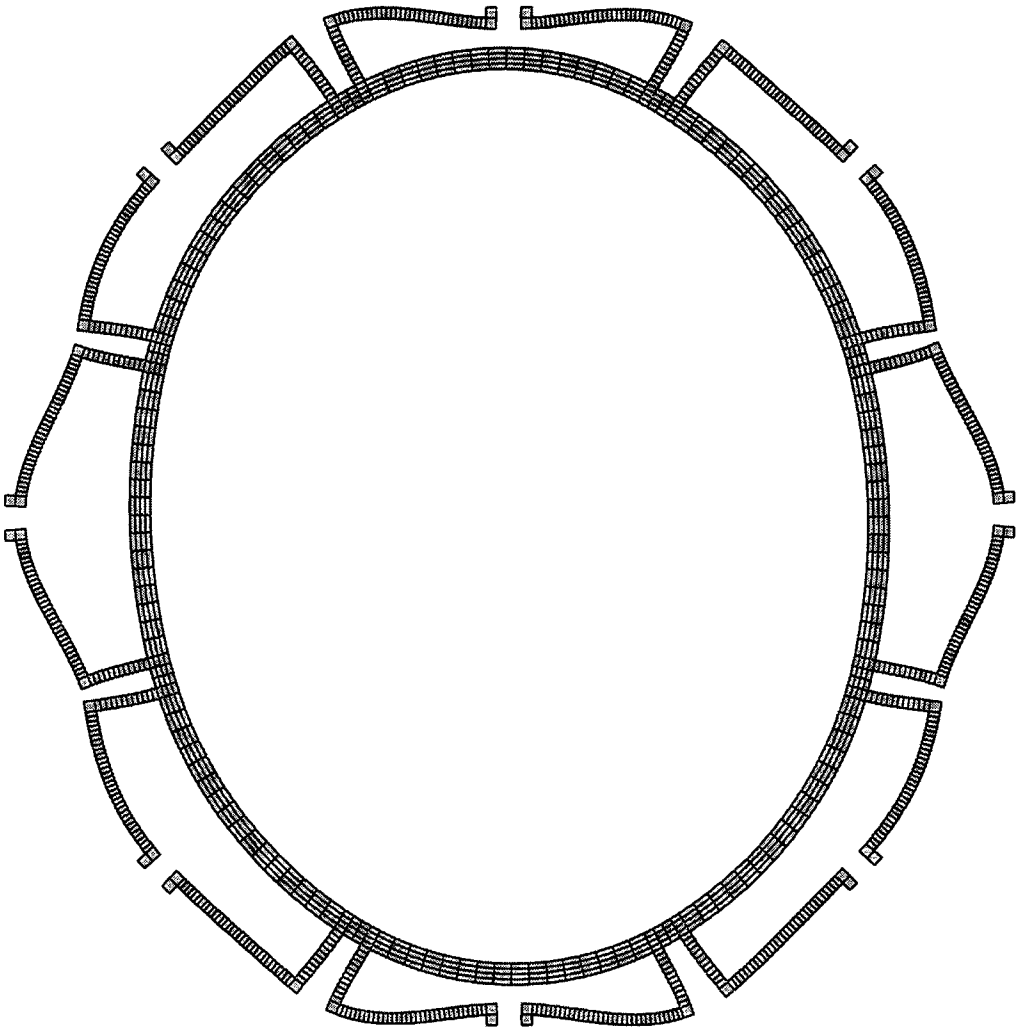

MODES-FREQ
MODE 1
0.362 E 5
(HZ)

ROTATION
X = 0
Y = 0
Z = 0

Y
X
Z

TITLE ***Figure 7.14.*** *First in-plane mode shape.*

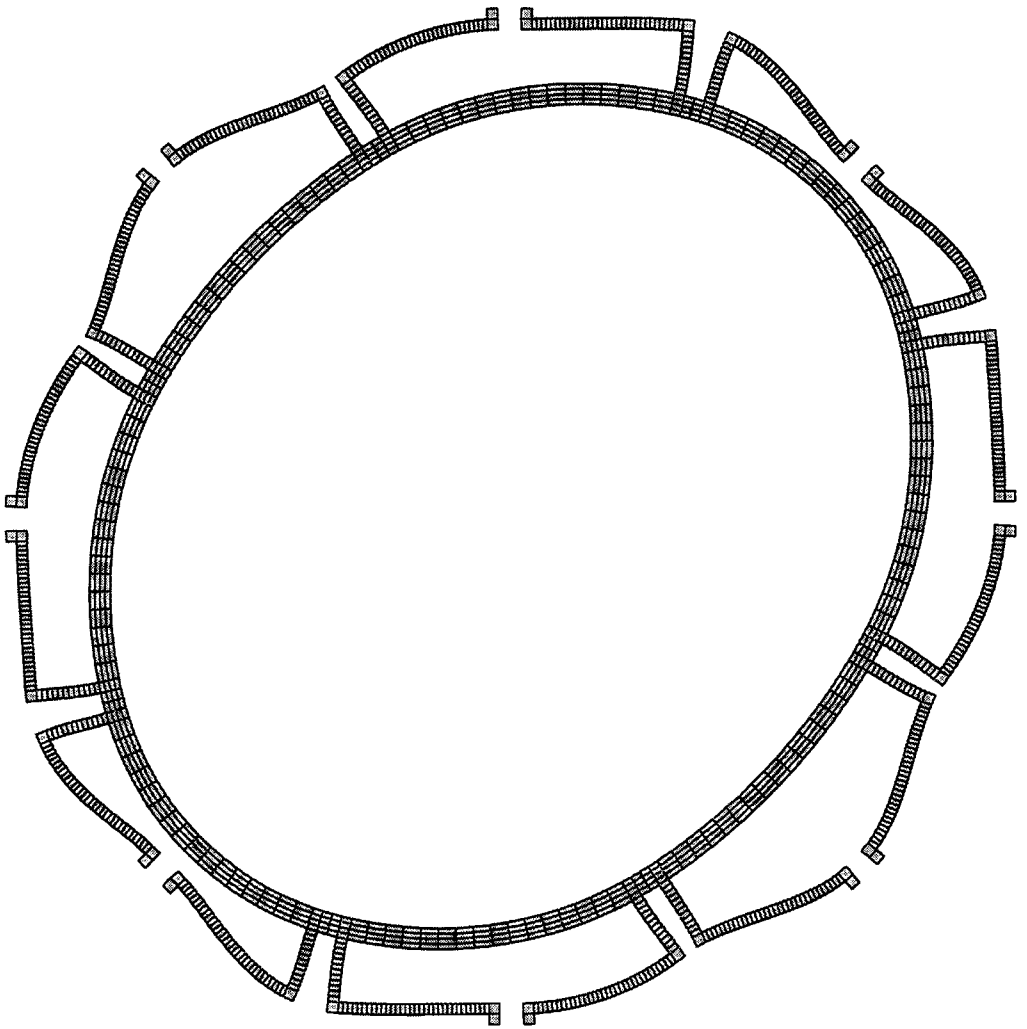

MODES-FREQ
MODE 2
0.362 E 5
(HZ)

ROTATION
X = 0
Y = 0
Z = 0

Y
X
Z

TITLE ***Figure 7.15.*** *Second in-plane mode shape.*

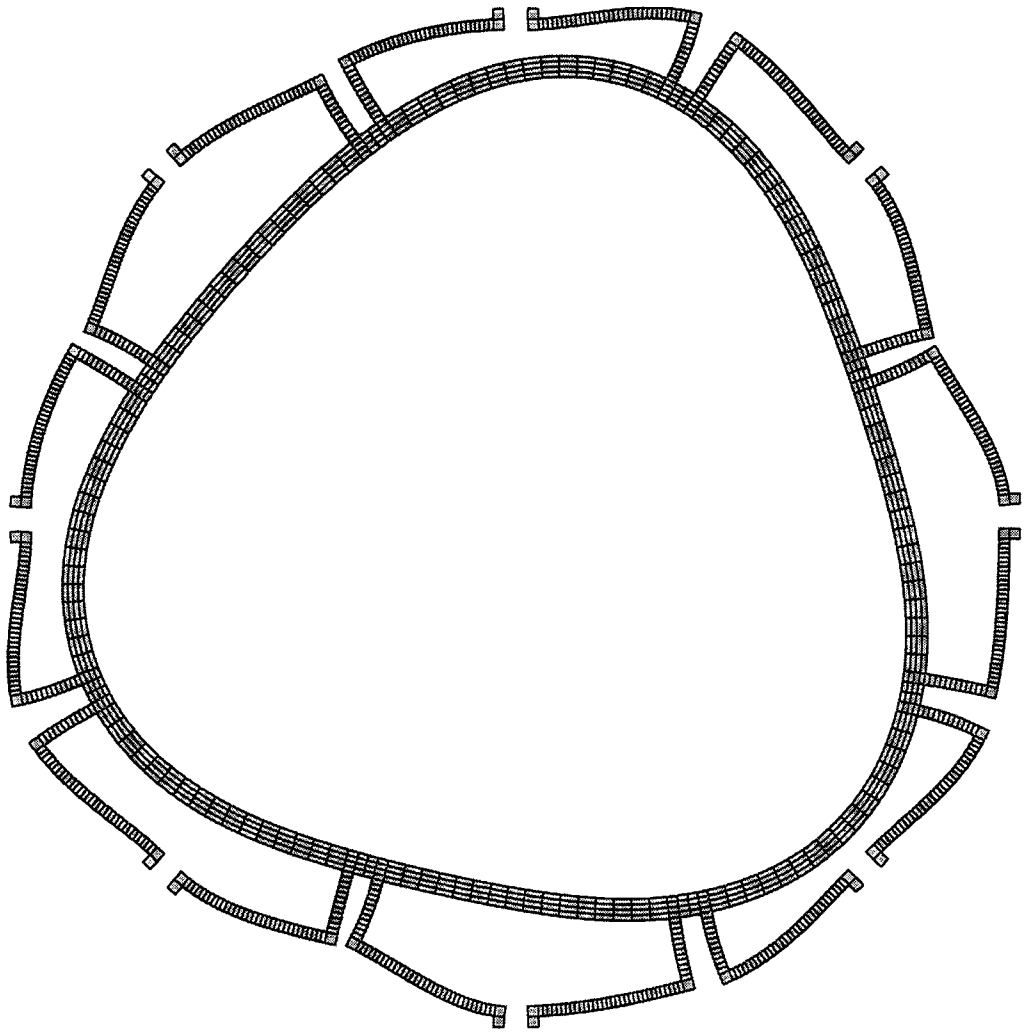

MODES-FREQ
MODE 3
0.467 E 5
(HZ)

ROTATION
X = 0
Y = 0
Z = 0

Y
X
Z

TITLE ***Figure 7.16.*** *Third in-plane mode shape.*

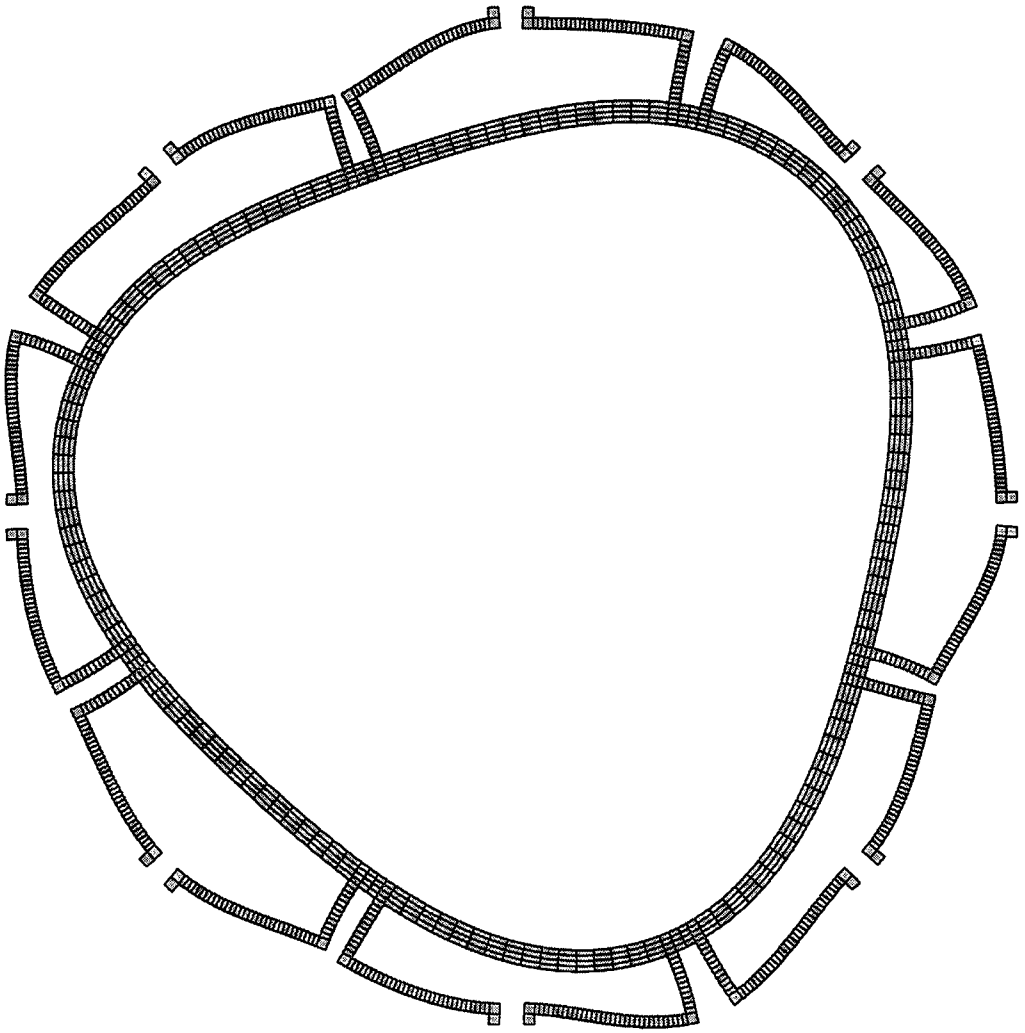

MODES-FREQ
MODE 4
0.467 E 5
(HZ)

ROTATION
X = 0
Y = 0
Z = 0

Y
X
Z.

TITLE ***Figure 7.17.*** *Fourth in-plane mode shape.*

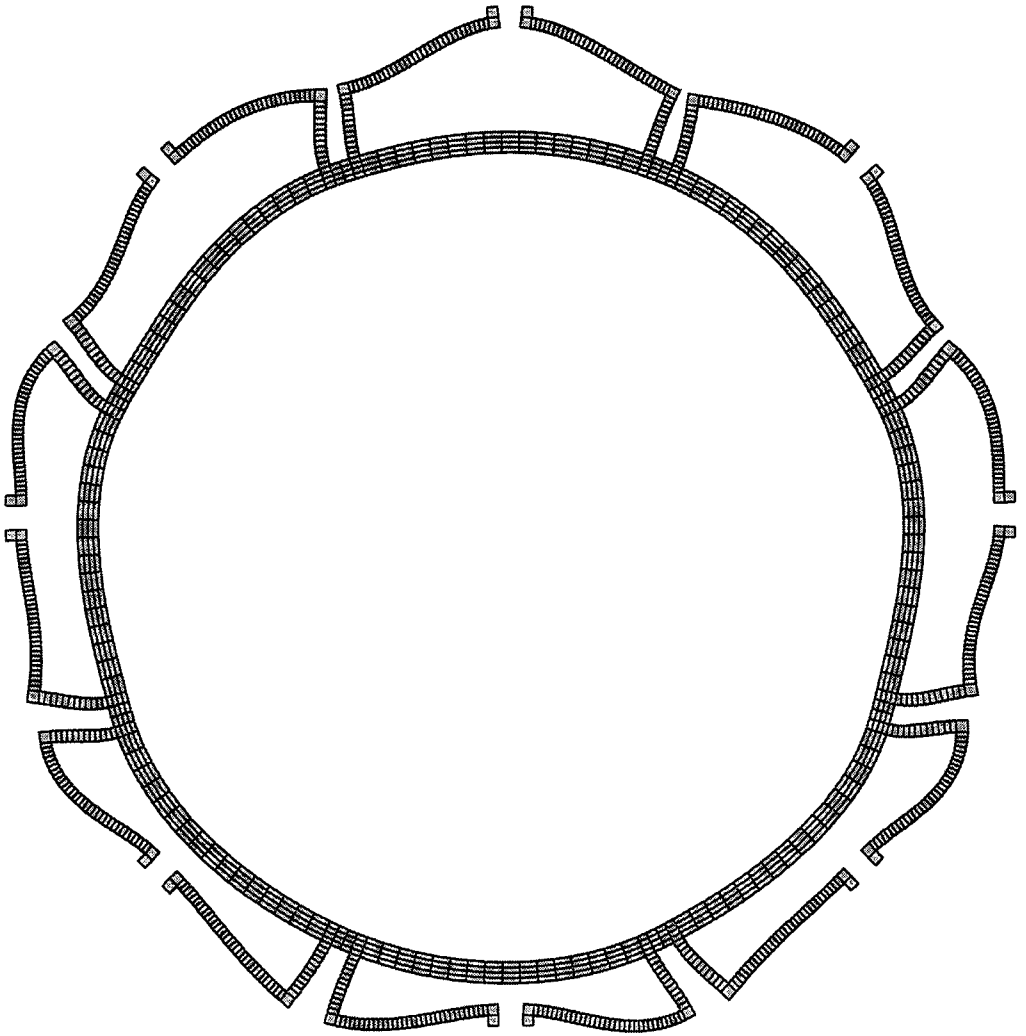

MODES-FREQ
MODE 5
0.617 E 5
(HZ)

ROTATION
X = 0
Y = 0
Z = 0

Y
x
z.

TITLE ***Figure 7.18.*** *Fifth in-plane mode shape.*

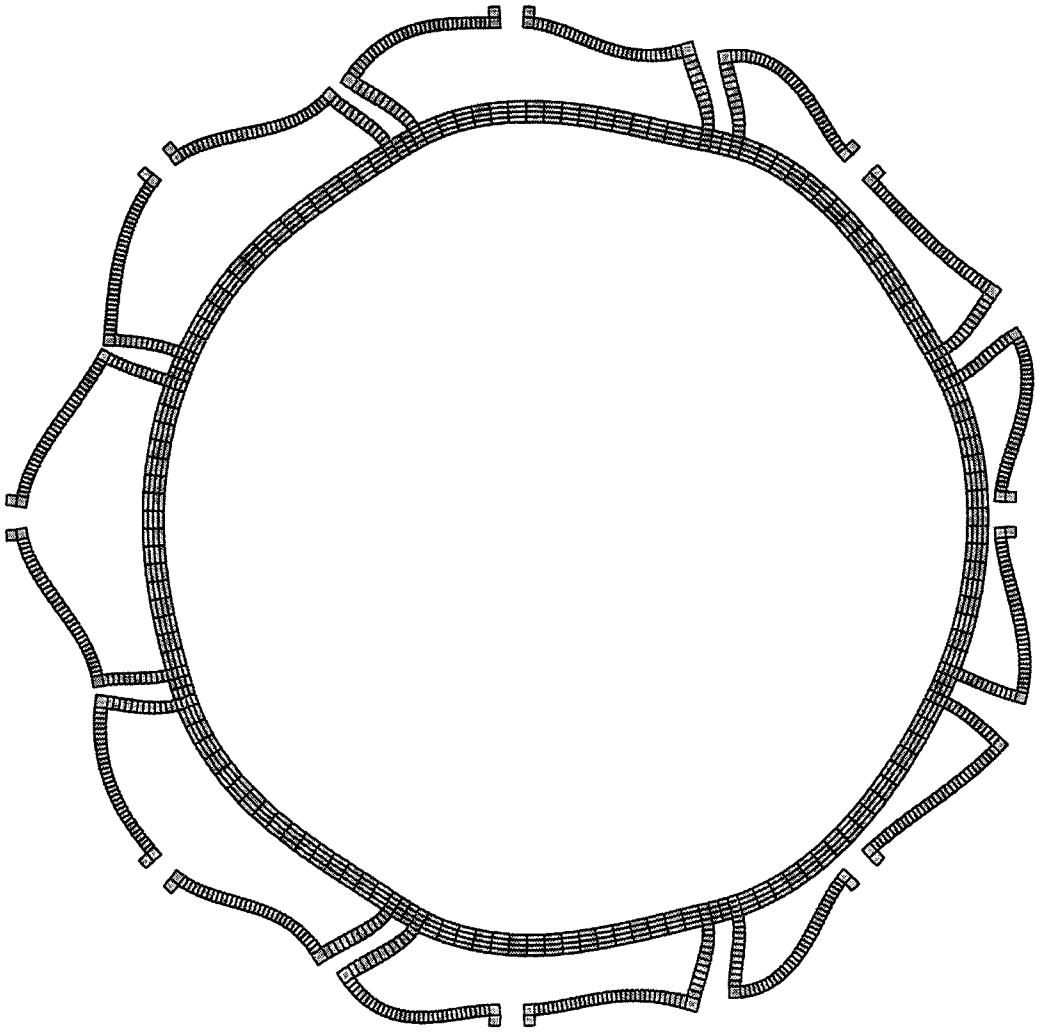

MODES-FREQ
MODE 6
0.618 E 5
(HZ)

ROTATION
X = 0
Y = 0
Z = 0

TITLE ***Figure 7.19.*** *Sixth in-plane mode shape.*

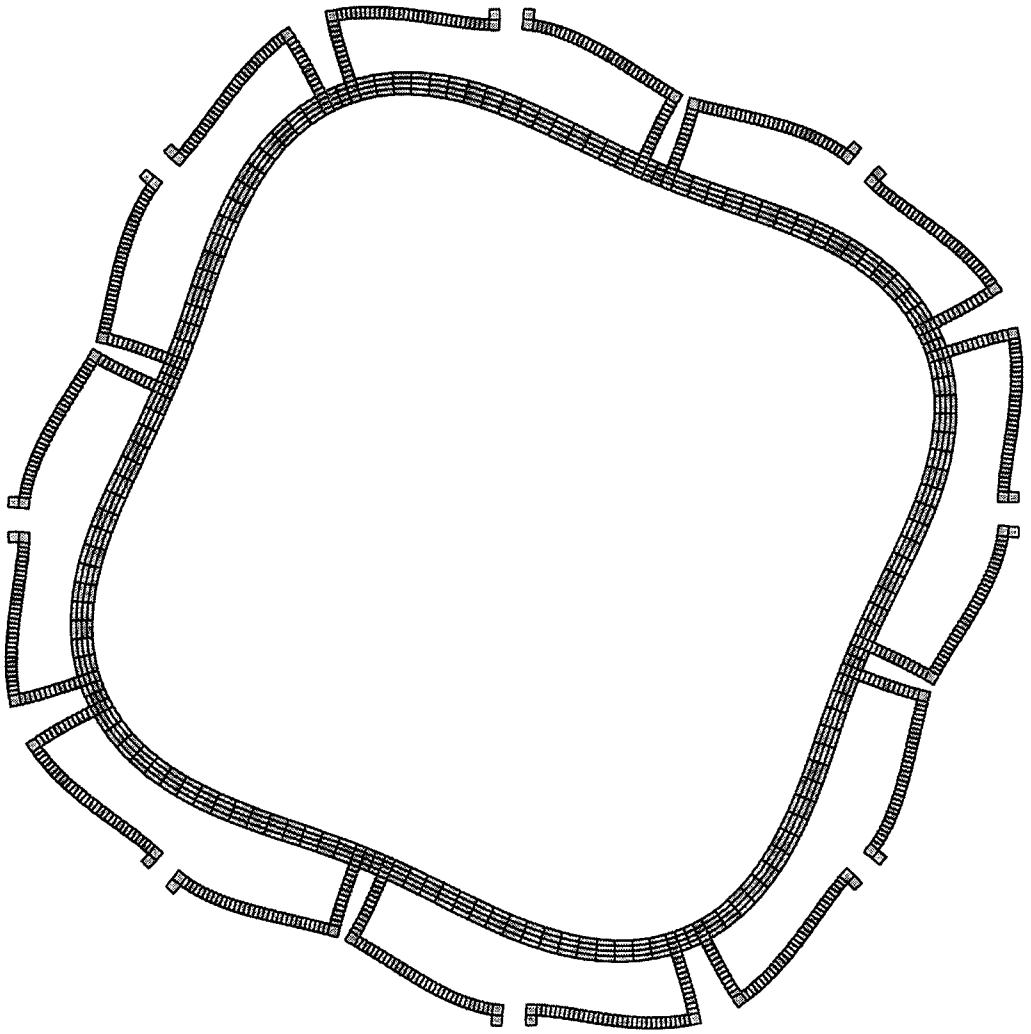

MODES-FREQ
MODE 7
0.703 E 5
(HZ)

ROTATION
X = 0
Y = 0
Z = 0

TITLE ***Figure 7.20.*** *Seventh in-plane mode shape.*

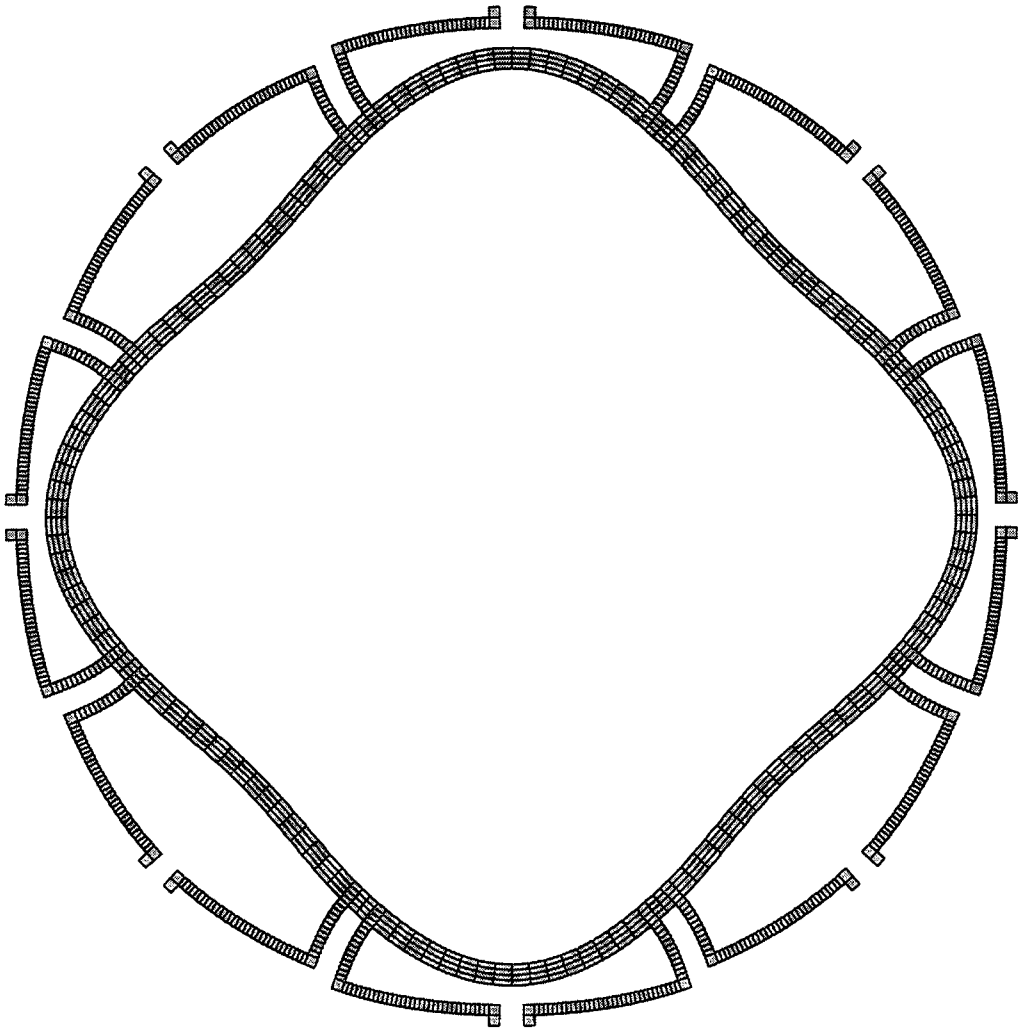

MODES-FREQ
MODE 8
0.922 E 5
(HZ)

ROTATION
X = 0
Y = 0
Z = 0

TITLE ***Figure 7.21.*** *Eighth in-plane mode shape.*

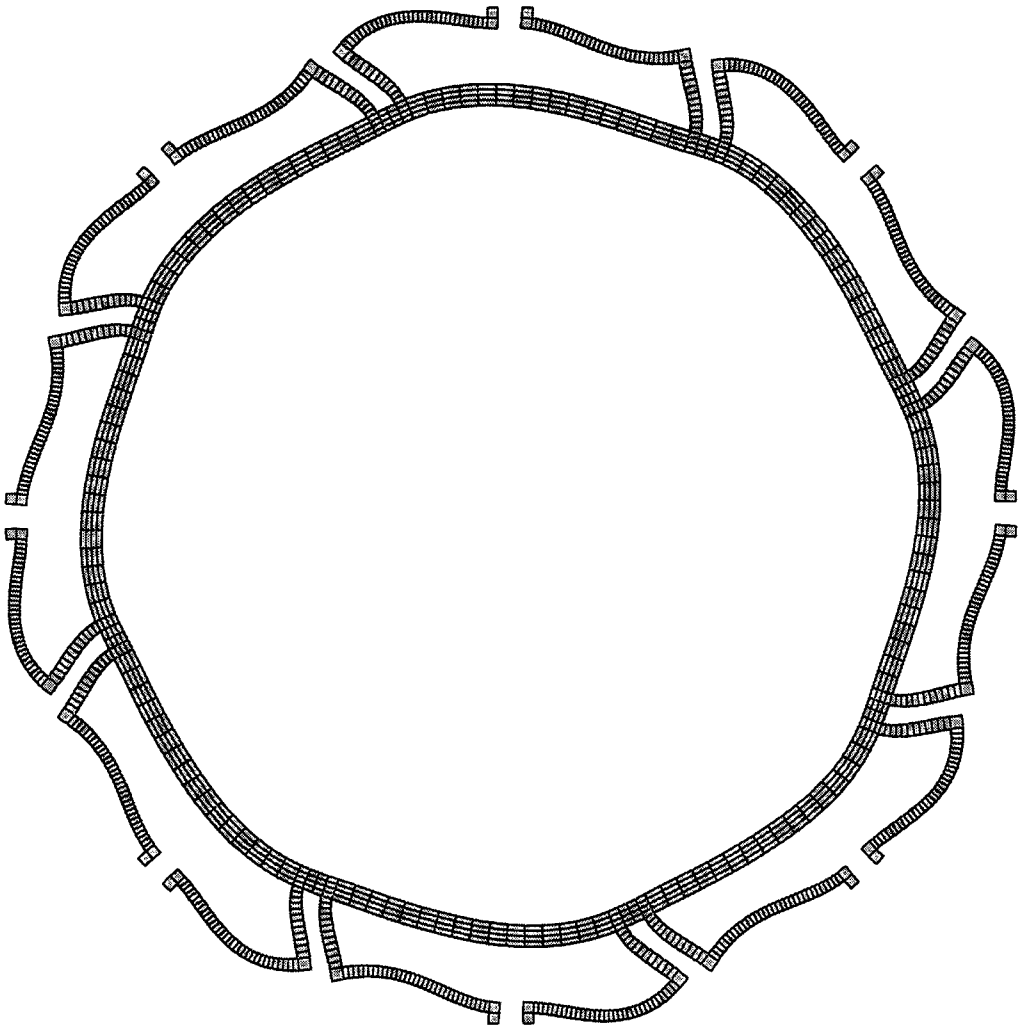

MODES-FREQ
MODE 9
0.987 E 5
(HZ)

ROTATION
X = 0
Y = 0
Z = 0

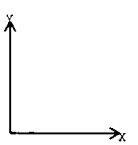

TITLE ***Figure 7.22.*** *Nineth in-plane mode shape.*

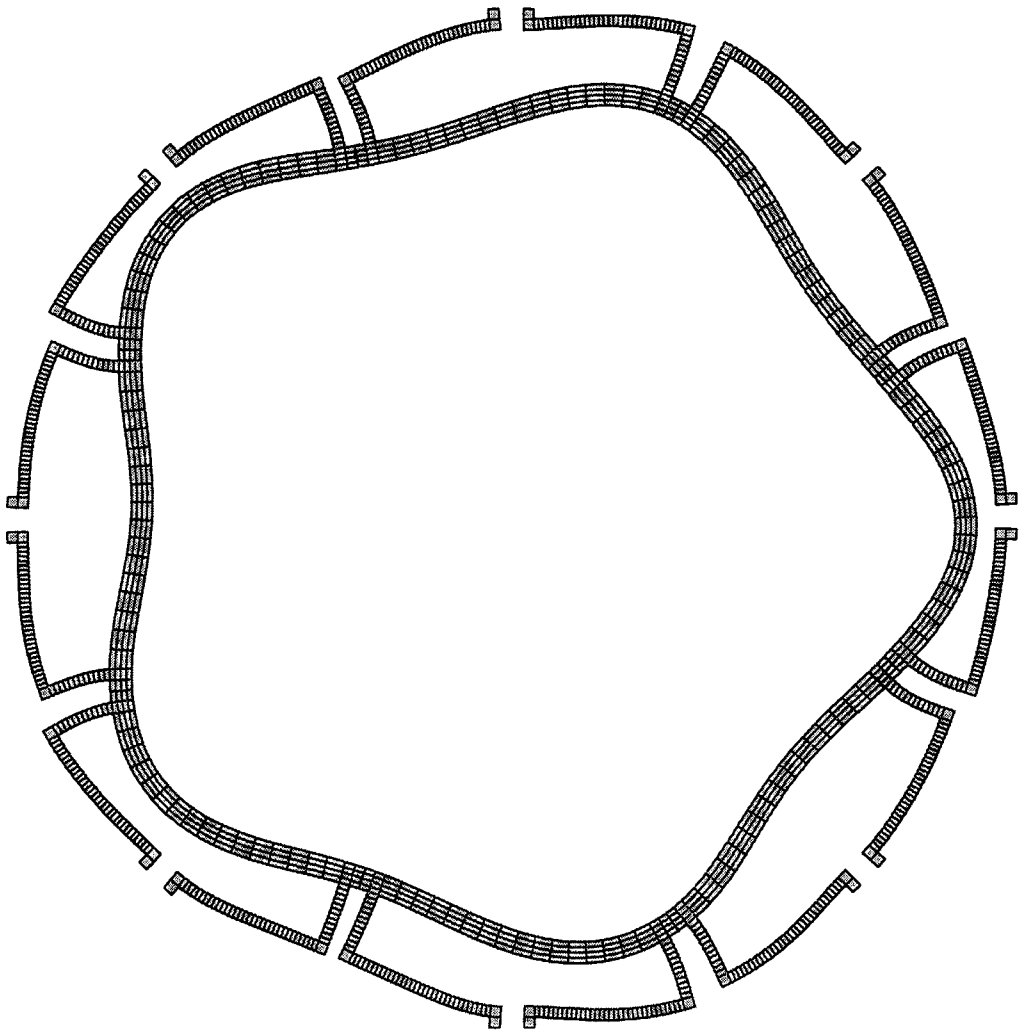

MODES-FREQ
MODE 10
1.263 E 5
(HZ)

ROTATION
X = 0
Y = 0
Z = 0

TITLE ***Figure 7.23.*** *Tenth in-plane mode shape.*

Higher flexural mode shapes are also represented: figures 7.16 and 7.17 show the '3θ' mode shapes, figures 7.20 and 7.21 '4θ' modes and 7.23 a '5θ' mode. In addition, various rigid body modes are predicted: figures 7.18 and 7.19 show rigid body translations of the ring and figure 7.22 shows a rigid body rotation.

7.3.2.1.3 Primary Amplitude

To maximise the sensitivity of the gyroscope it is desirable to generate a large primary amplitude of vibration. The magnitude of this motion is dependent upon the magnitude of the driving force and on the level of damping within the vibratory system. In order to accurately predict the primary amplitude it is therefore necessary to have a good estimate of both of these parameters. Figure 7.24 shows the predicted linear relationship between primary amplitude and electrostatic drive force for a 35μm thick device and different levels of damping.

It is intended that the gyroscope will be driven electrostatically using electrodes located around the circumference of the ring (section 7.2). The electrostatic force (F) generated at any given electrode is a function of the electrode spacing (x), cross sectional area (A) and the sinusoidal drive voltage (V):

$$F = \frac{\varepsilon_o \varepsilon_r A V^2}{x^2} \qquad (7.1)$$

where ε_o is the permitivity of free space and ε_r is the relative permitivity of the medium between the electrodes. In this case the medium is either air or a vacuum and so this term (ε_r) is approximately unity and can be neglected. In order to prevent the drive force assuming twice the frequency of the drive voltage (due to the V^2 relationship) it is necessary to superimpose a DC bias (greater than the drive voltage, V) on to the sinusoidal component. This can be done either by biasing the electrode itself, or the entire ring. The mechanism of electrostatic actuation is situation is only stable for deflections less than $^1/_3$ of the total electrode spacing.

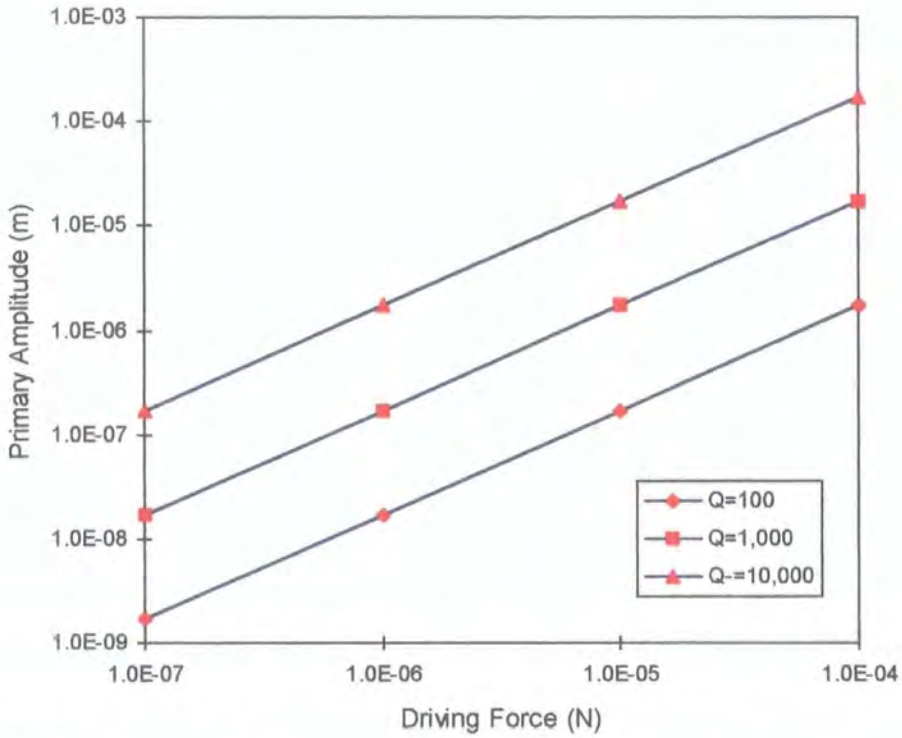

Figure 7.24. *Amplitude vs. drive force for different levels of damping.*

From equation 7.1, the magnitude of drive force that can be generated has been estimated in the region of 10^{-5} N. This was calculated for a 35μm thick structure with electrode spacings of 10μm, a drive voltage of $50V_{pk}$ and bias voltages of $50V_{dc}$. An estimate of the damping level has been found from the preliminary test results of chapter five. Q-factors of approximately 1000 have been found for nickel resonators under reduced atmospheric pressures. Using these figures an estimate of the primary amplitude of vibration can be found from figure 7.24 to be of the order of 1.0 μm.

7.3.2.1.4 Secondary Response

The magnitude of the secondary response (A_s) due to a constant rate of turn (Ω in rads/s) can be found from the following equation [81] (see appendix D):

$$A_s = \frac{2kQ_sA_p\Omega}{\omega} \qquad 7.2$$

where A_p is the amplitude of the primary motion, k is the gyroscopic coupling factor which is approximately equal to 1.0 for a ring, Q_s is the Q-factor of the secondary motion and ω is the angular frequency of both primary and secondary modes. Thus for a primary amplitude of 1.0μm, a Q-factor of 1000 and a resonant frequency of 36.2 kHz, the secondary response of the nickel ring gyro would be to a first approximation 1.5×10^{-4}μm/(°/s).

In order to calculate the theoretical gyro sensitivity it is necessary to know the minimum resolvable capacitance change that can be detected using the sense electrodes (figure 7.6). In other devices detectable capacitance changes of the order 30aF have been reported [82]. For the ring gyro, this equates to a minimum resolvable ring deflection of 0.7nm (appendix E). This to a first approximation gives a maximum theoretical resolution of 4.75°/s. This figure relates to 0.03°/s for the START cylinder gyro; 0.01°/s for the BAe VSG 2000 ring gyroscope; and 0.2°/s for the BAe silicon ring gyro (section 6.4.2). The greater resolution of the START gyro and VSG 2000 may be expected, as they are both macroscopic devices that benefit from greater mass, larger drive amplitudes and electrode areas. A better comparison can be made with the BAe silicon ring gyro, which again shows greater resolution. Once more this can be accounted for, as the Q-factor of the resonator directly contributes to the sensitivity of the device *cf.* equation 7.2. Silicon is typically a better resonator material than nickel and can routinely exhibit 1-3 orders of magnitude greater Q.

7.3.2 Design Modifications

The initial design (version 1) of the gyroscope was later modified to allow location of the drive and sense electrodes around the outer circumference of the ring. This design change was made to facilitate easy access to the electrodes for electrical connection. To achieve this, the support structure was redesigned so that the ring was supported from its centre. This made for an overall more compact design and is shown in figures 7.25 and 7.26. As the dynamic properties of this second design are principally unchanged from version 1, the resonant modeshapes produced from FE-analysis were comparable. The cos2θ and sin2θ mode shapes of this structure are shown in figures 7.27 and 7.28.

A third structure was also investigated. This structure employed a modified support arrangement and is shown in figures 7.29 and 7.30. Again as the ring remains the main dynamic element, the resonant modeshapes generated from the FE analysis were found to be equivalent to those of versions 1 and 2. The cos2θ and sin2θ mode shapes of this structure are shown in figures 7.31 and 7.32.

7.3.3 Silicon Ring Gyroscope

This section serves as a comparison between the two similar ring gyroscope structures being developed concurrently at the Universities of Durham and Newcastle-upon-Tyne. Although both gyroscopes employ the same basic design, the two devices utilise widely different structural materials and fabrication procedures. In addition the specific dimensions and geometries of the two devices differ, as the development and analysis of each progressed independently. However as each device has many features in common, it is still useful to compare their respective predicted performances.

Preliminary comparison of the predicted primary resonant frequencies of the two devices (both 4mm ring structures) shows a considerable deviation; 36kHz for the nickel device and 58kHz for the silicon device [81]. Although it would be expected that

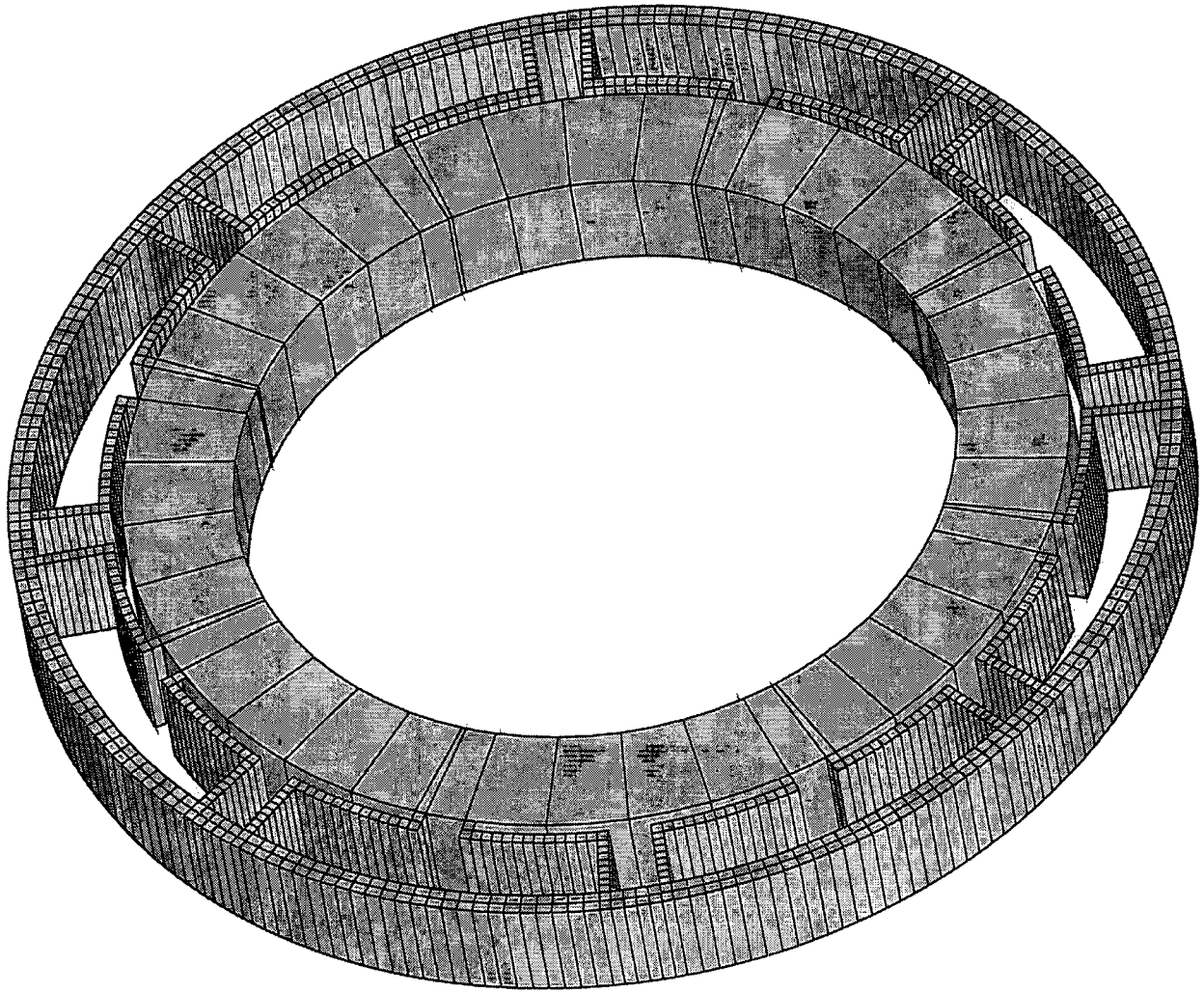

LINEAR

STATICS

ROTATION

X = 330

Y = 330

Z = 330

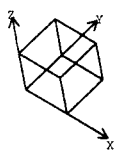

TITLE

Figure 7.25. *3D model of version 2..*

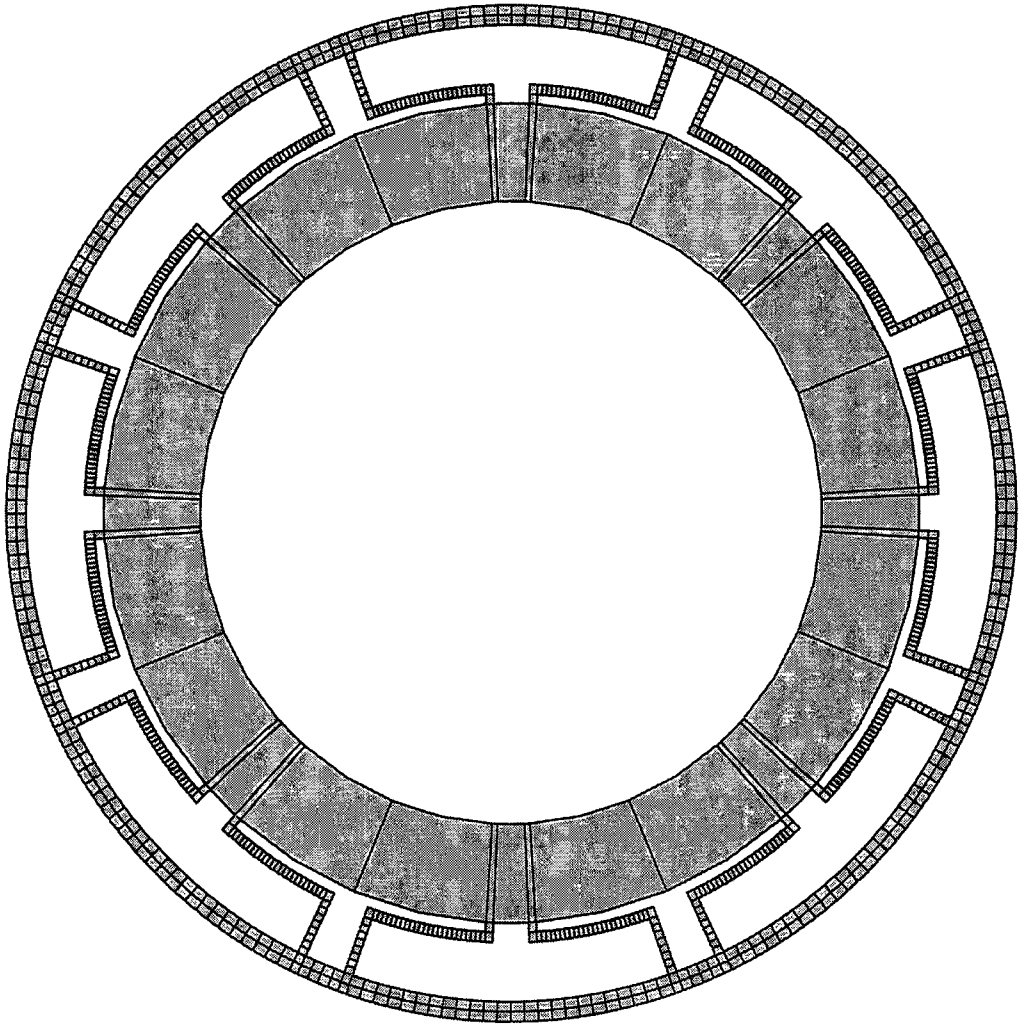

LINEAR

STATICS

ROTATION

X = 0

Y = 0

Z = 0

Y

X

Z.

TITLE ***Figure 7.26.*** *2D model of version 2.*

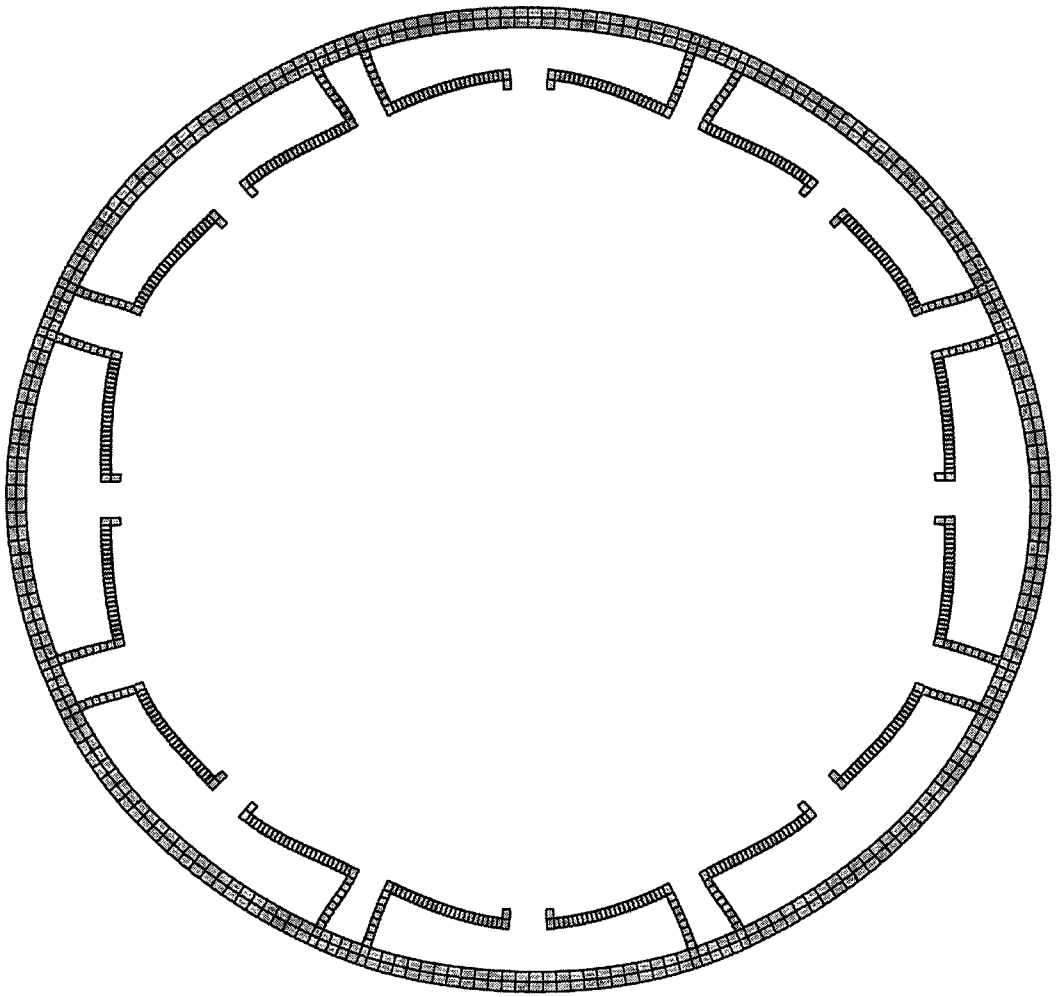

MODES-FREQ
MODE 1
0.580 E 5
(HZ)

ROTATION
X = 0
Y = 0
Z = 0

Y
X
Z.

TITLE

Figure 7.27. *Primary mode shape of version 2.*

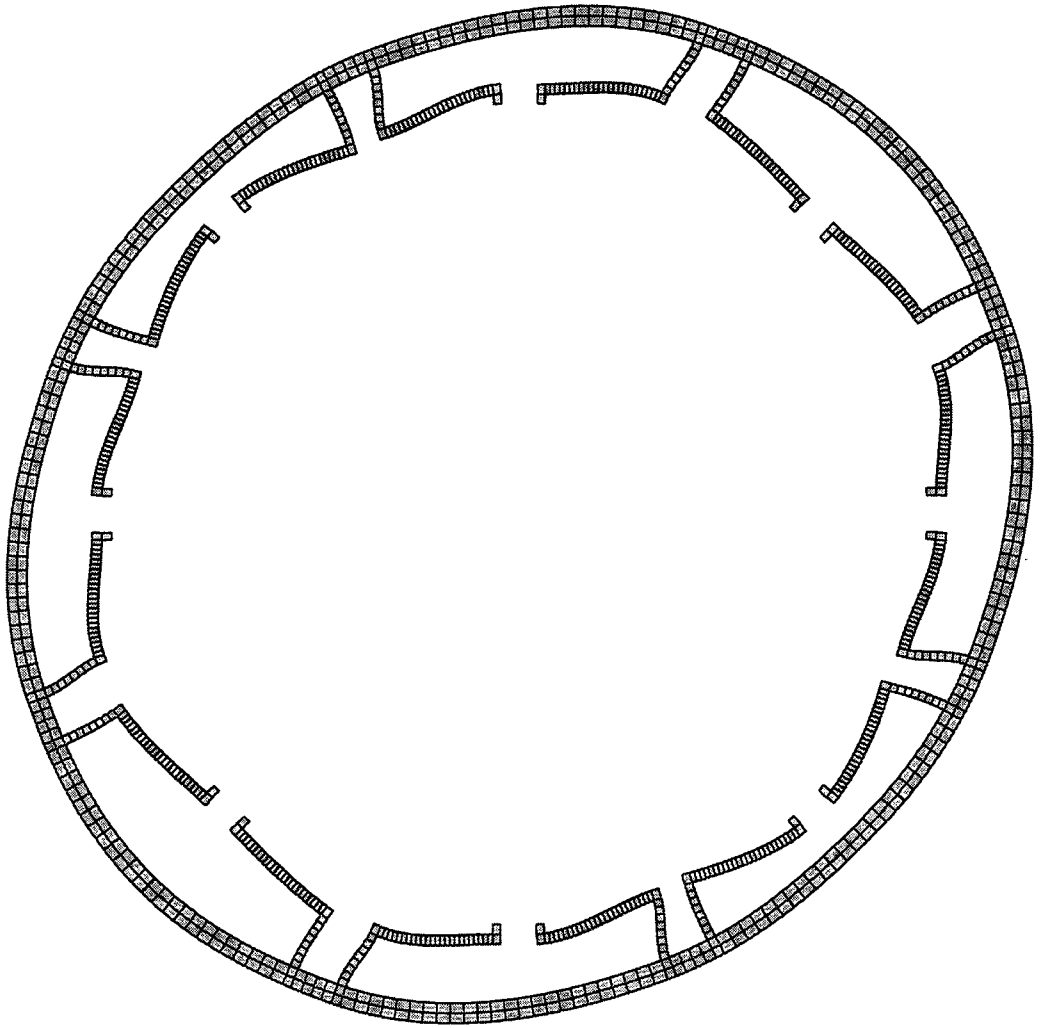

MODES-FREQ
MODE 2
0.581 E 5
(HZ)

ROTATION
X = 0
Y = 0
Z = 0

Y
X
Z.

TITLE ***Figure 7.28.*** *Secondary mode shape of version 2.*

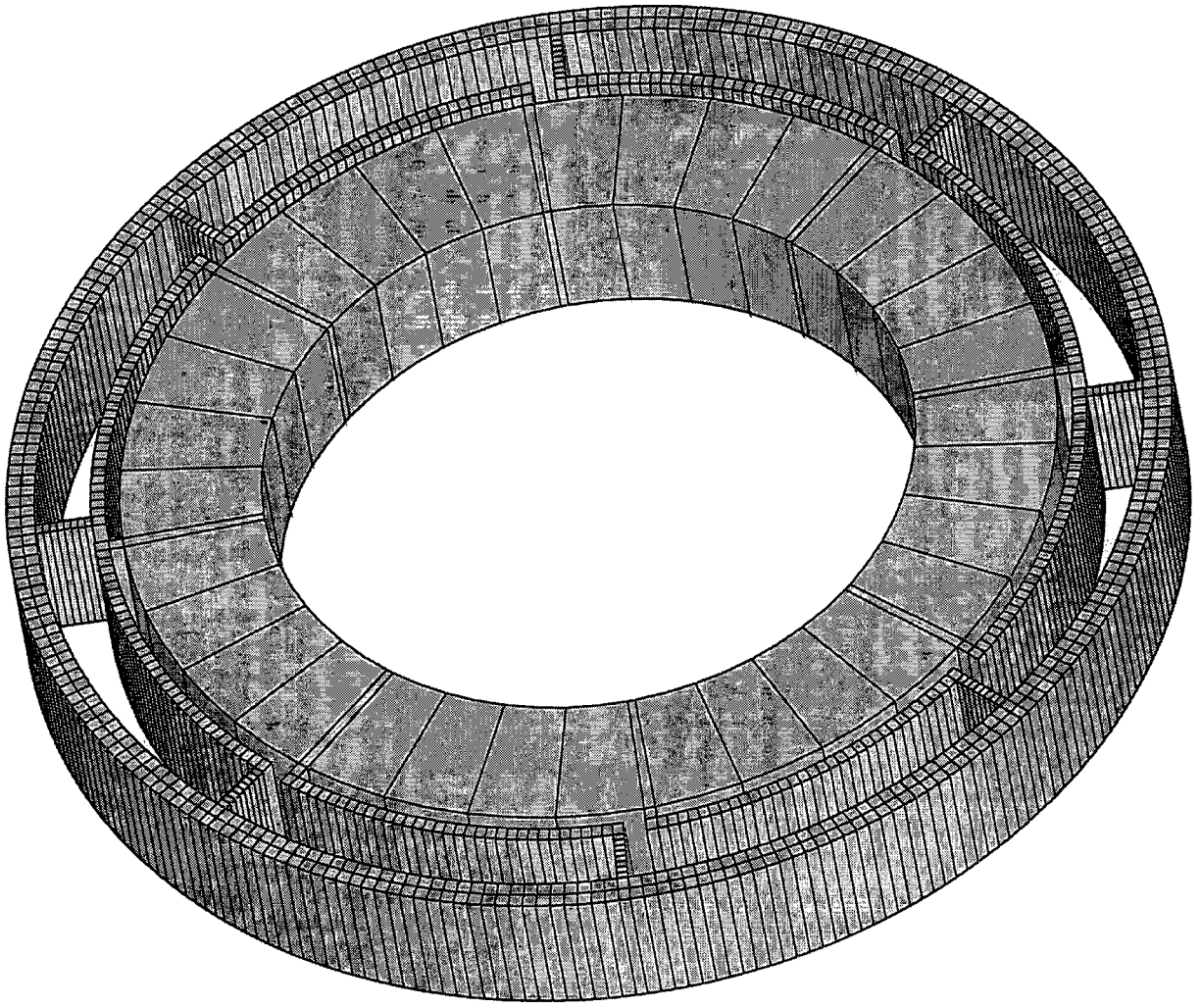

LINEAR

STATICS

ROTATION

X = 330

Y = 330

Z = 330

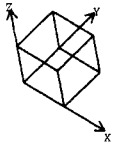

TITLE ***Figure 7.29.*** *3D mode of version 3.*

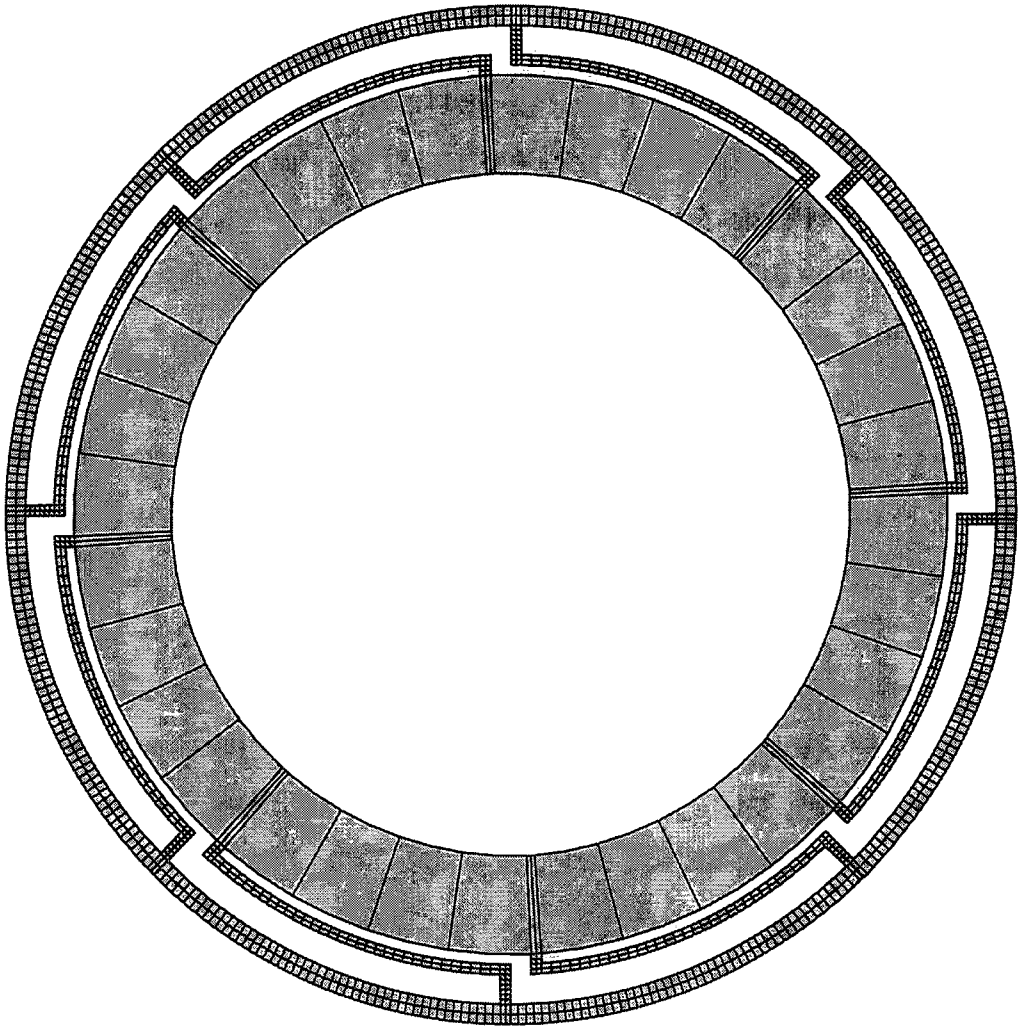

LINEAR

STATICS

ROTATION

X = 0

Y = 0

Z = 0

Y

X

Z

TITLE

Figure 7.30. *2D mode of version 3.*

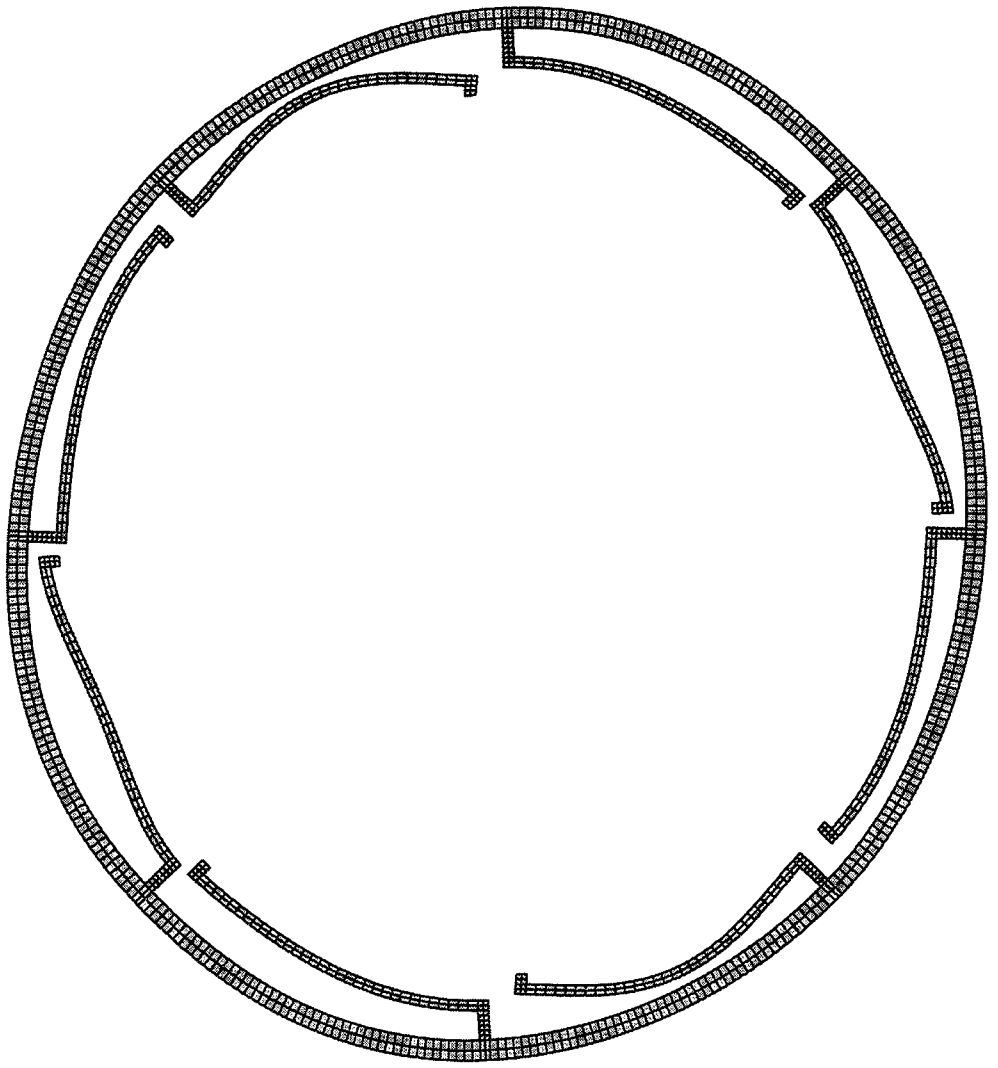

TITLE ***Figure 7.31.*** *Primary mode shape of version 3.*

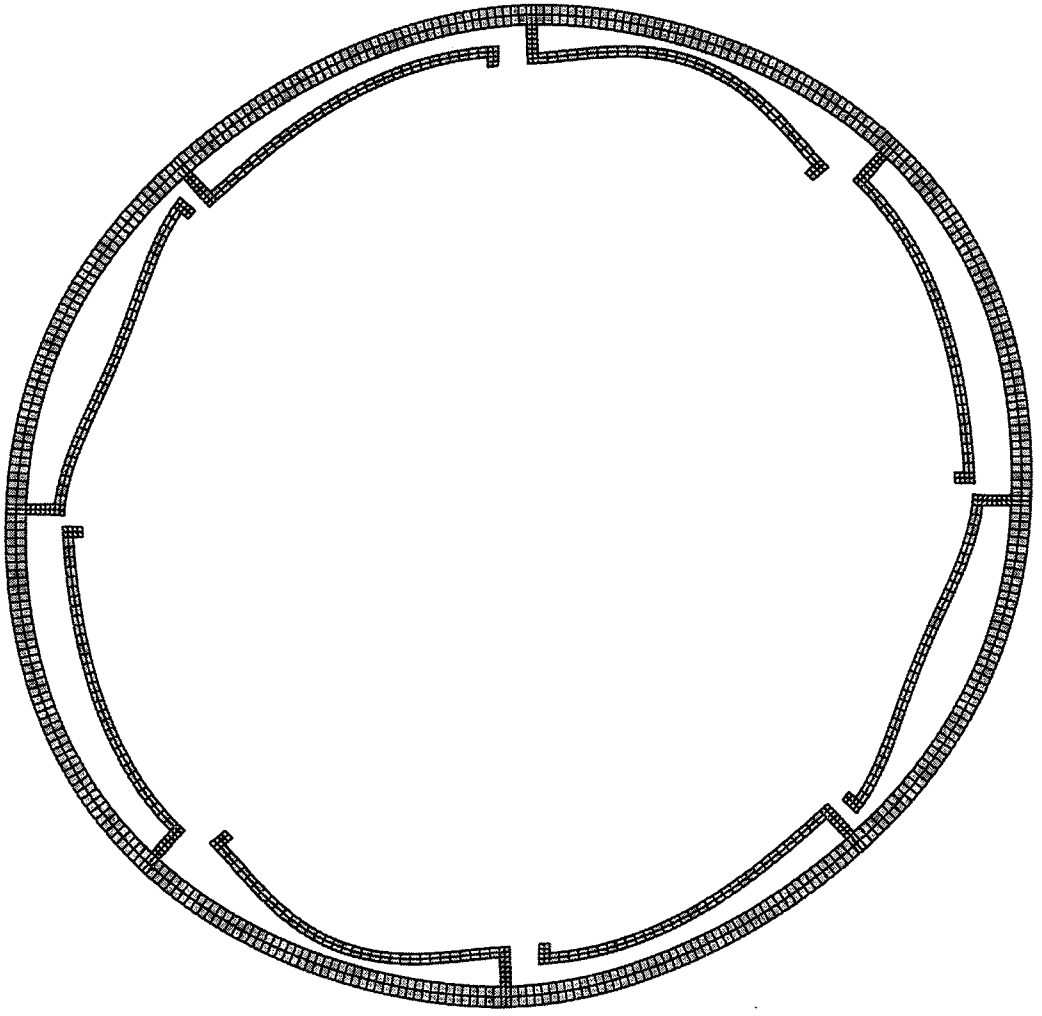

TITLE ***Figure 7.32.*** *Secondary mode shape of version 3.*

the silicon structure would have a higher resonant frequency due to the change of material properties, it would be expected that this would be approximately 1.9 times greater than the nickel device. This would give an expected resonant frequency of 68.8kHz. The remaining discrepancy of 10.8kHz is most likely caused by the small geometrical anomalies between the two devices, which can have a significant impact on dynamic properties.

The mechanisms of motion excitation and detection of the two gyros differs considerably. As discussed in section 7.3.2.1.3, motion of the nickel gyro is driven electrostatically and detected capacitively. In this way it is expected that primary amplitudes of the order 1.0μm are achievable. The silicon gyro is operated electromagnetically using Lorentz drive and detection principles and primary amplitudes of 0.5-2.5μm are expected.

Similarly the secondary response of the silicon gyroscope is comparable to that predicted for the nickel gyro. The predicted response of the silicon gyro is given as $3.6x10^{-5}$μm/(°/s) for a 0.75μm primary drive amplitude and pessimistic Q-factor of 500. This equates to a response of $9.6x10^{-5}$μm/(°/s) at a primary amplitude of 1.0μm and a Q-factor of 1000. This compares well to the value of $1.5x10^{-4}$μm/(°/s) calculated for the nickel gyro under the same conditions. It would be expected, however, that the sensitivity of the silicon device might be greatly increased if the Q-factor of the actual device was found to be comparable to that of other silicon resonators in the 10^3-10^6 region.

7.3.4 Summary

The finite element analysis of the proposed gyroscope structure has identified the required operational modes, and demonstrated the required dynamic behaviour. In addition the analysis has allowed prediction of the vibratory amplitudes and responses for particular levels of drive force. This data is summarised in table 7.3, which refers to the response predicted for a gyro with 10μm electrode gaps and drive conditions of 50V bias and $50V_{pk\text{-}pk}$ drive voltage.

Resonant frequency	*36.2 kHz*
Primary Amplitude	*1.0μm*
Resolution	*4.75 °/s*

Table 7.3. *Summary of gyro operating characteristics.*

Chapter Eight
Ring Gyroscope: Fabrication and Testing

This chapter details the fabrication and testing of version 1 of the ring gyroscope devices described and modelled in chapter seven. The fabrication sequence specific to the gyroscope structures is firstly described then the later sections present optical and electrical experimental results.

8.1 Gyro Fabrication

The nickel ring gyroscopes were fabricated using the general techniques described in chapters three and four. The specific fabrication sequence is presented in figure 8.1 and discussed below.

The first stage of the fabrication process involved the thermal oxidation of the silicon substrate. This was required to provide electrical isolation between the ring and the drive and sense electrodes. A 4 hour wet oxidation was typical to provide an oxide layer thickness of approximately 1.0μm.

In the second stage, the base electrodes were deposited to define the areas of the nickel structure that would ultimately be in mechanical contact with the substrate. This was necessary to provide a conducting surface for electrodeposition of the mechanical elements. Chromium (100Å) / gold (1000 Å) layers were evaporated using a Varian dual source e-beam evaporator.

The third stage involved the deposition and patterning of the sacrificial layer. Titanium films were sputtered up to a thickness of 1-4μm using a Chemex RF sputter unit at rates of approximately 1.0μm/hour. The titanium was patterned to open contacts to the base electrodes, and to blanket the remaining substrate surface to allow for electrical contact. The thickness of this sacrificial determined the final clearance of the ring from the substrate.

Stage four involved the production of the sacrificial plating mould. This produced a negative mould of the gyroscope into which nickel was electroformed. The mould was also used to blanket the remaining substrate surface to prevent deposition elsewhere.

In stage five all the nickel elements were electrodeposited through the plating mould.

After the removal of the plating mould, the final stage of the fabrication sequence involved the selective removal of the titanium sacrificial layer. This was achieved through a long soak in 10% HF solution, and yielded the final released structure.

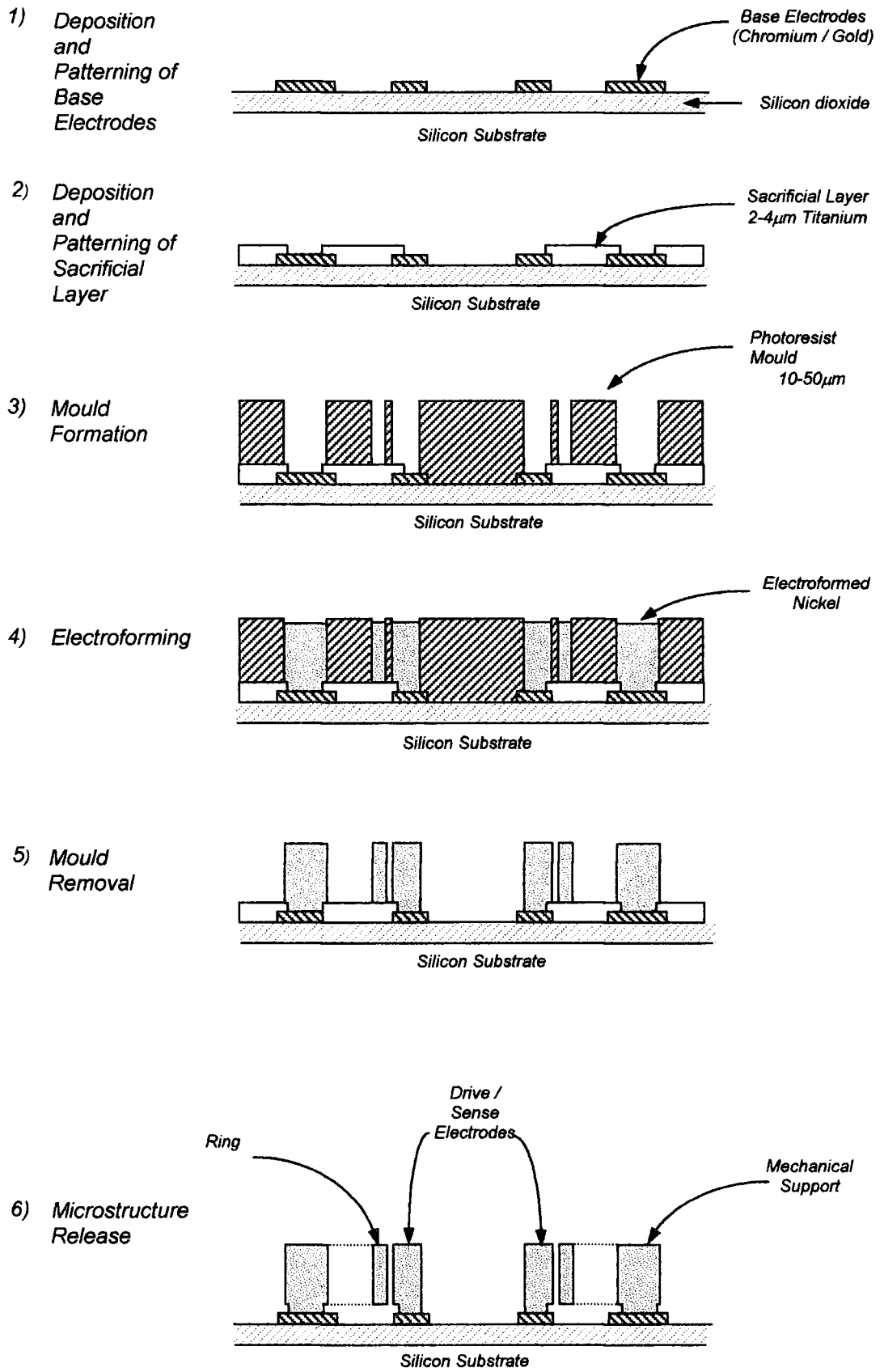

Figure 8.1 *Fabrication of nickel ring gyroscopes.*

Figures 8.2 and 8.3 present SEM images of various sections of a complete ring gyroscope structure. These included magnified images of the ligament structure, electrode arrangements and the suspension of the ring above the wafer surface.

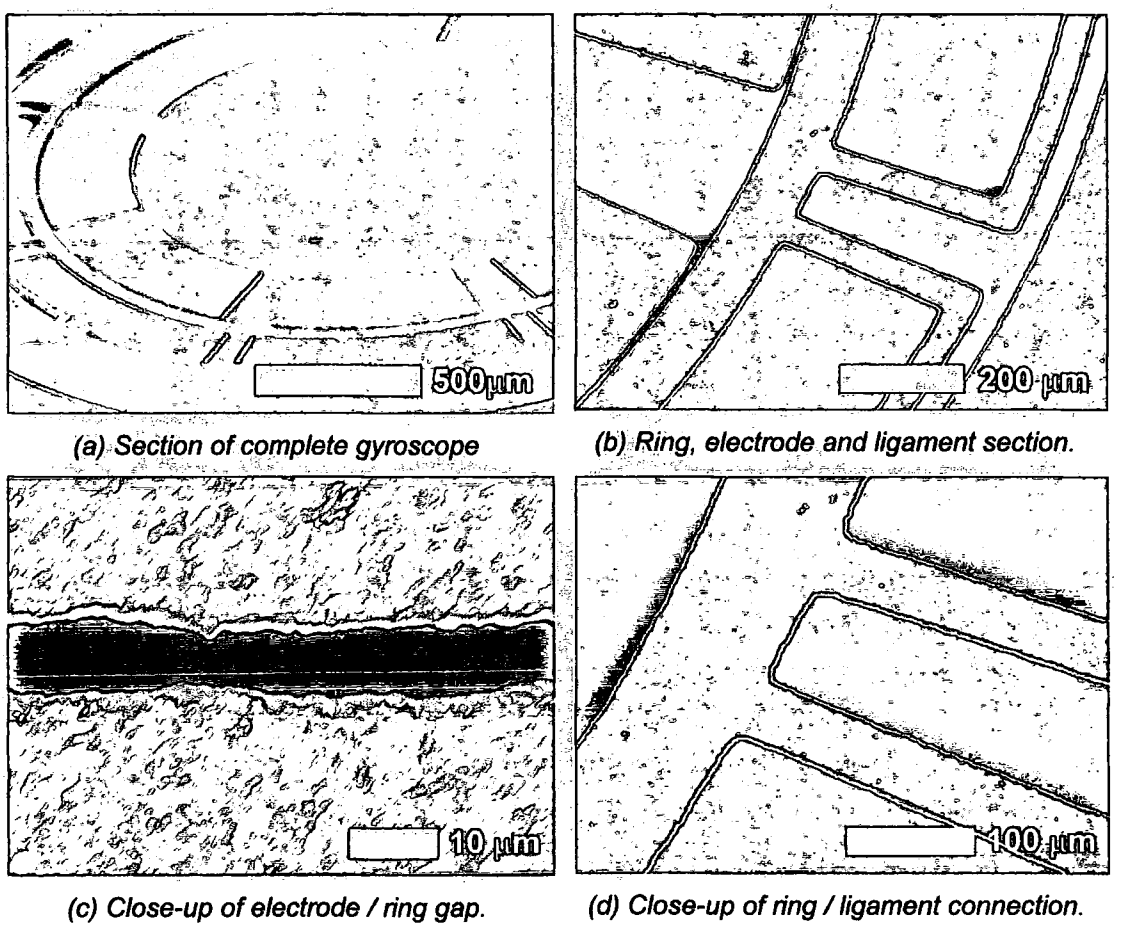

(a) Section of complete gyroscope

(b) Ring, electrode and ligament section.

(c) Close-up of electrode / ring gap.

(d) Close-up of ring / ligament connection.

Figure 8.2. *SEM Images of the nickel ring gyroscope.*

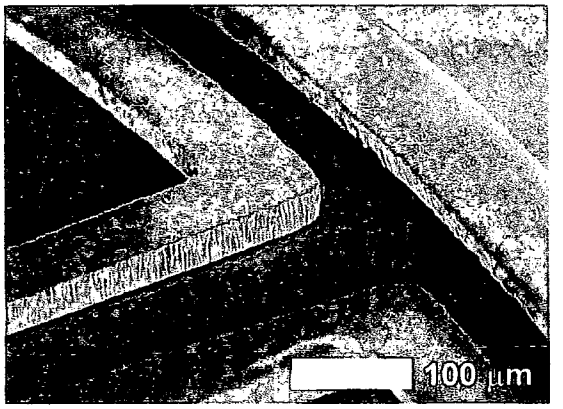

(a) Free-standing ligaments.

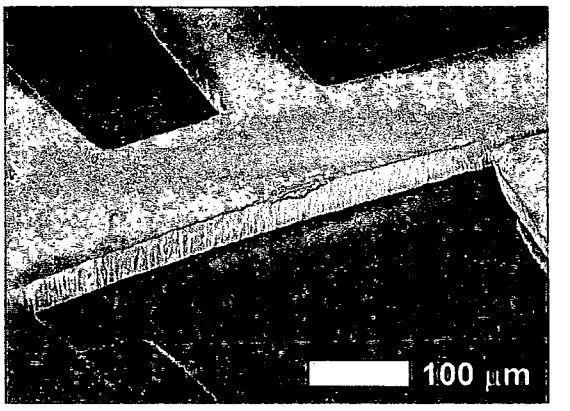

(b) Close-up of free-standing ring.

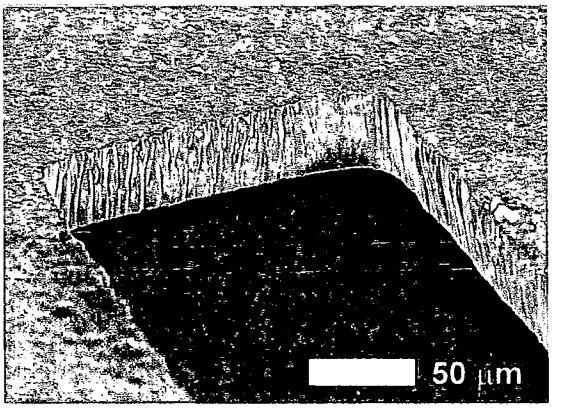

(c) Suspended ring section.

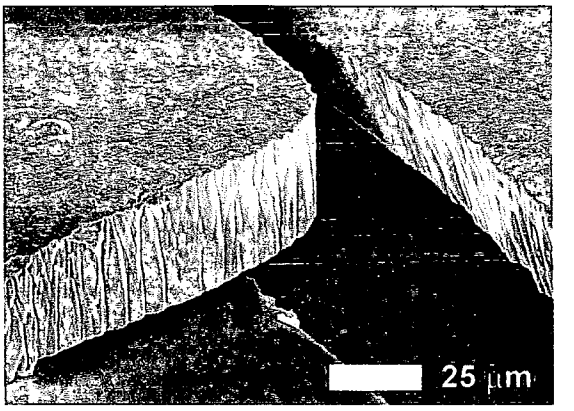

(d) Close-up of self-supporting structure.

Figure 8.3. *Close-up images of gyro elements.*

8.2 Optical Testing

In a practical arrangement the motion of the gyroscope will be driven and detected 'on-chip' using electrostatic and capacitive mechanisms as described in chapter seven. Detection of motion in this way can be very problematic and so prior to electrical testing, the motion of the gyro structure was excited externally and determined optically using the experimental set-up described previously in chapter five. Due to complications associated with the measurement system, only out-of-plane motion (which is ideally suppressed in gyro operation) could be evaluated. This data, however, would still supply useful information and provide a means of assessing performance prior to electrical testing. The following subsections present the optical data gathered including comparison with FE-predictions.

8.2.1 Frequency Response

Figures 8.4 to 8.6 show the experimentally derived frequency response functions of the first four (out-of-plane) resonances of the 27μm thick ring structure, as determined at 0.05mbar ambient pressure. A Nyquist plot combining this data is also presented in figure 8.7. From these graphs, values of resonant frequency and damping were determined and this data is compiled in table 8.1. Also presented are the predicted frequencies (see section 7.3.2.1.1) for comparison.

	Mode 1	Mode 2	Mode 3	Mode 4
Frequency	9.893 kHz	11.349 kHz	11.418 kHz	13.904 kHz
Frequency (FEM)	11.61 kHz	13.28 kHz	13.28 kHz	16.17 kHz
% error	17.4 %	17.01 %	16.31 %	16.30 %
Drive Voltage	1V	5V	5V	5V
Amplitude	400nm	77nm	200nm	11nm
Q-factor	1550.7	1659.2	1572.7	1407.3

Table 8.1. *Summary of optical measurements and simulation results.*

It can be seen that the errors between the measured and predicted resonant frequencies are quite large but are relatively constant between 16.3 and 17.4%. It is likely that these errors are generated within the simulation model, which is not ideal. Material properties were set to those of bulk crystalline nickel (as those of the electrodeposited nickel are not known) and any variations in density, Young's modulus or Poisson's ratio would cause a deviation of the predicted resonant frequencies.

It is possible however, to compare the structural properties of the model to the device, removing the material dependent influence, by comparing the ratio of frequencies (i.e. the ratio of the frequency of mode 2 to that of mode 1, and the ratio of mode 3 to mode 1). This data is presented in table 8.2 and shows low errors between actual and predicted values.

	f_{mode2}/f_{mode1}	f_{mode3}/f_{mode1}	f_{mode4}/f_{mode1}
Experimental	*1.147*	*1.154*	*1.405*
FEM	*1.147*	*1.147*	*1.400*
% error	*0.00 %*	*0.61 %*	*0.36 %*

Table 8.2. *Comparison of Experimental and FEM results.*

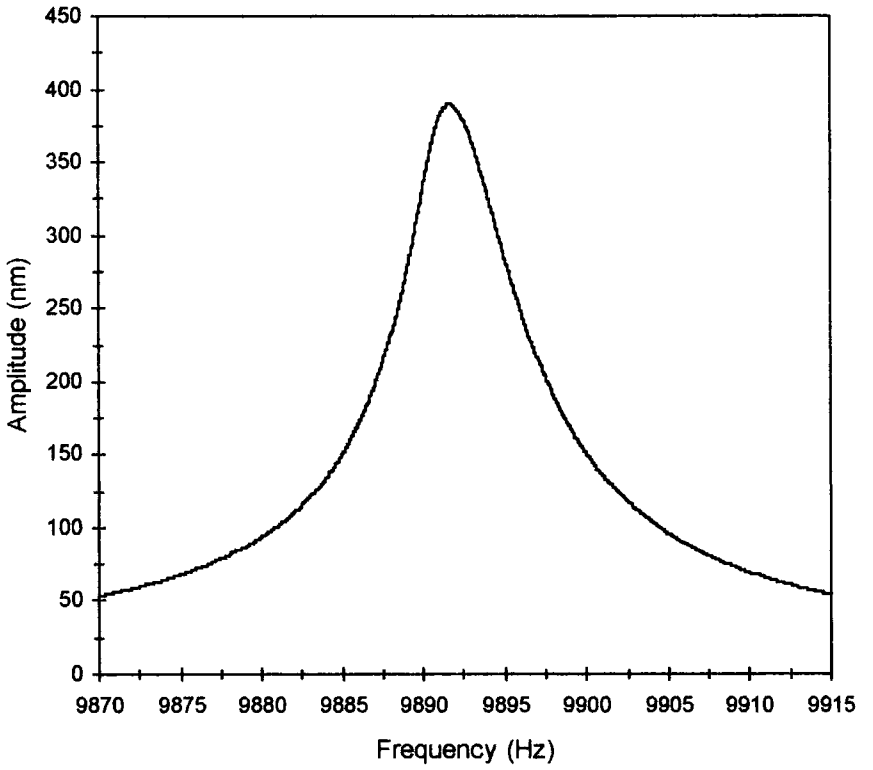

Figure 8.4a. *Frequency response of first flexural mode shape.*

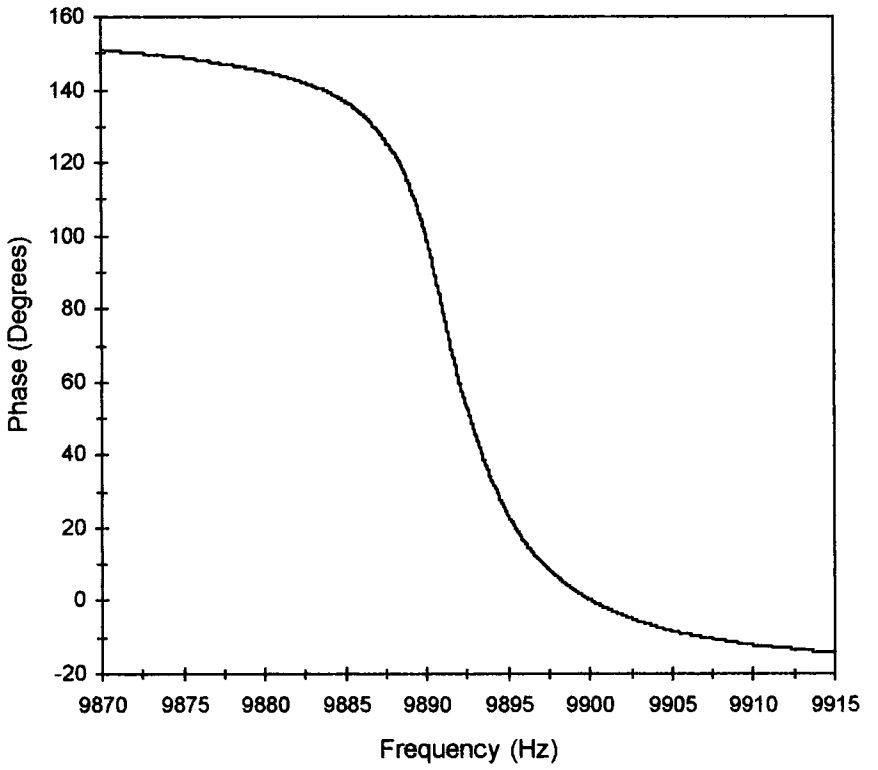

Figure 8.4b. *Phase response.*

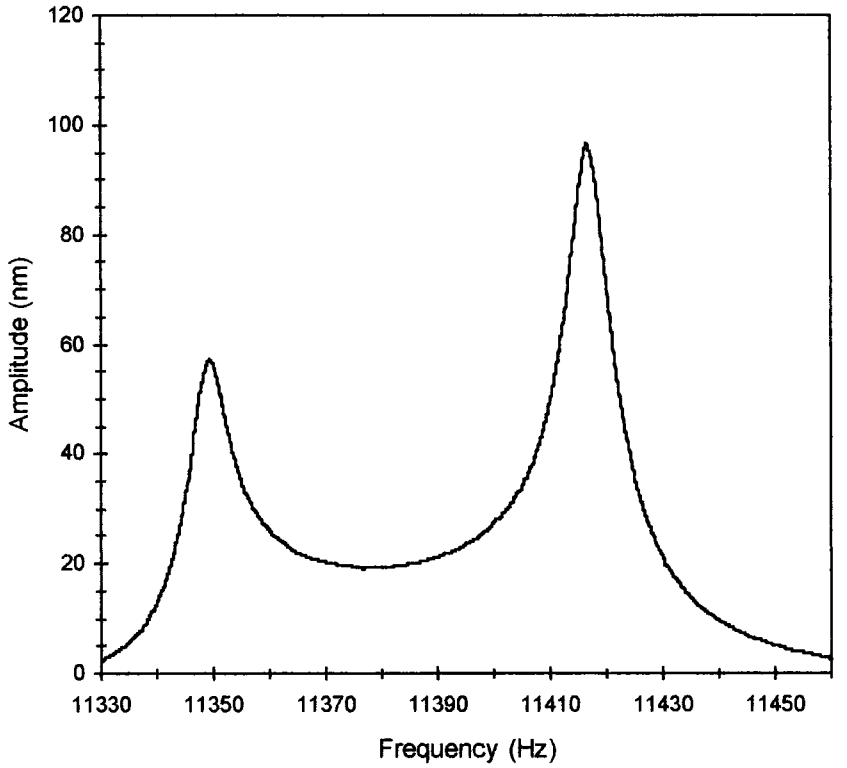

Figure 8.5a. *Amplitude frequency response of second and third modes.*

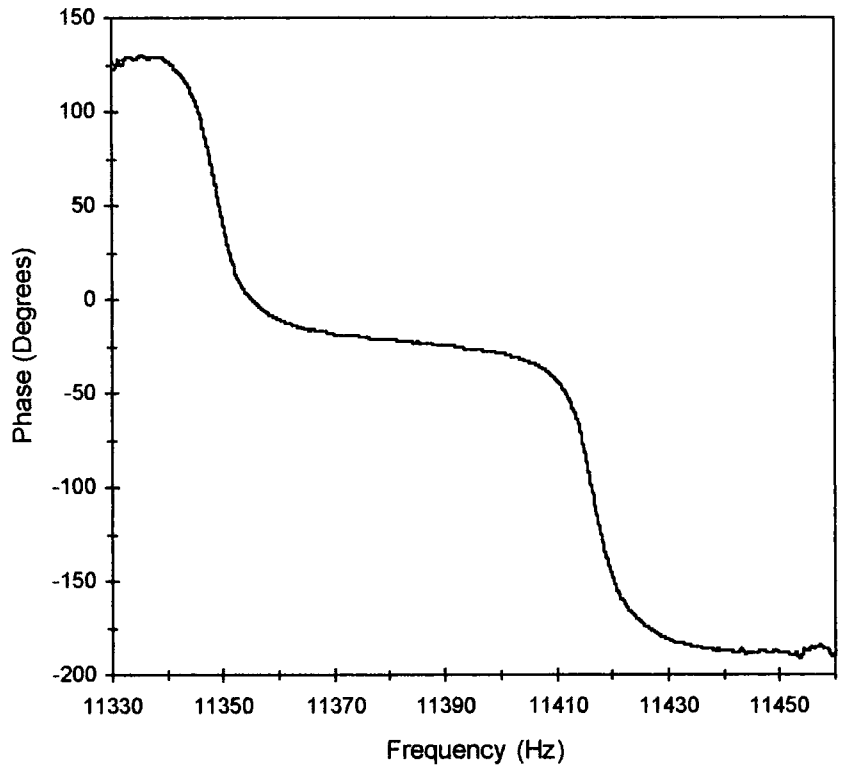

Figure 8.5b. *Phase response.*

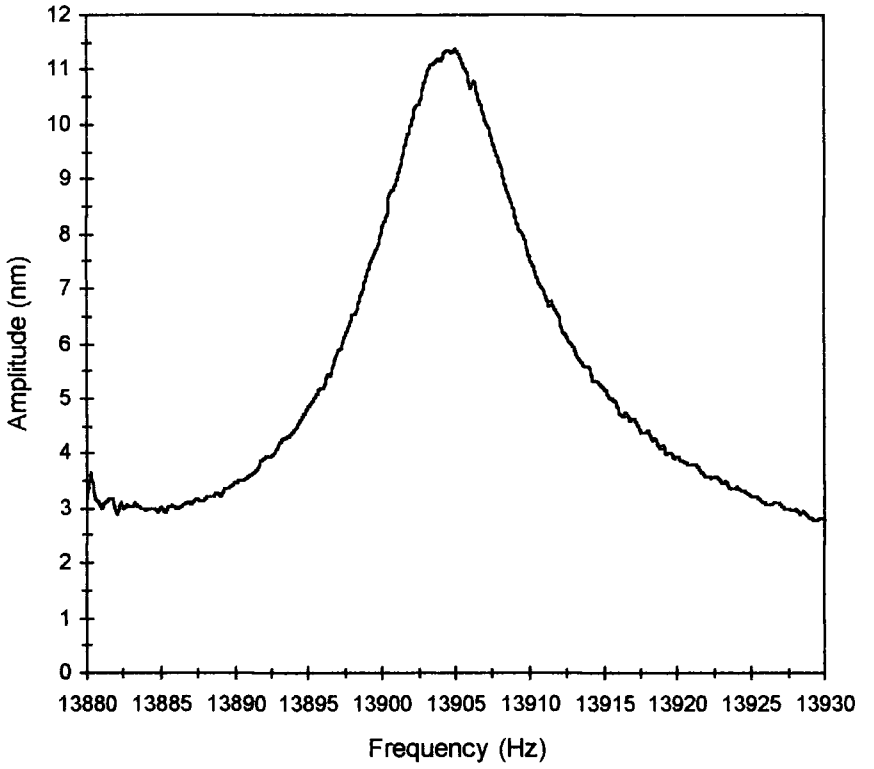

Figure 8.6a. *Frequency response of fourth mode.*

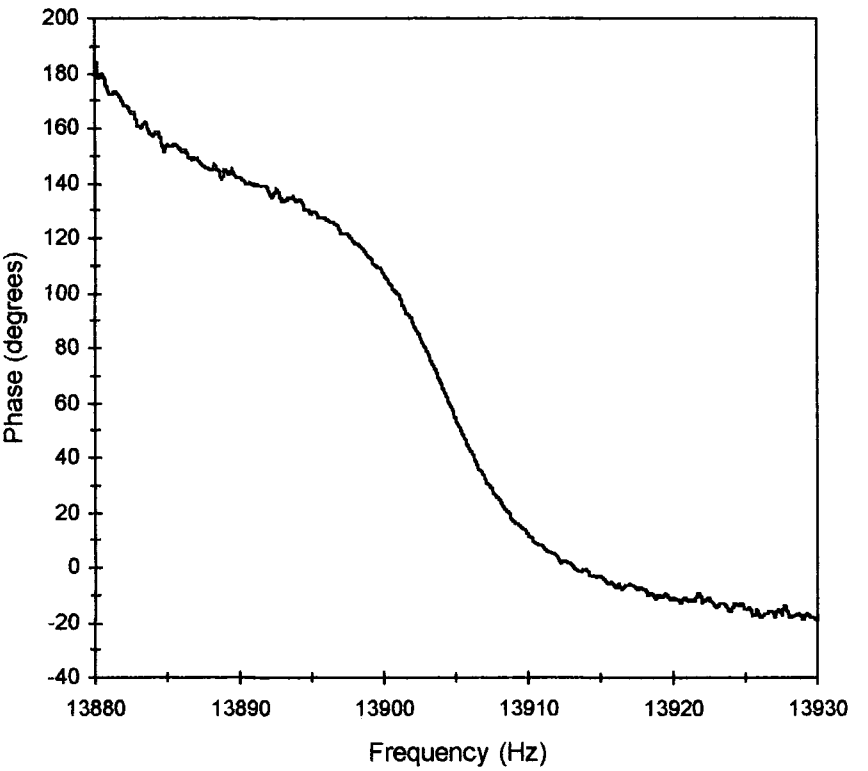

Figure 8.6b. *Phase response.*

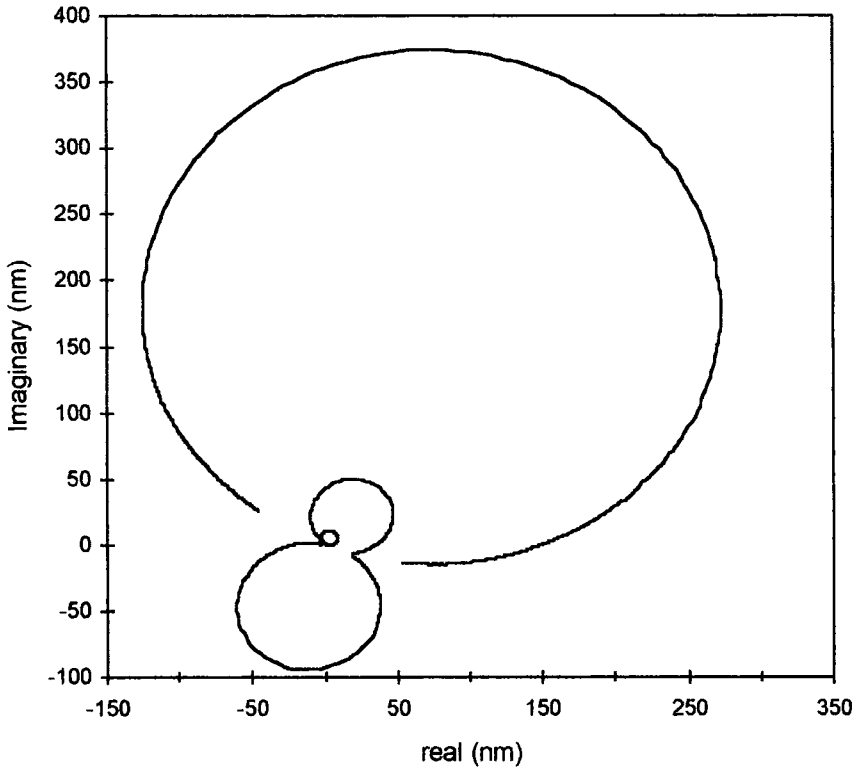

Figure 8.7. *Nyquist plot of first four out of plane resonances.*

8.2.2 Resonant Mode Shapes

As in chapter five, a series of optical measurements were used to determine the resonant mode shapes of the vibrating structure. Experimentally derived mode shapes (in this case displacement versus angular position) of the gyro structures are shown in figures 8.8 to 8.11. Also shown are additional curves showing FE predictions and adjusted curves that offer the best fit to experimental data. This data is summarised in table 8.3.

	Mode 1	Mode 2	Mode 3	Mode 4
Mode shape (FEM)	1	$\cos\theta$	$\sin\theta$	$\cos 2\theta$
Mode shape (best fit)	1	$\cos(\theta+4.0°)$	$\sin(\theta+21.7°)$	$\cos(2\theta-2.9°)$

Table 8.3. *Comparison of Experimental and FEM results*

The high correlation between the experimental and simulation data displayed in these graphs confirms that the structure is behaving as expected. A particular point to note is the phase difference between the experimentally derived mode shape and the theoretical model of figure 8.10. Ideally, this mode, and the previous mode of figure 8.9 should be spatially separated by 90° and completely uncoupled. However, due to mass asymmetries within the structure, it can be seen that their relative positioning deviates from this ideal. Mass asymmetry also leads to these two 'identical' modes having slightly different resonant frequencies. Comparison between the theoretical and experimental data shows a frequency split of approximately 67Hz, and a spatial separation of 107°.

The mass asymmetries within this device have two origins, both of which stem from the fabrication process; firstly, non-symmetries of the mask template, and secondly, non-linear mass distribution within the electroforming process. Regardless of these minor points, the high correlation between the experimental and simulation results provide the model with a great deal of credit, and provides confidence that the structure will also behave as predicted in the operational (in-plane) modes of vibration.

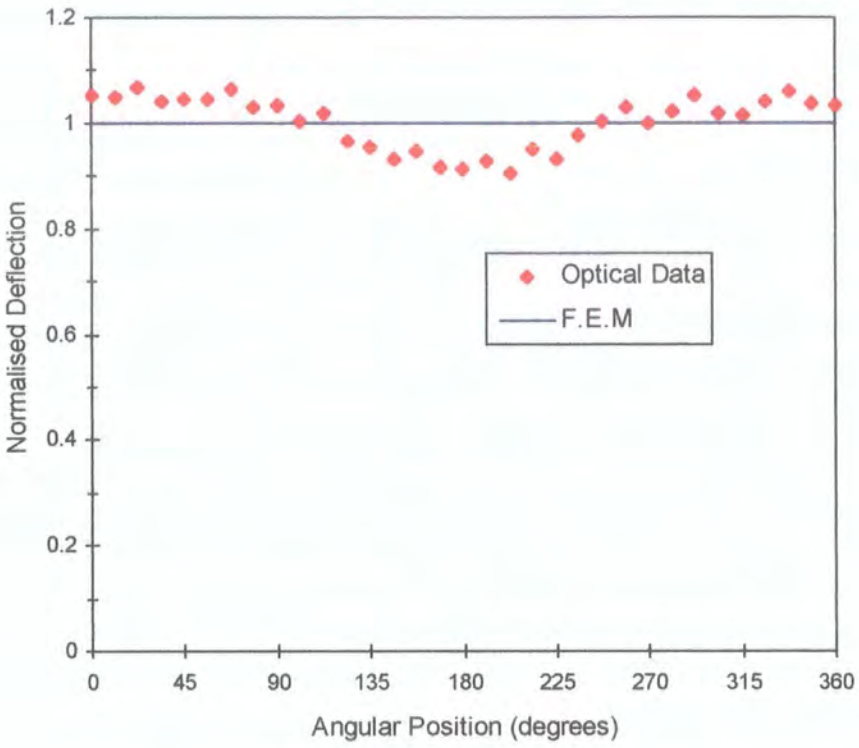

Figure 8.8. *Out-of-plane displacement as a function of radial position for first mode of vibration.*

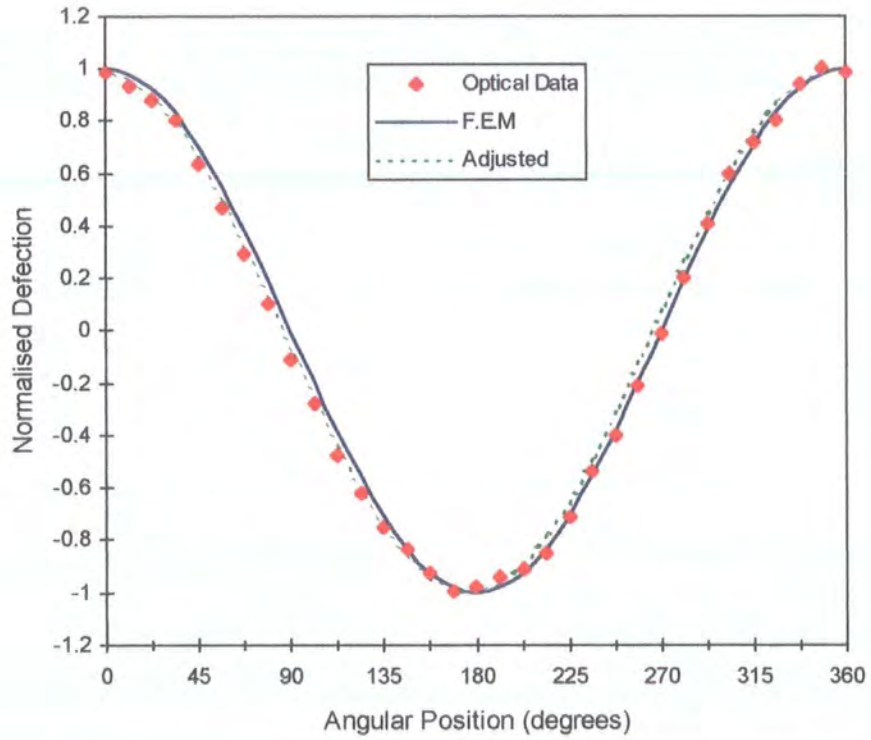

Figure 8.9. *Out-of-plane displacement as a function of radial position for second mode.*

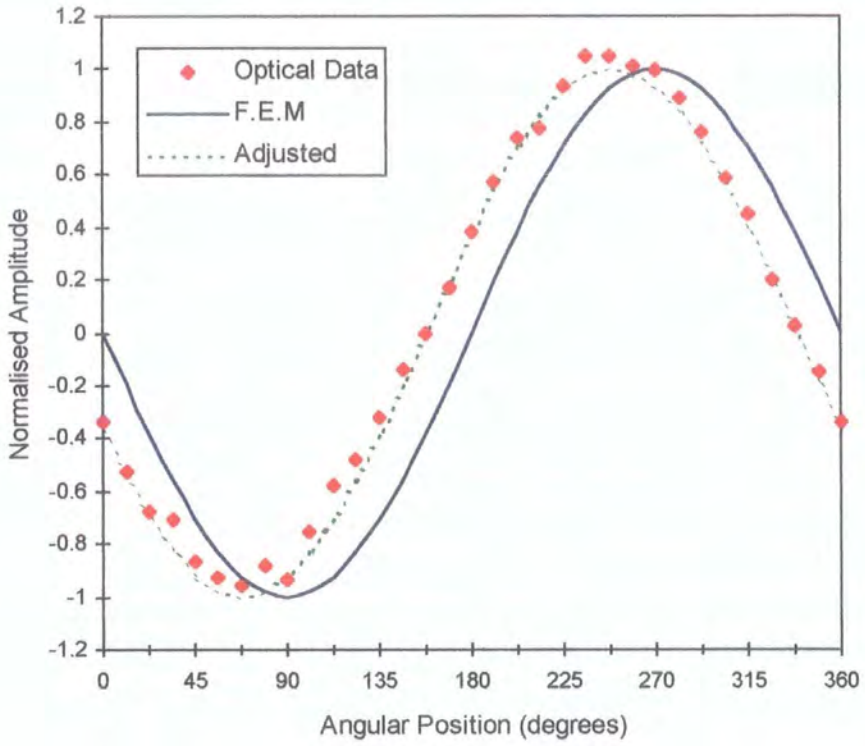

Figure 8.10. *Out-of-plane displacement as a function of radial position for third mode.*

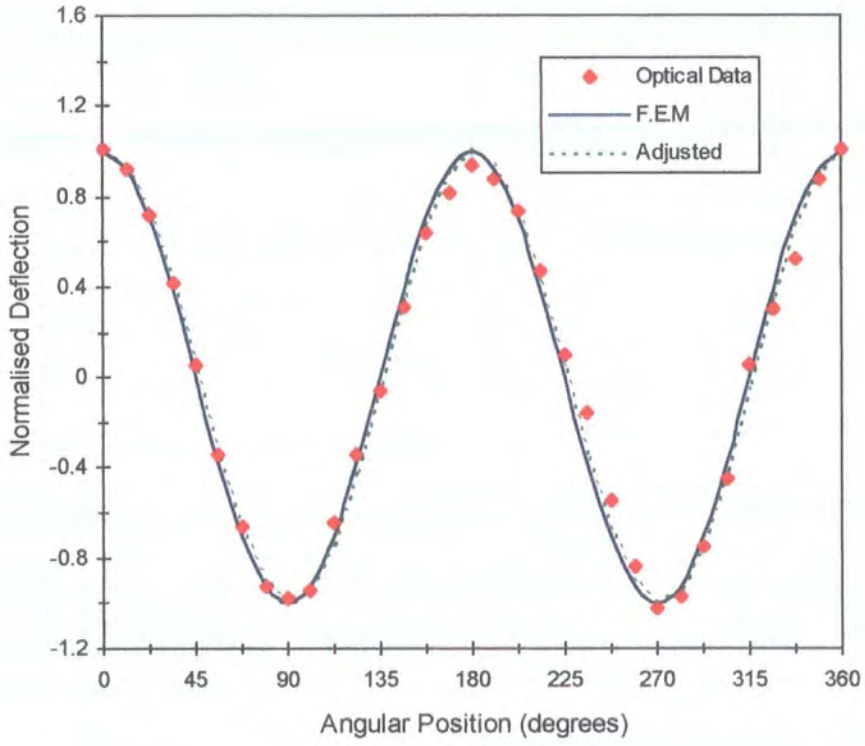

Figure 8.11. *Out-of-plane displacement as a function of radial position for fourth mode.*

Using STAR modal analysis software, the motion of the vibrating ring surface was animated in a Windows based environment. Figures 8.12 to 8.15 show the still frame animation of the first four out-of-plane modes of the ring.

8.2.3 Summary of Optical Data

Optical examination of the ring structures has shown excellent agreement between experimental observations and the simulation model. This has provided confidence in that the devices are functioning as expected and also in the accuracy of the FE model.

The results have also emphasised the problem of frequency separation between 'identical' modes of the structure. The two operational modes of the gyroscope are similarly 'identical' and any frequency separation would lead to loss of performance. This is, however, inevitable due to mass asymmetries within the device and like other such devices a process of 'trimming' would be necessary to match modes.

MODE 1
FREQUENCY = 9.893 kHz
Q-FACTOR = 1550.7

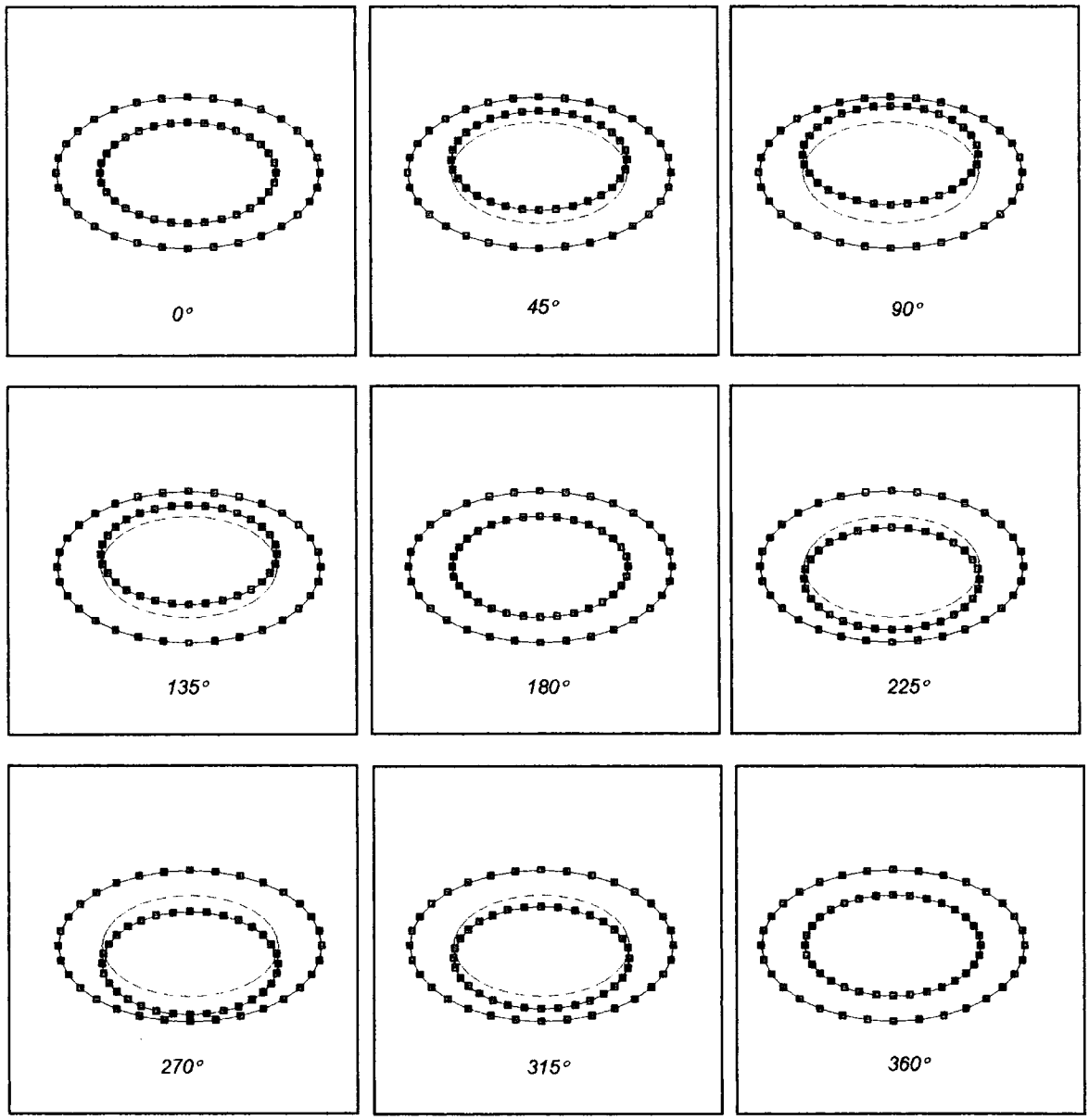

Figure 8.12. *Still frame animation of first out-of-plane mode shape.*

MODE 2
FREQUENCY = 11.349 kHz
Q-FACTOR = 1659.2

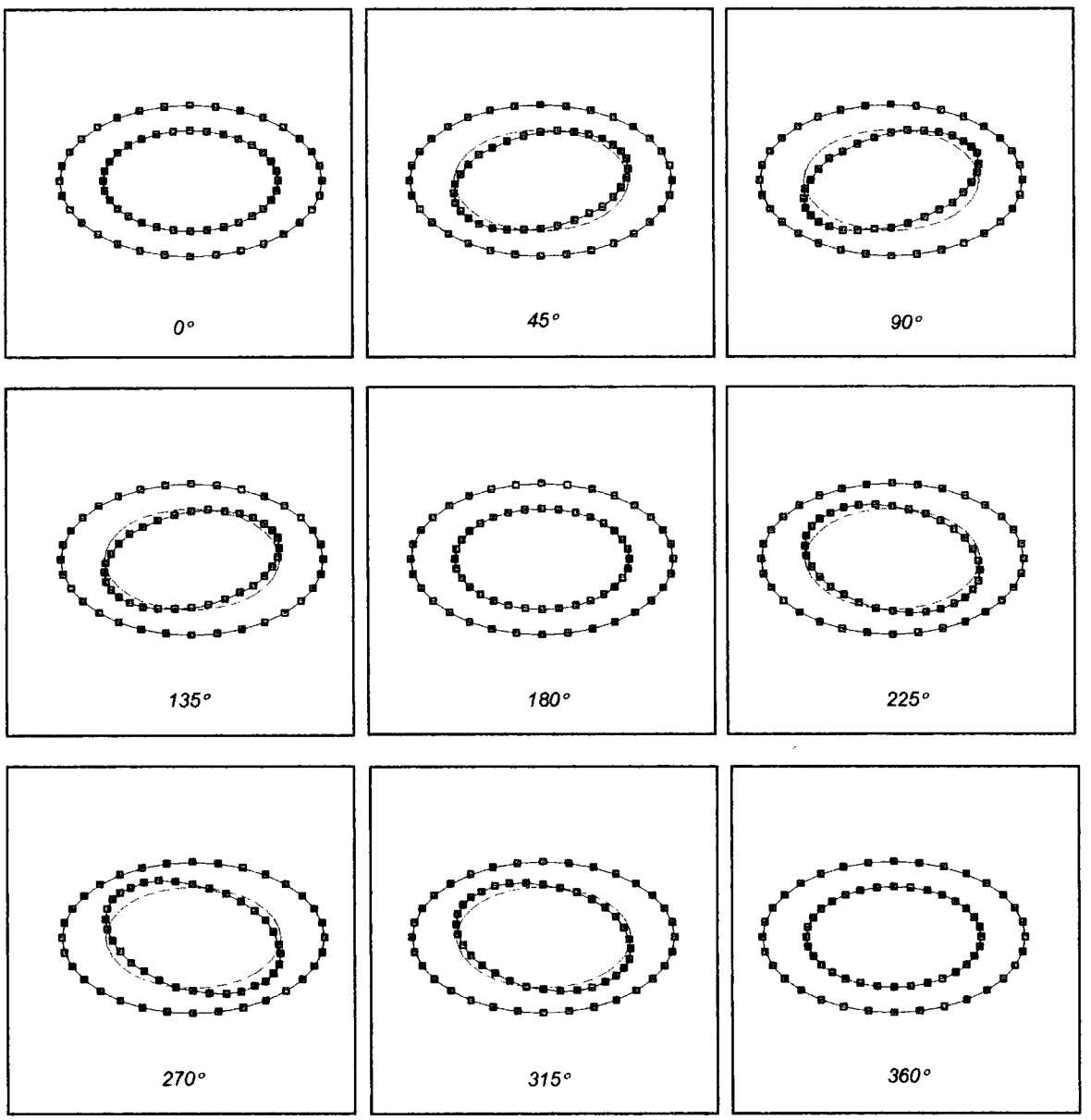

Figure 8.13. *Still frame animation of second out-of-plane mode shape.*

MODE 3
FREQUENCY = 11.418 kHz
Q-FACTOR = 1572.7

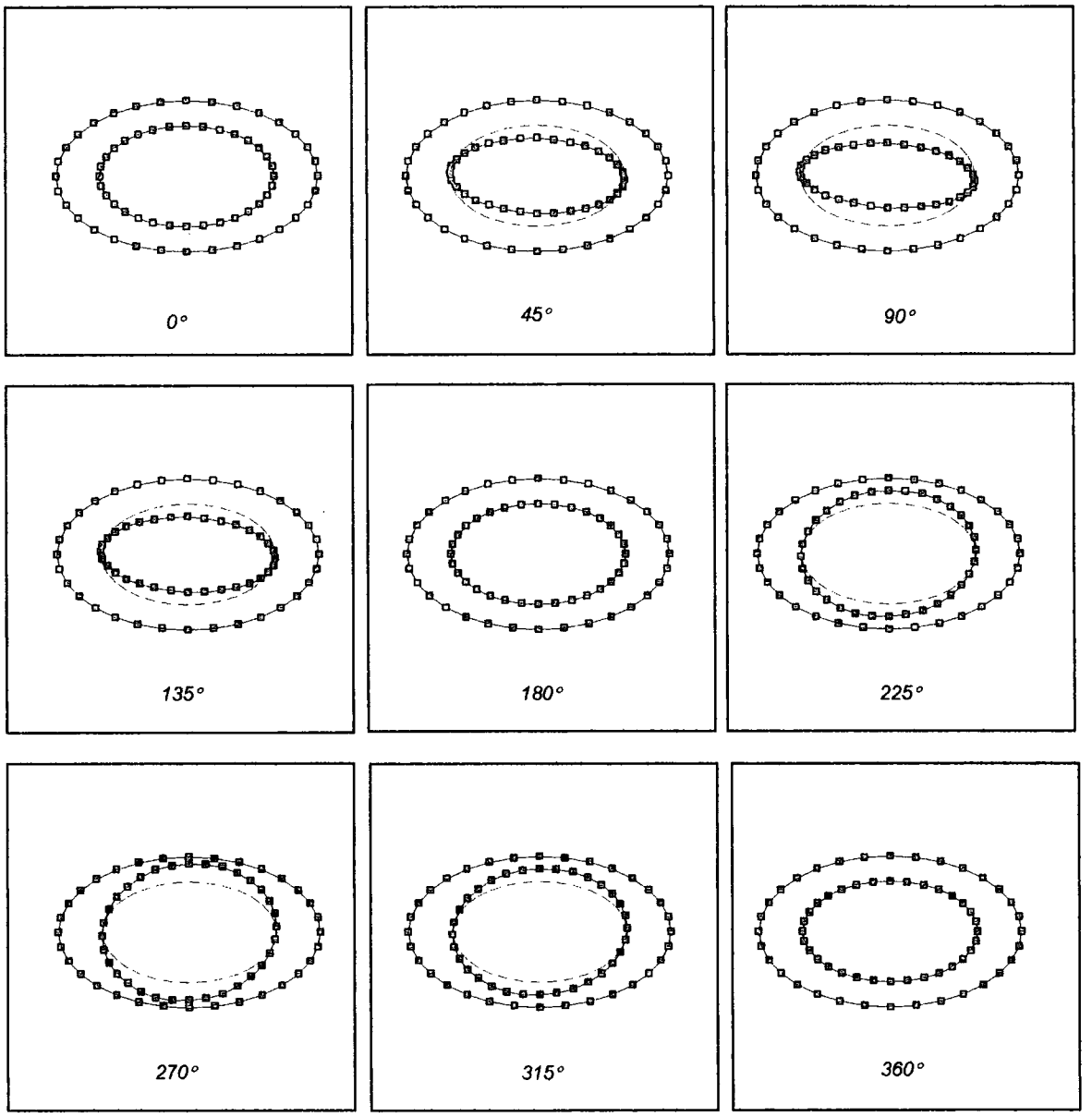

Figure 8.14. *Still frame animation of third out-of-plane mode shape.*

MODE 4
FREQUENCY = 13.904 kHz
Q-FACTOR = 1407.3

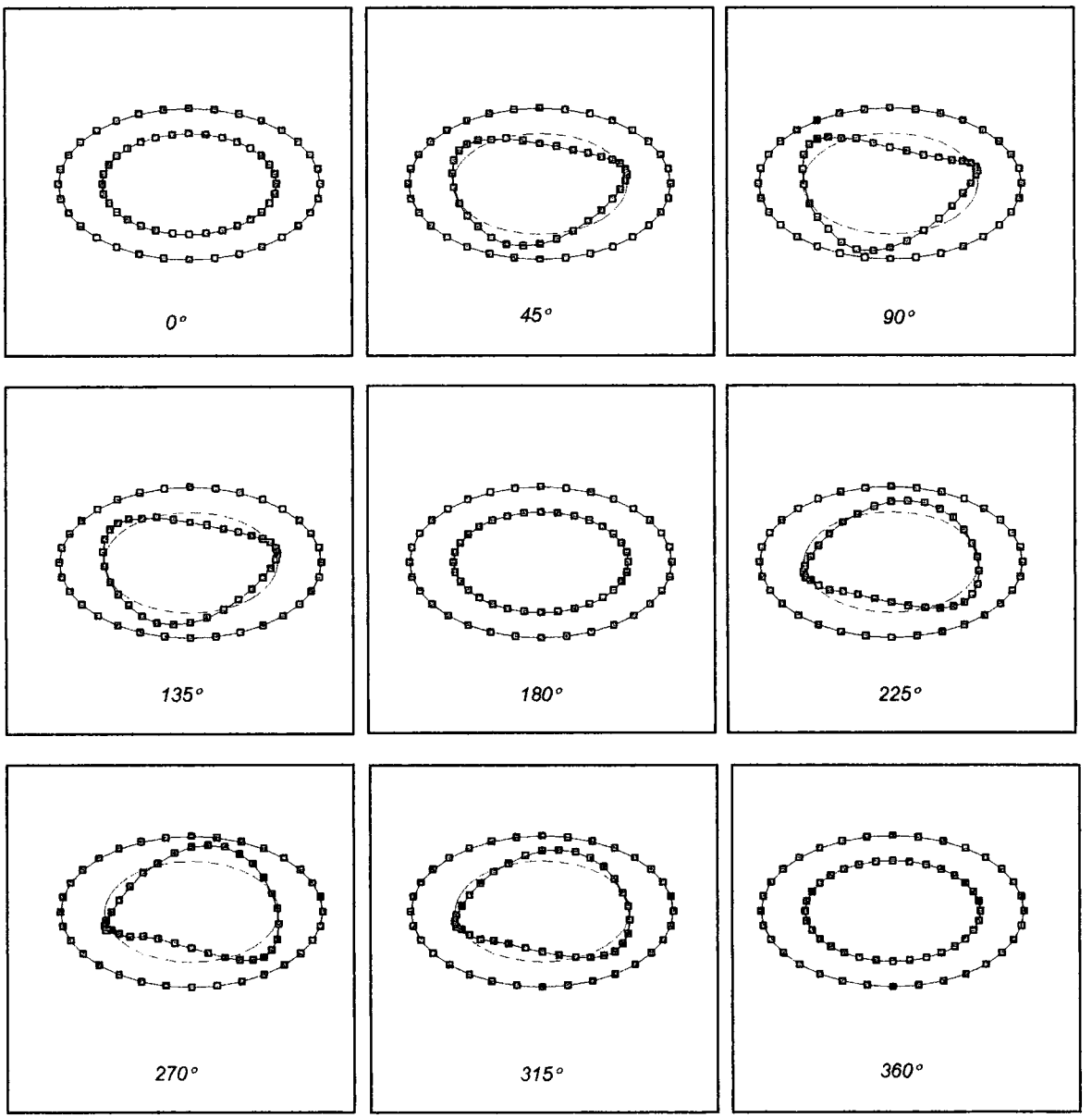

Figure 8.15. *Still frame animation of fourth out-of-plane mode shape*

8.3 Electrical Operation

With the out-of plane motion of the gyroscope structure displaying excellent correlation with FE-predictions, it was expected that the in-plane motion would likewise show good correlation. The only concern was whether the device could be driven with a large enough amplitude so that in-plane motion could be detected electrically. The following sub-sections detail the electrical operation of the ring gyroscopes and the measurements taken in order to assess their performance.

8.3.1 Vibration Excitation

As previously discussed in chapter seven, the primary motion of the gyroscope can be excited electrostatically using any arbitrary electrode. All the electrodes are fixed to the silicon dioxide substrate and located in close proximity (~10μm) to the ring. The situation constitutes a parallel plate capacitor with one fixed and one moveable plate (figure 8.16). Application of a potential difference across the two electrodes generates an electrostatic force that attracts the ring to the fixed drive electrode. Application of a sinusoidal potential forces the ring to vibrate, and the correct choice of frequency allows the system to resonate. The electrostatic force generated is a function of the electrode geometry and the applied potential difference and is given in equation 7.1.

Also as discussed in chapter seven, a practical device would employ a phase locked loop system to maintain the whole vibratory system at resonance. However, to simply confirm the required operation of the structure and to determine the open loop frequency response, a simple op-amp drive circuit was employed (figure 8.16). The transfer function of this circuit is governed by equation 8.1 and allows a sinusoidal input voltage to be amplified;

$$V_{out} = -\frac{R_2}{R_1} \qquad 8.1$$

where R_1 and R_2 are the resistor values as shown in figure 8.16.

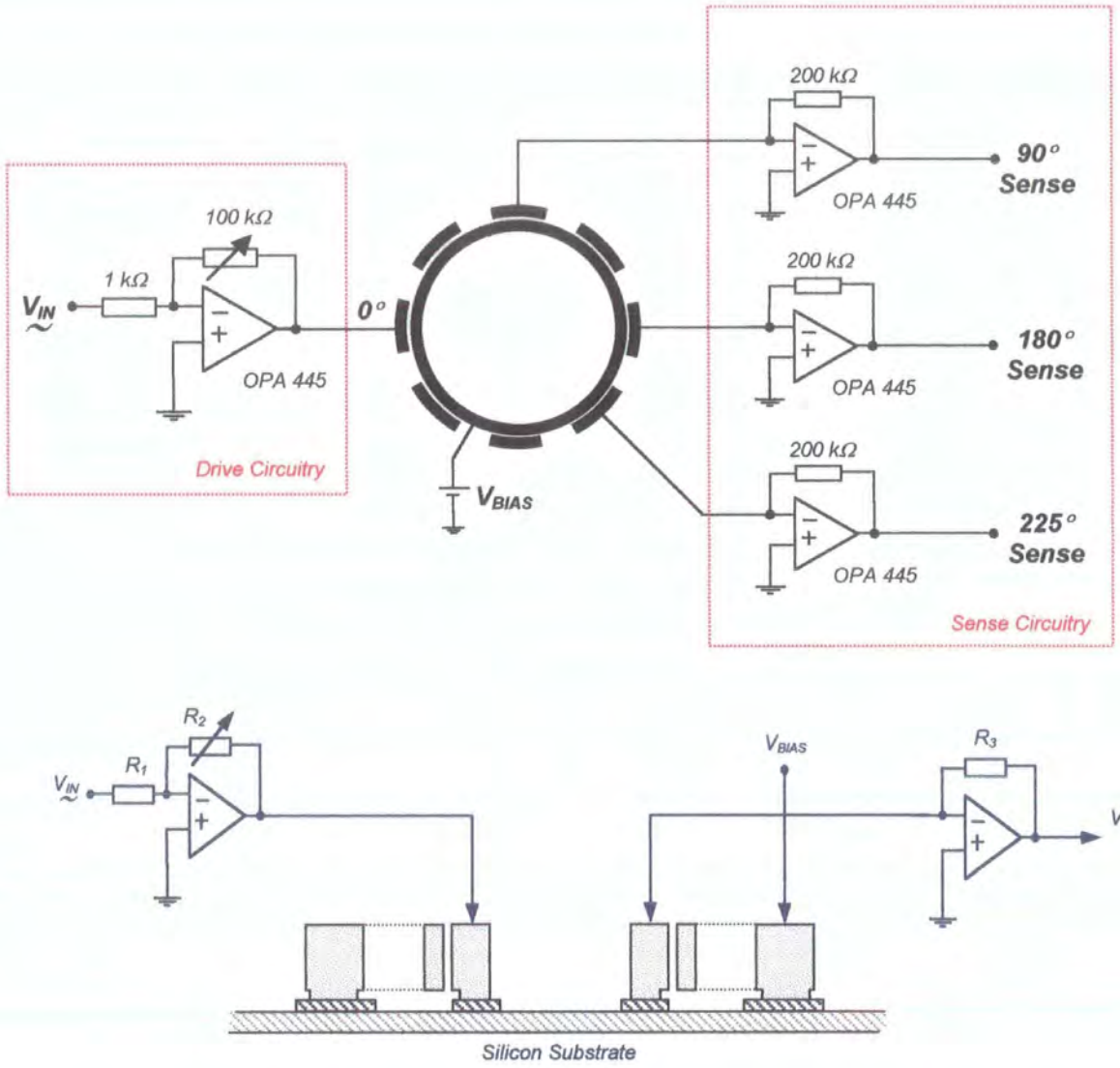

Figure 8.16. *Electrical operation of the ring gyroscope.*

8.3.2 Vibration Detection

With one of the electrodes located used to drive the motion of the ring, the remaining seven electrodes can be used to detect this subsequent motion. When the ring is biased, any motion generates charge flow in the sense capacitors due to modulation of the electrode spacing. The associated current can be detected and used to determine the motion of the ring. The magnitude of the current is given by:

$$i(t) = \frac{dq}{dt} = \frac{d(CV)}{dt} = V\frac{dC(t)}{dt} \qquad 8.2$$

where V is the electrode bias voltage and C is the time dependent capacitance. Expanding leads to:

$$i(t) = V\varepsilon_o\varepsilon_r A \cdot \frac{d}{dt}\left(\frac{1}{x}\right) = \frac{V\varepsilon_o\varepsilon_r A}{x^2} \cdot \frac{dx(t)}{dt} \qquad 8.3$$

where x is the static electrode spacing and $x(t)$ is the time varying electrode spacing. This simplifies to:

$$i(t) = \frac{V\varepsilon_o\varepsilon_r A}{x^2} \cdot v(t) \qquad 8.4$$

where $v(t)$ is the velocity of the ring.

The detection circuitry again employs a simple op-amp arrangement as shown in figure 8.16. The output voltage is determined by the following equation:

$$V_{out} = -i(t) \cdot R_3 \qquad 8.5$$

where R_3 is the value of the feedback resistor. Combining equations 8.4 and 8.5 shows the output voltage to be proportional to the ring velocity:

$$V_{out} = -\frac{\varepsilon_o\varepsilon_r VAR_3}{x^2} \cdot v(t) \qquad 8.6$$

8.3.3 Electrical Measurements

The following subsections document the electrical results obtained from version 1 of the ring gyroscope. These results include electrical determination of frequency response and general mode shape analysis. The in-plane motion of the gyroscope was driven and detected using the circuitry described in the previous section. Owing to the large electrode / ring separation, a large bias (50V) and drive voltages (50V pk-pk) were applied in order to excite the ring motion. All measurements were taken under vacuum at approximately 0.5mbar.

8.3.3.1 Electrical Coupling

Preliminary electrical measurements were taken to assess the amount of electrical coupling through the system from the drive to the detection circuitry. Such coupling originates from stray capacitances in and around the actual microstructure and can obscure the detection of small signals. This ultimately leads to the degradation of device performance. To a first approximation, it would be expected that the effect of the coupling signal would be to cause the gain of the system to increase linearly with frequency (see appendix F). However, it can be seen from figure 8.17 that although the gain does increase with frequency, the variation is not linear. The cause of this could be a number of factors. Firstly the model described in appendix F could be inaccurate; further effects caused by the combination of parasitic capacitances and resistances could have a significant influence (a combination of such impedances can effectively create low pass and/or high pass filters within the structure). Additionally the frequency response of the drive and sense circuitry (figure 8.16) was assumed to be linear, although practically this would not be the case. Also the limited slew rate of the drive circuitry could introduce further effects when providing high drive voltages (typically $50V_{pk\text{-}pk}$) at high frequency. To understand the non-linear behaviour of figure 8.17 it would be necessary to do more detailed measurements.

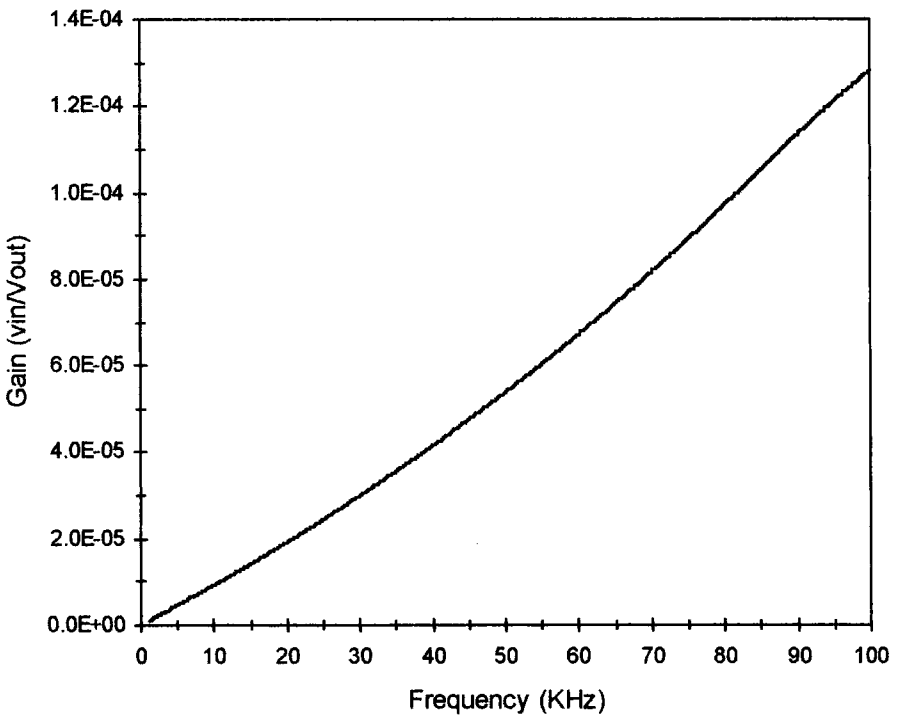

Figure 8.17. *Electrical coupling between drive and detection circuitry.*

8.3.3.2 Frequency Response

Despite the relatively high level of coupling it was still possible to identify the first three resonances of the structure. The frequency response plots corresponding to these modes are shown in figures 8.18 to 8.20. It can be seen from these graphs that the magnitude and phase response plots of each mode do not exhibit the classical characteristics associated with resonance. This is due to the contribution made by the unwanted coupling signal. However, as the phase of the coupling signal remains constant through the region of resonance, the Nyquist plot still exhibits the classical circular relationship but is simply displaced from the origin of the graph. The Nyquist plots confirm that these frequency response curves are resonant entities.

Due to the distortion of the detected signals and the presence of noise, it is difficult to identify the exact resonant frequencies from the magnitude response plots. To overcome this problem, and for the sake of consistency (and simplicity) the resonant frequency was determined from the peak (or trough) of the respective phase response plots. Although this is not an accepted definition it allows the relative values to remain consistent with each other without introducing significant errors. Table 8.4 lists the resonant frequencies of the first three modes as determined together with the predicted frequencies (chapter seven). It can be seen that experimental and theoretical values of the first three resonances show only small errors.

	Mode 1	Mode 2	Mode 3
Frequency	36.342 kHz	47.138 kHz	60.886 kHz
FEM	36.200 kHz	46.700 kHz	61.700 kHz
FEM Mode Shape	Cos 2θ	Cos 3θ	translation
% error	0.39 %	0.94 %	1.32 %

Table 8.4. *Frequency and Q-factor of first three in-plane modes.*

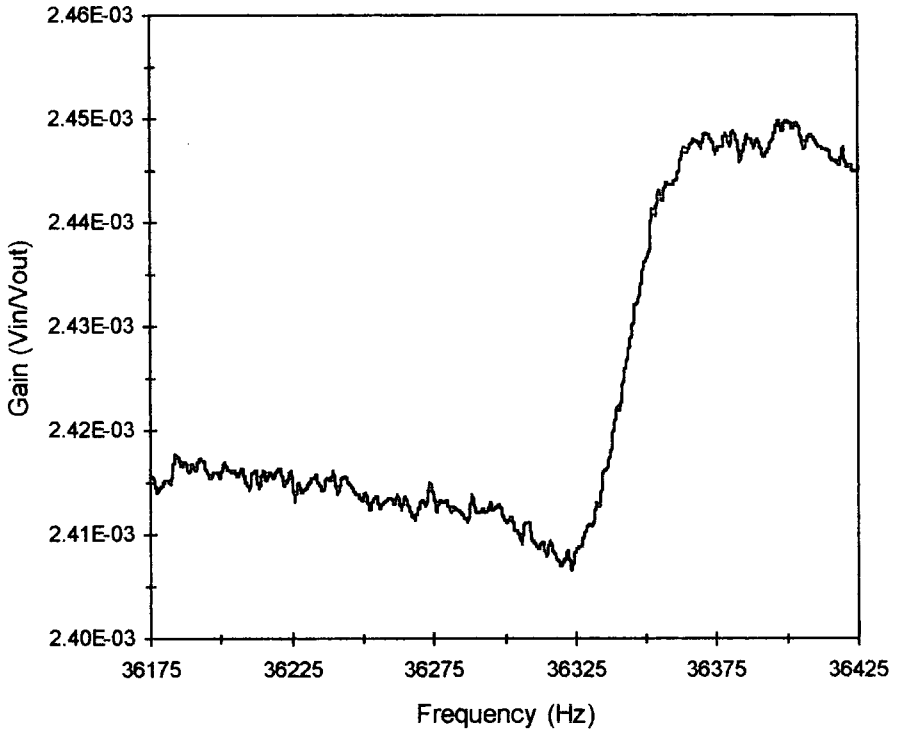

Figure 8.18a. *Magnitude response plot of first mode.*

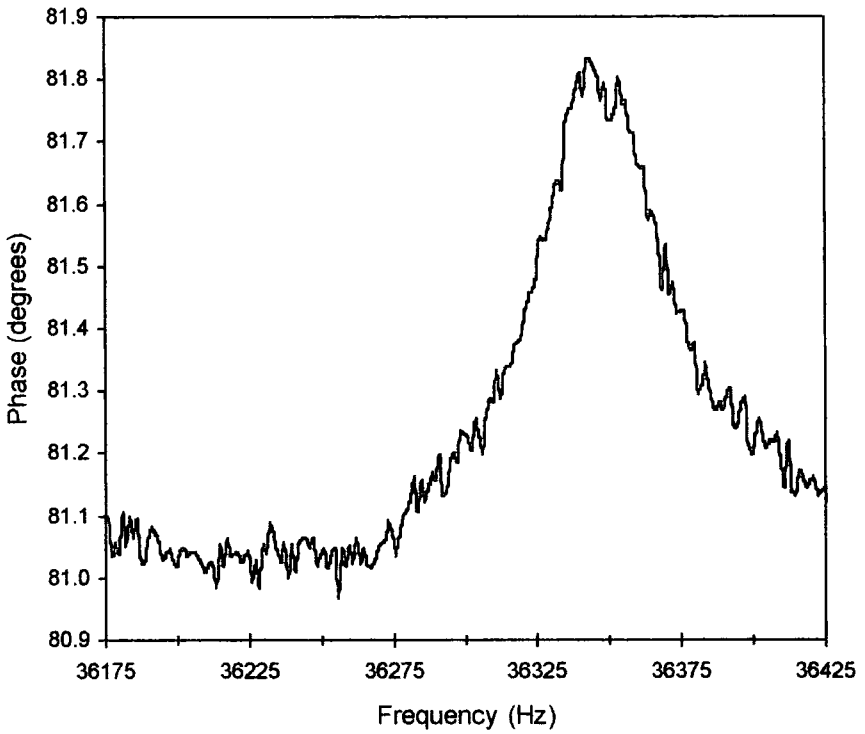

Figure 8.18b. *Phase response of first mode.*

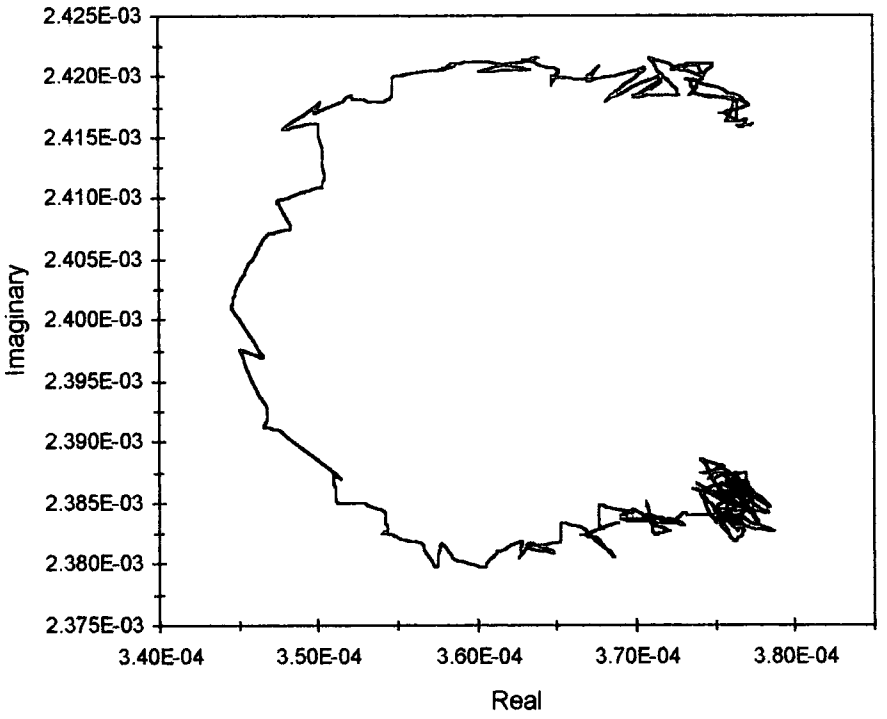

Figure 8.18c. *Nyquist plot of first mode.*

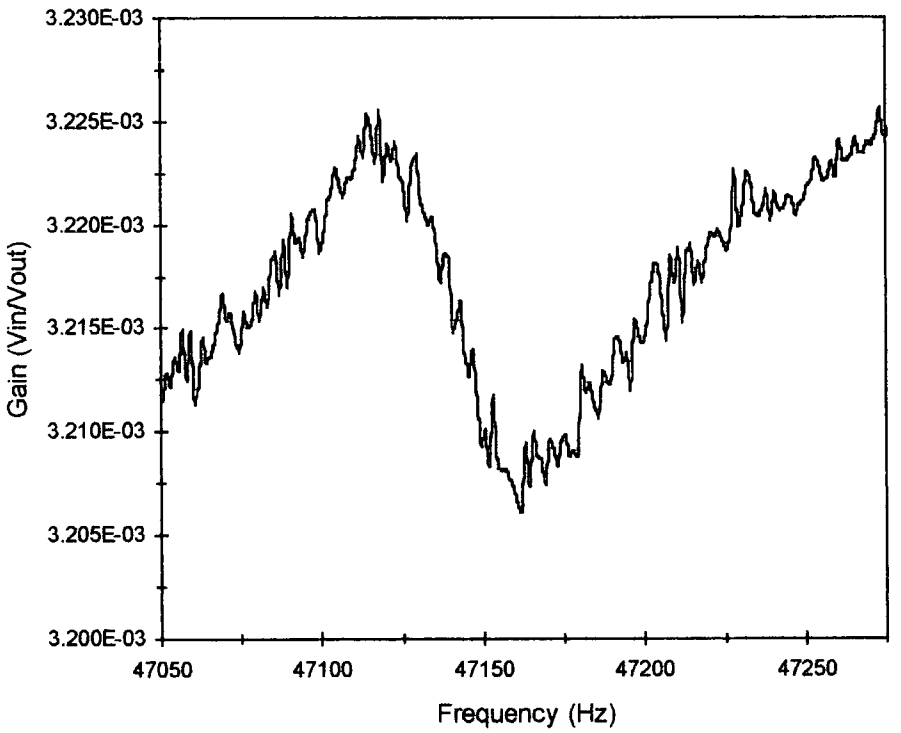

Figure 8.19a. *Magnitude response of second mode.*

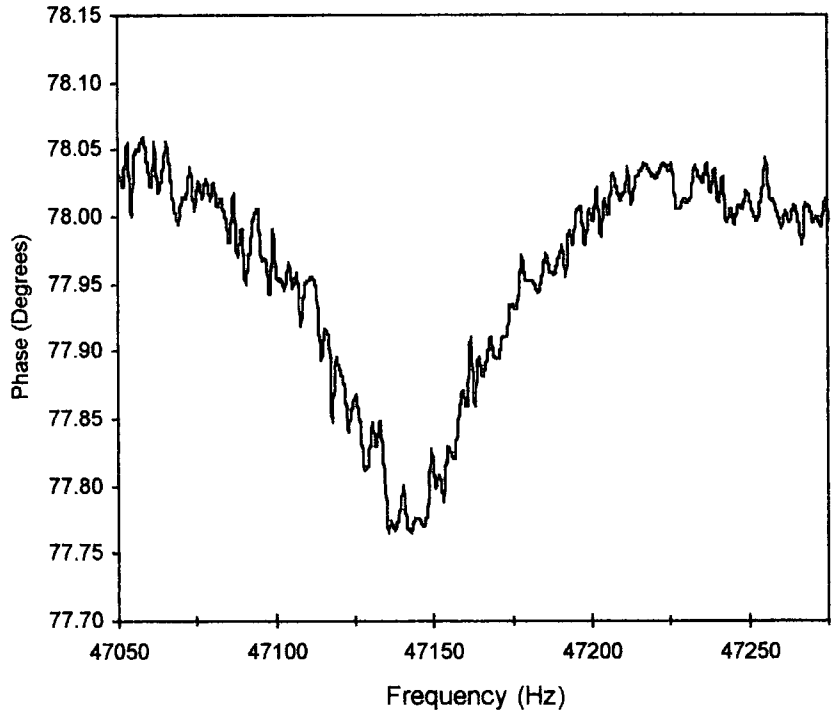

Figure 8.19b. *Phase response of second mode.*

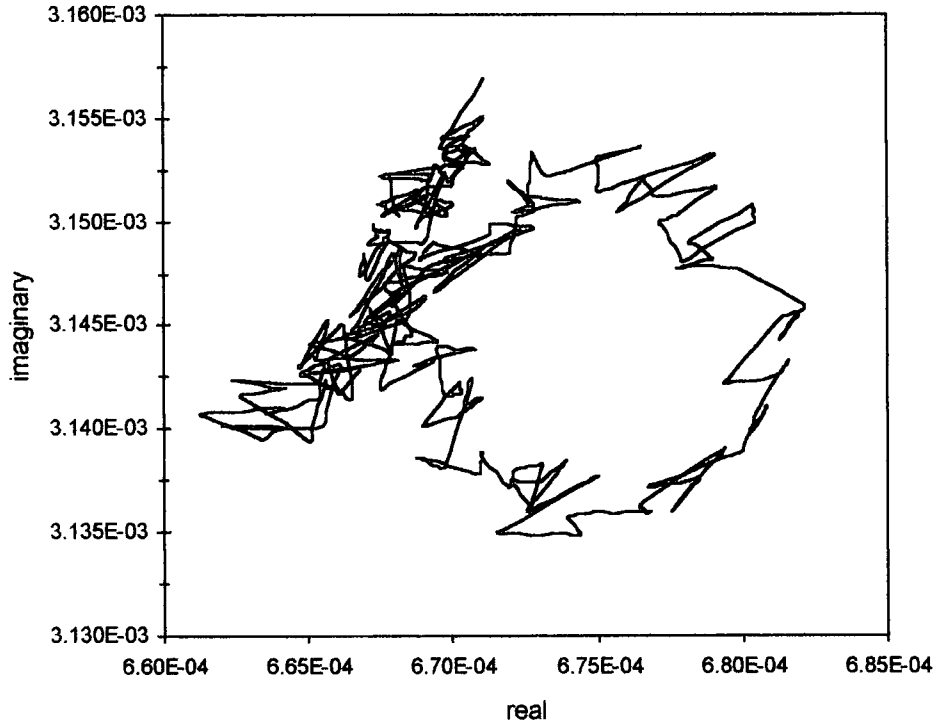

Figure 8.19c. *Nquist plot of second mode*

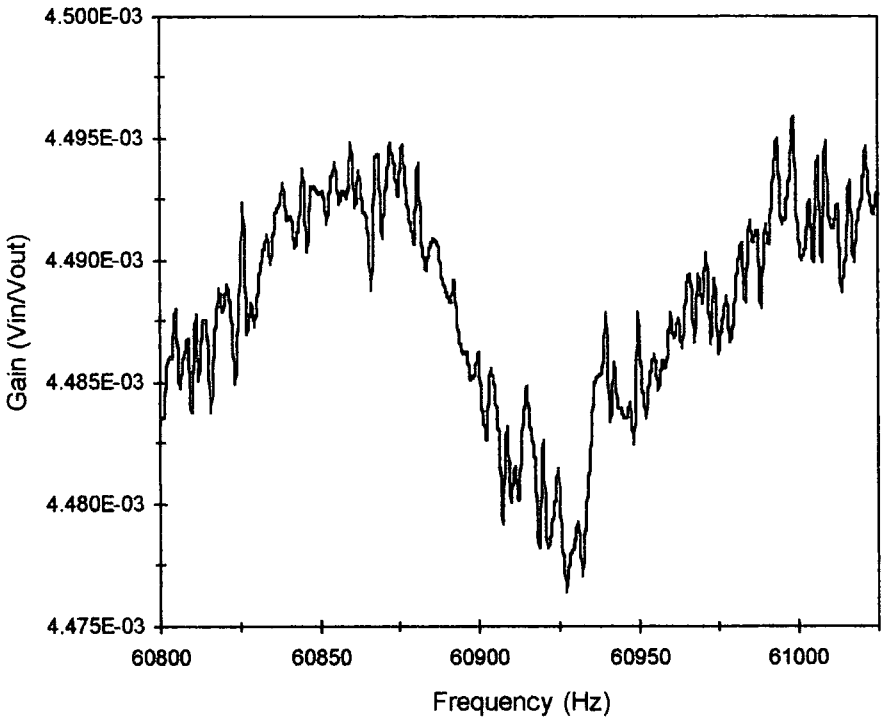

Figure 8.20a. *Magnitude response of third mode.*

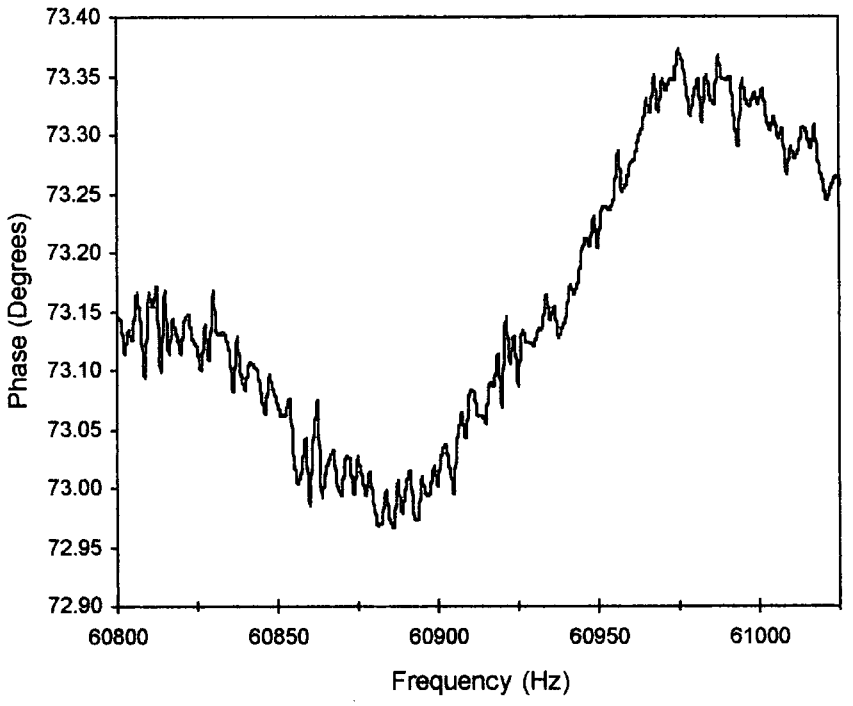

Figure 8.20b. *Phase response of third mode.*

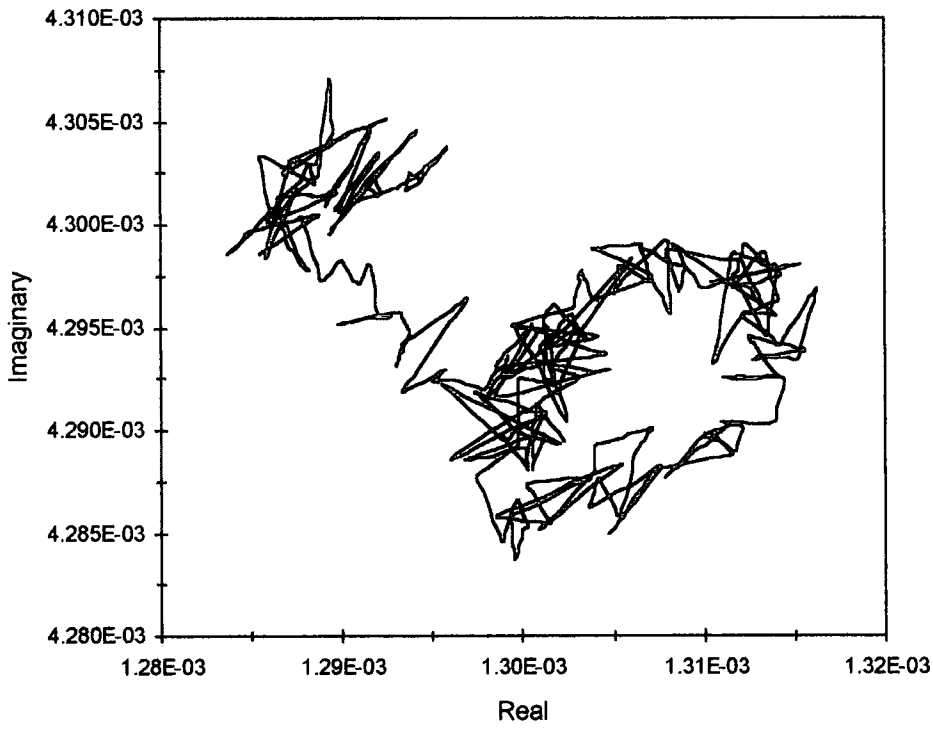

Figure 8.20c. *Nyquist plot of third mode.*

8.3.3.3 Resonant Mode Shapes

Determining the resonant mode shape of the in-plane motion electrically is much more difficult than measuring the out-of-plane mode shapes optically. Primarily, the number of measurement points is restricted to the number of detection electrodes that are situated around the device. The ring gyroscope has eight electrodes located around the inner circumference of the ring (chapter seven); driving at one of these electrodes (0°) leaves the remaining seven electrodes to be used for detection of the ring's motion. The magnitude and phase of the response at each of theses electrodes could be used to give a generalised picture of the ring's motion, but in practice this is difficult due to the distortion of the frequency response curves and also the presence of noise.

The frequency response was measured at each detection electrode for the first identified resonance. The frequency response curves for the 90° and 270° detection electrodes are shown in figures 8.21 and 8.22. No response could be found at the 45°, 135°, 225° or 315° electrodes.

Due to the limitations of the fabrication process, the gap between the ring and the electrodes is not constant and varies across individual features and from electrode to electrode. As this dimension has a critical influence on the magnitude of the detected signal, the relative magnitudes of the response at each electrode cannot be used to infer the motion of the ring. It is only the phase data that can be used to give an indication of the rings motion. From this (figures 8.21b and 8.22b), and also from the Nyquist plots (8.21c and 8.22c), it can be seen that the two measurements at 90° and 270° are in phase. Further comparison shows that these plots are 180° out of phase with the measurement taken at 180° (figure 8.18). With no response detected at the intermediate electrodes it can be inferred that the ring is undergoing the expected $\cos 2\theta$ motion.

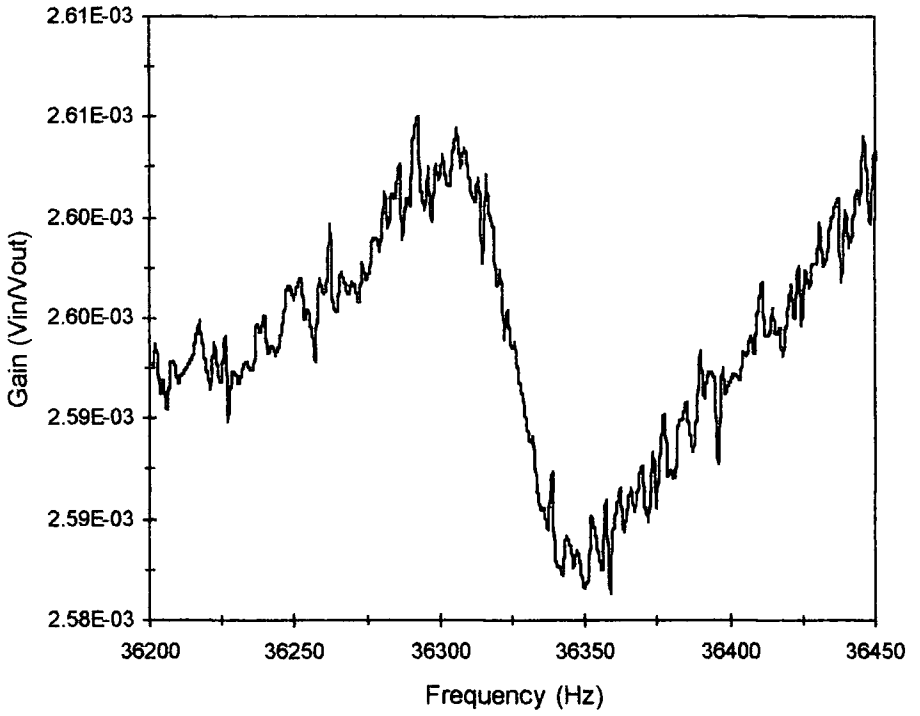

Figure 8.21a. *Magnitude response at 90° detection electrode.*

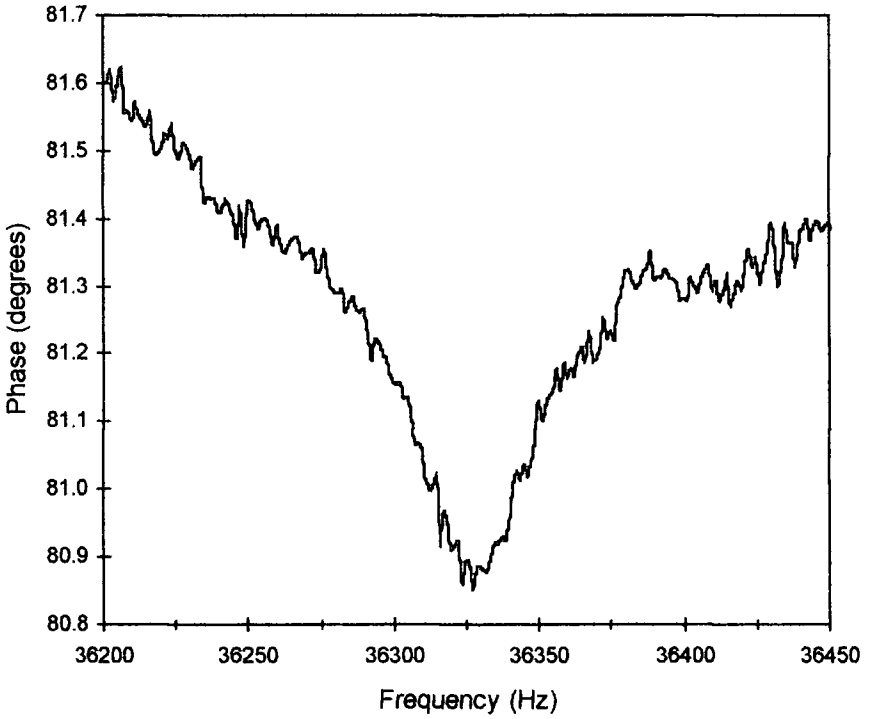

Figure 8.21b. *Phase response at 90° detection electrode.*

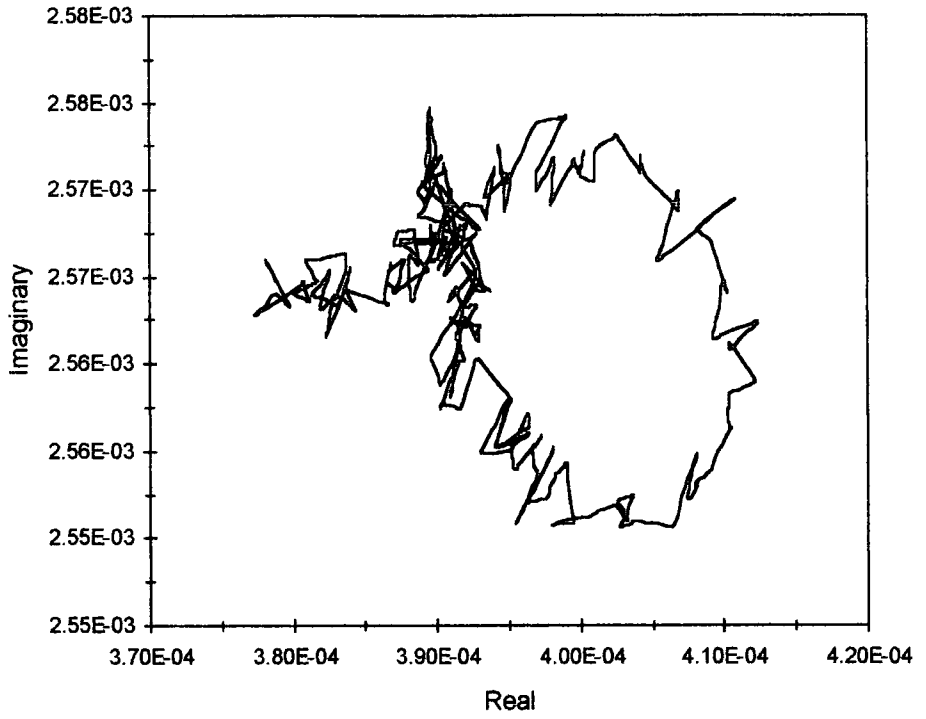

Figure 8.21c. *Nyquist plot of 90° response.*

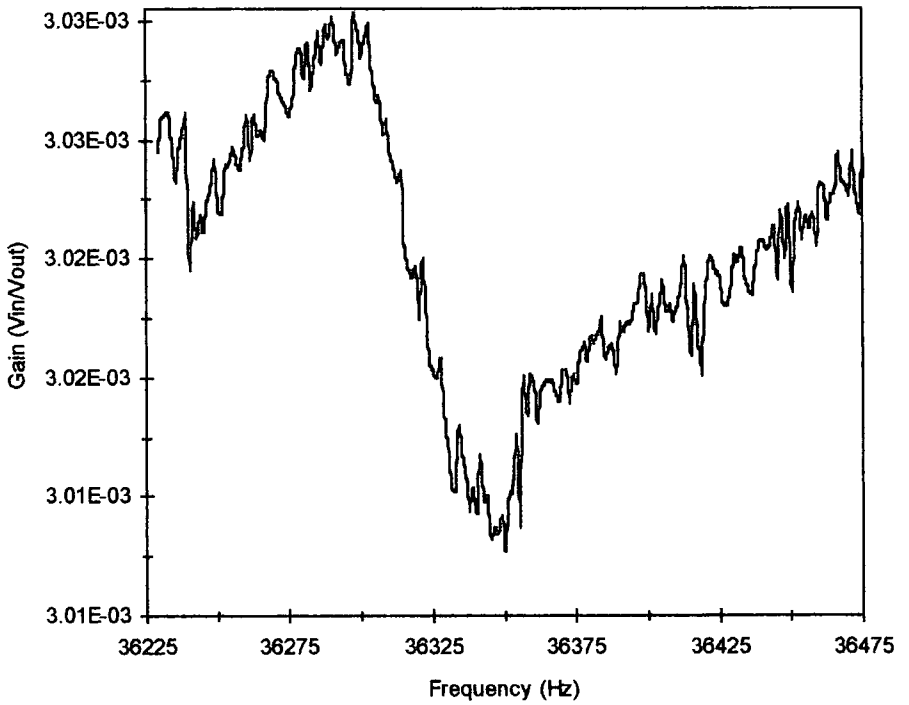

Figure 8.22a. *Magnitude response at 270° detection electrode.*

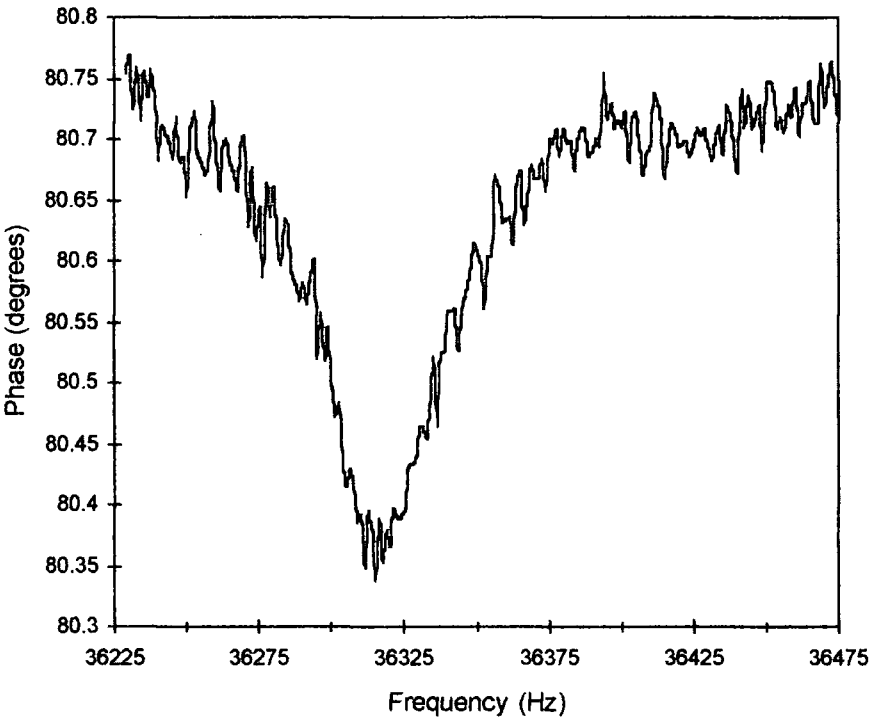

Figure 8.22b. *Phase response at 270° detection electrode.*

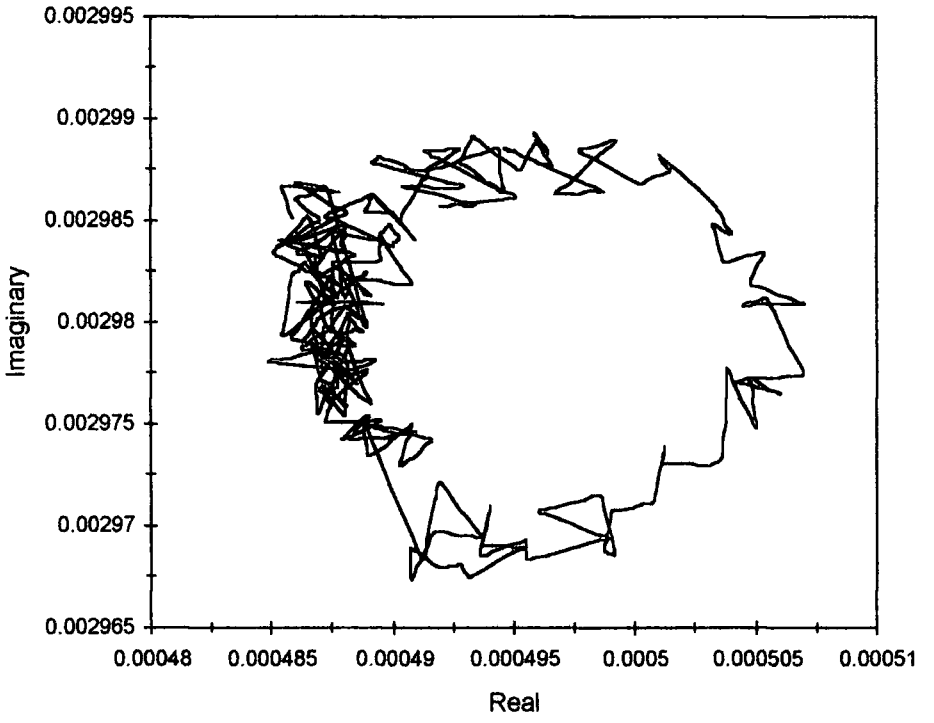

Figure 8.22c. *Nyquist plot of 270° response.*

8.3.3.4 Other Considerations

8.3.3.4.1 Tuning

One of the prime considerations of resonant gyroscopes is tuning. A tuned gyroscope has two normally uncoupled modes of vibration with identical frequencies. Gyroscopic action transfers energy between these two modes when the device is rotated about its sensitive axis. In order to achieve high sensitivity it is essential that the two modes of vibration be matched in frequency. In the ring gyroscope, the two operational modes of the gyroscope are identical modes spatially separated by 45° (chapter seven). In order to assess how balanced the device is, it is necessary to establish the frequency split between these two modes. This was achieved by driving the secondary mode of the gyroscope by exciting the resonance via a different location i.e. at 45°, 135°, 225° or 315° to the original. Comparison between the two resonant frequencies yields the required frequency split. This data is displayed in table 8.5.

Primary Frequency	*36.346 kHz ± 15Hz*
Secondary Frequency	*36.141 kHz ±19Hz*
Frequency Split	*205 ± 34Hz*

Table 8.5. *Frequency split between primary and secondary modes.*

The table shows the frequency split of 205 Hz between primary and secondary modes of the gyroscope. It must be stated that there is a degree of uncertainty to the validity of this value due to the poor quality of the frequency response functions from which it was derived. The value is however in the same order of magnitude as the frequency split found for the two identical out-of-plane vibrations of the ring (section 8.2.1).

8.3.3.4.2 Atmospheric Operation

It was found that the nickel devices could be operated at atmospheric pressure. The effect of this was to cause a slight shift in resonant frequency and a broadening of the response characteristics. The resonant frequency of the first mode under these conditions was determined to be 36.491 kHz, a frequency shift of 145 Hz from the value obtained under vacuum.

8.3.3.4.3 Power Dissipation

In order to drive and sense the vibration of the ring gyroscope it was necessary to employ large bias and drive voltages. Typical bias voltages of 50V and ac drive voltages of 50V pk-pk were required. Under these conditions it was found that the microstructures were dissipating typically 1.0 to 1.75W of power (25-35mA at 50V bias). The cause of the leakage current is likely to be the breakdown of the insulating silicon dioxide layer that covers the entire silicon surface. The effect of resistive heating on the samples was not investigated.

8.3.4 Summary of Electrical data

The electrical data has shown that the motion of the ring can be excited and detected electrically. The measurements were distorted by a large amount of electrical coupling but the response can be seen to be that of resonance. In order to obtain better quality response curves, the amount of electrical coupling must be further reduced. In addition the large electrode spacings has resulted in the need for high drive voltages that has ultimately resulted in the breakdown of the insulating oxide covering the silicon wafer. The use of smaller electrode gaps would significantly reduce power requirements and would minimise any effects of resistive heating.

Despite this it has been shown that the detected response of the gyroscope matches closely the results of the finite element analysis. Further it has been shown that the frequency split between the two operational modes of the gyroscope is approximately 205 Hz. With the use of commercially produced photomasks it must be expected that a more symmetrical device could be manufactured which would further reduce this value.

Finally, it is of some interest that the device has been shown to operate at atmospheric pressure. Although the effects off viscous damping are much reduced for in-plane motion it was still expected that the device would require low-pressure operation.

8.4 Conclusions

The initial optical analysis of the ring gyroscope showed clearly that its dynamic behaviour matched closely the finite element predictions. It did not, however, provide any information concerning the intended in-plane operation of the device. This data was provided by electrical operation using the 'on-chip' excitation and detection mechanisms. High levels of electrical coupling heavily distorted this experimental data but again close comparison with FE-data could still be made.

The combination of both optical and electrical data undoubtedly shows that the ring structure can and does operate in the way predicted by the finite element analysis.

Chapter Nine
Conclusions and Future Work

9.1 Summary of the Fabrication Process

A large proportion of research time was dedicated to developing the fabrication process used to construct the microstructures detailed within this thesis. It is therefore appropriate to appraise the success of this procedure prior the structures it was subsequently used to construct.

From the very onset the main aim of the research was to develop a micromachining process technology, novel to Durham, based around the concept of LIGA to construct microsensors. The outcome, the marriage of thick resist technology, nickel electroforming and sacrificial layer techniques, has been applied to produce free standing microstructures and to this end can be seen as a success. The process does however have its limitations and improvements could be made to increase its overall versatility.

Firstly the structural material has been restricted to nickel, due mainly its ease of deposition. Extending the process to encompass other metals / alloys would allow devices to be tailored to specific and individual requirements. Secondly, although maximum device heights of approximately 100μm can be attained, this is at the expense of lateral resolution. In order to maintain 1-2μm minimum feature sizes, maximum structural heights of 20-25μm must be maintained. Significant improvements could be made by incorporation of a photoresist recently developed by IBM. EPON-SU8 is a negative resist that can be applied in layers of up to 450μm and patterned with aspect ratios approaching 15 (roughly twice that of conventional thick resists) with near vertical sidewalls. Finally, the problem of thickness non-uniformity could be addressed for applications where tight dimensional control is required. This could be achieved through a post fabrication lapping procedure to ensure uniform dimensions across individual features and from feature to feature.

9.2 Summary of Beam Structures

The main aim concerning the fabrication and testing of the beam structures was to firstly confirm the success of the fabrication process and secondly to gather data that could be used to assess the dynamic properties of nickel resonators. The first aim was quickly established and the second highlighted the inherent problem of thickness non-uniformity associated with electroforming processes. These problems were not entirely unexpected and effects could be taken into account within the simulation models to yield excellent correlation with experimental data.

9.3 Summary of Ring Gyroscopes

By far the most limiting factor restricting the performance of the ring gyroscopes was the electrode spacings. Optical testing has established that these devices are behaving as expected but electrical testing has been hindered due to this constraint. In the structures produced, a minimum spacing of 10μm was achieved due to the constraints imposed by the lithographic process at the Durham facility. As a consequence, the electrical operation of the devices was significantly inhibited. However, the problem can be easily overcome by use of commercially manufactured photomasks. It is anticipated that optimum electrode spacings of 3μm could be routinely achieved and return a significant improvement to both power consumption and sensitivity. Additionally, the improved symmetry of the rings would reduce the mismatch between the two operational modes of the gyroscope.

9.4 Suggestions for Future Work

The main factors limiting the performance of the nickel devices tested within this thesis are related to the limitations imposed by the fabrication process rather than fundamental mechanical constraints. Therefore the first suggestions as to future work are geared towards improving this process using the ideas detailed above. With this in mind the problems of large electrode gaps would be eradicated reducing the problems associated with electrical operation and detection of lateral oscillators. Additionally, to overcome the relatively poor mechanical properties of electroformed nickel, other materials could be investigated; harder alloys such as brass could potentially increase the Q-factor of resonant devices and hence lead to improvements in sensitivity.

The fabrication process outlined in this thesis has been developed toward the construction of microsensors and in particular microgyroscopes. However, the process lends itself equally to the manufacture of microactuators, and further application could lie within these areas. For example fluidics - construction of fluid pumps, mixers and filters etc. but potential lies within all areas of micromechanics.

Appendix A

Interferometer Output

If the output from the laser is described by:

$$a_o = Ae^{i\omega t} = \sqrt{I}.e^{i\omega t} \tag{1}$$

where A is the amplitude of the light wave which is equal to the square root of intensity $\left(\sqrt{I}\right)$, then the amplitude of the two beams recombining at the photodetectors PD-1 and PD-2 (due to the two fold beam splitting in BS1 and BS2 in figure 5.1) can be described by:

$$a_1 = \frac{1}{2}Ae^{i(\omega t-\theta_1)} = \frac{1}{2}Ae^{i\omega t}e^{-i\theta_1} \tag{2}$$

$$a_2 = \frac{1}{2}Ae^{i(\omega t-\theta_2)} = \frac{1}{2}Ae^{i\omega t}e^{-i\theta_2} \tag{3}$$

where θ_1 and θ_2 are the relative phase shifts of each beam due to differences in path length. The total amplitude at PD-1 can be found by the addition of (2) and (3):

$$a_{tot} = a_1 + a_2 = \frac{1}{2}Ae^{i\omega t}\left[e^{-i\theta_1} + e^{-i\theta_2}\right] \tag{4}$$

and the intensity of the signal at PD-1 can be calculated from the amplitude by multiplication with its complex conjugate a^*.

$$I_1 = a_{tot}\cdot a_{tot}^* = \frac{1}{2}Ae^{i\omega t}\left[e^{-i\theta_1} + e^{-i\theta_2}\right]\cdot\frac{1}{2}Ae^{-i\omega t}\left[e^{i\theta_1} + e^{i\theta_2}\right] \tag{5}$$

$$= \frac{1}{4}A^2\left[2 + e^{-i\theta_1}e^{i\theta_2} + e^{-i\theta_2}e^{i\theta_1}\right] \tag{6}$$

$$= \frac{1}{4}A^2\left[2 + e^{-i(\theta_1-\theta_2)} + e^{i(\theta_1-\theta_2)}\right] \quad (7)$$

$$= \frac{1}{2}A^2\left[1 + \cos(\theta_1 - \theta_2)\right] \quad (8)$$

$$= \frac{1}{2}A^2\left[1 + \cos(\Delta\theta)\right] \quad (9)$$

Further, the intensity at PD-2 can be derived from the requirement of energy conservation; the output intensities at BS2 must at every point in time, add up to yield the laser intensity A^2. This is satisfied if:

$$I_2 = \frac{1}{2}A^2\left[1 - \cos(\Delta\theta)\right] \quad (10)$$

showing the sinusoidal relationship between the interferometer output (intensity) and phase difference.

Appendix B

The Coriolis Force and Frames of Reference

The Coriolis force acts upon all objects including ourselves as we travel over the rotating earth. Its effect on us goes unnoticed but the effects on large masses or rapidly moving objects is not so negligible; Coriolis forces account for the clockwise motion of weather systems in the northern hemisphere and consideration must be made for long distance air travel over the earth's surface.

To understand the operation of mechanical gyroscopes (rotary and vibratory) it is necessary to understand the nature of the Coriolis force. To do this it is useful to see how the perceived motion of a body can be influenced by the frame of reference from which it is observed. Consider the position of a body in space, figure A. Its perceived position depends upon the location from which it is observed. In reference frame 1 its location can be described by the position vector r_1 whilst from reference frame 2 its position vector is r_2.

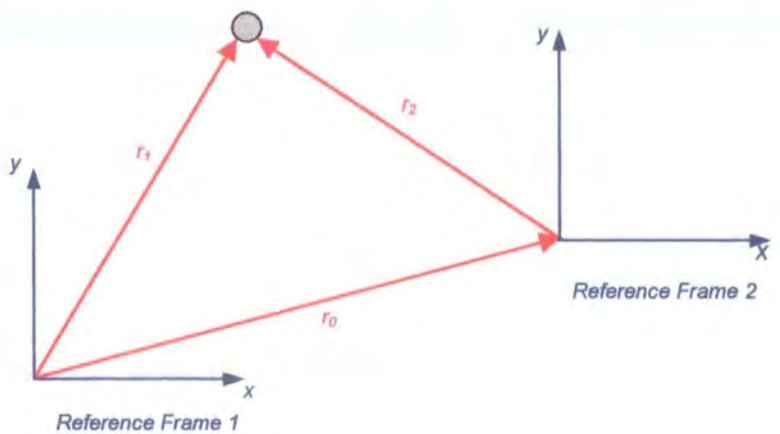

Figure A. *Determination of position from different frames of reference.*

In general the position of the body measured in one reference frame *(r_1)* will differ from that observed in the other *(r_2)*. The two position vectors r_1 and r_2 are related by:

$$r_1 = r_2 + r_0 \tag{11}$$

where r_o is the displacement between the two reference frames. If r_o is independent of time then the instantaneous velocity of the body will be related by:

$$\frac{dr_1}{dt} = \frac{dr_2}{dt} \tag{12}$$

Equations 11 and 12 show that when two reference frames are simply displaced from one another, the measured positions of a particular body will differ but the velocity will not. Further it can be found that the acceleration is also independent of reference frame.

If the displacement between reference frames is not independent of time but one frame moves at constant velocity, v_o, with respect to the other, then the relative positions will now be related by:

$$r_1 = r_2 + v_0 t \tag{13}$$

and the relationship between velocities becomes:

$$\frac{dr_1}{dt} = \frac{dr_2}{dt} + v_0 \tag{14}$$

The velocity observed now depends upon the frame of reference. An additional time independent component is present. The acceleration however still remains independent of reference frame:

$$\frac{d^2 r_1}{dt^2} = \frac{d^2 r_2}{dt^2} \tag{15}$$

Finally if one reference frame accelerates away from the other at a constant value, A_o, then the relationships between position vectors, velocity vectors and acceleration vectors become:

$$r_1 = r_2 + \frac{1}{2}A_0 t^2 \tag{16}$$

$$\frac{dr_1}{dt} = \frac{dr_2}{dt} + A_0 t \tag{17}$$

$$\frac{d^2 r_1}{dt^2} = \frac{d^2 r_2}{dt^2} + A_0 \tag{18}$$

It can be seen from equations 16, 17 and 18 that within the non-inertial (accelerating) reference frame neither the measured position, velocity nor acceleration of a moving body coincide with those measurements observed within an inertial reference frame. Since the acceleration differs, application of Newton's second law will show that the perceived forces must also differ:

$$m\frac{d^2 r_1}{dt^2} = m\frac{d^2 r_2}{dt^2} + mA_0 \tag{19}$$

where m is the mass of the body and the term mA_0 represents an additional 'inertial' or 'fictitious' force. Although such forces are truly imaginary their effects as observed within an inertial reference frame are very real. Such fictitious forces include centrifugal forces and the Coriolis force. Their existence manifests itself from the fact that the force an observer within an non-inertial reference frame is personally subject to (due to his acceleration), is naively perceived to be influencing the motion of the external world (including the observed body) and not his/her own.

A special case of an accelerating reference frame is one undergoing rotation. In this case the relationship between the rate of change of an arbitrary vector as measured in a non-inertial reference frame and as measured in a rotating reference frame is given by [83]:

$$\left(\frac{d}{dt}\right)_i = \left(\frac{d}{dt}\right)_r + \Omega \times \tag{20}$$

Using this operator, the velocity of a body within a rotating reference can be found by substitution of the position vector, r:

$$\left(\frac{dr}{dt}\right)_i = \left(\frac{dr}{dt}\right)_r + \Omega \times r \tag{21}$$

$$\Rightarrow v_i = v_r + \Omega \times r \tag{22}$$

Now, using operator 20 on equation 22, the expression for the acceleration of the body can be found:

$$\frac{dv_i}{dt} = \frac{d(v_r + \Omega \times r)}{dt} + \Omega \times (v_r + \Omega \times r) \tag{23}$$

$$= \frac{dv_r}{dt} + \Omega \times \frac{dr}{dt} + \Omega \times v_r + \Omega \times (\Omega \times r) \tag{24}$$

$$\Rightarrow a_i = a_r + 2\Omega \times v_r + \Omega \times (\Omega \times r) \tag{25}$$

From Newton's second law the forces observed are:

$$F_i = F_r + 2m\Omega \times v_r + m\Omega \times (\Omega \times r) \tag{26}$$

and therefore:

$$F_r = F_i - 2m\Omega \times v_r - m\Omega \times (\Omega \times r) \tag{27}$$

where F_r represents the force observed from within the rotating reference frame, F_i represents the force observed from within the non-inertial reference frame and the remaining two terms represent additional inertial forces. The last term is a vector of magnitude $m\Omega^2 r\sin\theta$ directed radially outward from the axis of rotation and represents a centrifugal component. When the body is stationary (within the rotating frame and hence $V=0$) this is the only inertial force observed. It can be seen that the centrifugal force is proportional to the square of rotation rate, Ω^2, and this force could be used to sense rotation. However, the presence of the position vector r means the force is proportional to the radius of rotation, which would not remain constant in real applications. From equation 27 it can be seen that when the body undergoes translation an additional inertial force (magnitude $2m\Omega v\sin\theta$) is observed; this is the Coriolis force. Further, if the direction of translation is perpendicular to the axis of rotation then the

sine term disappears and the expression for the Coriolis force simplifies to $F_c = 2mV\Omega$. The Coriolis force always acts in a direction orthogonal to both axes of translation and it is the effects of this force, which is proportional to the rotation rate and independent of the radius of rotation that can be used to calculate the rotation rate.

In general when a body, in a rotating frame of reference, is subject to both translational and rotational motion, Coriolis forces are generated in a direction orthogonal to both axes of rotation and translation. If the translational motion were harmonic then the response would be similarly harmonic. This is the principle by which all vibratory gyroscopes operate - the motion of a particular resonant mode of the device is excited; an applied rate of turn generates Coriolis forces which are used to excite a secondary vibration orthogonal to the primary. The amplitude of this secondary motion can be used as a measure of rotation.

Appendix C

Ring Gyroscope Simulation Model: 3D Version 1

```
TITLE RING STRUCTURE
C  4 MM DIAMETER
C 100 UM RING
C  50 UM LIGAMENTS
C
C ***************************************************************************
C
C                          CONTROL
C
C ***************************************************************************
C
CONTROL
DOUBLE
DOUBLE.BACKS
TOLERANCE=10E-8
CONTROL.END
C
C ***************************************************************************
C
C                          NODES
C
C ***************************************************************************
NODES
C RIGHT HANDED CYLINDERICAL AXIS
AXIS.NUMBER=4
NODE.NUMBER X Y Z
C *** SUBTRACT 22.5 FROM Z-VALUE TO OBTAIN SYMMETRY ***
 1  0 1.95E-3  25.0
 2  0 1.95E-3  26.47
 3  0 1.90E-3  25.0
 4  0 1.90E-3  26.50
 5  0 1.85E-3  25.0
 6  0 1.85E-3  26.55
 7  0 1.90E-3  41.0
 8  0 1.90E-3  42.5
 9  0 1.85E-3  40.95
 10 0 1.85E-3  42.5
 11 0 1.55E-3  40.65
 12 0 1.55E-3  42.5
 13 0 1.45E-3  40.52
 14 0 1.45E-3  42.5
 15 0 1.90E-3  33.75
 16 0 1.85E-3  33.75
 17 0 1.55E-3  45.0
 18 0 1.45E-3  45.0
 19 0 1.55E-3  22.5
 20 0 1.45E-3  22.5
C
 21 0 1.95E-3  20.0
 22 0 1.95E-3  18.53
 23 0 1.90E-3  20.0
 24 0 1.90E-3  18.5
 25 0 1.85E-3  20.0
```

```
 26  0  1.85E-3   18.45
 27  0  1.90E-3    4.0
 28  0  1.90E-3    2.5
 29  0  1.85E-3    4.05
 30  0  1.85E-3    2.5
 31  0  1.55E-3    4.35
 32  0  1.55E-3    2.5
 33  0  1.45E-3    4.48
 34  0  1.45E-3    2.5
 35  0  1.90E-3  11.25
 36  0  1.85E-3  11.25
C
C SUPPORT DONUT
C
 37 0 2.45E-3 25.0
 38 0 2.45E-3 26.47
 39 0 2.45E-3 20.0
 40 0 2.45E-3 18.53
 41 0 1.95E-3 22.5
 42 0 2.45E-3 22.5
 43 0 1.95E-3 45.0
 44 0 2.45E-3 45.0
 45 0 0 0
 46 0 0 0
 47 0 0 0
 48 0 0 0
 49 0 0 0
 50 0 0 0
C
NODES
X=500E-6
AXIS.NUMBER=4
NODE.NUMBER Y Z
 51    1.95E-3  25.0
 52    1.95E-3  26.47
 53    1.90E-3  25.0
 54    1.90E-3  26.50
 55    1.85E-3  25.0
 56    1.85E-3  26.55
 57    1.90E-3  41.0
 58    1.90E-3  42.5
 59    1.85E-3  40.95
 60    1.85E-3  42.5
 61    1.55E-3  40.65
 62    1.55E-3  42.5
 63    1.45E-3  40.52
 64    1.45E-3  42.5
 65    1.90E-3  33.75
 66    1.85E-3  33.75
 67    1.55E-3  45.0
 68    1.45E-3  45.0
 69    1.55E-3  22.5
 70    1.45E-3  22.5
C
 71    1.95E-3  20.0
 72    1.95E-3  18.53
 73    1.90E-3  20.0
 74    1.90E-3  18.5
 75    1.85E-3  20.0
```

```
76   1.85E-3   18.45
77   1.90E-3   4.0
78   1.90E-3   2.5
79   1.85E-3   4.05
80   1.85E-3   2.5
81   1.55E-3   4.35
82   1.55E-3   2.5
83   1.45E-3   4.48
84   1.45E-3   2.5
85   1.90E-3  11.25
86   1.85E-3  11.25
C
C SUPPORT DONUT
C
87   2.45E-3 25.0
88   2.45E-3 26.47
89   2.45E-3 20.0
90   2.45E-3 18.53
91   1.95E-3 22.5
92   2.45E-3 22.5
93   1.95E-3 45.0
94   2.45E-3 45.0
C
C ***************************************************************************
C
C                        PAFBLOCKS
C
C ***************************************************************************C
C
PAFBLOCKS
ELEMENT.TYPE=37110
PROPERTIES=1
N1 N5 N2 TOPOLOGY
C
C                        SECTOR 1
C
C
1 1 9   1  2  3  4 51 52 53 54
1 1 9   3  4  5  6 53 54 55 56
1 1 9   7  8  9 10 57 58 59 60
1 2 9   9 10 11 12 59 60 61 62
1 1 9  11 12 13 14 61 62 63 64
1 2 9   4  6  7  9 54 56 57 59        0  15  16 0 0 0 0 0 0  65  66 0
C
C
1 1 9   21  22  23  24 71 72 73 74
1 1 9   23  24  25  26 73 74 75 76
1 1 9   27  28  29  30 77 78 79 80
1 2 9   29  30  31  32 79 80 81 82
1 1 9   31  32  33  34 81 82 83 84
1 2 9   24  26  27  29 74 76 77 79      0  35  36 0 0 0 0 0 0  85  86 0
C
C                         RING
C
3 4 9   32  34 812 814  82 84 862 864    0 817 818 0 0 0 0 0 0 867 868 0
3 5 9   31  33  11  13  81 83  61  63    0  19  20 0 0 0 0 0 0  69  70 0
C
C                        SUPPORT
C
```

```
6 6 9   1  2   37  38 51 52  87  88
6 6 9   21  22  39  40 71 72  89  90
6 6 9   1  37  21  39 51 87  71  89     0  41  42 0 0 0 0 0 0  91  92 0
6 8 9   2  38 222 240 52 88 272 290     0  43  44 0 0 0 0 0 0  93  94 0
C
C
C                       SECTOR 2
C
C
1 1 9   201 202 203 204 251 252 253 254
1 1 9   203 204 205 206 253 254 255 256
1 1 9   207 208 209 210 257 258 259 260
1 2 9   209 210 211 212 259 260 261 262
1 1 9   211 212 213 214 261 262 263 264
1 2 9   204 206 207 209 254 256 257 259      0 215 216 0 0 0 0 0 0 265 266 0
C
C
1 1 9   221  222  223  224 271 272 273 274
1 1 9   223  224  225  226 273 274 275 276
1 1 9   227  228  229  230 277 278 279 280
1 2 9   229  230  231  232 279 280 281 282
1 1 9   231  232  233  234 281 282 283 284
1 2 9   224  226  227  229 274 276 277 279    0  235 236 0 0 0 0 0 0 285 286 0
C
C                       RING
C
3 4 9   232  234  12  14 282 284  62  64     0  17  18 0 0 0 0 0 0  67  68 0
3 5 9   231  233 211 213 281 283 261 263      0 219 220 0 0 0 0 0 0 269 270 0
C
C                       SUPPORT
C
6 6 9    201 202 237 238 251 252 287 288
6 6 9    221 222 239 240 271 272 289 290
6 6 9    201 237 221 239 251 287 271 289      0 241 242 0 0 0 0 0 0 291 292 0
6 8 9    202 238 322 340 252 288 372 390      0 243 244 0 0 0 0 0 0 293 294 0
C
C
C                       SECTOR 3
C
C
1 1 9   301 302 303 304 351 352 353 354
1 1 9   303 304 305 306 353 354 355 356
1 1 9   307 308 309 310 357 358 359 360
1 2 9   309 310 311 312 359 360 361 362
1 1 9   311 312 313 314 361 362 363 364
1 2 9   304 306 307 309 354 356 357 359      0 315 316 0 0 0 0 0 0 365 366 0
C
C
1 1 9   321  322  323  324 371 372 373 374
1 1 9   323  324  325  326 373 374 375 376
1 1 9   327  328  329  330 377 378 379 380
1 2 9   329  330  331  332 379 380 381 382
1 1 9   331  332  333  334 381 382 383 384
1 2 9   324  326  327  329 374 376 377 379    0  335 336 0 0 0 0 0 0 385 386 0
C
C                       RING
C
3 4 9   332  334 212 214 382 384 262 264      0 217 218 0 0 0 0 0 0 267 268 0
3 5 9   331  333 311 313 381 383 361 363      0 319 320 0 0 0 0 0 0 369 370 0
```

```
C
C                    SUPPORT
C
6 6 9   301 302 337 338 351 352 387 388
6 6 9   321 322 339 340 371 372 389 390
6 6 9   301 337 321 339 351 387 371 389     0 341 342 0 0 0 0 0 0 391 392 0
6 8 9   302 338 422 440 352 388 472 490     0 343 344 0 0 0 0 0 0 393 394 0
C
C
C                    SECTOR 4
C
C
1 1 9  401 402 403 404 451 452 453 454
1 1 9  403 404 405 406 453 454 455 456
1 1 9  407 408 409 410 457 458 459 460
1 2 9  409 410 411 412 459 460 461 462
1 1 9  411 412 413 414 461 462 463 464
1 2 9  404 406 407 409 454 456 457 459     0 415 416 0 0 0 0 0 0 465 466 0
C
C
1 1 9  421  422  423  424 471 472 473 474
1 1 9  423  424  425  426 473 474 475 476
1 1 9  427  428  429  430 477 478 479 480
1 2 9  429  430  431  432 479 480 481 482
1 1 9  431  432  433  434 481 482 483 484
1 2 9  424  426  427  429 474 476 477 479   0  435 436 0 0 0 0 0 0 485 486 0
C
C                    RING
C
3 4 9  432  434 312 314 482 484 362 364     0 317 318 0 0 0 0 0 0 367 368 0
3 5 9  431  433 411 413 481 483 461 463     0 419 420 0 0 0 0 0 0 469 470 0
C
C                    SUPPORT
C
6 6 9   401 402 437 438 451 452 487 488
6 6 9   421 422 439 440 471 472 489 490
6 6 9   401 437 421 439 451 487 471 489     0 441 442 0 0 0 0 0 0 491 492 0
6 8 9   402 438 522 540 452 488 572 590     0 443 444 0 0 0 0 0 0 493 494 0
C
C
C                    SECTOR 5
C
C
1 1 9  501 502 503 504 551 552 553 554
1 1 9  503 504 505 506 553 554 555 556
1 1 9  507 508 509 510 557 558 559 560
1 2 9  509 510 511 512 559 560 561 562
1 1 9  511 512 513 514 561 562 563 564
1 2 9  504 506 507 509 554 556 557 559     0 515 516 0 0 0 0 0 0 565 566 0
C
C
1 1 9  521  522  523  524 571 572 573 574
1 1 9  523  524  525  526 573 574 575 576
1 1 9  527  528  529  530 577 578 579 580
1 2 9  529  530  531  532 579 580 581 582
1 1 9  531  532  533  534 581 582 583 584
1 2 9  524  526  527  529 574 576 577 579   0  535 536 0 0 0 0 0 0 585 586 0
C
C                    RING
```

```
C
3 4 9  532  534 412 414 582 584 462 464    0 417 418 0 0 0 0 0 0 467 468 0
3 5 9  531  533 511 513 581 583 561 563    0 519 520 0 0 0 0 0 0 569 570 0
C
C                    SUPPORT
C
6 6 9   501 502 537 538 551 552 587 588
6 6 9   521 522 539 540 571 572 589 590
6 6 9   501 537 521 539 551 587 571 589     0 541 542 0 0 0 0 0 0 591 592 0
6 8 9   502 538 622 640 552 588 672 690     0 543 544 0 0 0 0 0 0 593 594 0
C
C
C                    SECTOR 6
C
C
1 1 9  601 602 603 604 651 652 653 654
1 1 9  603 604 605 606 653 654 655 656
1 1 9  607 608 609 610 657 658 659 660
1 2 9  609 610 611 612 659 660 661 662
1 1 9  611 612 613 614 661 662 663 664
1 2 9  604 606 607 609 654 656 657 659     0 615 616 0 0 0 0 0 0 665 666 0
C
C
1 1 9  621  622  623  624 671 672 673 674
1 1 9  623  624  625  626 673 674 675 676
1 1 9  627  628  629  630 677 678 679 680
1 2 9  629  630  631  632 679 680 681 682
1 1 9  631  632  633  634 681 682 683 684
1 2 9  624  626  627  629 674 676 677 679   0  635 636 0 0 0 0 0 0 685 686 0
C
C                    RING
C
3 4 9  632  634 512 514 682 684 562 564    0 517 518 0 0 0 0 0 0 567 568 0
3 5 9  631  633 611 613 681 683 661 663    0 619 620 0 0 0 0 0 0 669 670 0
C
C                    SUPPORT
C
6 6 9   601 602 637 638 651 652 687 688
6 6 9   621 622 639 640 671 672 689 690
6 6 9   601 637 621 639 651 687 671 689     0 641 642 0 0 0 0 0 0 691 692 0
6 8 9   602 638 722 740 652 688 772 790     0 643 644 0 0 0 0 0 0 693 694 0
C
C
C                    SECTOR 7
C
C
1 1 9  701 702 703 704 751 752 753 754
1 1 9  703 704 705 706 753 754 755 756
1 1 9  707 708 709 710 757 758 759 760
1 2 9  709 710 711 712 759 760 761 762
1 1 9  711 712 713 714 761 762 763 764
1 2 9  704 706 707 709 754 756 757 759     0 715 716 0 0 0 0 0 0 765 766 0
C
C
1 1 9  721  722  723  724 771 772 773 774
1 1 9  723  724  725  726 773 774 775 776
1 1 9  727  728  729  730 777 778 779 780
1 2 9  729  730  731  732 779 780 781 782
1 1 9  731  732  733  734 781 782 783 784
```

```
1 2 9  724  726  727  729 774 776 777 779   0  735 736 0 0 0 0 0 0 785 786 0
C
C                        RING
C
3 4 9  732  734 612 614 782 784 662 664     0 617 618 0 0 0 0 0 0 667 668 0
3 5 9  731  733 711 713 781 783 761 763     0 719 720 0 0 0 0 0 0 769 770 0
C
C                        SUPPORT
C
6 6 9   701 702 737 738 751 752 787 788
6 6 9   721 722 739 740 771 772 789 790
6 6 9   701 737 721 739 751 787 771 789      0 741 742 0 0 0 0 0 0 791 792 0
6 8 9   702 738 822 840 752 788 872 890      0 743 744 0 0 0 0 0 0 793 794 0
C
C
C                        SECTOR 8
C
C
1 1 9  801 802 803 804 851 852 853 854
1 1 9  803 804 805 806 853 854 855 856
1 1 9  807 808 809 810 857 858 859 860
1 2 9  809 810 811 812 859 860 861 862
1 1 9  811 812 813 814 861 862 863 864
1 2 9  804 806 807 809 854 856 857 859      0 815 816 0 0 0 0 0 0 865 866 0
C
C
1 1 9  821  822  823  824 871 872 873 874
1 1 9  823  824  825  826 873 874 875 876
1 1 9  827  828  829  830 877 878 879 880
1 2 9  829  830  831  832 879 880 881 882
1 1 9  831  832  833  834 881 882 883 884
1 2 9  824  826  827  829 874 876 877 879   0  835 836 0 0 0 0 0 0 885 886 0
C
C                        RING
C
3 4 9  832  834 712 714 882 884 762 764     0 717 718 0 0 0 0 0 0 767 768 0
3 5 9  831  833 811 813 881 883 861 863     0 819 820 0 0 0 0 0 0 869 870 0
C
C                        SUPPORT
C
6 6 9   801 802 837 838 851 852 887 888
6 6 9   821 822 839 840 871 872 889 890
6 6 9   801 837 821 839 851 887 871 889      0 841 842 0 0 0 0 0 0 891 892 0
6 8 9   802 838  22  40 852 888  72  90     0 843 844 0 0 0 0 0 0 893 894 0
C
C
MESH
REFERENCE SPACING.LIST
1          1  C LIGAMENT SEGMENT
2          6  C LIGAMENT SEGMENT
3          1  C RING WIDTH
4          2  C RING SEGMENT (MINOR)
5         16  C RING SEGMENT (MAJOR)
6          1  C SUPPORT
7          2  C SUPPORT
8          5  C SUPPORT
9          1  C THICKNESS
C ****************************************
AXES
```

```
AXISNO. TYPE RELAXISNO NODE.NO  ANG2 ANG3
 4     2    2      0     90    0
 5     2    4      0      0   45
 6     2    4      0      0   90
 7     2    4      0      0  135
 8     2    4      0      0  180
 9     2    4      0      0  225
 10    2    4      0      0  270
 11    2    4      0      0  315
C ********************************************************
SIMILAR.NODES
ORIGINAL.NODE  NUMBER.OF.NODES  COPY.NODE  AXIS.OF.NEW.NODES
   1            94          201          5
   1            94          301          6
   1            94          401          7
   1            94          501          8
   1            94          601          9
   1            94          701         10
   1            94          801         11
C ********************************************************
PLATES.AND.SHELLS
PLATE.OR.SHELL.NUMBER MATERIAL.NUMBER THICKNESS
      1              11       35E-6
MATERIAL
MATERIAL.NUMBER    E     NU    RO
     11     2.07E11  0.31  8.9E3
RESTRAINTS
NODE.NUMBER PLANE AXIS.NO DIRECTION
  1      2    4     0
 37      2    4     0
C
C
CCCCCCCCCCCCCCCCCCCCCCCCCCCCCCCCCCCCCCCCCCCCCCCCCCCCCCCCCCCCCCCCCCCC
C
C             STATIC RESPONSE
C
C
CCCCCCCCCCCCCCCCCCCCCCCCCCCCCCCCCCCCCCCCCCCCCCCCCCCCCCCCCCCCCCCCCCCC
C LOADS
C CASE.OF.LOAD NODE.NUMBER DIRECTIONS.OF.LOAD VALUE.OF.LOAD
C   1        817           2          -1E-3
C   2         17           2          -.70710678E-3
C   2         17           1          -.70710678E-3
C   3         19           2          -.92387953E-3
C   3         19           1          -.38268343E-3
C
C
CCCCCCCCCCCCCCCCCCCCCCCCCCCCCCCCCCCCCCCCCCCCCCCCCCCCCCCCCCCCCCCCCCCC
C
C             DYNAMIC RESPONSE
C
C
CCCCCCCCCCCCCCCCCCCCCCCCCCCCCCCCCCCCCCCCCCCCCCCCCCCCCCCCCCCCCCCCCCCC
C MODES.AND.FREQUENCIES
C MODES START
C 2  1
C MASTERS
C NODE.NUMBER DIRECTION
C 817 12
```

```
C 17  12
C 19   12
C 719 12
C 819 12
C DAMPING
C CASE.OF.LOAD MODE DAMPING.RATIO
C 1 1 .01
C 1 2 .001
C
CCCC
```

```
C FREQUENCIES.FOR.ANALYSIS
C TYPE START FINISH STEP
C 1   20000  40000  10
END.OF.DATA
```

Appendix D

Secondary Response of a Vibratory Gyroscope

The secondary response of a general vibratory gyroscope (see figure 6.2) is governed by the generation of the Coriolis forces that act on an inertial mass undergoing both translation and rotation. As determined in appendix A, the magnitude of this force is given by:

$$F_c=2mV_p\Omega \tag{28}$$

where V_p is the velocity of the primary vibration and Ω is the angular rate of rotation. Now, assuming that the primary motion is a general harmonic vibration, described by:

$$A_p = A_0 e^{i\omega_p t} \tag{29}$$

then the velocity term can be described by:

$$V_p = \frac{dA_p}{dt} = A_0\omega_p e^{i\omega_p t} \tag{30}$$

$$= A_p\omega_p \tag{31}$$

Substituting equation 31 into 29 gives:

$$F_c = 2mA_p\omega_p\Omega \tag{32}$$

Now, for a viscously damped system under the influence of a harmonic force (say $F=F_oCos(\omega t)$ for example), it can be shown that the vibrational amplitude, A, is related to the Q-factor of the vibration by [84]:

$$A = Q \cdot x \tag{33}$$

where x is the static displacement of the system under the influence of a constant force of magnitude F_o. Given that from Hook's law:

$$F_o = -kx \tag{34}$$

(k being the mechanical spring constant of the single degree of freedom system) then substitution of equation 34 into 33 gives:

$$A = -\frac{Q \cdot F_0}{k} \qquad (35)$$

An expression for the secondary response of the vibratory gyroscope can now be formed by substitution of equation 32 into the general equation of 35:

$$A_s = -\frac{Q_s \cdot 2mA_p\omega_p\Omega}{k_s} \qquad (36)$$

Also, the angular frequency of the secondary vibration is determined by:

$$\omega_s = \sqrt{\frac{k_s}{m}} \qquad (36)$$

where k_s and m are the spring constant and mass of the vibrating element. Rearranging equation 36 gives:

$$m = \frac{k_s}{\omega_s^2} \qquad (37)$$

Substituting equation 37 into 36 gives:

$$A_s = -\frac{2k_sQ_sA_p\omega_p\Omega}{k_p\omega_s^2} \qquad (38)$$

For a well-tuned gyroscope, the spring constants of the primary and secondary motions, k_p and k_s, are equal, leading to the resonant frequencies of the primary and secondary modes to be matched i.e. $\omega_p=\omega_s=\omega$. The magnitude of the secondary response of a tuned gyroscope can therefore be simplified to:

$$A_s = \frac{2Q_sA_p}{\omega} \cdot \Omega \qquad (39)$$

In order to take into account the very different geometries of practical devices, it is necessary to introduce a constant term, the gyroscopic coupling factor *K*, into equation 39. Practically, this generally has a value in the range of 0.8 and 1.0. This finally leads to:

$$A_s = \frac{2KQ_sA_p}{\omega} \cdot \Omega \qquad (40)$$

Appendix E

Gyroscope Sensitivity

For the gyro structure given in figure 7.6 the electrode area *A*, can be found from:

$$A = \frac{a}{360°}[\pi D t] \qquad (44)$$

where *a* is the angle each electrode subtends from the centre of the ring, *D* is diameter of the ring, and *t* is the thickness of the structure. For *a* =35°, *D* =4mm and *t*=35μm, this gives an effective electrode area of $4.28 \cdot 10^{-8} m^2$.

The capacitance of each electrode is given by:

$$C = \frac{A\varepsilon_o}{d} \qquad (41)$$

where d is the static electrode spacing. Differentiating gives:

$$\frac{dC}{dd} = -\frac{A\varepsilon_o}{d^2} = \frac{\Delta C}{\Delta d} \qquad (42)$$

and rearranging:

$$|\Delta d| = \frac{d^2}{A\varepsilon_o}\Delta C \qquad (43)$$

where $\square C$ is the minimum resolvable capacitance change and $\square d$ is the corresponding minimum resolvable deflection of the electrode gap. Hence for an optimum electrode separation of 3μm (although not achievable with the current lithographic photomasks), the minimum detectable deflection of the ring can be calculated from equation (43) to be approximately 0.7nm.

Appendix F

Capacitive Coupling

The following diagram represents the equivalent electrical coupling arrangement between the drive and sense circuits.

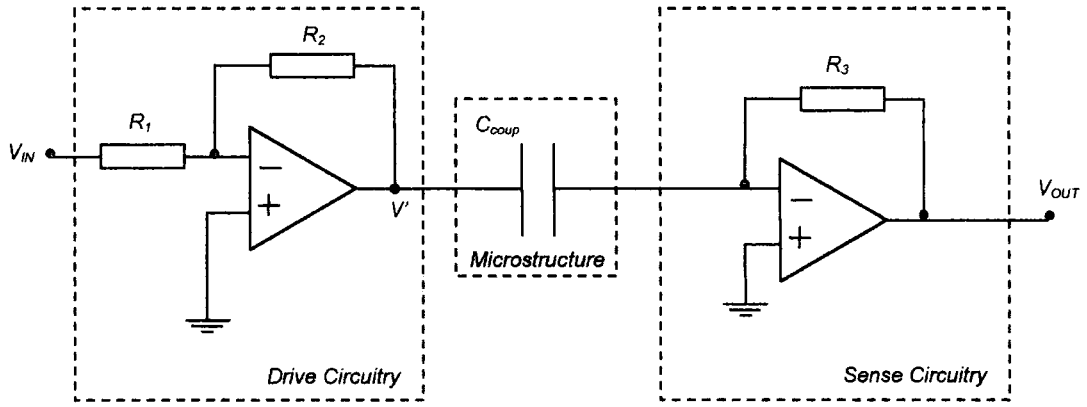

It can be shown that the output (V_{OUT}) and input (V_{IN}) are electrically coupled through the microstructure (C_{coup}) and the output is directly proportional to frequency of the input:

$$\frac{V'}{V_{IN}} = -\frac{R_2}{R_1} \tag{45}$$

$$\frac{V_{OUT}}{V'} = -\frac{R_3}{\left(1/j\omega C_{coup}\right)} = -j\omega R_3 C_{coup} \tag{46}$$

$$\left|\frac{V_{OUT}}{V'}\right| = -2\pi R_3 C_{coup} \cdot f \tag{47}$$

$$\left|\frac{V_{OUT}}{V_{IN}}\right| = \frac{2\pi R_2 R_3 C_{coup}}{R_1} \cdot f \tag{48}$$

$$\left|\frac{V_{OUT}}{V_{IN}}\right| \propto f \tag{49}$$

References

[1] J.Bryzek, 'Impact of MEMS technology on Society', *Sensors and Actuators A, **56** (1996) pp.1-9.*

[2] P.J.French, 'Surface versus Bulk Micromachining: The Contest for suitable Applications.', *Proc. Micromechanics Europe (MME) 1997, Southampton (UK), pp.18-30.*

[3] J.Söderkvist, 'Micromachined gyroscopes', *Sensors and Actuators A, **43** (1994) pp.65-71.*

[4] P.Gravesen, J.Branebjerg, O.S.Jensen, 'Microfluidics - A Review', *Proc. MicroMechanics Europe (MME) 1993, Neuchâtel (Switzerland) 1993, pp. 143-164.*

[5] *New Scientist, No. 2137, 6 June 1998, p.11.*

[6] K.E.Peterson, 'Silicon as a Mechanical Material', *Proc. IEEE, **70** No. 5 (1982) pp. 420-457.*

[7] J.W.Gardener, 'Microsensors', *Wiley (1994), Chapter 2.*

[8] E.Peeters, D.Lapadatu, W.Sansen and B.Peuers, 'Developments in Etch Stop Techniques', *Proc. MicroMechanics Europe (MME) 1993, Neuchâtel (Switzerland) 1993, pp. 35-49.*

[9] S.C.Chang, M.W.Putty, D.B.Hicks, C.H.Li, R.T.Howe, 'Resonant-Bridge Two-Axis Microaccelerometer', *Sensors and Actuators A, **21-23** (1990) pp.342-345.*

[10] J.Greenwood, 'Etched Silicon Vibrating Sensor', *J. Phys. E: Sci. Instrum., **17** (1984) pp. 650-652.*

[11] E.Stemme, G.Stemme, 'A Balanced Resonant Pressure Sensor', *Sensors and Actuators A, **21-23** (1990) 336-341.*

[12] A.J.Harris, J.S.Burdess, J.Cruickshank, D.Wood, G.Cooper, 'A Silicon Membrane Gyroscope with Electrostatic Actuation', *Electronic Letters, **31**, 21, (1995), pp. 1567-1568.*

[13] G.Stemme, 'Resonant Silicon Sensors', *J. Micromech. Microeng., **1** (1991) pp. 113-125.*

[14] S.Wolf and R.N.Tauber, 'Silicon Processing', *Lattice Press 1986, Chp.16.*

[15] H.Jansen, H.Gardeniers, M. de Boer, M.Elwenspoek, J. Fluitman, 'A Survey on the Reactive Ion Etching of Silicon in Microtechnology', *J. Micromech. Microeng.* ***6*** *(1996) pp. 14-28.*

[16] Y.Gianchandani, K.Najafi, 'Micro-Sized, High Aspect Ratio Bulk Silicon Micromechanical Devices', *Proc. Microelectromechanical Systems 1992, Travemünde (Germany), February 4-7 (1992) pp. 208-213.*

[17] J. Bernstein, S.Cho, A.T. King, A. Kourepenis, P. Maciel, M. Weinberg, 'A Micromachined Comb-Drive Tuning Fork Rate Gyroscope', *Proc. Microelectromechanical Systems, Florida USA (1993), pp. 143-146.*

[18] N.Tas, T.Sonnenberg, H.Jansen, R.Legtenbergm and M.Elwenspoek, 'Stiction in Surface Micromachining', *J. Micromech. Microeng.,* ***6,*** *(1996), pp.385-397.*

[19] M.Bartek, R.F.Wolffenbuttel, 'Dry Release of Metal Structures in Oxygen Plasma: Process Characterisation and Optimization', *Proc. Micromechanics Europe (MME) 1997, Southampton (UK), pp.72-74.*

[20] D.Kobayagi, T.Hirano, 'An Integrated Lateral Tunneling Unit', *Proc. Microelectromechanical Systems, Travemunde (Germany), Feb 4-7 (1992) pp. 214-219.*

[21] M.Habibi, E.Lueder, T.Kallfass, D.Horst, 'A Surface Micromachined Capacitive Absolute Pressure Sensor Array on a Glass Substrate', *Sensors and Actuators A,* ***46*** *(1995) pp.125-128.*

[22] L.J.Ristic, R.Gutteridge, B.Dunn, D.Mietus and P.Bennett, 'Surface Micromachined Polysilicon Accelerometer', *Technical Digest IEEE Solid State Sensor and Actuator Workshop, Hilton Head, SC, 1992, pp.118-121*

[23] S.Tachi, K.Tsujimoto, S.Okudaira, 'Low-Temperature Reactive Ion Etching and Microwave Plasma Etching of Silicon', *Appl. Phys. Lett.,* ***52*** *8 (1988) pp. 616-618*

[24] K.Murakami, Y.Wakabayashi, K.Minami, M.Esashi 'Cryogenic Dry Etching for High Aspect Ratio Microstructures', *Proc. IEEE Micoelectromechanical Systems Fort Lauderdale, Florida (1993) pp. 65-70.*

[25] 'Advanced Silicon Anisotropic Processes', *European Semiconductor July/August (1997) pp.35-39.*

[26] E.H.Klaassen, K.Petersen, J.M.Noworolski, J.Logan, N.I.Maluf, J.Brown, C.Storment, W. McCulley, G.T.A.Kovas, 'Silicon Fusion Bonding and Deep Reactive Ion Etching: A New Technology for Microstructures', *Sensors and Actuators A,* ***52*** *(1996) pp.132-139.*

[27] E.W.Becker, W.Ehrfeld, P.Hagmann, A.Maner, D.Münchmeyer, 'Fabrication of Microstructures with High Aspect Ratios and Great Structural Heights by Synchrotron Radiation Lithography, Galvanoformung, and Plastic Moulding', *Microelectronic Engineering,* ***4*** *(1986) pp. 35-56.*

[28] P.Bley, 'The LIGA Process for Fabrication of Three Dimensional Microscale Structures', *Interdisciplinary Science Reviews,* ***18*** *3 (1993) pp. 267-272.*

[29] C.Burbaum, J.Mohr, P.Bley, W.Ehrfeld, 'Fabrication of Capacitive Acceleration Sensors by the LIGA Technique', *Sensors and Actuators A,* ***25-27*** *(1991) pp. 559-563.*

[30] H.Guckel, K.J.Skrobis, T.R.Christenson, J.Klein, 'Micromechanics for Actuators via Deep X-Ray Lithography', *Proc. SPIE, Orlando (Florida 1994) pp. 39-47.*

[31] K.Suzuki, 'Study on Fine Patterning Processes with a Thick Resist', *Sensors and Actuators A,* ***43*** *(1994) pp. 254-258.*

[32] H.Miyajima, M.Mehregany, 'High-Aspect-Ratio Photolithography for MEMS Applications.', *J. Microelectromechanical Systems,* ***4*** *4 (1995) pp. 220-228.*

[33] A.Bruno Frazier, M.G.Allen, 'Metallic Microstructures Fabricated Using Photosensitive Polyimide Electroplating Moulds.', *J. Microelectromechanical Systems,* ***2*** *2 (1993) pp. 87-94.*

[34] G.Engelmann, O.Ehrmann, J.Simon, H.Reichl, 'Fabrication of High Depth-to-Width Aspect Ratio Microstructures', *Proc. Microelectromechanical Systems, Travemunde Germany, (1992) pp.93-98.*

[35] G.Engelmann, O.Ehrmann, R.Leutenbauer, H.Schmitz, H.Reichl, 'Fabrication of Perfectly Three dimensional Microstructures by UV depth Lithography', *SPIE* ***2045*** *39 (1994) pp. 306-313.*

[36] B.Löchel, A.Maciossek, M.König, H.L.Huber, G.Bauer, 'Fabrication of Magnetic Microstructures by Using Thick Layer Resists', *Microelectronic Engineering* ***21*** *(1993) pp. 463-466.*

[37] E. Cullmann, B.Löchel, G.Engelmann, C.Reyerse, '3D Structures for Micro-System Technology using Proximity Lithography.', *Solid State Technology, March 1993 pp.93-96*

[38] H.Lorenz, M.Despont, N.Fahrni, N.LaBianca, P.Renaud, P.Vettiger, 'SU-8: A Low Cost Negative Resist for MEMS', *J. Micromech. Microeng. 7 (1997) pp. 121-124.*

[39] Materials Science and Technology, *Volume 15, VCH(1991).*

[40] Shipley Technical Data Information

[41] Hoechst Technical Data Information.

[42] Polytec Reference Manual.

[43] J.S.Burdess, A.J.Harris, D.Wood, R.J.Pitcher, D.Glennie, 'A System for the Dynamic Characterisation of Microstructures', *J. Microelectromechanical Systems, **6** (1997) pp. 322-328.*

[44] D.J.Ewins, 'Modal Testing: Theory and Practice', *Research Studies Press 1984.*

[45] S.S.Rao, 'Mechanical Vibrations', *Addison-Wesley 1986 p.399.*

[46] F.Lärmer, A.Schilp, K.Funk, C.Burrer, 'Experimental Characterisation of Dynamic Micromechanical Transducers', *J. Micromech. Microeng. **6** (1996) pp. 177-186.*

[47] D.F.L.Jenkins, M.J.Cunningham, W.W.Clegg, M.M.Bakush, 'Measurement of the Modal Shapes of Inhomogenous Cantilevers using Optical Beam Deflection', *Meas. Sci. Technol. **6** (1995) pp. 160-166*

[48] M.Dufour, M.T.Delaye, F.Michel, J.S.Danel, B.Diem, G.Delapierre, 'A Comparison Between Micromachined Pressure Sensors using Quartz or Silicon Vibrationg Beams', *Sensors and Actuators A, **34** (1992) pp. 201-209.*

[49] J.D.Zook, D.W.Burns, H.Guckel, J.J.Sniegowski, R.L.Engelstad, Z.Feng, 'Characteristics of Polysilicon Resonant Microbeams', *Sensors and Actuators A, **35** (1992) pp. 51-59.*

[50] L.Kiesewetter, J.M.Zhang, D.Houdeau, A.Steckenborn, 'Determination of Young's Moduli of Micromechanical Thin films using the Resonance Method', *Sensors and Actuators A, **35** (1992) pp. 153-159.*

[51] A.Lawrence, 'Modern Inertial Technology: Navigation, Guidance and Control', *Springer-Verlag (New York) 1993.*

[52] R.M.Langdon, 'The Vibrating Cylinder Gyro', *The Marconi Review, Fourth Quarter,* 1982 pp. 231-249.

[53] H.T. Califino, 'Minitact Gyroscope - The Low Cost Alternative', *IEEE AES Systems Magazine (1994) pp. 12-16.*

[54] British Aerospace Technical Data (Product Brochure).

[55] C.B.Williams, C.Shearwood, P.H.Mellor, A.D.Mattingley, M.R.J.Gibbs, R.B.Yates, 'Initial Fabrication of a Micro-Induction Gyroscope', *Microelectronic Engineering, **30** (1996) pp. 531-534.*

[56] *Science 1998, **280,** 5364, pp.28.*

[57] Murata Electronics Company Technical Data.

[58] A. Hiroshi, T. Yoshida, K. Turuga, 'Piezoelectric-Ceramic Cylinder Vibratory Gyroscope', *Jpn. J. Appl. Phys., **31** (1992) pp. 3061-3063.*

[59] K.Shuta, A. Hiroshi, 'Compact Vibratory Gyroscope', *Jpn. J. Appl. Phys., **34** (1995) pp. 2601-2603.*

[60] Systron Donner Technical Data (http://www.systron.com/)

[61] A.Satoh, K. Ohnishi, K. Sakurai, Y. Tomikawa, 'Finite Element Analysis of Trident Type Tuning Fork Resonator for Vibratory Gyroscope', *Jpn. J. Appl. Phys., **34** (1995) pp. 2604 -2609.*

[62] E.J.Loper, D.D.Lynch, 'Projected System Performance based on recent HRG Test Results', *Proc. 5TH Digital Avionics System Conference, Washington 1983*

[63] J.T. Anders, R. Pearson, 'Applications of the START Vibratory Gyroscope', *GEC Review, **9,** 3, (1994), pp.168-175.*

[64] A.Reppich, R.Willig, 'Yaw rate sensor for Vehicle Dynamics Control System', *Symposium Gyro Technology, Germany 1995, Chp 16, pp. 287-296.*

[65] B.Kanani, J.S.Burdess, 'The Piezoelectric Cylinder Gyroscope', *Proc. Inst. Mechanical Engineers, Part C, **200,** No.4, pp.271-281.*

[66] J.C.Stiles, 'Vibrating Ring Gyro', *US Patent No. 3,924,475 (1975).*

[67] B.Johnson, I.M.Longden, 'Vibrating Structure Gyroscopes and their Application', *Proc. Symposium Gyro Technology, 1994.*

[68] K.Maenaka, T.Shiozawa, 'A study of silicon angular rate sensors using anisotropic etching technology', *Sensors and Actuators A, **43,** (1994), pp. 72-77*

[69] K. Maenaka, T.Fujita, Y. Konishi, M. Maeda, 'Analysis of a Highly Sensitive Silicon Gyroscope with a Cantilever beams as Vibrating Mass', *Sensors and Actuators A, **54**, (1996), pp. 568-573.*

[70] F.Paoletti, M.A. Gretillat, N.F. de Rooij, 'A Silicon Micromachined Vibrating Gyroscope with Piezoresistive Detection and Electromagnetic Excitation', *Symposium on Gyro Technology (1996), pp.162-167.*

[71] K.Tanaka, Y.Mochida, M.Sugimoto, T. Hasegawa, K. Atsuchi, K. Ohwada, 'A Micromachined Vibrating Gyroscope', *Sensors and Actuators A, **50**, (1995), pp. 111-115.*

[72] Electronics Times, No. 846, March 1997.

[73] M.W.Putty, K.Najafi, 'A Micromachined Vibrating Ring Gyroscope', Solid State Sensor and Actuator Workshop, South Carolina, June 1994, pp. 213-220.

[74] M.W.Putty, D.S.Eddy, 'Microstructure for Vibratory Gyroscope', *US Patent No. 5,450,751 (1995).*

[75] P.Greiff, B.Boxenhorn, T.King, L.Niles, 'Silicon Monolithic Micromechanical Gyroscope', *Proc. IEEE 1991, pp. 966-968.*

[76] W.Geiger, B.Folkmer, U.Sobe, H.Sandmaier, W.Lang, 'New Designs of Micromachined Rate Gyroscopes with Decoupled Oscillation Modes', *Sensors and Actuators A, **66**, (1998), pp.118-124.*

[77] T.Bourouina, A.Exertier, S.Spirkovitch, B.Chaumet, E.Pleska, 'Preliminary Results on a Silicon Gyrometer Based on Acoustic Mode Coupling in Small Cavities', *J. Microelectromechanical Systems, **6** 4 (1997) pp.347-354.*

[78] British Aerospace Press Release (http://www.bae.co.uk/)

[79] *New Scientist, No. 2014 October 1997 p.23*

[80] J.P.D.Hartog, 'Mechanical Vibrations', *McGraw-Hill 1956, p.165*

[81] A.J.Harris, J.S.Burdess, D.Wood, R.Langford, G.Williams, M.C.L.Ward and M.E.McNie, 'Design, Fabrication and Testing of a Silicon Ring Gyroscope', *Submitted to J. Micromech. Microeng.*

[82] J.T.Kung, H.Lee, 'An Integrated Air-Gap-Capacitor Pressure Sensor and Digital Readout with Sub-100 Atto-farad Resolution', *J.Microelectromechanical J. Microelectromechanical Systems, **1** (1992) pp.121-129.*

[83] R.N.Arnold and L.Maunder, 'Gyrodynamics and its Engineering Applications', *Academic Press 1961, chapter 3.*

[84] S.S.Rao, 'Mechanical Vibrations', *Addison-Wesley 1986 p.123-127.*